Revisiting Nitride Semiconductors: Epilayers, p-Type Doping and Nanowires

Chito E. Kendrick

A thesis submitted in partial fulfilment
of the requirements for the degree of
Doctor of Philosophy
in
Electrical and Electronic Engineering
at the
University of Canterbury,
Christchurch, New Zealand.

September 2008

ABSTRACT

This dissertation investigates the growth of high quality GaN and InN thin films by plasma assisted molecular beam epitaxy (PAMBE). It also explores the growth of self-seeded GaN branching nanowires and p-type doping of InN, two topics of particular interest at present.

The growth of high quality III-Nitride semiconductor thin films have been shown to be dependent on the group-III (metal) to nitrogen ratio. A metal-rich growth environment enhances the diffusion of the group-III adatoms through the formation of a group-III adlayer. By using a metal-rich growth environment, determined by growth rate studies using laser reflection interferometry or RHEED analysis of the surface, both GaN and InN films have been grown with a smooth surface morphology. Additionally the smooth surface morphology has beneficial effects on the electrical and optical properties of both materials. However, with the growth using a metal-rich environment, group-III droplets are present on all film surfaces, which can be an issue for device fabrication, as they produce facets in the crystal structure due to enhanced growth rates.

MBE growth of GaN nanowires via the vapour liquid solid (VLS) and vapour solid (VS) growth techniques have so far been based on the N–rich growth regime. However, we have shown that the Ga–rich growth regime can be used to grow self-seeded one dimensional and hierarchical GaN nanowires. 7 μm long hierarchical GaN nanowires with at least three branches were grown and shown to have a high crystalline quality. The suggested growth mechanism is a self-seeding VLS process driven by liquid phase epitaxy at the nanoscale, while the branching growth was nucleated due to the Ga–rich growth regime by excess Ga droplets forming on the trunk during growth. The growth

of vertical GaN nanowires has also been achieved using the same self-seeding process and the critical parameter seems to be the Ga to N ratio. Also, the growth rate of the Ga–rich grown GaN nanowires can supersede the growth rates reported from N–rich grown GaN nanowires by at least a factor of two.

The fabrication of vertical and planar GaN nanowire devices has been demonstrated in this study. Two point and three point contacts were fabricated to the branching GaN nanowires in the planar direction with resistive measurements ranging from 200 - 900 $k\Omega$, similar to chemical vapour deposition and MBE grown GaN nanowires. The nonlinear current-voltage characteristics from the three point contacts may lead to unique nano-devices. The planar nanowires have also shown to have potential as UV detectors. Schottky diodes were fabricated on the vertical nanowires, with values for the barrier heights consistent with bulk diodes.

Mg and Zn doping studies of InN were also performed. Both InN:Mg and InN:Zn have strong photoluminescence only at low doping concentrations. However, the InN:Mg films have reduced mobilities with increased Mg content, whereas the mobility determined from the InN:Zn films is independent of Zn. When the InN:Zn film quality was improved by growing under the In–rich growth regime, electrochemical capacitance-voltage results suggest n–type conductivity, and strong photoluminescence was obtained from all of the films with four features seen at 0.719 eV, 0.668 eV, 0.602 eV and 0.547 eV. The features at 0.719 eV and 0.668 eV are possibly due to a near band edge to valence band or shallow acceptor transition, while the 0.547 eV has an activation energy of 60 meV suggesting a deep level acceptor.

ACKNOWLEDGEMENT

Firstly I have to thank my supervisor Associate Professor Steven M. Durbin for his experience and guidance. I would also like to thank my co-supervisor Professor Richard Blaikie for helping with issues facing the development of the nanowire devices, and his time with getting the AFM set up for I-V measurements.

Operation of the molecular beam epitaxy system requires a team of graduate students. Over my time as a graduate student I have had the pleasure with working with Daniel Lee (III-nitrides), Dr. Phillip Anderson (III-nitrides), Dr. William Lee (ZnO) and presently Jess Chai (ZnO) who will be lead graduate student when I hand in this dissertation. These people have made the lab an enjoyable place to work and also without them the MBE system would not have run as efficiently. A special thank you has to go to Dr. Phillip Anderson, as without his strange way of conducting experiments the direction of my dissertation may have been very different.

Outside of operating the MBE, I have to thank the two post-docs, Dr. Robert Kinsey and Dr. Craig Swartz, and also Mr. Martin Allen (ZnO Schottky diodes) for allowing me to discuss ideas with them and also helping with laboratory work. Additionally I would like to thank the laboratory technicians, Mr Gary Turner and Ms Helen Devereux, for keeping the laboratory well stocked, purchasing our requests, signing the piles of liquid nitrogen request forms and keeping the equipment running.

There is always a time in research when you want to conduct an experiment and the equipment is unavailable. In my case this was overcome through people from other departments and universities who allocated some of their time to perform experiments on my samples. Optical measurements were performed by Associate Professor Roger Reeves (InN photoluminescence), Mr. Reuben Mendelsberg (GaN photoluminescence

and weekend fishing buddy) and Mr. Y. W. Song (InN photoluminescence) in the Department of Physics and Astronomy at the University of Canterbury. TEM measurements were performed with Dr. Richard Tilley at the School of Chemical and Physical Sciences at Victoria University of Wellington. Cathodoluminescence measurements by Professor Kobayashi (Cosmo) at Waseda University in Tokyo are much appreciated, as are variable magnetic field Hall effect measurements by Professor Tom Myers and Dr. Craig Swartz in the Department of Physics at West Virginia University.

Behind all good research is a support group. The MacDiarmid Institute for Advanced Materials and Nanotechnology was co-founded by the University of Canterbury and has been my support through my research. The MacDiarmid Institute provided funding for my research through a Doctoral scholarship and allowed me to attend overseas conferences to present my results.

Finally I would like to thank my parents for supporting my decisions in life. Also to my wife who has supported me through my graduate years and accepting that sometimes I am going to be spending the night at University.

CONTENTS

Abstract i
Acknowledgements iii
List of Figures vii
List of Tables xvi

CHAPTER 1 INTRODUCTION 1
1.1 Motivation 1
1.2 Overview of Nitride Semiconductors 4
1.2.1 GaN 5
1.2.2 InN 6
1.3 Gallium Nitride Nanowires by MBE 9
1.4 Thesis Outline 14

CHAPTER 2 GROWTH AND CHARACTERISATION TECHNIQUES 15
2.1 Epitaxy 15
2.2 Fundamentals of PAMBE 17
2.2.1 University of Canterbury MBE System 17
2.2.2 Substrate Heating 18
2.2.3 Group III Source 18
2.2.4 Nitrogen Source 22
2.2.5 Reflection High Energy Electron Diffraction 25
2.2.6 Laser Reflection Interferometry 25
2.3 Surface Characterisation 27
2.3.1 Atomic Force Microscopy 27
2.3.2 Scanning Electron Microscopy 28
2.4 Optical Characterisation 29
2.4.1 Photoluminescence 29
2.4.2 Cathodoluminescence 29
2.5 Electrical Characterisation 30
2.5.1 Single Magnetic Field Hall Effect 30
2.5.2 Variable Magnetic Field Hall Effect 34
2.5.3 Capacitance Voltage Profiling 37
2.5.4 Electrochemical Capacitance Voltage Profiling 39

CHAPTER 3 GROWTH OF GALLIUM NITRIDE AND INDIUM NITRIDE EPILAYERS 44
3.1 Gallium Nitride Growth 44
3.1.1 Gallium Nitride Growth Regimes: N–rich, Ga–rich and Intermediate 45
3.1.2 Determination of the Growth Regimes 49
3.1.3 Gallium Flux Dependence 51
3.1.4 Temperature Effect 57
3.2 Indium Nitride Growth 61
3.2.1 Indium Nitride Growth Regimes 61
3.2.2 Determination of the InN Growth Regimes 64
3.2.3 Substrate Choice 69
3.2.4 Film Thickness Effect on the InN Film Quality 73
3.2.5 Imaging of the Accumulation Layer 78
3.3 Summary 78

CHAPTER 4 SELF SEEDED GALLIUM NITRIDE NANOWIRES 82
4.1 Unexpected Growth 82
4.2 Analysing the Branching Nanowires 83
4.2.1 Branching Nanowire Composition 86
4.2.2 Branching Nanowire Structural Analysis 87
4.2.3 Optical Properties of the Branching Nanowires 93
4.3 Explaining the Growth 95
4.3.1 Role of the Catalyst 95
4.3.2 Supersaturation and Nanowire Growth 100
4.3.3 Branching Nucleation and Growth 102
4.3.4 Growth Sequence 104
4.4 Issues Pertaining to Control of Growth 106
4.4.1 GaN Nanowire Growth Rate 106
4.4.2 Effect of Nitrogen Species 107
4.4.3 Nanowire Growth Mode 108
4.4.4 Nanowire Diameter Control 110
4.5 Summary 111

CHAPTER 5 GALLIUM NITRIDE NANOWIRE DEVICE FABRICATION AND CHARACTERISATION 113
5.1 Planar Devices 113
5.1.1 Fabrication 113
5.1.2 I-V Characteristics 118
5.2 Vertical Devices 126
5.2.1 Fabrication 127
5.2.2 I-V Characteristics 128
5.3 Summary 131

CHAPTER 6 ACCEPTOR DOPING OF INDIUM NITRIDE 133
6.1 Magnesium Doping Theory 137
6.2 Magnesium Doping 140
6.3 Structural Analysis 142
6.4 Magnesium Content 143
6.5 Polarity 143
6.6 Electrical Trends 146
6.7 ECV Analysis 148
6.8 Optical Measurements 150
6.9 Summary 160

CHAPTER 7 ZINC-DOPING OF III-NITRIDES 162
7.1 Overview 163
7.2 Electrical and Optical Properties of Zinc–doped Indium Nitride on (111)YSZ 165
7.3 Zinc–doped Indium Nitride on Gallium Nitride 168
7.4 Summary 178

CHAPTER 8 CONCLUSIONS AND FUTURE WORK 180
8.1 III-nitride Thin Films 180
8.2 Branching Gallium Nitride Nanowires 182
8.3 Nanowire Devices 185
8.4 Indium Nitride Doping 186

References 190
Appendix A 210

LIST OF FIGURES

1.1 Span of the accepted InGaN band gap prior to and subsequent to 2001 as compared to the standard solar spectrum known as AM1.5g. 2

1.2 Moore's Law. 4

1.3 Wurtzite and zincblende crystal lattice structure. 5

1.4 Publications per year for nanostructures, based on advanced search on the Web of Science using (nanowire* and nanorod*). 10

1.5 Schematic of the vapour liquid solid process of Wagner and Ellis. 11

1.6 Number of times Wagner and Ellis 1964 paper has been cited plotted as a function of publication year. 12

2.1 Plan view of the University of Canterbury 430 Perkin Elmer MBE system. 19

2.2 Diagram of a typical effusion cell. 20

2.3 Schematic of the eight effusion cell ports in relation to the substrate. 21

2.4 Flux curves for indium and gallium determined using equation 2.2; the cross-hatched region is the typical operation zone for the effusion cells in this study. 22

2.5 OES spectrum taken at 100 W RF and a nitrogen chamber pressure of 1×10^{-5} Torr, using the 276 hole aperture plate. 24

2.6 RHEED images taken from GaN a)under metal-rich conditions leading to 2D growth also shown is the direct beam and b) under nitrogen-rich conditions leading to 3D growth. 26

2.7 Schematic of the laser reflection interferometry system. 27

2.8 AFM imaging issues due to feature size relative to tip geometry. The top image shows the real surface and the bottom represents what would be expected from a line scan. 28

2.9 Schematic representation of donor- or acceptor- related and direct radiative recombinations. 30

2.10 Schematic illustrating the Hall effect in a n-type sample. 31

2.11 Model of a three layer semiconductor, containing a degenerate buffer layer, bulk layer and a surface accumulation layer. 35

2.12 Energy band diagram for the ideal metal semiconductor contact, for the case when the metal work function ϕ_M is greater than the semiconductor work function ϕ_S: (a) instant of contact formation and (b) equilibrium conditions. 38

2.13 Charge density as a function of position in the depletion approximation. 39

2.14 Schematic diagram of the electrochemical capacitance voltage measurement setup. 41

2.15 Current-voltage plot from the ECV measurement of film 683-InN/YSZ(111) under dark and illuminated conditions. Inset is a magnified view of the stable region showing some decrease in the current when illuminated. 42

3.1 Evolution of the GaN growth regimes for GaN grown by MBE. a) Heying et al. published in 2000, b) Adelmann et al. published in 2002, and c) Koblmüller et al. published in 2007. 46

3.2 Reflection interferometry analysis using the semiconductor laser. 49

3.3 Growth rate study for Ga-polar and N-polar GaN. 51

3.4 SEM images of GaN films grown to resolve the growth regime. 52

3.5 AFM image of film 633-GaN-GaN, grown under intermediate regime conditions. 53

3.6 Photoluminescence (log scale) from the N–rich growth regime film 632–GaN–GaN. 55

3.7 Photoluminescence (log scale) from the intermediate growth regime film 633–GaN–GaN. 56

3.8 Full spectrum of the GaN films showing the difference in the UV band and the defect band at 2.5 eV. 56

3.9 SEM and RHEED images (inset) of the temperature dependent GaN growths. Top left: 667–GaN–GaN (730°C); Top right: 633-GaN–GaN (750°C); bottom left: 635–GaN–GaN (770°C); and bottom right: 636–GaN–GaN (790°C). 59

3.10 Electrical properties of the substrate temperature dependent GaN growths. 60

3.11 Near band edge 4 K photoluminescence (log scale) of the temperature dependent GaN growths. 62

3.12 4 K photoluminescence (log scale) of the temperature dependent GaN growths across the visible and UV range. 62

3.13 Initial InN growth rate diagram published in 2006 by Gallinat et al., In-polar growth rate diagram published in 2007 by Gallinat et al., N-polar growth rate diagram published in 2007 by Koblmüller et al. 65

3.14 RHEED sequence for InN on (111)YSZ (film 634–InN–YSZ(111)) for different In fluxes. 66

3.15 Surface morphology of the etched InN/(111)YSZ film grown under In-rich conditions. 67

3.16 QMSA plot of an InN film on (111)YSZ, as measured by variable magnetic field Hall effect at 150 K. 68

3.17 Photoluminescence from the InN film (637–InN–InN) grown under In–rich conditions. 69

3.18 RHEED spacing for InN/(111)YSZ and InN(GaN); the InN/GaN plot shows the absolute values as the RHEED spacing of GaN is larger than InN. 71

3.19 SEM images of the InN/GaN films a) grown under In-rich conditions (660–InN–GaN) and b) grown under near N-rich conditions (657–InN–GaN). 72

3.20 Electrical properties for the thickness dependent InN/YSZ(111) films using single magnetic field Hall effect to determine the electrical properties. 76

3.21 Comparison of the electrical properties determined using single magnetic field Hall effect and variable magnetic field Hall effect, for the thickness dependent InN/YSZ(111) films. 77

3.22 Photoluminescence spectra from the thickness dependent InN/YSZ(111) thin films, a) 5000 nm b) 500 nm, c) 200 nm, d) 100 nm, e) 50 nm and f) 5 nm. 79

3.23 Capacitance versus forward bias voltage obtained using ECV with 0.2 molar NaOH and 0.2 molar EDTA electrolyte at a frequency of 3 kHz; also shown is C^{-2} versus voltage. 80

3.24 Carrier concentration versus depth determined using ECV, with a 0.2 molar NaOH and 0.2 molar EDTA electrolyte at a frequency of 3 kHz. 80

4.1 a) Gallium flux dependent growth sequence for GaN on sapphire. b) Subsequent temperature dependent growth of GaN on the same substrate used in the gallium flux dependent growth. 84

4.2 SEM micrographs taken for several regions of the substrate. 85

4.3 EDS analysis of the branching GaN nanowires that were dispersed onto a silicon substrate to reduce the imaging from the GaN substrate. 88

4.4 SEM imaging a branching GaN nanowire with the gallium droplets removed by wetting with HCl. 89

4.5 TEM images showing surface morphology of polar and non-polar nanowire growth: left – GaN trunk grown in the c-axis direction (polar surface); center – GaN branch growth in the m-axis direction (non-polar direction), and right – Junction region. 89

4.6 SAED analysis of the branch to trunk junction. 90

4.7 HRTEM images of the the crystal structure in the branching GaP nanowires and branching InAs nanowires of Dick et al. 91

4.8 Analysis of 20 GaN branching nanowires, extracting a) number of branches versus trunk length (the solid line is a linear fit through the data points showing an increasing number of branches with trunk length), b) distance between pairs of branches, as describe by the inset (the solid line is a linear fit through all the data points, while the dash line is a linear fit ignoring the distance of the first branch to the tip of the trunk) and c) length of branches compared to position on trunk, as describe by the inset (the line is a linear fit through all the data points, showing that branches near the base have a longer length). 92

4.9 Cathodoluminescence, conducted at 80 K, examining a single GaN nanowire and the interface of the nanowire with the GaN underlying epilayer. The nanowire exhibits luminescence at 3.44 eV (360 nm), while the interface of the nanowire with the GaN epilayer luminescence at 3.1 eV (400 nm). 94

4.10 SEM images of GaN of a) Ga deposited on sapphire, b) Ga deposited on GaN and c) growth using the Ga–rich droplet formation. 98

4.11 Droplet contact angle dependence on the interfacial energies, a) non-wetting and b) wetting. 98

4.12 HCl etching of the micron size gallium droplets that form during the nanowire growth. 101

4.13 Branch nucleation through the accumulation of excess gallium on the trunk. 102

4.14 Self–seeding GaN nanowires that have a secondary droplet near the droplet of the trunk. 103

4.15 Self-seeding GaN nanowire process diagram. 105

4.16 Additional self-seeded growths of GaN nanowires/rods using the growth diagram in fig. 4.15. 106

4.17 Optical emission spectroscopy for a) atomic nitrogen and b) molecular nitrogen. 108

4.18 Growth rate dependence on the nanowire diameter, obtained from the vertical GaN nanostructures. 109

4.19 Modification of the diameter of the GaN nanowires by adjusting the gallium flux during growth. 111

5.1 Typical structures of a) planar and b) vertical nanowire devices without a gating contact. 114

5.2 SEM micrograph taken of a GaN nanowire that was attempted to be contacted, which exhibits both incomplete metal wrapping and also the nanowire is not flat on the Si_3N_4 surface. The 116

5.3 Process sequence used to fabricate contacts to the branching GaN nanowires. a) Starting with a Si_3N_4/Si substrate, b) nanowires are applied, c) 400 nm PMMA bilayer is spun on, d) markers are exposed using the EBL system, e) Ti/Au (10 nm/40 nm) contacts evaporated, f) markers are lifted off, g) 800 nm PMMA bilayer is spun on, h) contacts to the nanowire are exposed, i) Ti/Au (10 nm/90 nm) contacts evaporated and j) contacts are lifted off in boiling acetone. 117

5.4 SEM image of a GaN nanowire that has been embedded into a PMMA layer, which was exposed with a dose twenty times stronger than typically required to expose contact areas into electron beam resist, then a Ti/Au contact has been applied on top of the PMMA. 118

5.5 a) Non-linear I-V from the GaN nanowires, which can be represented as back to back leaky diodes (shown in the inset). 119

5.6 I-V scans taken from branching GaN nanowires that exhibited linear I-V. 121

5.7 The resistivity of the GaN nanowires as a function of the nanowire diameter. 121

5.8 (a) Branching GaN nanowire device. (b) Current-voltage measurements for all combination of terminals. 123

5.9 Gated current–voltage characteristics of the three terminal contacted branching GaN nanowire shown in 5.8a, with linear and log plots. 124

5.10 I-V from a GaN nanowire under dark conditions and then illuminated with a UV lamp. 125

5.11 Transition from a) UV on to off and b) UV off to on, using a 100 mV bias applied across the GaN nanowire. 126

5.12 I-V from the attempted FET structure using the silicon substrate as the gate. 127

5.13 GaN nanowires from film 535-GaN-GaSa. 128

5.14 AFM setup for measuring the I-V from the vertical GaN nanowires without the PMMA layer. 130

5.15 I-V measurement taken from the GaN nanowires using the gold coated AFM tip. a) linear scale and b) log scale. 130

5.16 Semilog plot of the current - voltage characteristics of GaN nanowires contacted with gold, silver and Ti/Al contact pads respectively, fabricated by evaporating through a shadow mask placed in contact to a sample of GaN nanowires coated in PMMA and etched in HCl. 132

6.1 Band diagrams illustrating the ionisation of donors and acceptors with increasing temperature. 134

6.2 Abbreviated periodic table highlighting possible acceptor (blue) and donor (red) dopants for III-nitride semiconductors. 135

6.3 Dopant incorporation into the crystal lattice: a) substitution; b) interstitial; and c) complex. 136

6.4 Quantitative mobility spectrum analysis (QMSA) of a Mg-doped InN film showing a clear hole feature at approximately $650 cm^2 V^{-1} s^{-1}$. 139

6.5 Theoretical flux curves for magnesium and indium. 141

6.6 SEM images from the InN:Mg films; inset are the corresponding RHEED images at end of growth. 144

6.7 Magnesium incorporation into InN, grown under N–rich conditions, based on SIMS analysis. 145

6.8 Valence band XPS spectra from the InN:Mg films. 146

6.9 Room temperature electrical properties from the InN:Mg films from single magnetic field Hall effect, as a function of Mg flux. a) electron concentration; b) electron mobility. 149

6.10 ECV results from the InN:Mg/YSZ(111) films, using a KOH solution as the electrolyte. 151

6.11 4 K Photoluminescence spectra of InN:Mg on (111)YSZ obtained using a 532 nm diode laser and an InSb detector. 154

6.12 Photoluminescence peak position a) as a function of the magnesium cell temperature and b) of the magnesium content determined by SIMS. 155

6.13 Photoluminescence intensity a) as a function of the magnesium cell temperature and b) of the magnesium content determined by SIMS. Insets are the log scale plots. 156

6.14 Arrhenius plots of the photoluminescence intensity versus temperature for peaks at a) 0.63 eV and b) 0.68 eV from film 577-InN:Mg. 158

6.15 Arrhenius plot of the photoluminescence intensity (log scale) for the PL at 0.60 eV versus temperature for film 555-InN:Mg. 159

6.16 Time dependent transmission from the InN:Mg films and also film 148-InN (undoped InN) grown under N-rich conditions, and 661-InN undoped InN grown under In-rich conditions. 160

7.1 Theoretical flux curve for zinc produced from the 10 cc and 60 cc effusion cells. 164

7.2 Zinc incorporation into InN, grown under N–rich and In–rich conditions, as determined using PIXE. 166

7.3 Room temperature electrical properties from the InN:Zn films as a function of Zn cell temperature. 167

7.4 Room temperature electrical properties from the InN:Zn films as a function of zinc concentration determined by PIXE. 167

7.5 SEM micrographs for the InN:Zn/YSZ(111) films grown under N-rich growth conditions for Zn cell temperature of a) 75°C, b) 192°C and c) 248°C. 168

7.6 ECV C^{-2} versus voltage plots for the InN:Zn/YSZ(111) films grown under N-rich conditions. 169

7.7 4 K photoluminescence from film 617–InN:Zn/YSZ(111) grown with a zinc cell temperature of 75°C. 169

7.8 SEM micrographs for the InN:Zn/GaN films. 170

7.9 ECV measurements from the InN:Zn films grown under In-rich growth conditions, the electrolyte was 0.2 Mol NaOH and 0.2 Mol KOH using a 1V ac bias voltage. 171

7.10 Variable magnetic field Hall effect measurements from the InN:Zn/GaN films grown under In-rich conditions. 172

7.11 Photoluminescence spectra of the InN:Zn/GaN films that were grown under In-rich growth conditions. 174

7.12 Arrhenius plots of the photoluminescence intensity versus temperature for peaks at a) 0.677 eV and b) 0.705 eV from film 656-InN:Zn/GaN. 175

7.13 Arrhenius plots of the photoluminescence intensity versus temperature for peaks at a) 0.719 eV, b) 0.668 eV, c) 0.602 eV and d) 0.547 eV from film 655-InN:Zn/GaN. 177

7.14 Time dependent transmission from the InN:Zn films and also an undoped InN film grown under N-rich conditions, and an undoped InN film grown under In-rich conditions. 178

LIST OF TABLES

1.1 Properties of wurtzite GaN 7

1.2 Properties of wurtzite InN 8

3.1 Effects of gallium flux on growth rate. 52

3.2 Electrical properties of the gallium flux dependent growths. 57

3.3 Substrate temperature effect on growth rate. 58

3.4 Electrical properties of the substrate temperature dependent growths. 60

3.5 InN growth on GaN MOCVD templates. 70

3.6 Single magnetic field Hall effect electrical properties from the thickness dependent InN/YSZ(111) films (* - InN films that were grown on the annealed YSZ(111), which also required a high indium flux to sustain streaky RHEED). 74

3.7 Variable magnetic field Hall effect electrical properties of the thickness dependent growths of InN/YSZ(111) films (* - InN films that were grown on the annealed YSZ(111), which also required a high indium flux to sustain streaky RHEED). 77

5.1 Tabulated results for the Schottky contacts to GaN nanowires. 129

6.1 Magnesium doped InN films on (111)YSZ. Flux values were calculated, Mg content was measured using SIMS, with that of film 554 estimated by curve fitting the SIMS to the theoretical flux curve. 142

6.2 Magnesium doped InN films on (111)YSZ and analysed using valence band XPS and KOH etching to determine the film polarity. Samples marked with "—" were samples that were not studied due to the lack of a suitable piece of the film. 147

6.3 Analysis of the temperature dependent photoluminescence of Film 577-InN:Mg/YSZ, using single and double path models. 157

7.1 Zinc doped InN films on YSZ(111). 165

7.2 Zinc doped InN films on GaN template. 165

7.3 Results of multiple carrier fitting to variable magnetic field Hall effect data for the InN:Zn/GaN films grown under In-rich conditions. In each case two distinct electron population could be resolved. 173

7.4 Values from fitting the equations 6.1 and 6.2 to the temperature dependent photoluminescence of Film 656-InN:Zn/GaN (fig. 7.12). 174

7.5 Values from fitting the equations 6.1 and 6.2 to the temperature dependent photoluminescence of Film 655-InN:Zn/GaN (fig. 7.13). 176

Chapter 1

INTRODUCTION

1.1 MOTIVATION

In November 1993, Shuji Nakamura released the first report of 1 candela indium gallium nitride (InGaN) light emitting diodes (LEDs) [1]; following this, in 1996, he also reported violet InGaN laser diodes [1, 2, 3, 4, 5]. The success of III-nitrides was somewhat surprising, in that although the alloy family has a direct band gap across the compositional range from InN to GaN, a high defect density results from growth on non lattice matched substrates. Despite two decades of intensive research, there remain many areas of continued interest, particularly concerning fundamental properties of InN and In-rich alloys, which have until recently been neglected, and structured engineering at the nanoscale to improve device performance as well as enabling new applications.

The use of fossil fuels for the production of electricity also leads to the production of carbon dioxide when mined and burnt, which is having adverse affects on the climate [6]. One way of reducing the world's need for carbon based fuels is by utilising the largely untapped solar resource through improved photovoltaic technology. The slow uptake of solar power is primarily due to its high cost in relation to other power generation processes. This situation will improve with increasing energy conversion efficiencies of photovoltaic cells. At present, silicon is widely used for fabricating photovoltaic cells, but as its indirect band gap of 1.12 eV is a poor match to the solar spectrum, the maximum energy conversion efficiency is only 30% [7].

There are several properties of a semiconductor that have to be taken into consid-

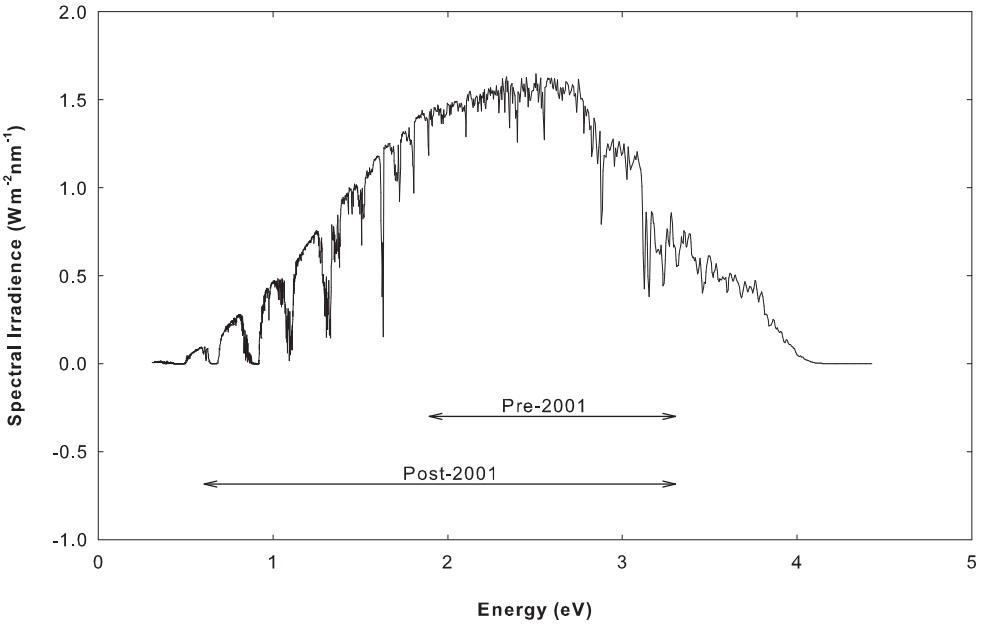

Figure 1.1 Span of the accepted InGaN band gap prior to and subsequent to 2001 as compared to the standard solar spectrum known as AM1.5g.

eration for photovoltaic cells, although the main ones are the type of band gap (direct or indirect) and the matching of the band gap to the solar spectrum. A semiconductor alloy with a direct band gap and tunability through the visible spectrum by compositional variation would be a major advantage. In 2001, a number of highly controversial reports on the InN band gap were published, which proclaimed that the originally reported band gap of 1.9 eV for InN [8] was incorrect, with a revised value of approximately 0.9 eV [9]. This has since been confirmed by many others [10, 11, 12, 13], with a currently accepted value of approximately 0.65 eV, although some uncertainty in the precise value remains. This new band gap value has opened up the possibility of new applications for InGaN, as the revised spectral range of InGaN spans the visible spectrum and includes the near infrared and near ultraviolet, shown in fig. 1.1. A two junction photovoltaic cell, with the band gap values of 0.98 eV and 1.88 eV, would theoretically have an energy conversion efficiency of 42% [14], which would far surpass what is available at present; the only way to presently achieve the required band gap values would be to use a material like InGaN to engineer the band gap. At present the best solar cell has a 1.83 eV $Ga_{0.51}In_{0.49}P$ top junction lattice-matched to the GaAs

substrate, a metamorphic 1.34 eV $In_{0.04}Ga_{0.96}As$ middle junction, and a metamorphic 0.89 eV $In_{0.37}Ga_{0.63}As$ bottom junction; which is 40.8% efficient under 600 suns [15]. As discussed in this thesis, however, InN and In-rich InGaN alloys suffer from several problems, particularly with regard to controlling their electrical properties, which has so far hampered device development.

In contrast, GaN and Ga-rich InGaN devices have been demonstrated and have become a mature technology, at least in terms of discrete devices. In 1965, Intel co-founder Gordon Moore noted that the number of transistors that could be placed on an integrated circuit was doubling roughly every two years (fig. 1.2). "Moore's law" has since since contributed to a series of goals for integrated circuit companies to follow, although the limitations of standard photolithography techniques are being reached and other alternatives need to be examined. One possibility is either interfacing or developing transistor structures based on nanowires; nanowire transistors based on vertical [16, 17] and planar [18, 19, 20] nanowires have already been fabricated. Compound semiconductors, such as GaN, may prove competitive for nanowire devices or allow for integration with silicon for fabrication of nanowire circuits, as growth processes allow for the reduction of the effect of lattice mismatch.

Already next generation nanostructures are being considered, for example hierarchical nanowires /citeLieber:2007. In the future, such structures could be used for interlinking vertical nanowire transistors, or for applications where increased surface area to volume ratio is required, for example in gas sensors. Nanowires may also improve photovoltaic cells by decoupling the absorption process from electron collection [21]. Hierarchical nanowires would also improve light trapping due to the increased roughness. This thesis demonstrates the first reported growth of self-seeding hierarchical GaN nanowires by molecular beam epitaxy, investigates their characteristics and also their potential for device fabrication.

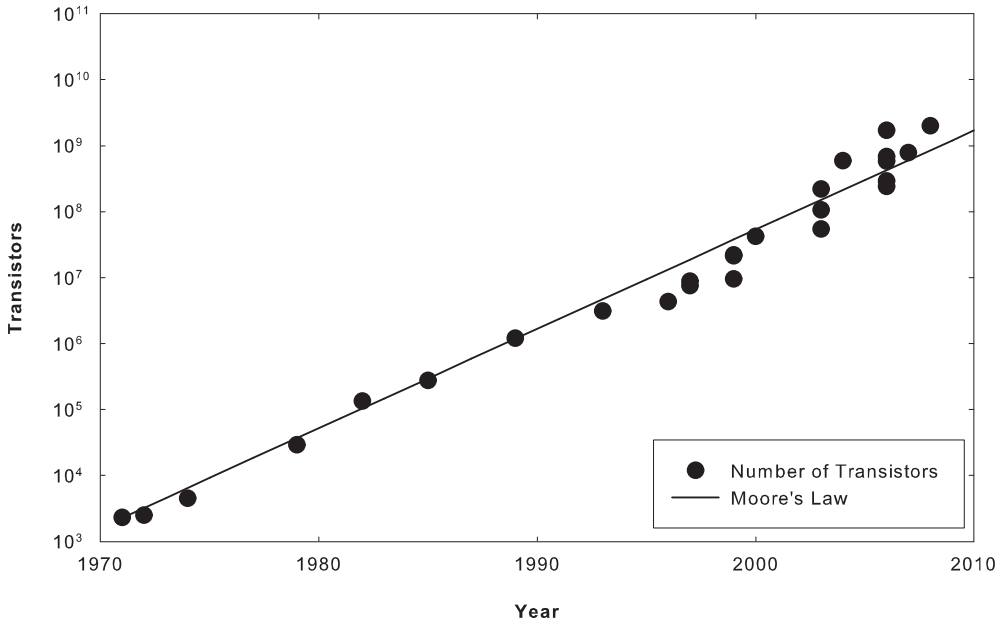

Figure 1.2 Moore's Law (Intel Corporation, http://www.intel.com/technology/mooreslaw/index.htm, accessed: 12th May 2008) showing the correlation between 1970 and 2008.

1.2 OVERVIEW OF NITRIDE SEMICONDUCTORS

The III-nitride family of semiconductors consists not only of InN and GaN; research has also been conducted into aluminium nitride (AlN) and boron nitride (BN). AlN has an extremely wide band gap of 6.2 eV, making it a potential material for deep ultraviolet optoelectronic devices [22]. BN is seen as a special case as it has four stable polytypes and is primarily used for its structural properties with the cubic form used as an abrasive. Pyrolytic BN (BN) is used widely in molecular beam epitaxy (MBE) for crucibles, as BN is a very good electrical insulator and has good thermal conductivity. At present, GaN and InN are seen as the leading III-nitride semiconductors and are being heavily investigated, as summarised below.

GaN and InN crystals can grow in two different stable phases. The most thermodynamically stable phase is the wurtzite crystal structure (fig. 1.3). Due to the lack of inversion symmetry of the wurtzite structure along the c-axis direction, growth can either occur on the metal, or nitrogen polar face, depending on the termination of the substrate. This has to be taken into consideration, as the surface chemistry is

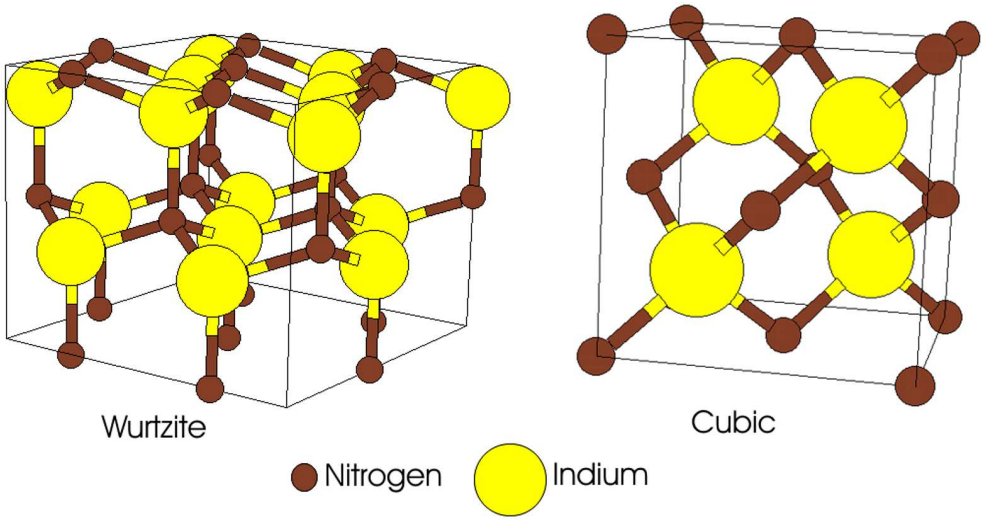

Figure 1.3 Wurtzite and zincblende crystal lattice structure.

different for each face and therefore the optimal growth parameters also. Under certain conditions it is also possible to grow the zincblende phase which has a more symmetrical crystal structure (fig. 1.3). Under poorly controlled conditions, both phases can co-exist in a thin film.

1.2.1 GaN

GaN is a direct band gap semiconductor, with a wide band gap of 3.4 eV. It has two known growth phases: hexagonal wurtzite (WZ) and cubic zincblende (ZB), the WZ being more common with lattice constants a = 3.2 Å, c = 5.2 Å. Due to the lack of an economically viable lattice-matched substrate, c-plane sapphire is the preferred substrate with a lattice mismatch of 16%. As-grown GaN is typically n-type; N-vacancies and/or residual O and Si from the growth are known to cause the n-type nature [23, 24, 25]. Undoped GaN grown by molecular beam epitaxy (MBE) has reached carrier concentrations as low as 3.2×10^{16} cm^{-3} with an electron mobility of 1098 $cm^2V^{-1}s^{-1}$ [26]. Researchers have been able to achieve p-type GaN by MBE with magnesium without the need for post annealing. P-type GaN:Mg is reported to have carrier concentration and mobility values of up to $1.4\times10^{18}cm^{-3}$ and 7.5 $cm^2V^{-1}s^{-1}$ respectively for rf-plasma assisted MBE [27], and $8\times10^{17}cm^{-3}$ and 26 $cm^2V^{-1}s^{-1}$ for

NH_3 MBE [23], respectively. Further information on the properties and growth of GaN can be found in reference [28], some of which is summarised in table 1.1.

1.2.2 InN

Before 2001 the accepted value of the band gap energy for InN was 1.9 eV, as determined by Tansley and Foley [8]. Those InN samples were grown by RF sputtering of a pre-nitrided metallic indium target in a nitrogen ambient. Optical analysis was done by optical absorption and electrical measurements were conducted on photolithographically defined clover leaf contacts. These polycrystalline InN films were n-type and a maximum mobility of 5000 $cm^2V^{-1}s^{-1}$ at 150 K was reported [29]. In 2001, Davydov et al. published a short communication citing evidence that the InN band gap was in fact closer to 0.9 eV [9], based on single crystal InN grown by MBE. Optical measurements of the band gap consisted of not only optical absorption, but also for the first time photoluminescence spectroscopy, with emission detected at 0.9 eV [9]. The lower energy optical feature was not only observed by Davydov et al. but by several subsequent reports for both MBE and MOCVD grown material [10, 11, 12, 13], although the reported value of the band gap ranged from 0.6–0.9 eV.

There are several reasons for the wide range in reported values for the InN band gap. One of the main reasons is the Burstein-Moss effect where the Fermi level moves further up the conduction band with increasing carrier concentration, thereby increasing the energy of the absorption edge as seen by optical absorption analysis [30]. Walukiewicz et al. suggested that the Burstein-Moss effect could increase the absorption edge energy from 0.7 eV to as much as 2.3 eV at a carrier concentration of 10^{21} cm^{-3} [31]. Butcher et al. suggested an origin based on the fact that the RF sputtered material has a N/In stoichiometry of 1.2 instead of 1.0 for the case of single crystalline InN thin films [32]. Arguments based on quantum size effects [33] and oxygen uptake [34] have also been suggested, but have been largely dismissed as having insufficient effect on the InN band gap.

Aside from the debate regarding the InN band gap, the recent availability of higher quality material has enabled researchers to study other properties. InN has a small

Table 1.1 Properties of wurtzite GaN

Band gap energy	E_g (300 K) = 3.39 eV E_g (1.6 K) = 3.5 eV
Band gap temperature coefficient (T >180 K)	-6.0×10^{-4} eV/K
Band gap pressure coefficient (T = 300 K)	4.2×10^{-3} eV/kbar
Lattice constant (T = 300 K)	a = 3.189 Å c = 5.185 Å
Coefficient of thermal expansion (T = 300 K)	Δa/a = 5.59×10^{-6} K^{-1} Δc/c = 3.17×10^{-6} K^{-1}
Ga – site density	N_{Ga} = 4.28×10^{22} cm^{-3}
Ga – surface site density	N_{surf} = 1.1×10^{15} cm^{-2}
Monolayer thickness	2.59 Å(along c-axis)
Bilayer thickness	5.18 Å(along c-axis)
Thermal conductivity	κ = 1.3 W/cm K
Index of refraction	n(1.00 eV) = 2.33 n(3.38 eV) = 2.67
Dielectric constant	ε_0 = 8.9
Electron effective mass	m_e^* = 0.20±0.02m_0
Hole effective mass	m_h^* = 0.80±0.02m_0

Table 1.2 Properties of wurtzite InN

Band gap energy	E_g = 0.6 – 0.7 eV
Lattice constant (T = 300 K)	a = 3.53 Å c = 5.71 Å
Monolayer thickness	2.86 Å(along c-axis)
Bilayer thickness	5.71 Å(along c-axis)
Dielectric constant	$\varepsilon_0 = 13.1$
Electron effective mass	$m_e^* = 0.04m_0$ $m_e^* = 0.14m_0$

electron effective mass of $0.04m_o$ [35] (also a value of $0.14m_o$ has been reported [36]), therefore it is expected that InN will have a high electron mobility. The original InN films grown by Tansley et al. were reported to have a room temperature electron mobility of 2700 $cm^2V^{-1}s^{-1}$ [29], although this result has never been confirmed and now seems unlikely. Undoped InN films produced by MBE typically have electron mobilities of 500 - 1000 $cm^2V^{-1}s^{-1}$. However, electron mobilities above 2000 $cm^2V^{-1}s^{-1}$ have been recently reported for films with thickness greater than 5 μm, the highest being 3500 $cm^2V^{-1}s^{-1}$ (at room temperature) for a sample with an electron concentration of approximately 10^{17} cm^{-3} [37]. Theoretical values for the maximum electron mobility have ranged around 4000 $cm^2V^{-1}s^{-1}$ [38, 39], although a recent publication suggests it could be as high as 14000 $cm^2V^{-1}s^{-1}$ [40]. There is some limitation to the measurements because like InAs [41], InN suffers from an electron accumulation layer at the surface, which can short out electrical measurements [42]. The electron accumulation layer is due to ionised donor-type surface states pinning the surface Fermi level above the conduction band edge [42].

For InN to be used in device structures, p-type doping is essential. Magnesium is being investigated as an acceptor due to the success of p-type GaN:Mg. So far all reports of Mg-doping of InN describe films with apparent n-type conductivity as determined using standard measurement techniques [43]. However, as the surface electron

accumulation layer is known to mask the bulk properties, other techniques are required to determine the true conductivity. Ager et al. [44] and Anderson et al. [45] have shown using electrochemical capacitance voltage (ECV) measurements that a change in slope of inverse squared capacitance versus bias voltage can signal the presence of a p-type buried layer, although this is qualitative and a somewhat indirect technique. Another way of measuring the bulk properties of InN is the use of the variable magnetic field Hall effect; Anderson et al. have used this technique to observe parallel light hole, heavy hole, and electron conduction in a highly magnesium doped InN film [45]. Schaff et al. have also examined InN:Mg, InGaN:Mg and InAlN:Mg films using the hot probe technique, which also produces results showing p-type behaviour [46, 47]. Still, without a way of directly measuring/contacting the p-type conductivity of the InN:Mg films significant steps toward InN devices cannot be taken.

Aside from only being able to indirectly measure the p-type conductivity, researchers have also faced issues with measuring optical properties. In InN:Mg films the photoluminescence typically red shifts and becomes quenched at high levels of magnesium, limiting its use for InN:Mg films [48]. Understanding the quenching mechanism may also further explain some of the issues with the electrical properties.

1.3 GALLIUM NITRIDE NANOWIRES BY MBE

Epitaxial layers can be photolithographically patterned into nanoengineered structures and devices, however directly formed nanostructures can be fabricated using essentially the same technique used for epilayer growth. Over the past decade there has been a vast amount of research into semiconductor nanostructures, as shown by the number of peer-reviewed publications on nanowires and nanorods as plotted in fig. 1.4. The study of nanostructures is driven by the need to improve upon present devices. Nanostructures allow for devices with smaller footprints, and also different functionality due to quantum effects, as the size of the nanostructures approach the Bohr radius. Moreover, nanostructures have increased surface to volume ratio compared to thin films, with a correspondingly enhanced sensitivity to biological agents and light detection. It is also expected that novel nanodevices may be produced, e.g. ZnO nanogenerators that are

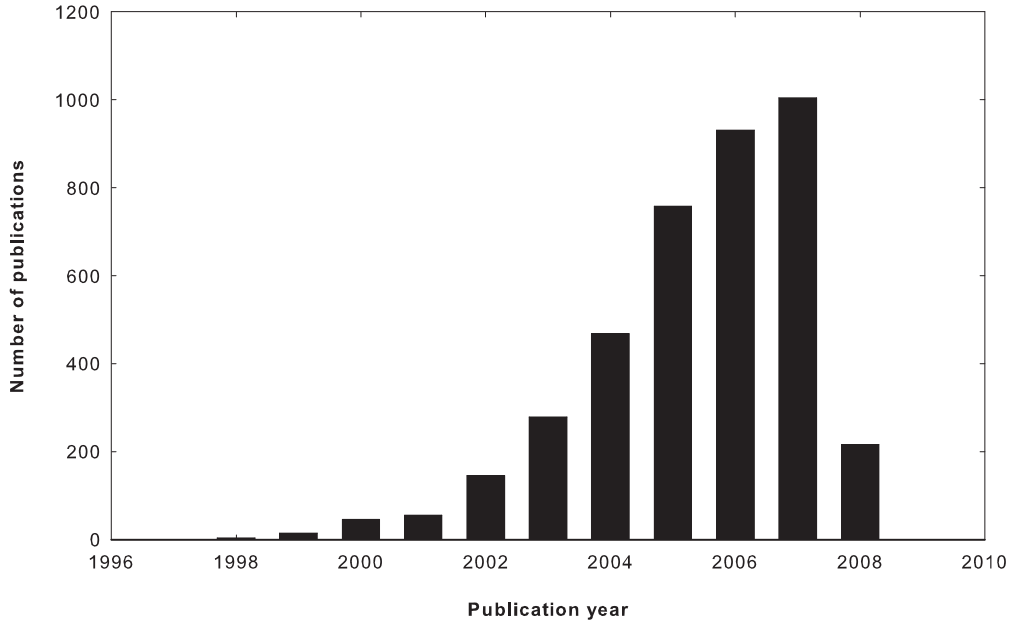

Figure 1.4 Publications per year for nanostructures, based on advanced search on the Web of Science using (nanowire* and nanorod*)(Web of Science, http://isiknowledge.com/, accessed: 4th April 2008).

based on harvesting mechanical energy through piezo effects [49, 50].

There are two approaches for producing nanostructures, these being the top–down and the bottom–up processes. The top–down method uses patterning followed by wet or dry etching. This process is limited by the ability to grow defect free material and also the size restrictions inherent to the chosen patterning process. The bottom–up technique is where the nanostructured material is directly grown into the desired shape. One of the most dramatic examples was demonstrated by researchers at IBM who showed that atoms could be manipulated using a scanning tunnelling microscope to produce atomic scale structures [51]. A faster and more conventional bottom–up process is the vapour liquid solid (VLS) approach, where a metal catalyst is used to excite the growth of nanostructures using typical semiconductor grow techniques.

The VLS technique was developed by Wagner and Ellis for the growth of silicon whiskers [52]. In their process, Wagner and Ellis used a silicon wafer coated with a thin film of gold. When heated, the gold forms droplets and undergoes a phase change from solid to liquid above the silicon-gold eutectic temperature. The gold droplets control the nucleation sites and the lateral size of the whiskers. On exposing the substrate to

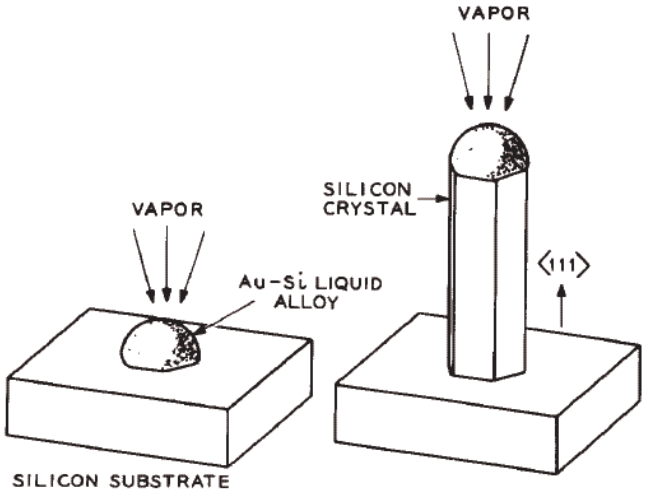

Figure 1.5 Schematic of the vapour liquid solid process of Wagner and Ellis [52].

the silicon flux, the droplets act as preferred sites for the silicon adatoms, due to the lower surface energy. As the gold droplet becomes saturated with silicon, the silicon atoms diffuse to the liquid solid interface (interface of the gold droplet with the silicon wafer), where they undergo a liquid to solid phase change and start the growth of the whisker. As long as the growth material is sustained, the growth of the whiskers continues and the gold droplet rides the top of the whisker (see fig. 1.5). The VLS process was introduced for actual nanoscale growth by Charles Lieber's group around 1998, as proof of concept that the VLS process is useful for nanowire growth [53]. Fig. 1.6 shows the number of times the Wagner and Ellis paper on VLS growth has been cited and shows it is a commonly used method for nanowire growth with essentially exponentially increasing interest.

There are several problems with using the VLS process for growing III-V nanostructures. For Si nanowires the phase diagram is typically based on only two elements: silicon and gold. For the growth of III-V nanostructures using the VLS process the catalyst is not the group III or group V material, so a third element is introduced as the catalyst. Therefore what actually drives the growth is not clear and the phase

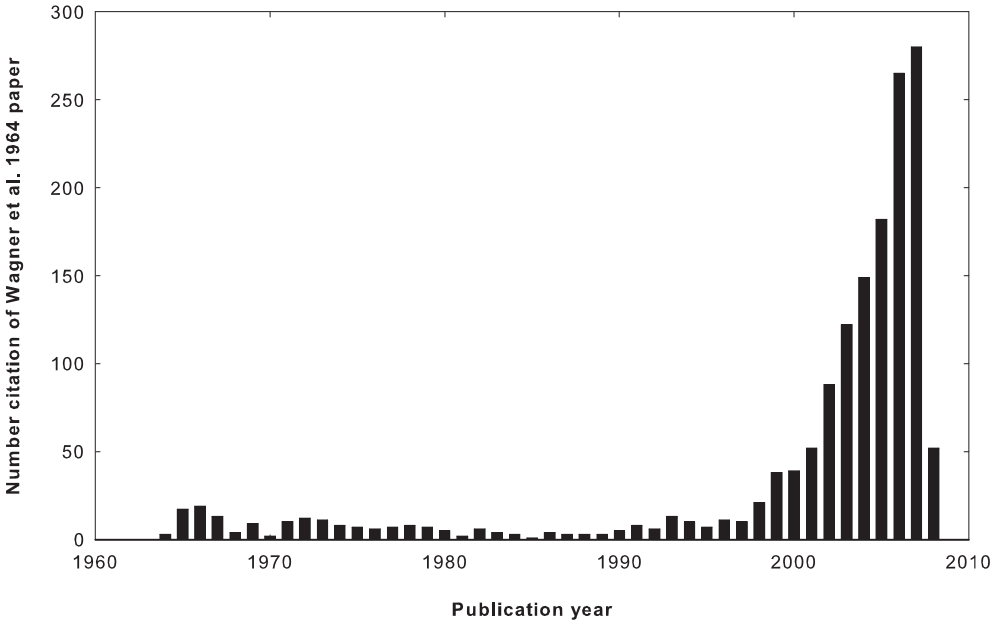

Figure 1.6 Number of times Wagner and Ellis 1964 paper has been cited plotted as a function of publication year(Web of Science, http://isiknowledge.com/, accessed: 4th April 2008).

diagram is more complex as it is a ternary system. It has been reported that for III-As nanowires the group III element alloys with the catalyst, typically gold, and forms the liquid phase, while the As diffuses into the solid-liquid interface to grow the III-As nanowire [54]. In contrast, Persson et al. suggests that the catalyst is actually solid in the case of III-V nanowire growth and the presence of the catalyst is enough to confine the growth; this is known as vapour solid solid growth. [55]. The exact growth mechanism is therefore dependent on the semiconductor of interest, growth temperature, and the catalyst used.

To the present date the growth of GaN nanowires by MBE using the VLS process has involved the use of a nickel catalyst and N-rich growth, which sees the nickel particle riding the tip of the nanowires, therefore resembling the VLS process [56]. Another reported method of growing GaN nanowires by MBE uses only the N-rich growth regime and Si or AlN substrates [57, 58]. The N-rich growth regime promotes the growth of three dimensional crystal growth and, in the long term, nanostructures due to the reduced adatom diffusion length. The N-rich growth also means that the growth rates are restricted by the gallium flux, therefore several hours are required

to produce micron long nanowires. The N-rich growth process is also a valid way of growing other III-nitride nanowires [59].

Even with the issues faced with growing GaN nanowires, devices have already been fabricated as both p-type and n-type nanowires are not required. For example as-grown GaN nanowires with two contacts have been used for photodetectors [60]. Also, GaN nanowire Schottky diodes have been fabricated using a two step metallisation [61, 62], and by using a scanning probe microscope (SPM) to contact one end of the nanowire to form the Schottky contact [63]. Due to good optical confinement properties, Pauzauskie et al. have used GaN nanowires as waveguides [64], and with the addition of a wrap around contact the optical intensity can be electrically modulated [65]. Researchers have also shown that optical pumping of GaN nanowires can lead to lasing [66]. One of the most well developed devices is the nanowire field effect transistor (FET), which is created by adding a gate contact to the nanowire or by using the substrate as the gate. The FET devices also allow for determination of the carrier concentration and mobility of individual nanowires. To produce a P-N junction p-type GaN substrates have been substituted, LEDs have been fabricated and tested [67]. Improvements to the P-N junction have involved Mg-doping of GaN nanowires, and junction fabrication by n-type and p-type nanowires crossing over each other [68] or by a junction in one nanowire [69]. Also, the incorporation of quantum wells has been achieved [70]. So far the focus of nanowire devices has been on recreating present devices using nanowires as the active region, although nanowires may offer more unique devices which have not yet been envisioned.

Despite the extensive research into the development of GaN nanowire devices, MBE grown nanowires are limited by growth rate due to the use of the N-rich growth regime, and also what can be achieved by MBE has already been accomplished with CVD GaN nanowires. However, in this thesis it will be shown that the growth of GaN can also be conducted under Ga-rich conditions, thereby improving growth rates. Moreover, the Ga-rich growth allows for self-seeding growth and the possibility of hierarchical nanowires for unique devices.

1.4 THESIS OUTLINE

This thesis will give the reader an insight into the growth of InN and GaN epilayers and nanostructures, also covering the p-type doping of InN. Following Chapter One, the molecular beam epitaxy system and the structural, electrical and optical characterisation techniques used in this thesis will be introduced (Chapter Two). The third chapter is the optimisation of the growth of InN and GaN epilayers. Chapter Four highlights the discovery of self-seeding growth of GaN branching nanowires and models for how the growth occurred, supported by additional self-seeded GaN nanowire growth experiments. The fabrication of both vertical and planar nanowire device structures is discussed in Chapter Five. Investigation of the doping of InN using Mg and Zn are discussed in Chapter Six. The last chapter (Chapter Seven) of this thesis synthesises and draws conclusions on Chapters Three through Six, and includes a discussion of future opportunities.

Chapter 2

GROWTH AND CHARACTERISATION TECHNIQUES

2.1 EPITAXY

Epitaxy comes from the two Greek words, epi "above" and taxis "in ordered manner". Epitaxial growth of thin films (such as semiconductors) is the growth of a single crystal layer, such that the crystal lattice of the semiconductor grows to match the crystal structure of a carefully chosen substrate. There are several epitaxial growth techniques, each with its particular advantages. The three processes that will be discussed here are liquid phase epitaxy (LPE), chemical vapour deposition (CVD) and molecular beam epitaxy (MBE) due to their relevance to the semiconductor industry as well as growth of nanostructures.

In the LPE process, the semiconductor layers are grown from a melt onto a seed crystal or a solid substrate. Semiconductor precursors are dissolved in another material; gallium is a commonly used melt solution. The growth is undertaken close to an equilibrium condition between the dissolution and deposition region. Growth out of the melt can be controlled by forced cooling. LPE has fast growth rates (GaN can be grown at 1-2 $\mu \mathrm{m} hr^{-1}$ [71]) and can produce device quality semiconductor layers at low cost. However, the growth of complex structures is limited, as each different melt needs to be mounted in the same system therefore allowing the substrate to be transferred between the melts.

CVD is a commonly used process for the growth of the highest quality GaN thin films for optoelectronic devices. Organic precursors are exposed to a hot substrate mounted in a vacuum system. Near the vicinity of the hot substrate the precursors dis-

sociate, releasing the growth materials that then reform on the substrate as the desired semiconductor. CVD has high growth rates (GaN can be grown at 1 $\mu m hr^{-1}$ [72]) and the composition of the thin films can be controlled by the precursor concentration and dissociation rate of the individual precursors. However, high growth temperatures are typically required to achieve dissociation, and scrubbers are also required to break down the toxic exhaust gases.

MBE was employed by Davydov et al. to grow the high quality single crystal InN used to study the band gap [9]. One major difference between MBE and the other two epitaxial growth processes is that the MBE system is held under ultrahigh vacuum (UHV), at least for idle periods; growth of nitrides requires a much higher pressure, on the order of 10^{-5} torr, MBE growth is conducted far from thermodynamic equilibrium and is governed mainly by the kinetics of the surface processes occurring when the impinging beams of adatoms react with the outermost atomic layers of the substrate. MBE is a versatile growth technique for the growth of thin epitaxial structures. Not only can single atomic layer thin films be grown, but as the composition of a thin film is dependent on the arrival rate of the different adatoms, control of complex alloys are achievable. Moreover, due to the slow migration of the adatoms, smooth surfaces through layer by layer growth are achievable. Atomic scale changes in the composition can be easily achieved by shuttering sources, allowing for the growth of complex quantum well and superlattice structures. Even though the running costs are increased (due to the requirement of a continuous vacuum) the system is enclosed, so toxicity is reduced. Also, the consumption of source material is reasonably small.

With the growth of epitaxial thin films there are three possible growth modes. Each mode depends on the interaction of the growth adatoms with surface sites and additional growth adatoms. In Volmer-Weber growth, the adatom to adatom interaction is stronger than that of the adatom to substrate sites, therefore this leads to the growth of islands, or clusters. Frank-van der Merwe growth is the opposite, due to the adatoms preferentially interacting with surface sites leading to a thin film grown layer-by-layer. Stranski-Krastanov growth is where is the growth starts out layer-by-layer but once the film exceeds a crystal thickness, islanded growth occurs; the critical

thickness is dependent on the surface energies as well as lattice parameters.

Homoepitaxy is the growth of a semiconductor on a crystalline substrate of the same material (native substrate), which should lead to high quality thin films due to near perfect lattice matching. For III-nitrides, presently substrates of AlN and GaN are available but very expensive, therefore sapphire is typically substituted. Still, the strain introduced by lattice mismatch can often be contained by the film growth to achieve high enough quality films for devices; growth on a non-native substrate is known as heteroepitaxy. For a thin film to be able to accommodate the effects of strain, dislocations are created in the film. The two common dislocation types are edge and screw dislocations; it is also possible to have a mixed dislocation which has both edge and screw components. An edge dislocation is where an additional half-plane of atoms is introduced, leading to the distortion of the surrounding planes of atoms. The screw dislocation is more complex and is where the atomic planes form a spiral ramp winding around the line of the dislocation. Dislocations do lead to reduced crystal quality, but with optimal growth conditions and the aid of buffer layers, their density can be controlled to be able to grow device quality thin films of GaN and InN.

2.2 FUNDAMENTALS OF PAMBE

2.2.1 University of Canterbury MBE System

The growth experiments described in this thesis were performed using the University of Canterbury Perkin Elmer 430 MBE system. The system consists of three stages as shown in Fig. 2.1, where each stage has a different vacuum requirement. The initial stage allows for the transfer of substrates into the vacuum system, known as the intro–hatch (load–lock). Up to six substrates, each mounted on a 75 mm diameter molybdenum growth block using indium or indium/tin, can be loaded into the system simultaneously. To achieve a vacuum, the load–lock is pumped down using liquid nitrogen cooled sorption pumps from atmosphere to 10^{-4} Torr, at which point a cryogenic pump then further reduces the pressure down to 10^{-8} Torr. Removal of water vapour is done by baking the load–lock for one hour at 100°C. The next vacuum stage is the

transfer tube, which is held under vacuum with an ion pump, allowing for the substrates to be held at a pressure of 10^{-9} Torr. Outgassing of the individual growth blocks is done in the transfer tube at a temperature of approximately 650°C, therefore reducing the amount of impurities entering the ultra clean growth chambers. This system is equipped with two growth chambers, one designated for III-nitrides and the other for the growth of another extensively studied wide band gap material, zinc oxide. The growth chambers are held at an idle pressure of 10^{-10} Torr, using a combination of ion and cryogenic pumps. Film growths are performed at 10^{-5} Torr, so only the cryogenic pump is used during growth.

2.2.2 Substrate Heating

The Perkin Elmer 430 MBE system is designed so that the growth blocks can be moved in and out of the growth chamber. Thus, a thermocouple cannot be permanently coupled to the substrate to determine the substrate temperature. Instead, a thermocouple is pressed against the back of the molybdenum growth block. This can lead to a false reading of the substrate temperature, due to the thermal losses in the growth block and the transition through the liquid indium or indium/tin mounting layer. Preliminary measurements of the substrate surface temperature using BandiT, an optical absorption edge system from k-Space Associates Ltd, suggest that the difference between the thermocouple reading and substrate substrate can be between $50-100$°C; typically the difference is larger at higher temperatures. Temperature measurements in this thesis were based on the thermocouple placed on the back of the growth block which is also the feedback for the heater controller, and are therefore approximate.

2.2.3 Group III Source

For the growth of III-nitrides the atomic metal flux is produced from effusion cells. The effusion cells used in this study were single heating zone cells, equipped with 60 cc conical pyrolytic boron nitride (BN) crucibles, similar to the effusion cell shown in fig. 2.2. The crucibles are a third filled with 6-9s purity indium or gallium. The shape of a crucible orfice is designed to give uniform coverage across the substrate; however, the

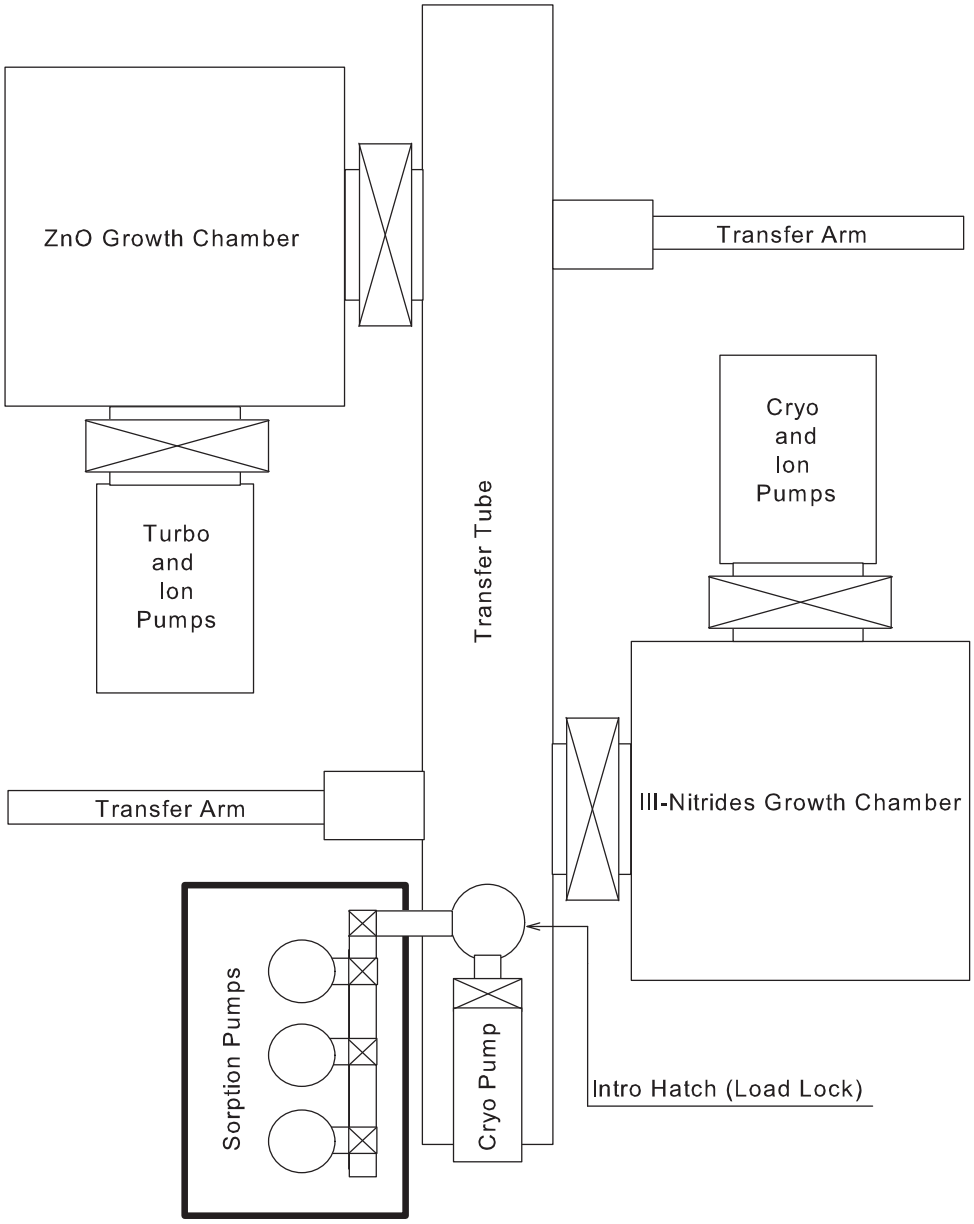

Figure 2.1 Plan view of the University of Canterbury 430 Perkin Elmer MBE system.

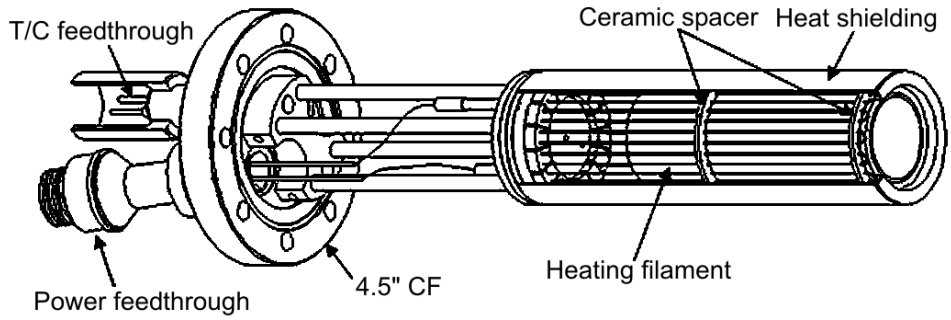

Figure 2.2 Diagram of a typical effusion cell.

single heating zone leads to the formation of a cold zone at the opening of the effusion cell. This can lead to the build up of excess metal on the mouth of the crucible, which is especially problematic for gallium and indium. The excess metal is known to produce oval defects on the film surface through spitting [73].

Vapour pressure curves for indium and gallium are well established from experimental results. Both indium and gallium are low vapour pressure metals, and the typical growth fluxes require temperatures well above their melting points. The Knudsen equation [74] is used to calculate the maximum flux for an element in a particular effusion cell geometry:

$$I_A = 1.118 \times 10^{22} \frac{pA_e}{{r_A}^2\sqrt{MT}} \tag{2.1}$$

where I_A is the impinging flux on the substrate (atoms·cm^{-2}s^{-1}), p is the pressure from a vapour pressure curve (Torr), A_e is the area of the orifice of the crucible in the effusion cell (cm^2), r_A is the distance from the effusion cell orifice to the substrate (cm), M is the molecular weight of the metal (g·mol^{-1}) and T is the temperature (K). The effusion cells are arranged so they are not perpendicular to the substrate, as shown in fig. 2.3. Therefore, equation 2.1 is modified by a cosine term:

$$I_A = 1.118 \times 10^{22} \frac{pA_e}{{r_A}^2\sqrt{MT}} \cos\theta \tag{2.2}$$

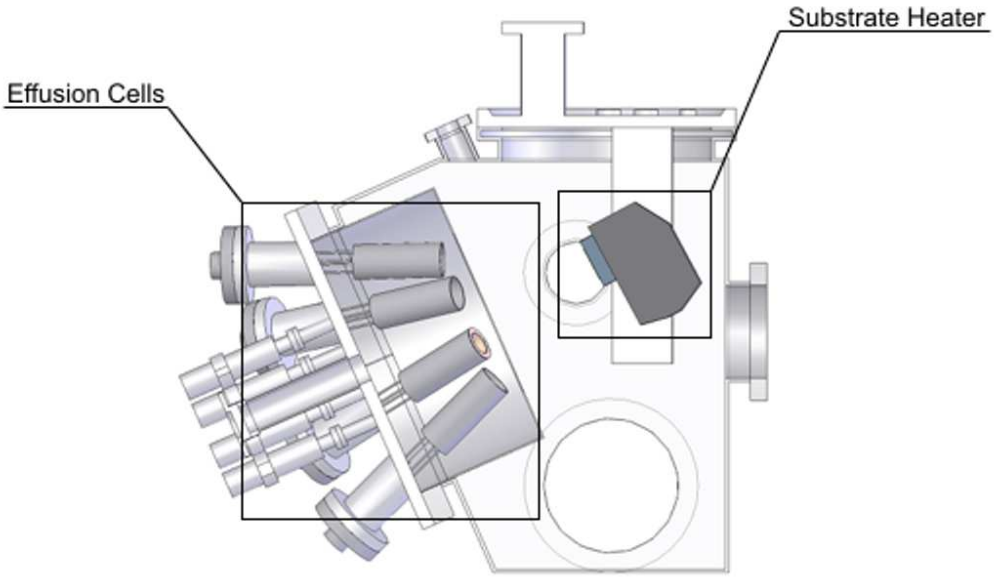

Figure 2.3 Schematic of the eight effusion cell ports in relation to the substrate.

The 60 cc pBN crucibles have an orifice diameter of 3.8 cm. The lip of the effusion cell is 20 cm from the substrate and at a tilt of 25° with respect to the substrate normal. Using these parameters the flux curves for indium and gallium are shown in fig. 2.4 using equation 2.2.

The theoretical curves (fig. 2.4) are used to decide on the initial temperatures of the effusion cells. In-situ flux determination is done using a quartz crystal microbalance (QCM). The QCM head is water cooled to ensure a sticking co-efficient of near unity. For flux measurements the QCM head is lowered in place of the substrate, and therefore in direct line of site of the molecular beams. The QCM is run at a frequency of 6 MHz when unloaded; as material collects on to the crystal, the resonant frequency is reduced and his is typically sampled every five seconds. The frequency difference should be a constant value, corresponding to a constant flux. The magnitude of the frequency difference can then be used to determine the impinging flux, based on:

$$\Delta M = \frac{\Pi\phi^2\Delta f \times\sqrt{Sheer \times D_q}}{2tF^2} \tag{2.3}$$

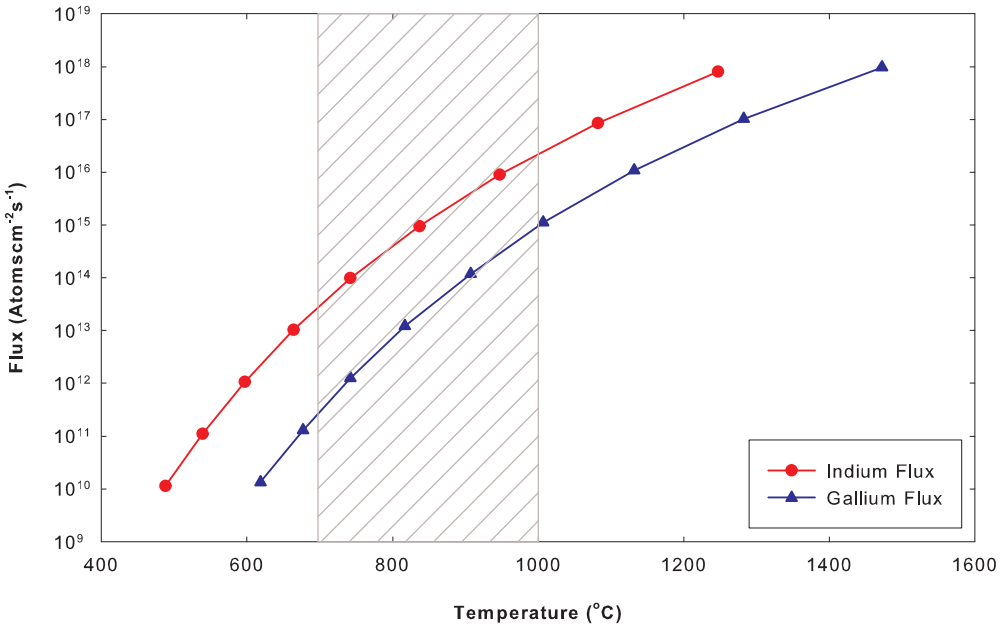

Figure 2.4 Flux curves for indium and gallium determined using equation 2.2; the cross-hatched region is the typical operation zone for the effusion cells in this study.

and

$$I_F = \frac{\Delta M N_A}{M} \tag{2.4}$$

where ΔM is the change in mass (g·mol^{-1}), ϕ is the diameter of the quartz crystal (cm), Δf the change in the frequency of the QCM (Hz), *Sheer* is the sheer modulus of the quartz (g·$cm^{-1}s^{-2}$), D_q is the density of quartz (g·cm^{-3}), t is the sample time (s), F is the frequency of the unloaded crystal (Hz), I_F is the impinging metal flux, N_A is Avogadro's number and M is the molar mass of the material measured (g·mol^{-1}).

2.2.4 Nitrogen Source

Ammonia is a commonly used nitrogen source for gas source MBE and CVD techniques. Active nitrogen flux is produced through the ammonia dissociating with the hot substrate. However, the typical growth temperatures of InN range only between $400 - 600$°C; at these temperatures the dissociation rate of ammonia is too low. An

alternative nitrogen source is produced by creation of a plasma, where RF or microwave power is used to excite pure nitrogen gas into active species. As the plasma source efficiency is independent of the substrate temperature, this allows for high growth rates at the growth temperatures required for InN.

In this study an HD25 Oxford Applied Research plasma source was used. The HD25 plasma source inductively couples RF power through the copper water lines to a pBN tube that is terminated with an interchangeable aperture plate. The energetic nitrogen species that are produced from the plasma source include molecular nitrogen, atomic nitrogen and ionised nitrogen [75]. Each species has its own optical signature and through optical emission analysis (OES) quantitative information regarding nitrogen species can be determined [76]. Collection of the optical spectrum may be done through the back of the plasma source, as the viewport used to monitor the plasma looks directly into the pBN cavity. A typical optical spectrum from the back of the HD25 plasma source is shown in fig. 2.5. The atomic nitrogen (N) species is seen at 747 nm and the electrically excited nitrogen atoms (N^*) appear in the spectral lines of 822, 868, 906, 920 and 940 nm. Compared to the atomic species, the nitrogen molecules are represented by a band due to the accumulation of vibrational and rotational energy in molecular species. The 1^{st}-negative series of nitrogen ions (N_2^+) forms the 391 and 428 nm features. The 1^{st}-positive series of the N_2 band is the main feature in the 600 nm region, while the 2^{nd}-positive series of the N_2 band is represented by the features at 316, 337, 357, and 380 nm.

From the OES of our HD25 plasma source the plasma appears to be dominated by the atomic nitrogen species at 747 nm. The composition of the nitrogen species can be manipulated by varying the RF power or the nitrogen chamber pressure. With increasing RF power the N_2:N ratio decreases mainly due to the atomic N increasing, determined by peak intensity comparison of the 1^{st}-positive series of the N_2 band at 660 nm and the electrically excited nitrogen atoms (N^*) at 869 nm. Part way through this study the plasma source aperture plate was changed from having 276 holes to 488 holes. This caused the N_2:N ratio to decrease while the N_2:N^* ratio decreased at low RF power (<200 W); however at high RF power (>200 W) the N_2:N^* ratio is slightly

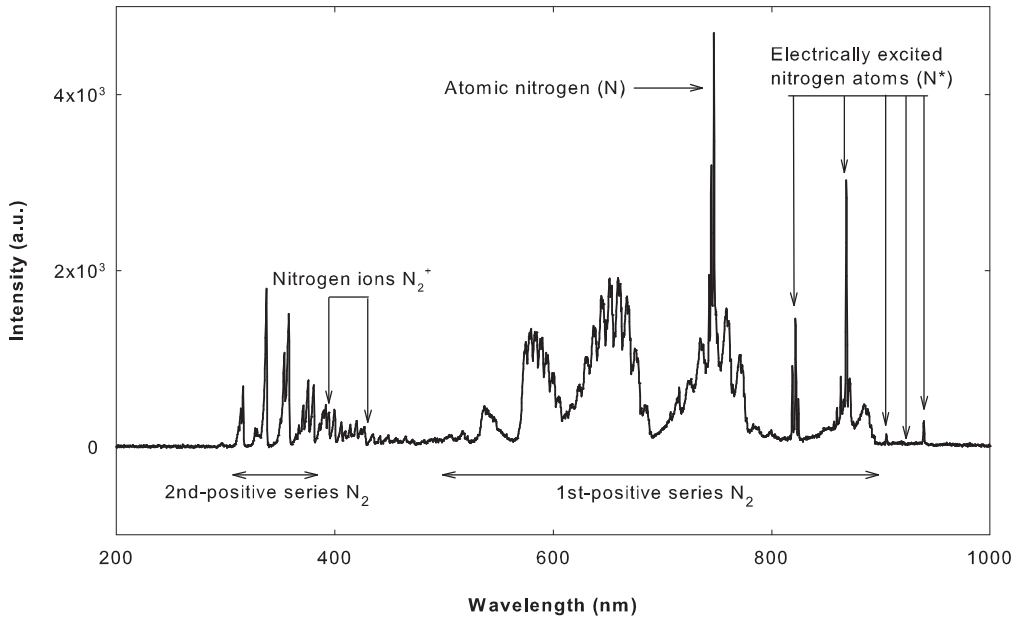

Figure 2.5 OES spectrum taken at 100 W RF and a nitrogen chamber pressure of 1×10^{-5} Torr, using the 276 hole aperture plate.

lower for the 488 hole aperture plate compared to the 276 hole aperture plate.

The use of OES is a common technique and other groups have already used it to determine the desired species for the growth of GaN by plasma-assisted MBE (PAMBE). Iliopoulos et al. who employ a similar HD25 plasma source, claim that the 869 nm atomic feature is the dominant feature [76]. The 869 nm peak only becomes the dominant feature for our source when it is operated at high RF powers, however. Iliopoulos et al. have mapped out the molecular and atomic species and report that the N_2^* concentration increases with RF power and nitrogen flow rate, while the N^* concentration increases predominantly with RF power and only at high power is there much change in the N* with nitrogen flow rate. The growth of GaN under N-rich conditions shows that incorporation is sensitive to changes in N_2^* [76]. Support for N_2^* as the dominant growth specie is also suggested by Ptak et al. who reported that atomic nitrogen appears to be relatively inefficient for growing GaN, requiring about ten atoms in the flux for each one incorporated into the growing layer [77]. In contrast, Osaka et al., using an SVT Associates model RF 4.5 with a 25 hole aperture plate (0.5 mm diameter holes), suggested that N^* dominates the growth [78]. To summarise, there seems to be some

uncertainty in the relative importance of various nitrogen species within a particular plasma, but OES plays an important role in allowing different plasmas to be compared.

2.2.5 Reflection High Energy Electron Diffraction

An additional advantage that MBE has over CVD growth systems is that the ultra high vacuum allows for in-situ diffraction based analysis techniques to be used. One such technique is reflection high energy electron diffraction (RHEED), which allows the crystal grower to obtain real-time information about the film surface quality, strain relaxation and growth rate. The RHEED system involves exposing the film surface, at a low grazing angle ($1-3^{\circ}$), to an electron beam and collecting the diffracted electrons on a phosphor screen. The RHEED pattern is composed of three features: a direct beam which is seen due to the low grazing angle used, the shadow edge of the substrate and also the reciprocal lattice pattern. The grazing electrons only penetrate a few atomic layers, so the information gained can be assumed to originate from a nearly 2D surface lattice; in reciprocal space the distance between the streaks (they are streaks due in part to the lack of atomic-scale flatness over the sampling area) are the inverse distance of the lattice spacing being probed. The assumption that the surface can be treated as a 2D surface lattice can only be used to gain a partial understanding, as often in real epitaxy the surface experiences 3D island growth. For a terraced 2D surface, the RHEED pattern consists of complete streaks (fig. 2.6a), whereas the 3D surface produces a spotty RHEED pattern (fig. 2.6b) due to surface roughness inducing transmission diffraction. In this work, Staib RH20 RHEED system was used with a k-Space Associates kSA 400 CCD based capture and analysis system. The electron source was typically operated at 20 kV and 1.5 A. Further information about the RHEED process and applications are available in reference [79].

2.2.6 Laser Reflection Interferometry

RHEED analysis can be used to determine the growth rate of the semiconductor by monitoring the spectral spot reflection intensity [80]. However, in cases where the thin film surface is not of high enough quality or the growth mode is not layer by layer,

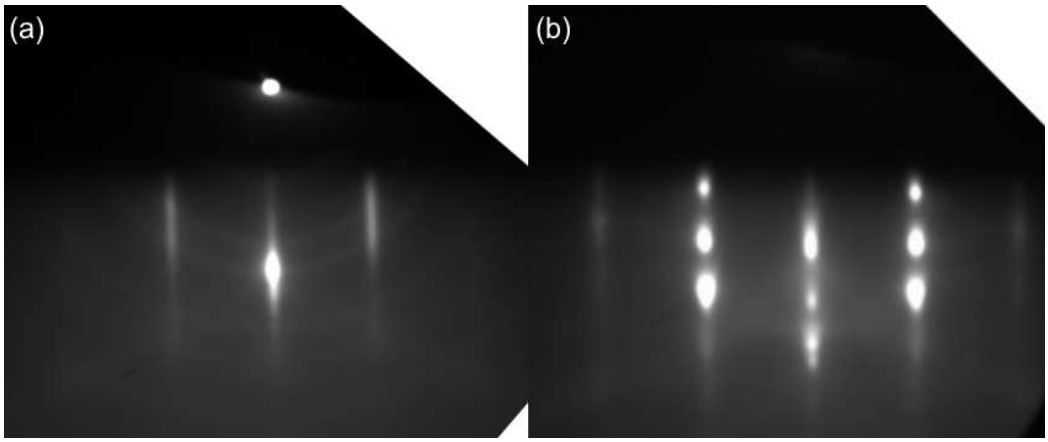

Figure 2.6 RHEED images taken from GaN a)under metal-rich conditions leading to 2D growth and b) under nitrogen-rich conditions leading to 3D growth.

RHEED oscillations cannot be observed. Another way of obtaining the growth rate is by using laser reflection interferometry (LRI), where a light source operating at a photon energy which is less than the band gap of the material of interest is reflected from the thin film/substrate at near normal incidence, as shown in fig. 2.7.

The reflected beam undergoes constructive and destructive interference as the film thickness changes. With the added knowledge of the sampling time, the growth rate of the film can be calculated from,

$$\left(\frac{4\pi dn}{\lambda}\right) = m\pi \tag{2.5}$$

where d is the film thickness as a function of the number of $\frac{1}{2}$ oscillations (m), and n is the refractive index of the thin film being studied at the wavelength (λ) of the probing light source. Equation 2.5 can then be rearranged and differentiated to give the growth rate, R(t),

$$R(t) = \left(\frac{\lambda}{4n}\right)\left(\frac{dm}{dt}\right) \tag{2.6}$$

The light sources used in this study were a semiconductor laser diode (675 nm) and a

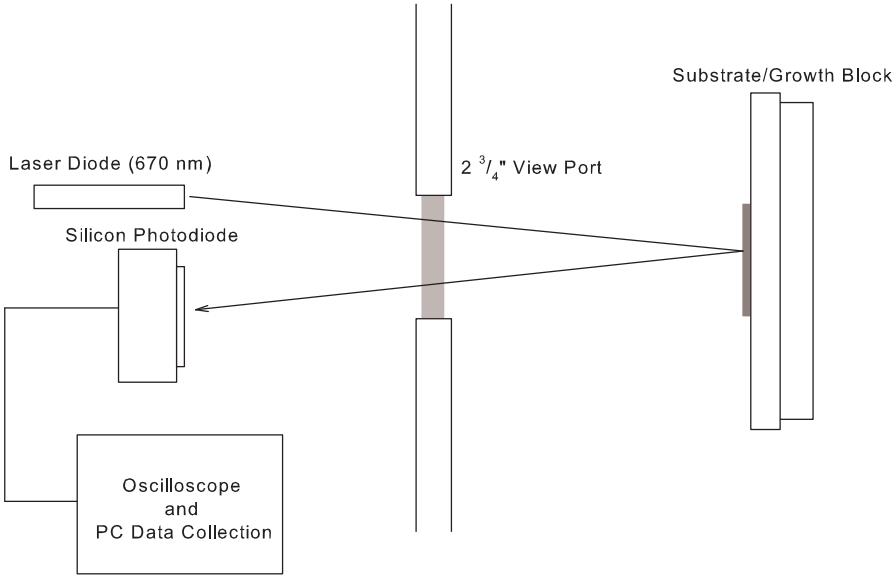

Figure 2.7 Schematic of the laser reflection interferometry system.

white light source from the k-Space Associates BandiT system.

2.3 SURFACE CHARACTERISATION

RHEED analysis of the surface quality only indicates if the surface is rough or smooth. Ex-situ techniques are relied on to clarify the surface morphology and quantify the roughness. Two such techniques are atomic force microscopy and scanning electron microscopy. Both are heavily used depending on the quality of the surface, so an overview is given here.

2.3.1 Atomic Force Microscopy

Atomic force microscopy (AFM) is used to profile the surface of thin films at a nanometre scale. A cantilever with a fine tip is raster scanned over the thin film; when the tip comes into contact with the thin film surface the cantilever deflects. A laser is used to measure the magnitude of deflection, therefore determining the height in relation to a set point. There are two modes of operation, tapping and contact. Tapping mode vibrates the cantilever, and reduces both the lateral forces on the tip (and the possi-

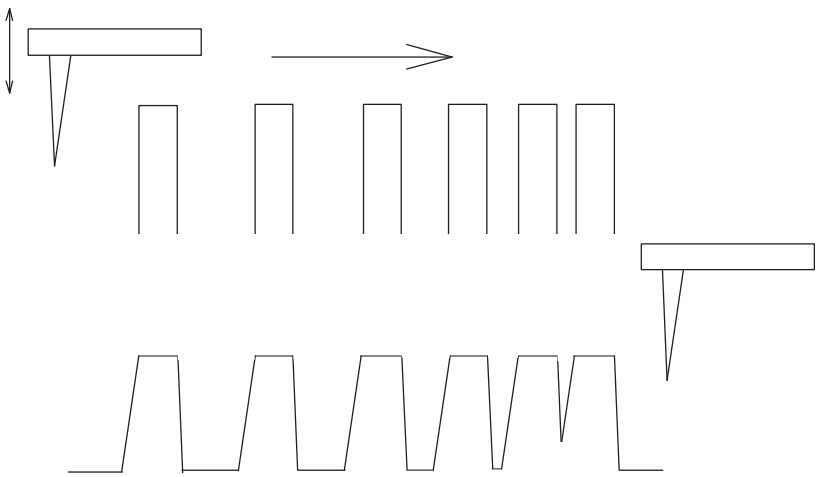

Figure 2.8 AFM imaging issues due to feature size relative to tip geometry. The top image shows the real surface and the bottom represents what would be expected from a line scan.

bility of breakage) as well as collection of impurities on the tip. Contact mode is often an order of magnitude faster (30 sec per scan) and allows for atomic scale resolution, although it suffers from tip wear due to direct contact. AFM does have issues imaging rough samples or samples where the spacing between features is smaller than the size of the AFM tip, as this leads to improper imaging of the sidewalls of the features, as illustrated in fig. 2.8. In this thesis a Digital Instruments 3100 AFM was extensively used to image thin films of InN and GaN that had atomically flat features.

2.3.2 Scanning Electron Microscopy

To overcome the imaging issues faced by AFM for rough and/or nanostructured surfaces scanning electron microscopy (SEM) can be used. In contrast to a standard optical microscope, SEM employs electrons instead of photons to image the sample. The electron wavelength is dependent on the acceleration voltage; in this study the voltage was typically 10 keV. This relates to a wavelength of 0.012 nm, which is significantly below the wavelength of 400 to 700 nm used in a conventional optical microscope, therefore leading to higher resolution images. A focused beam of electrons is exposed

to the sample and secondary electrons are emitted from the surface which are attracted to and collected by a detector. From the density of electrons a map of the surface can be obtained. In this study the SEM micrographs were produced using a Leica field emission SEM.

2.4 OPTICAL CHARACTERISATION

2.4.1 Photoluminescence

Optical characterisation is a very precise technique for identifying the slightest impurities in a thin film. Photoluminescence (PL) is one of the most commonly used optical techniques, with a photon source (laser) used to excite an electron into the conduction band, after which the electron then relaxes to a lower state by emitting a photon. The optical emission may involve other states, so that features may correspond to conduction to valence band transitions (C-V), free excitons (X), excitons bound to neutral donors or acceptors (A^oX), conduction band to acceptor transitions (CA), or donor to acceptor transitions (DA) as illustrated schematically in fig. 2.9. Photoluminescence measurements were conducted in the Physics department at the University of Canterbury, with the experimental data taken on the GaN thin films and nanostructures by Mr Reuben Mendelsberg and InN thin films investigated by Prof. Roger Reeves and Mr. Y.W. Song.

2.4.2 Cathodoluminescence

Photoluminescence probes an area the size of the laser spot, typically on the order of $500\,\mu$m, which is too large for probing individual nanowires. To obtain information about individual nanowires cathodoluminescence (CL) can be used, which is based on the emission of light from electron beam excitation using a SEM. With the enhanced resolution achieved with the SEM, spatial variation in the optical properties can be directly mapped to physical features, as has been seen in ZnO nanowires where there is a distinctive difference in the luminescence observed from the wetting layer and the nanowire [81]. In this study the CL measurements were conducted using a

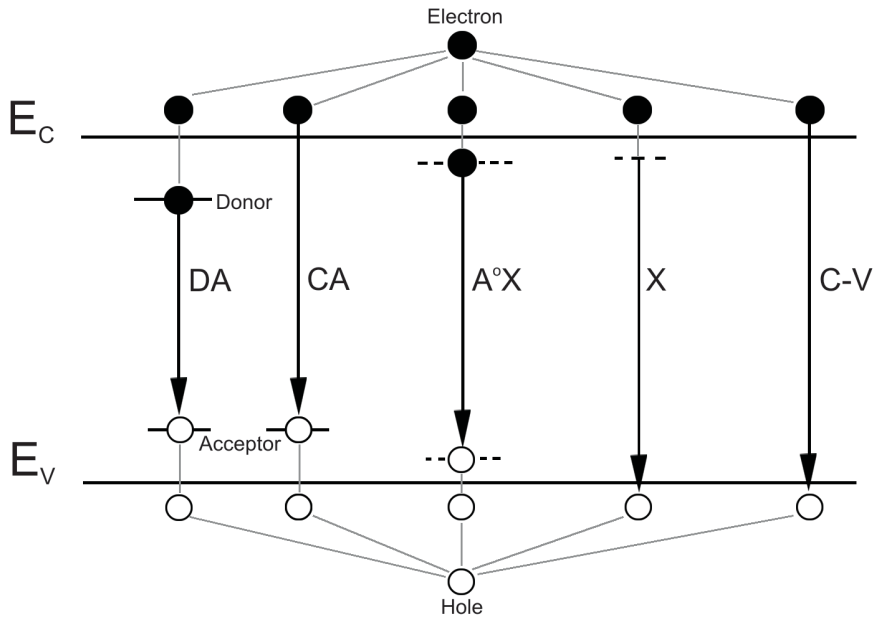

Figure 2.9 Schematic representation of donor- or acceptor- related and direct radiative recombinations.

JEOL JSM-6500F field emission SEM equipped with a Gatan MonoCL3 cathodoluminescence spectrometer and imaging system. The measurements were conducted by Prof. Masakazu Kobayashi at Waseda University, Tokyo.

2.5 ELECTRICAL CHARACTERISATION

2.5.1 Single Magnetic Field Hall Effect

A very quick and simple analysis tool for determining the electrical properties of semiconductors is the Hall effect. This requires only a current supply, voltmeter and magnetic field. The Hall effect measurement gives the resistivity, the carrier density and the mobility of the semiconductor. Using four ohmic contacts in the Van der Pauw layout (corner contacts on a square sample) the sheet resistance (R_S) of the sample is determined by measuring the resistance across the horizontal and vertical sides allowing for

$$e^{-\pi R_{\text{vertical}}/R_S} + e^{-\pi R_{\text{horizontal}}/R_S} = 1 \tag{2.7}$$

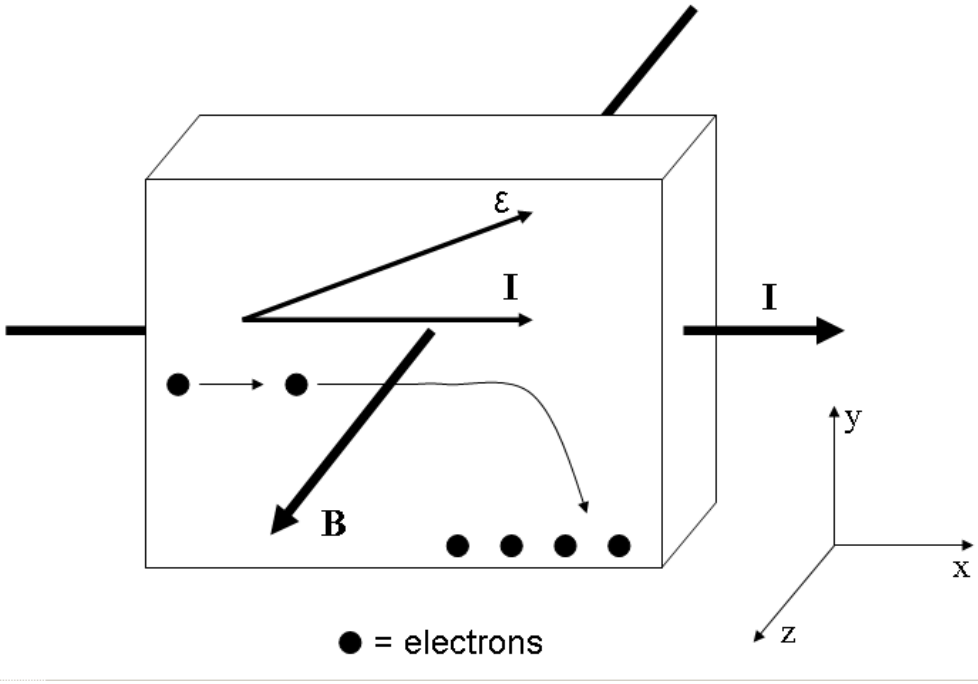

Figure 2.10 Schematic illustrating the Hall effect in a n-type sample.

to be solved [82, 83]. With the use of a magnetic field (0.51 T for this study) perpendicular to the current flow, the electrons accumulate on one side of the sample. This then can be used to determine the carrier density and mobility. The force due to the magnetic field is known as the Lorentz force and is given by,

$$F = q\mathbf{v} \times \mathbf{B} = q(v_x B_z) \tag{2.8}$$

where q is the electrical charge of an electron, **B** the magnetic field and **v** is the drift velocity. The accumulation of electrons at the bottom of the sample (-y direction) from the downward deflected current gives rise to a upward-directed electric field (+y direction) (2.10), ε, which balances the Lorentz force to give the Hall field,

$$\varepsilon_y = -v_x B_z \tag{2.9}$$

The creation of the electric field ε_y is known as the Hall effect, and the terminal voltage $V_H = \varepsilon_y W$ (W is the film thickness) is the Hall voltage. The drift velocity is defined as,

$$v = \frac{J}{qn} = \frac{I}{Aqn} \tag{2.10}$$

where J is the current density, n is the number of electrons traversing the cross sectional area A, and I is the electrical current. This can be substituted into equation 2.9 to yield

$$\varepsilon_y = -\left(\frac{J_n}{qn}\right) B_z \equiv R_H J_n B_z \tag{2.11}$$

where R_H is the Hall coefficient and is expressed as,

$$R_H = -\frac{1}{qn} \tag{2.12}$$

for electrons. Therefore by measuring the Hall voltage for a known current and magnetic field the carrier concentration and carrier type can be determined by rearranging equation 2.12, and assuming a homogeneous structure,

$$n = -\frac{1}{qR_H} = \frac{J_n B_z}{q\varepsilon_y} = \frac{IB_z W}{qV_H A} \tag{2.13}$$

where all the right hand terms are known. The equation for sample resistivity can be written in terms of the mobility of the carriers as,

$$\rho = \frac{1}{q(n\mu_n + p\mu_p)} \tag{2.14}$$

where μ_n, μ_p are the electron and hole mobility, respectively. Assuming an n-type semiconductor such that μ_nn >> μ_pp, we may write

$$\rho = \frac{1}{qn_n\mu_n} \tag{2.15}$$

$$R_s = \frac{1}{qn_s\mu_n} \tag{2.16}$$

$$\mu_n = \frac{1}{qn_sR_s} \tag{2.17}$$

Implicitly assumed in the analysis is that the sample is homogeneous.

To determine the mobility and carrier concentration the Van der Pauw method is typically used. The technique is broken up into two measurements, determination of the resistivity and a Hall measurement. For the resistivity measurement Van der Pauw determined that for an arbitrary shape one only needs to measure the resistance along the horizontal and vertical directions to be able to resolve the sheet resistance. This is done by applying a voltage across one edge of the sample and measuring the current flowing along the opposing edge. Further improvements can be made to the measurement by swapping the sides that the current and voltage are measured from and also by changing the current polarity, and taking appropriate averages. By changing the polarity the influence of the thermoelectric Seebeck effect can be reduced. From the averaged (a total of four resistance measurements per direction) resistance measurements the sheet resistance can be resolved using equation 2.7 by a suitable iteration method.

For the Hall measurements a known magnetic field is applied perpendicular to the sample, while a known current is passed across the in-plane diagonal of the sample and the resulting voltage (Hall voltage) is measured along the opposite in-plane diagonal. From the Hall voltage the carrier concentration can be resolved using equation 2.13

and therefore the mobility can be calculated using equation 2.17

To properly use the Van der Pauw method for an arbitrary shaped semiconductor sample one must have:

1. A sample of known uniform thickness, with no holes.

2. Four infinitely small ohmic contacts close to the boundary of the sample as possible. The size of the error introduced from the contacts is on the order of D/L, where D is the average diameter of the contact and L is the distance between the contacts.

3. Stable temperature conditions to reduce any thermomagnetic effects

4. It is preferred that the measurements are taken in the dark to reduce photoconductance or photovoltaic effects.

2.5.2 Variable Magnetic Field Hall Effect

For thin films, the use of buffer layers grown at low temperatures means that a Hall effect sample will be inhomogeneous [84, 85, 86, 87]. The situation is further complicated in the case of InN, as it suffers from a surface accumulation layer that can easily dominate electrical measurements. Therefore, a typical InN film can be qualitatively represented by three parallel resistors, with current flowing through each layer. However, instead of having equal resistances which would be the case for a homogeneous film, the buffer layer is likely degenerate (high carrier concentration) therefore having a small resistivity. The same is true of the surface accumulation, so the overall measurement is dominated by the buffer layer and surface accumulation layer fig. (2.11). The contribution of any non-degenerate conduction path can be eliminated through variable temperature measurements. However, the buffer layers and surface layers are always degenerate - and to date, there have been no reports of clearly nondegenerate bulk layers, requiring an alternative.

Fortunately, the sample temperature is not the only variable that can be changed during the Hall effect measurement; the magnetic field is also a controllable quantity.

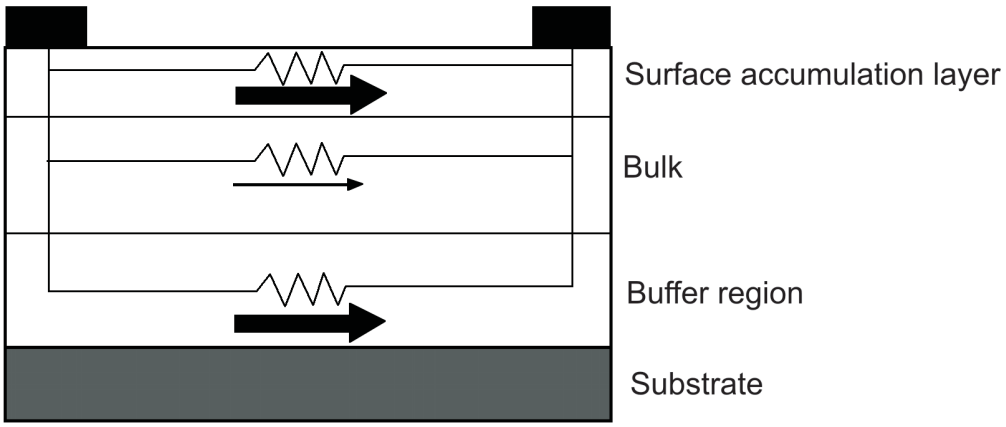

Figure 2.11 Model of a three layer semiconductor, containing a degenerate buffer layer, bulk layer and a surface accumulation layer. In this case the current path is dominated by the low resistance of the surface accumulation layer and buffer layer so the effect of the bulk layer is not observed in the single field Hall effect.

The variable magnetic field Hall effect (VFH) can be used to the determine the influence of the various carriers and has been extensively used for the analysis of HgCdTe (see references [88, 89] and references therein). Where n-type HgCdTe can be easily determined using the standard single field Hall effect (SFH), SFH measurements from p-type HgCdTe exhibit an anomalous Hall effect [89]. VFH has been able to clarify that the anomalous Hall effect is either due to multiple carrier layers, or inhomogeneities [90, 91]. VFH was initially used to investigate InN due to the surface accumulation layer, with results confirming at least two carrier populations one with an unresolvable low mobility, and the other a higher mobility attributed to the bulk [92]. Despite its success, use of VFH has been limited in part due to the requirement of a 10 Tesla magnet.

VFH adds a significant degree of complexity to the process of characterising thin films, so only a selected range of samples were measured using the VFH technique. The samples are prepared with the same four point contacts as for the standard SFH method, although several measurements are taken across a range of magnetic field strengths. The current density - electric field relationship can be expressed as

$$J = \sigma E \tag{2.18}$$

where σ is the conductivity. However, σ is actually a tensor quantity due to the combined effects of the electric field and the magnetic field and therefore equation 2.18 can be written as the matrix equation

$$\begin{bmatrix} J_x \\ J_y \end{bmatrix} = \begin{bmatrix} \sigma_{xx}\, \sigma_{xy} \\ \sigma_{yx}\, \sigma_{yy} \end{bmatrix} \begin{bmatrix} E_x \\ E_y \end{bmatrix} \tag{2.19}$$

with the magnetic field along the axis. As long as the semiconductor is isotropic in the measurement plane, $\sigma_{yy} = \sigma_{xx}$ and σ_{yx} = -σ_{xy} from symmetry. The Hall coefficient and resistivity equations can then be defined as

$$R_H(B) = \frac{V_H}{wJ_xB} = \frac{\sigma_{xy}/B}{\sigma_{xx}^2 + \sigma_{xy}^2} \tag{2.20}$$

and

$$\rho(B) = \frac{V_x}{LJ_x} = \frac{\sigma_{xx}}{\sigma_{xx}^2 + \sigma_{xy}^2} \tag{2.21}$$

The conductivity tensor components derived from the experimental Hall and resistivity data as a function of magnetic field are then fitted to the following forms:

$$\sigma_{xx}\,(B) = \sum_k \frac{n_k e \mu_k}{1 + {\mu_k}^2 B^2} \tag{2.22}$$

$$\sigma_{xy}\,(B) = \sum_k \frac{S_k n_k e {\mu_k}^2 B}{1 + {\mu_k}^2 B^2} \tag{2.23}$$

where n_k is the electron or hole concentration for a given layer k, μ_k is its corresponding

mobility, and S_k is +1 for holes and -1 for electrons. It can be seen that the conductivity is proportional to the mobility and carrier density, also it is dependent on the magnetic field. To evaluate the experimental data the conductivity tensor is typically analysed using either the quantitative mobility spectrum analysis program (QMSA) [93] or multiple-carrier fitting (MCF) techniques [84]. The data that can be extracted is the influence of the electrons, holes and surface charges on the electrical properties, however resulting fits cannot resolve where the features are from unless one is able to modify regions of the film, possibly the surface, and monitoring what features in VFH are changed. The VFH is limited by the magnetic field; if only the transverse component of the conductivity tensor is used, then the lowest carrier mobility that can be extracted with some accuracy is of the order of B^{-1}, where B is the maximum magnetic field used. In this work, field strengths of up to 12 T were available.

2.5.3 Capacitance Voltage Profiling

Even though VFH is able to determine that distinct carrier populations exist in an inhomogeneous film, their location within the film cannot be resolved. One way of determining the carrier profile of a semiconductor is through capacitance voltage profiling (CV). The CV technique relies on the fact that the width of a reverse biased space charge region (SCR) (and hence depth being probed) of a semiconductor junction device depends on the applied voltage to the rectifying contact. To be able to determine the carrier density from the SCR a small ac signal is applied to the bias voltage. The small ac signal adds a charge increment to the rectifying contact and an equal charge of the opposite sign is induced on the edge of the SCR, which causes a change in capacitance. This change in capacitance enables the carrier density at a specific depth to be calculated. The CV profiling is limited to the depth of the depletion layer, so information about the carrier profile is typically limited to the near surface region.

The main requirement for CV profiling is the fabrication of a rectifying junction. The simplest junction is that formed by a metal sputtered or evaporated onto a clean semiconducting surface, known as a Schottky diode. When the Fermi energy in the metal and semiconductor align by a flow of electrons from the semiconductor, a near

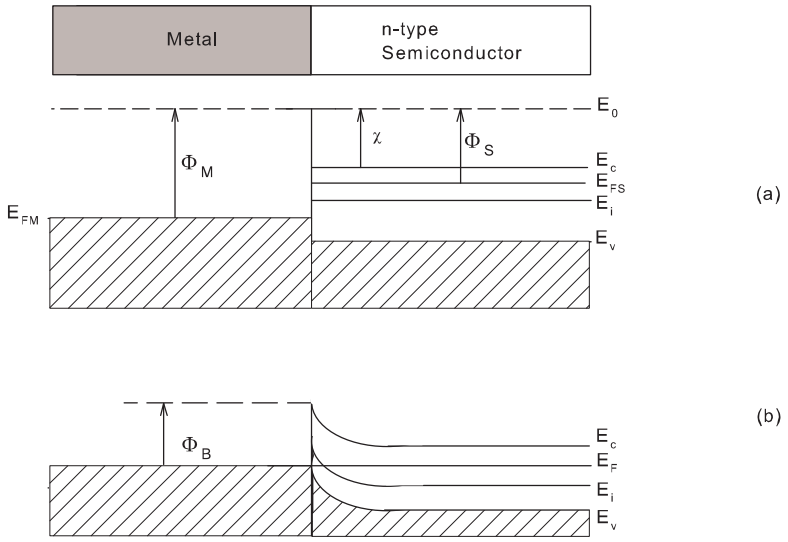

Figure 2.12 Energy band diagram for the ideal metal semiconductor contact, for the case when the metal work function ϕ_M is greater than the semiconductor work function ϕ_S: (a) instant of contact formation and (b) equilibrium conditions. ϕ_B is the barrier height of the Schottky contact, χ is the electron affinity, E_o is the vacuum level, E_{FM} is the fermi level of the metal, and E_{FS} is the fermi level of the semiconductor.

surface depletion region is generated inside the semiconductor, as shown in fig. 2.12. The width of the depletion region is given by,

$$W = \left[\frac{2K_s\epsilon_o}{qN_d}\left(V_{bi} - V_A\right)\right]^{\frac{1}{2}} \tag{2.24}$$

where K_s is the semiconductor dielectric constant, N_d is the carrier density, V_{bi} is the built in potential and V_A is the applied bias. This is assuming that the depletion region has abrupt boundaries; inside this region the semiconductor is fully depleted and outside of this it is electrically neutral, as shown in fig. 2.13.

When a small ac signal is superimposed on the reverse bias dc voltage the charge fluctuates inside the diode. Modelling this with a simple parallel plate capacitor,

$$C = \frac{K_s\epsilon_o A}{W} \tag{2.25}$$

Inserting equation 2.25 into equation 2.24 results in,

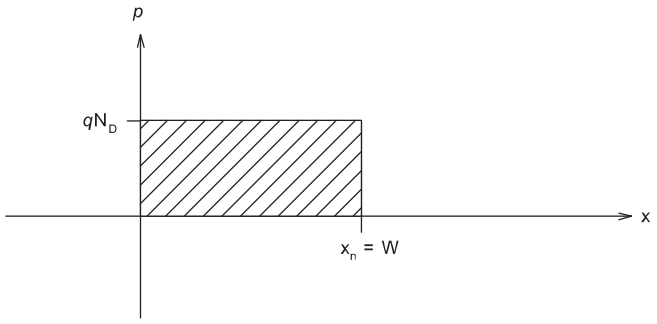

Figure 2.13 Charge density as a function of position in the depletion approximation.

$$C = \frac{K_s \epsilon_o A}{\left[\frac{2K_s\epsilon_o}{qN_D}\left(V_{bi} - V_A\right)\right]^{\frac{1}{2}}} \tag{2.26}$$

which can be manipulated to yield,

$$\frac{1}{C^2} = \frac{2}{K_s \epsilon_o q N_D A^2}(V_{bi} - V_A) \tag{2.27}$$

Therefore the semiconductor doping density can be determined from the slope of a $\frac{1}{C^2}$ versus voltage curve, and the V_{bi} value is determined by extrapolating to $\frac{1}{C^2} = 0$. One assumption that is made when deriving equation 2.27 is that N_D does not vary over the distance W, as variations of N_D over the distance W can not be resolved by the C-V technique [94].

2.5.4 Electrochemical Capacitance Voltage Profiling

For CV profiling a semiconductor junction has to be fabricated. As shown above a simple rectifier can be made using a Schottky diode. However, for InN no metal Schottky contacts have been able to be fabricated, even with mercury which is known to easily form a Schottky contact to essentially all III-V semiconductors [95], suggestive of a surface accumulation layer. It has been determined by Mahboob et al. using high resolution electron energy loss spectroscopy that there is an intrinsic electron accumulation

layer present on even clean InN surfaces [96]. An alternative method of fabricating a Schottky contact for CV is by using an electrolyte to enable electrochemical capacitance voltage (ECV) measurements. The technique has a few drawbacks, however, including the possibility of etching the sample (sometimes an advantage), and a much weaker/leakier junction. A good review on principles, capabilities, limitations and potential of the ECV technique is in reference [97].

The early ECV measuring systems were known as Post Office plotters due to the affiliation of its originators [97]. The setup involves films grown on either conductive substrates, or on bulk material to allow the substrate to act as a back contact [98]. To create the diode area the sample is pressed against a sealing O-ring on the vessel containing the electrolyte solution. A carbon rod was employed as the working cathode, and a saturated calomel electrode was used as a reference electrode. A window for illuminating the sample and a pump used to agitate the solution were also included as the ECV process can etch the sample surface.

As the InN samples in this study were grown on insulating substrates the ECV setup used in this study is slightly different, but also takes into consideration some of the issues with using a back contact and definition of the diode area using the O-ring. For the ohmic contact a low resistivity Ti/Au contact ring was formed on the InN surface. The low resistivity of the ohmic contact ensures that the series resistance is only dependent on the diode area. Also a low series resistance is required to ensure a good quality electrochemical Schottky diode which can be determined by the dissipation factor (D, which is also the inverse of the quality factor (Q)). The smaller the value of D the better the diode; for our InN films a typically value was 0.3-0.5 (Q 2 - 3). Sell et al. determined that D should not exceed 0.4 to ensure an error of less than 2.5% [99].

To insulate the ohmic contact from the electrolyte, and also define the diode area, a layer of photoresist was applied over the entire sample and exposed using standard lithography processes. Using the photoresist allows for a set area to be defined that does not suffer from area change due to electrolyte leakage which can occur in the case of an O-ring. ECV is very sensitive to changes in area, as the capacitance calculations

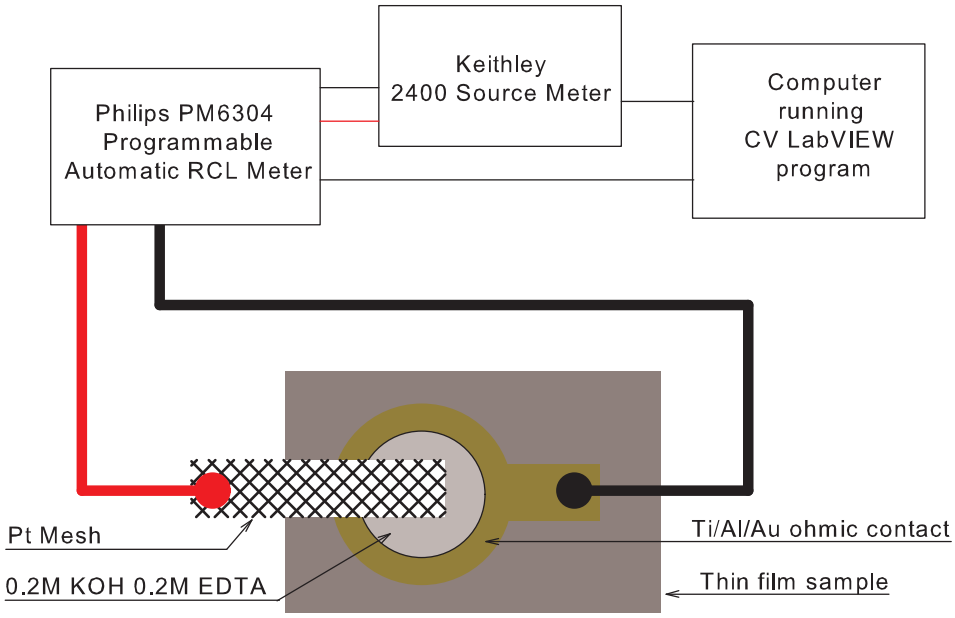

Figure 2.14 Schematic diagram of the electrochemical capacitance voltage measurement setup.

are dependent on the area being precisely known. Also, a smaller area can be created than by an O-ring, thereby further reducing the series resistance. To complete the system a drop of the electrolyte is applied to the exposed semiconductor area and contacted with a platinum mesh probe. Over time the drop does evaporate but three or four scans can be taken before it will affect the measurement. Fig. 2.14 shows the schematic diagram of the ECV setup used in this study.

To finalise the setup of the ECV system an electrolyte has to be chosen. The electrolyte has two functions in the ECV technique: 1) the electrolyte forms a Schottky contact with semiconductor and 2) the electrolyte has a controlled electrochemical dissolution reaction with the semiconductor. Thus a given amount of material is removed with each scan. A range of electrolytes have been used with III-V semiconductors, these being Tiron, NaOH:EDTA, NaOH and H_2SO_4 [94]. Electrolytes used for InN are typically 0.2 M NaOH or 0.2 M KOH with the addition of 0.2 M of EDTA, where the EDTA neutralises the pH of the solution so that it does not etch the photoresist, and also improves the etch uniformity. A current-voltage plot for a 0.2 M NaOH with 0.2 M EDTA electrolyte on film 683-InN-YSZ(111), a 1200 nm thick InN film growth on

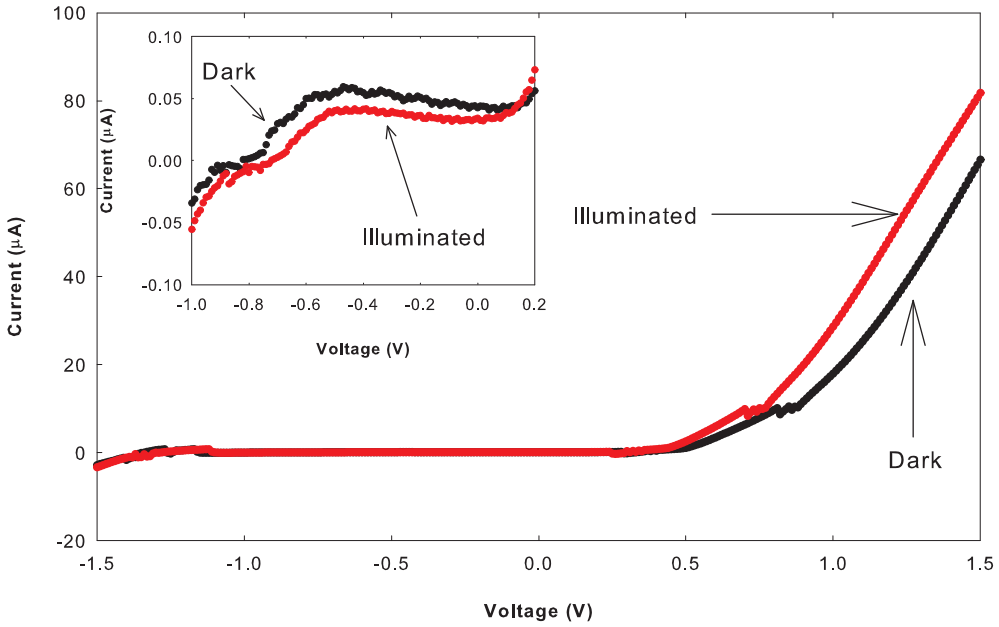

Figure 2.15 Current-voltage plot from the ECV measurement of film 683-InN/YSZ(111) under dark and illuminated conditions. Inset is a magnified view of the stable region showing some decrease in the current when illuminated.

(111)YSZ), is shown in fig. 2.15. It should be noted that KOH and NaOH electrolytes takes several hours to etch InN at room temperature, therefore profiling of the surface accumulation layer, which is around 5 nm thick, can be easily achieved using the ECV process.

When performing ECV some groups report a rest potential [97, 100], which is a factor that needs to be considered. There are two types of rest potential, dark and light. The dark rest potential is a shift of the voltage from the origin due to electrochemical potential and is often used as the starting point for the measurement as it is assumed that this is the zero point potential [97]. However, in the ECV setup used in this study we do not have a reference probe, therefore the dark reference potentials cannot be determined. The light rest potential is where the reverse current is increased due to electron flow from the semiconductor into the electrolyte. Shown in fig. 2.15 is the dark and illuminated I-V, as the ECV scans were typically conducted under normal room lightly, there is not a significant change in the I-V under lighting conditions so it has been assumed to be negligible in this study.

The standard equation used to determine the carrier concentration for the Schottky diode (equation 2.27) is slightly modified for the ECV process. Instead of the voltage term being $(V_{bi}-V_A)$ it is replaced with just the applied voltage. Therefore the equation for the carrier concentration is given by,

$$N_A(w) = \frac{2}{qK_s\varepsilon_o A^2 \left[\frac{d\frac{1}{C^2}}{dV}\right]} \tag{2.28}$$

also often written as

$$N_A(w) = -\frac{C^3}{qK_s\varepsilon_o A^2 \left[\frac{dC}{dV}\right]} \tag{2.29}$$

as $\frac{d\left(\frac{1}{C^2}\right)}{dV} = \frac{-2}{C^3}\left(\frac{dC}{dV}\right)$. Equation 2.25 still applies for resolving the depth profile. Also, integrating the $1/C^2$ versus V curve can be used to determine the sheet concentration of the surface accumulation layer.

Chapter 3

GROWTH OF GALLIUM NITRIDE AND INDIUM NITRIDE EPILAYERS

3.1 GALLIUM NITRIDE GROWTH

For the growth of GaN, sapphire, silicon carbide (SiC) and GaN MOCVD templates are typically used [28]; the lattice mismatch exceeds 16% and 2.5% for sapphire and SiC, respectively. Sapphire is often used as the substrate as it is relatively inexpensive. To reduce the effect of the lattice mismatch the surface can be nitrided, through exposing the sapphire to a nitrogen plasma; this process forms at least a partial AlN layer [101]. However, it can also lead to a mixture of cubic and hexagonal AlN (and hence GaN) phases in the film [102]. A low temperature GaN buffer layer can also be used to reduce the strain effects arising from the lattice mismatch, and poor wetting of the substrate at high growth temperatures. An alternative substrate is an MOCVD grown GaN template, as it allows for the use of a lattice matched surface with threading dislocation densities as low as $5 \times 10^8\, cm^{-2}$. In this study Ga–polar GaN templates from Lumilog (semi-insulating GaN templates by Fe-doping) were used, as they are commerically available and provide a consistent starting surface. Issues faced with buffer layers and nitridation are therefore eliminated. Further, the Ga–face is known to be more favourable for the incorporation of dopants [103].

GaN templates are exposed to atmosphere through handling, leading to oxidation and carbon layers on the GaN surface. This surface contamination layer may disrupt epitaxy, and so must be removed. To do this the MOCVD template is initially heated to 600°C; at this substrate temperature gallium will still stick to the GaN surface. A

layer of gallium is then deposited for a period of 2 mins. Examination of the surface by RHEED at this point shows the streaky single crystal pattern has faded to an amorphous layer. This amorphous layer is expected to be composed of Ga_2O_3 and gallium metal. The substrate is then heated to 800°C, where Ga_2O_3 is volatile and will evaporate off the surface, leaving an oxygen free GaN surface ready for growth [104].

3.1.1 Gallium Nitride Growth Regimes: N–rich, Ga–rich and Intermediate

To grow device quality GaN by MBE it is important to appreciate that there are three distinctive growth regimes: nitrogen rich (N–rich); gallium rich (Ga–rich) - sometimes called the gallium droplet regime; and intermediate. What sets these regions apart is a combination of gallium to active nitrogen ratio (Ga:N) and substrate temperature. Several growth diagrams have been proposed and a simple model was initially developed for these three parameters by Heying et al. [105], as shown in fig 3.1a. As understanding of the MBE growth of GaN has evolved, the accepted growth diagram has increased in complexity, including the division of the central intermediate regime (fig. 3.1b), and the inclusion of the Ga coverage at each region and the growth modes that occur (fig. 3.1c). It is worth noting that the precise role of each 'active' nitrogen species remains a subject of ongoing study, and therefore each system requires fine tuning to determine transition points between growth regimes.

The N–rich growth regime (N-stable) is where the active nitrogen flux exceeds the gallium flux (Ga:N <1). This leads to a GaN surface that is terminated with nitrogen bonds, therefore the nitrogen would have one bond terminated to the Ga and three dangling bonds that would lead to significant reduction of the Ga adatom surface mobility [108]. Theoretical calculations of the diffusion barrier for a N-terminated surface have shown that the barrier is about five times greater compared to a Ga-terminated surface [109]. Due to the increased diffusion barrier, the diffusion length of Ga adatoms is small, therefore leading to statistical roughening of the surface. Also, the increased diffusion barrier can lead to stacking faults, as Ga adatoms become at non optimal sites. An example give by Zywietz et al. is a Ga atom which becomes trapped

(a)

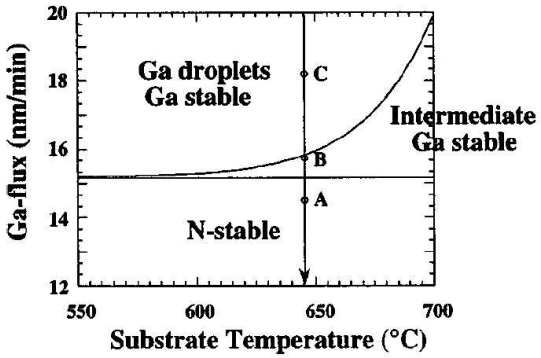

(b)

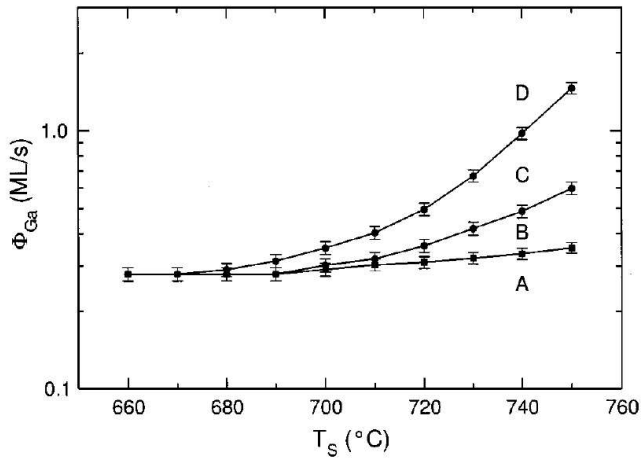

(c)

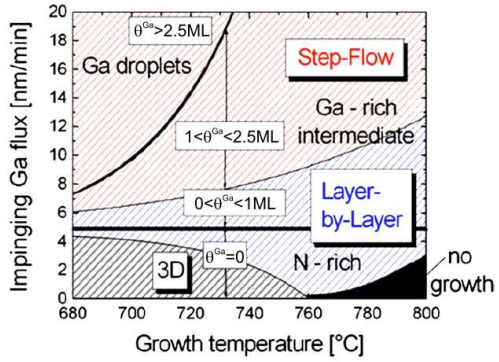

Figure 3.1 Evolution of the GaN growth regimes for GaN grown by MBE. a) Heying et al. published in 2000 [105], b) Adelmann et al. published in 2002 [106], and c) Koblmüller et al. published in 2007 [107].

at the face centred cubic (fcc) position and does not hop to the wurtzite hexagonal close packed (hcp) site; a fcc nucleation center is formed, therefore leading to a possible cubic inclusion [109]. Growth of GaN under the N–rich regime leads to three dimensional crystal growth, which is indicated by a spotty RHEED pattern. Moreover, the N-rich grown layers are often insulating due to the incomplete coalescence of the grains; in the extreme case nanowires are grown instead of a thin film [110].

The Ga–rich growth regime is produced at low substrate temperatures ($< 650°\mathrm{C}$) in conjunction with a gallium flux greater than the nitrogen flux (Ga:N > 1). Under Ga–rich conditions the crystal quality of the GaN films is improved due to the reduced diffusion barrier of a Ga–terminated surface, known as the Ga–adlayer. The Ga–adlayer allows for longer diffusion lengths and a step-flow mode resulting in 2D growth [109]. GaN films grown under Ga-rich conditions have flat single crystal regions, producing a streaky RHEED pattern. However, at these low growth temperatures excess gallium remains on the surface which leads to the formation of droplets. Compared to the N–rich growth regime the surface morphology produced is atomically flat, except for the gallium droplets, and can lead to semiconducting layers with electron mobilities of around 800 $cm^2V^{-1}s^{-1}$ and carrier concentrations as low as $3 \times 10^{16} cm^{-3}$ [26]. Further optimisation, however, can be achieved.

To overcome the formation of gallium droplets, which would hinder device fabrication, the substrate temperature is typically increased to $720 - 770°\mathrm{C}$, which leads to excess gallium being evaporated from the growth surface before gallium droplets can form. This growth regime is known as the intermediate (or Ga-stable) growth regime. As the growth environment is under Ga–rich conditions a Ga–adlayer still exists on the surface of the film and therefore high quality single crystal GaN films can be obtained. At present the intermediate region is used in MBE growth of active layers for GaN devices. The improvements from the higher substrate temperature and removal of the gallium droplets led to increased electron mobilities of around $1000\, cm^2V^{-1}s^{-1}$, while the carrier concentration remains unchanged at $3 \times 10^{16}\, cm^{-3}$ [26].

In fig. 3.1b the intermediate regime is shown as two separate regions, b and c, classified by the thickness of the Ga–adlayer. Aldmann et al. established the thickness

of the Ga–adlayer by growing a GaN layer and then monitoring the RHEED intensity after terminating the growth at a fixed substrate temperature of 740°C. Growth in the N–rich growth regime gives no change in the RHEED intensity during and after growth whereas a gallium layer will attenuate the intensity of the RHEED. Therefore the time taken for the beam intensity to saturate indicates the thickness of Ga-adlayer [106]. In the intermediate growth regime, the Ga–adlayer thickness increases from zero monolayer (ML) coverage to 2.5 ML (region b in 3.1a and b), or a laterally contracted bilayer of gallium (Ga–bilayer). Following the formation of the Ga–bilayer, Aldmann et al. observed that the second region of the intermediate region existed, and this was where the Ga–adlayer had a constant thickness of 2.5 ML (region c in3.1b). The two different intermediate regimes that Aldmann et al. distinguished are therefore when the Ga–adlayer is developing (region b), so the thickness of the Ga–adlayer ranges from 0 - 2.5 ML, and when the Ga–adlayer is a constant thickness of 2.5 ML (region c) [106]. The region b is the desired growth regime due to the complete formation of the Ga-adlayer.

More recently Koblmüller et al. considered GaN grown at higher growth temperatures (>750°C) in conjunction with RHEED and line-of-sight quadrupole mass spectroscopy (QMS) to determine the gallium coverage [107]. Using this approach the Ga–adlayer was determined to range between 0 and 2.5 ML thick, with no saturation region before the formation of gallium droplets [111]. Also, for Ga–adlayer thickness above 1 ML, Koblmüller et al. reported that RHEED oscillations are not able to be measured, but streaky RHEED is sustained. This transition relates to a change in the growth mode: from layer–by–layer to step–flow growth mode. Moreover, for high growth temperatures, typically categorised as >750°C, the layer-by-layer growth extends into the N–rich growth regime. The support for the layer-by-layer growth is possibly due to increased diffusion length from thermal energy transfer to the adatoms. The Koblmüller et al. growth diagram is shown in fig. 3.1c. Also observed by Koblmüller et al. is a dead zone where GaN growth does not occur at all.

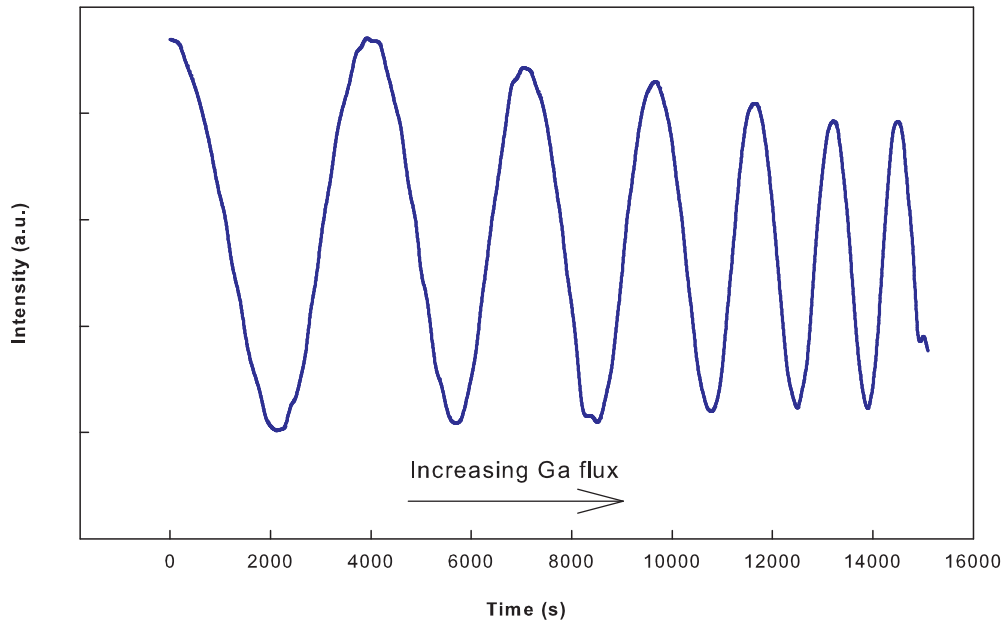

Figure 3.2 Reflection interferometry analysis using the semiconductor laser.

3.1.2 Determination of the Growth Regimes

Clearly, an accurate determination of the growth regimes is critical in terms of film quality. They can be determined by monitoring the RHEED pattern intensity, as already discussed, but also by monitoring the real time growth rate [80]. There are several growth rate analysis methods available including RHEED and laser reflection interferometry (LRI). RHEED is good for smooth films growing under the layer–by–layer growth mode, and oscillation measurements require only several tens of seconds of growth. However, to study the growth rate over a large range of growth modes aside from layer–by–layer growth, LRI is a better option. As LRI uses a long wavelength (600 nm) the effects of surface roughness, typically an order of magnitude smaller than the incident wavelength, have a negligible effect on the growth rate measurement. However, as the time taken to measure an oscillation is dependent on the wavelength of the light source, which is usually in the visible spectrum for alignment purposes, a precise measurement of the growth rate can take several hours (fig. 3.2).

For this study, the white light source from a k-Space Associates Inc. BandiT band edge spectroscopy based temperature measurement system was used to illuminate the

film. The BandiT system uses a white light produced by a quartz-halogen lamp, which is focused onto the sample. The reflected beam is collected in the detector optics (the maximum detection diameter is 25 mm) and focused onto a 400 μm optical fiber that is connected to a solid state spectrometer. The user can therefore determine the growth rate through intensity oscillations at any wavelength from 380 1100 nm, as long as the beam intensity does not saturate at the desired wavelength. The spot size of the white light source was adjusted to the size of the substrate. As a result, the growth rate measured is an average from the entire film. Furthermore, using a larger spot size allows for more uniform detection of the growth regimes over the substrate; With imperfect coincidence of various beams, a small spot size may inaccurately characterize the growth regime that best describes most of the growing surface.

The growth rate study involved growing GaN and monitoring the reflected beam intensity. Once a maximum and minimum intensity was measured, the gallium cell temperature was increased by 10°C. Fig. 3.3 shows the growth rate versus gallium flux for a substrate temperature of 750°C and nitrogen plasma settings of 150 W and 1×10^{-5} Torr. Two different runs are shown: Ga-polar growth on an MOCVD template and N-polar growth on a sapphire substrate. The plasma settings were chosen to have the highest $N_2 : N$ ratio to maximise the molecular nitrogen species, based on the work by Ptak et al. as summarised in section 2.2.4 [77].

The transition from the N–rich to intermediate/Ga–rich growth regime is observed when the GaN growth rate saturates. For the Ga–polar GaN (MOCVD GaN template) the growth regime transition occurs at a gallium flux of 1.7×10^{14} atoms$\cdot$cm^{-2}s^{-1}, while for the N–polar GaN (sapphire substrate) the growth regime transition occurs at a lower flux of 1.3×10^{14} atoms $\cdot$ cm^{-2}s^{-1}. Koblmüller et al. determined that the maximum Ga–adlayer thickness supported by the Ga–polar and N–polar GaN surfaces was 2.5 ML and 1 ML, respectively [112]. This difference in the maximum supported Ga–adlayer thickness may explain why for the N–polar surface we observe the saturation of the GaN growth rate occurring at a lower gallium flux. For both of the growth rate studies, when the growth rate saturation occurred, the GaN films became coated with a grey layer, later determined by ex-situ analysis to be metal droplets.

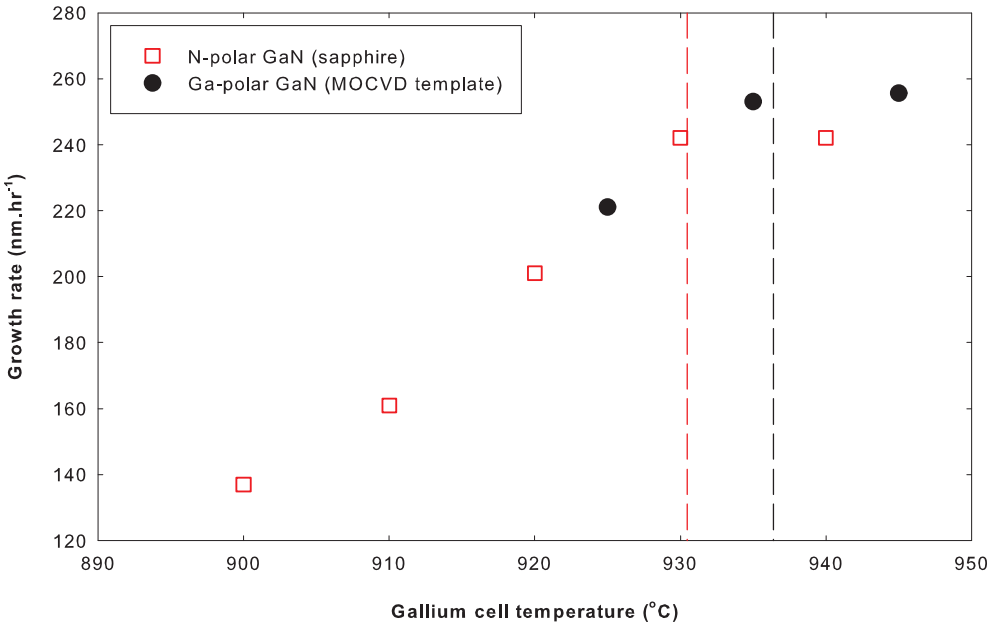

Figure 3.3 Growth rate study for Ga-polar and N-polar GaN. The dashed lines represent the transition from the N–rich to intermediate/Ga-rich growth regimes.

3.1.3 Gallium Flux Dependence

The growth rate studies give an indication of the gallium flux required to achieve the desired growth regime. However, they do not determine the transition from the intermediate to Ga-rich growth regime, which can be resolved during or after growth by checking for the formation of gallium droplets on the surface. To resolve the transition more clearly two GaN films were grown, as given in table 3.1. The difference in the growth rate between the growth rate sweep and the single film growth is possibly due to stability of the gallium flux, or film surface quality. The initial GaN film, 632–GaN–GaN, was grown with a gallium flux of 1.6×10^{14} atoms $\cdot$ cm^{-2}s^{-1} on an MOCVD template. This resulted in a spotty RHEED pattern and SEM which exhibited a rough granular surface, as shown in fig. 3.4, which is consistent with N–rich growth. Increasing the gallium flux to 2.0×10^{14} atoms $\cdot$ cm^{-2}s^{-1}, 633–GaN–GaN, retained a streaky RHEED pattern for the entire three hour growth period. Therefore a gallium flux of 2.0×10^{14} atoms $\cdot$ cm^{-2}s^{-1} is enough to achieve a Ga–adlayer at a substrate temperature of 750°C for the plasma settings used.

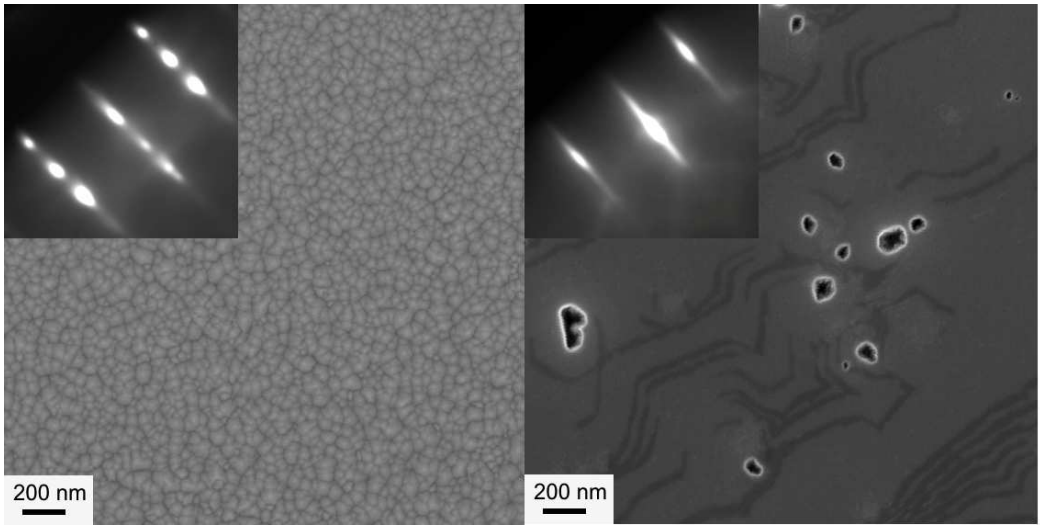

Figure 3.4 SEM images of GaN films grown to resolve growth regime. Left — N–rich growth regime; right — growth under the intermediate growth regime. Inserts are the RHEED images taken at the end of growth.

Table 3.1 Effects of gallium flux on growth rate.

Film number	Gallium temperature (°C)	Gallium flux (atoms $\cdot$ cm^{-2}s^{-1})	Growth rate (nmh^{-1})
632-GaN-GaN	930	1.6×10^{14}	279
633-GaN-GaN	940	2.0×10^{14}	357

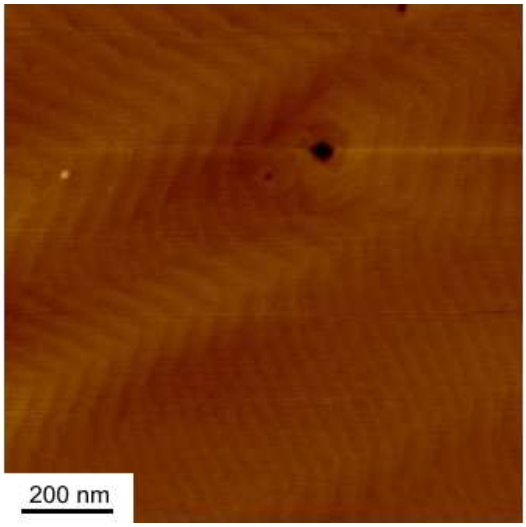

Figure 3.5 AFM image of film 633-GaN-GaN, grown under intermediate regime conditions.

Ex-situ surface analysis of the film 633–GaN–GaN exhibited a flat surface, although some pitting occurred. Closer examination of the film surface between pits, with AFM, confirms a terraced surface, as shown in fig. 3.5. The height of the terraces are 2.73 Å , which is consistent with Nowak et al. who reported step heights of 2.7 Å, but from N-polar GaN. Also the step height agrees with the expected height of 2.6 Å from one bilayer of (0001) GaN (one Ga-N layer thickness in the direction of the c-axis) [113].

The pits observed in the AFM of film 633–GaN–GaN are about 100 nm in diameter and have a generally hexagonal shape. These pits are possibly one of two things: 1) nanotubes [114] or 2) pinholes [115]. Nanotubes generally have diameters less than 40 nm, while pinholes can range up to 800 nm in diameter at the surface. The pinholes usually have a V-shaped cross-section with each side sloped at 60°. In some cases the bottom of the V lines up with a dislocation, suggesting a likely origin. The cross section of the pits in the film 633–GaN–GaN cannot be cleanly resolved using the AFM, suggestive of a nanotube that terminates at the MOCVD GaN template.

Even though film 633–GaN–GaN was grown under intermediate regime growth conditions, there are some nonuniformities on the surface with two different regions observed with the naked eye: one grey in colour and the other transparent. Using optical microscopy the grey area was confirmed to contain metal droplets, suggestive of

the Ga-rich growth regime. The transparent region was free of droplets, suggestive of the intermediate region. Further, the transparent region was observed at the centre of the substrate, compared to the grey area that approached from the edges. Therefore, the growth is most probably occurring within a region on the GaN growth regime diagram best characterised as a narrow intermediate growth regime. Improvements of the surface uniformity might then be achieved through higher growth temperatures.

The 4 K photoluminescence spectrum of the MOCVD template used in the GaN growth study is shown in fig. 3.6. Indicated on the spectrum are the main features. The donor bound exciton (D_h^0X) is the dominant peak, located at 3.476 eV, and is due to either oxygen or silicon contamination [116]. Free A and B excitons (FX_A and FX_B) are located at 3.483 eV and 3.489 eV respectively [116, 117, 118, 119]. A neutral acceptor bound exciton (A^0X) appears as a doublet at 3.461 eV. Also seen are two LO phonon replicas from the FX_A, D_h^0X and A^0X peaks. Separation of the LO phonon replicas is 92 meV, as expected [120]. The feature at 3.497 eV has been reported to be the excited state of the FX_A [121]. In comparison to the MOCVD sample, the film grown under N–rich conditions (632–GaN–GaN) has a single broad dominating feature at 3.453 eV (fig. 3.6), which does not line up with any of the features of the MOCVD sample. A band at 3.45 eV has been observed in N-polar films containing a high density of inversion domains ($10^{11}\,cm^{-2}$) and relatively low density of threading dislocations ($10^{9}\,cm^{-2}$) [122]. Reshchikov et al. tentatively allocated the 3.45 eV feature to be due to excitons bound to inversion domain boundaries [122, 123]. A peak in the 3.45 eV region has also been observed in GaN films that contain columnar growth, which is typical for the N–rich growth regime, although the feature in that case is a doublet between 3.452 and 3.458 eV, and attributed to an exciton bound to a donor or acceptor involving a hole from the A or B valence subbands, respectively [124]. Therefore this feature at 3.45 eV is more than likely a defect related feature due to the poor crystalline quality of the GaN film grown under N–rich conditions.

For the GaN film grown under the intermediate growth regime conditions (633–GaN–GaN) the PL produced similar features to the MOCVD sample, for both the transparent and greyish regions on the 633–GaN–GaN film. The main feature is ex-

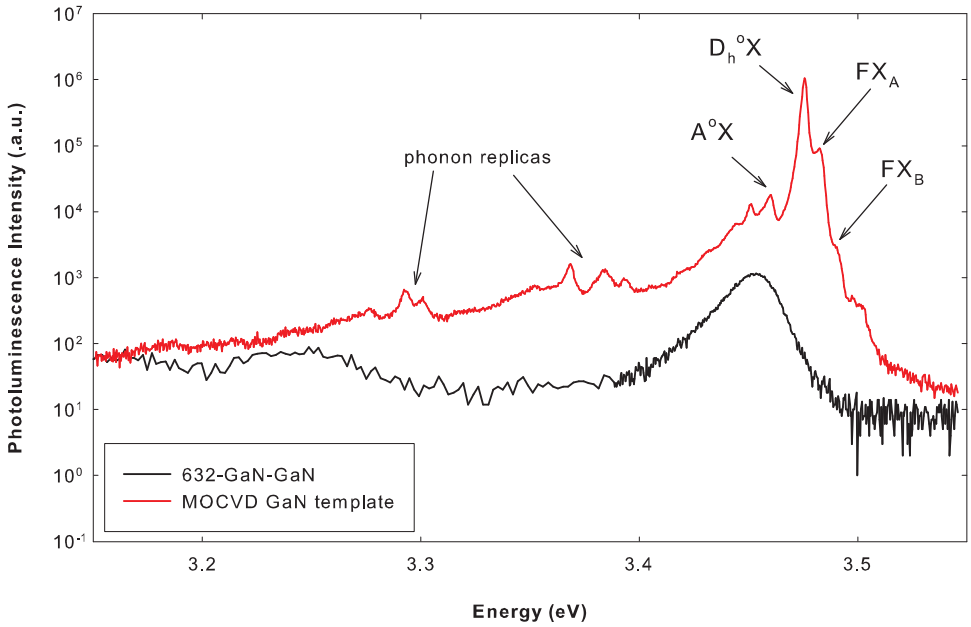

Figure 3.6 Photoluminescence (log scale) from the N–rich growth regime film 632–GaN–GaN. As-measured spectrum.

pected to still be the D_h^0X, and due to strain in the film the PL spectrum has blue shifted by 11.7 meV. The PL spectrum corrected for strain effect is shown in fig. 3.7, which also sees the other features lining up with the MOCVD spectrum. The MBE sample has three peaks which are not in the MOCVD sample; they are at positions 3.430, 3.368 and 3.229 eV. The peak at 3.430 eV may be associated with oxygen [125]. The peak at 3.368 eV is possibly due to cubic inclusions [126]. The third peak, at 3.229 eV, has not yet been assigned a possible origin.

The well-known defect band of GaN, appearing in the visible portion of the spectrum, is due to deep level defects in unintentionally doped GaN. In fig. 3.8 the visible to UV spectra of the GaN films are shown, all of which exhibit a significant defect band around 2.5 eV. However, the grey region of the film 633–GaN–GaN has a smaller defect band. The lack of a defect band may be due to improved crystal quality through a slightly higher gallium flux incident on the substrate in that region. Also, under the Ga–rich growth regime, gallium vacancies can be reduced, which also leads to reduction of the defect band intensity [127].

The electrical properties from the gallium flux growth experiment films are given

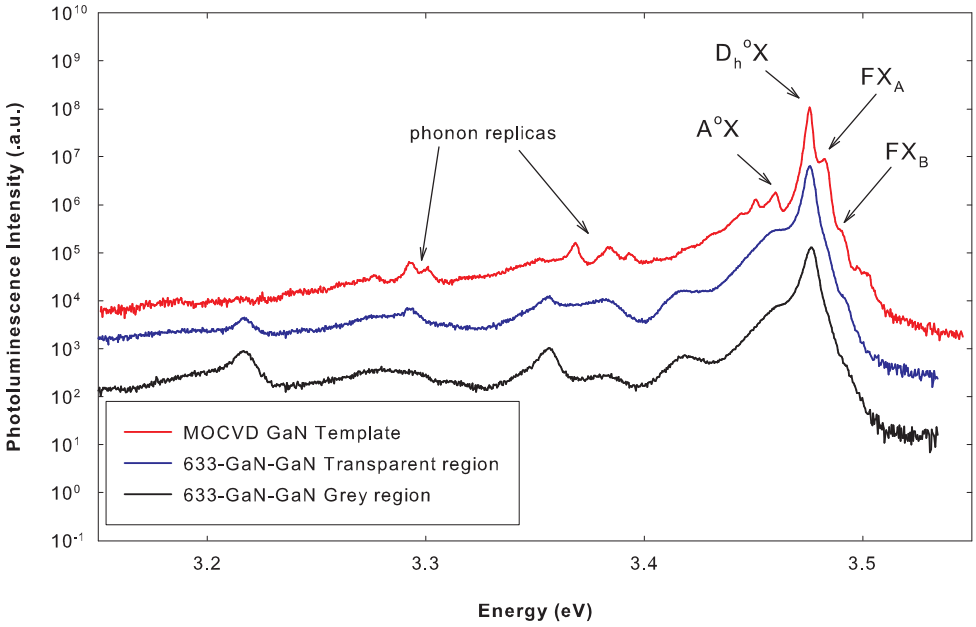

Figure 3.7 Photoluminescence (log scale) from the intermediate growth regime film 633–GaN–GaN. Film 633 spectrum has been shifted by 11.7 meV due to strain effects.

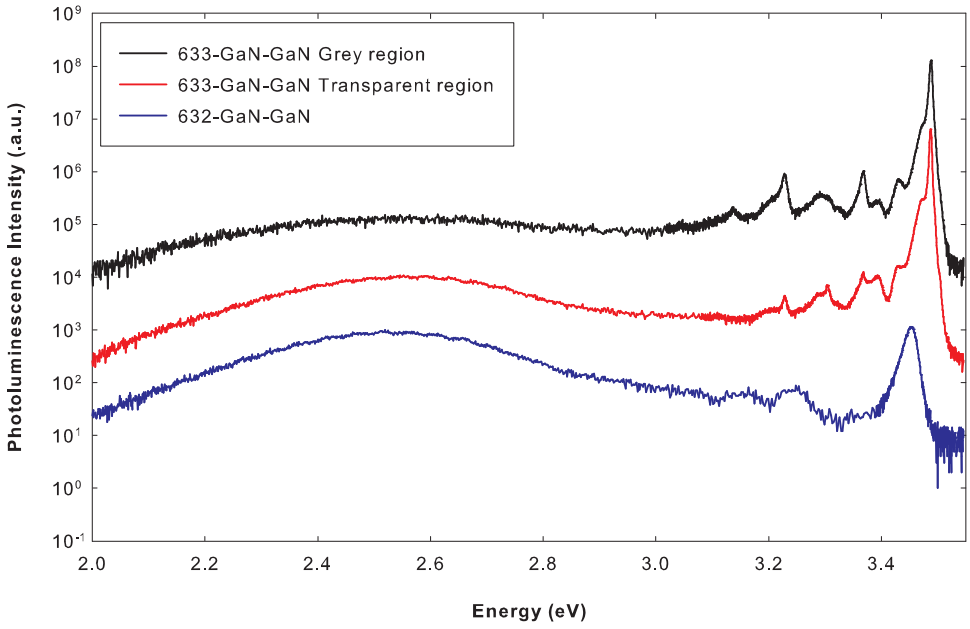

Figure 3.8 Full spectrum of the GaN films showing the difference in the UV band and the defect band at 2.5 eV.

Table 3.2 Electrical properties of the gallium flux dependent growths.

Film number	Gallium flux $(atoms \cdot cm^2 s^{-1})$	Mobility $(cm^2 V^{-2} s^{-1})$	Carrier Concentration (cm^{-3})
632-GaN-GaN	1.6×10^{14}	n.a.	n.a.
633-GaN-GaN	2.0×10^{14}	138	5.8×10^{17}

in table 3.2. For the film 632-GaN-GaN, which was grown under N–rich growth conditions, no electrical measurements could be performed. This is because the N–rich growth regime produces films by coalescing islands, therefore there are grain boundaries between each island which can be a poor conduction path; alternatively, coalescence of the islands has not occurred and the grains are still individual entities with no conduction path between them. By going to the intermediate growth regime the electrical measurements give reasonable values for MBE grown GaN. The improvement is due to the increase of the gallium diffusion length through the formation of a Ga-adlayer, therefore leading to step-flow or layer-by-layer growth. However, in comparison to Heying et al. who measured mobilities of around 800 $cm^2 V^{-1} s^{-1}$ and an order of magnitude lower carrier concentration of ($3 \times 10^{16}\, cm^{-3}$) [26], there is still room for improvement. Their Hall measurements, however, were taken from an area of 30 μm $\times$ 30 μm compared to 4 mm $\times$ 4 mm for our study.

3.1.4 Temperature Effect

Film 633–GaN–GaN, grown under the intermediate growth regime, actually had two distinct surface morphologies. One region had gallium droplets, indicating the growth occurred locally under Ga–rich growth conditions, whereas the other did not. The co-existence of two distinctive regions suggests that the growth temperature is near the intersection of the three growth regimes of GaN. To expand the intermediate region regime, the growth temperature can be increased to reduce the gallium droplets. However, there is an upper growth temperature limitation. With increasing growth temperature the amount of gallium that sticks to the surface is reduced, and if the gallium flux is only slightly Ga–rich this may lead to N–rich growth instead (fig. 3.1c). Also, at growth temperatures above 750°C, the GaN crystal is known to start to dis-

Table 3.3 Substrate temperature effect on growth rate.

Film number	Gallium flux ($\text{atoms} \cdot \text{cm}^{-2}\text{s}^{-1}$)	Substrate temperature (°C)	Growth rate ($nm \cdot h^{-1}$)
667-GaN-GaN	2.0×10^{14}	730	Not available
633-GaN-GaN	2.0×10^{14}	750	357
635-GaN-GaN	2.0×10^{14}	770	300
636-GaN-GaN	2.0×10^{14}	790	293

sociate according to [128],

$$2GaN(s) = N_2(g) + 2Ga(v) \tag{3.1}$$

which will see a reduction in the growth rate and a degradation of the electrical properties [129].

A series of GaN films were grown with varying substrate temperature, as shown in table 3.3, to investigate the effect on the film quality. All of the films in table 3.3 exhibited streaky RHEED patterns for the entire three hour growth period. Investigating the films post–growth using SEM showed flat surfaces containing pits, as shown in fig. 3.9. Imaging of the surfaces with AFM showed terracing had occured. Films 633–GaN–GaN and 635–GaN–GaN have RMS roughness of 3.2 Å and 3.4 Å, respectively, however, the film 636–GaN–GaN had an RMS roughness of 8.3 Å. This increase in the surface roughness is possibly due to the onset of dissociation of the GaN film, or the growth regime is becoming N-rich. However, on all of the films, micron sized gallium droplets are seen on the growth surfaces. The growth rate has decreased in going from $750 - 770$°C, although the trend does not continue at 790°C suggestive of possible flux issues or error in the growth rate measurement.

From the temperature series the electrical properties peak at a substrate temperature around $750 - 770$°C, as shown in fig. 3.10. There are some issues with the uniformity of the films as, film 635–GaN–GaN (grown at a substrate temperature of 770°C) produced mobilities from 870 - 86 $cm^2V^{-1}s^{-1}$ and carrier concentrations from 10^{14} to 10^{16} cm^{-3} depending on the area probed. So far the highest mobilities that

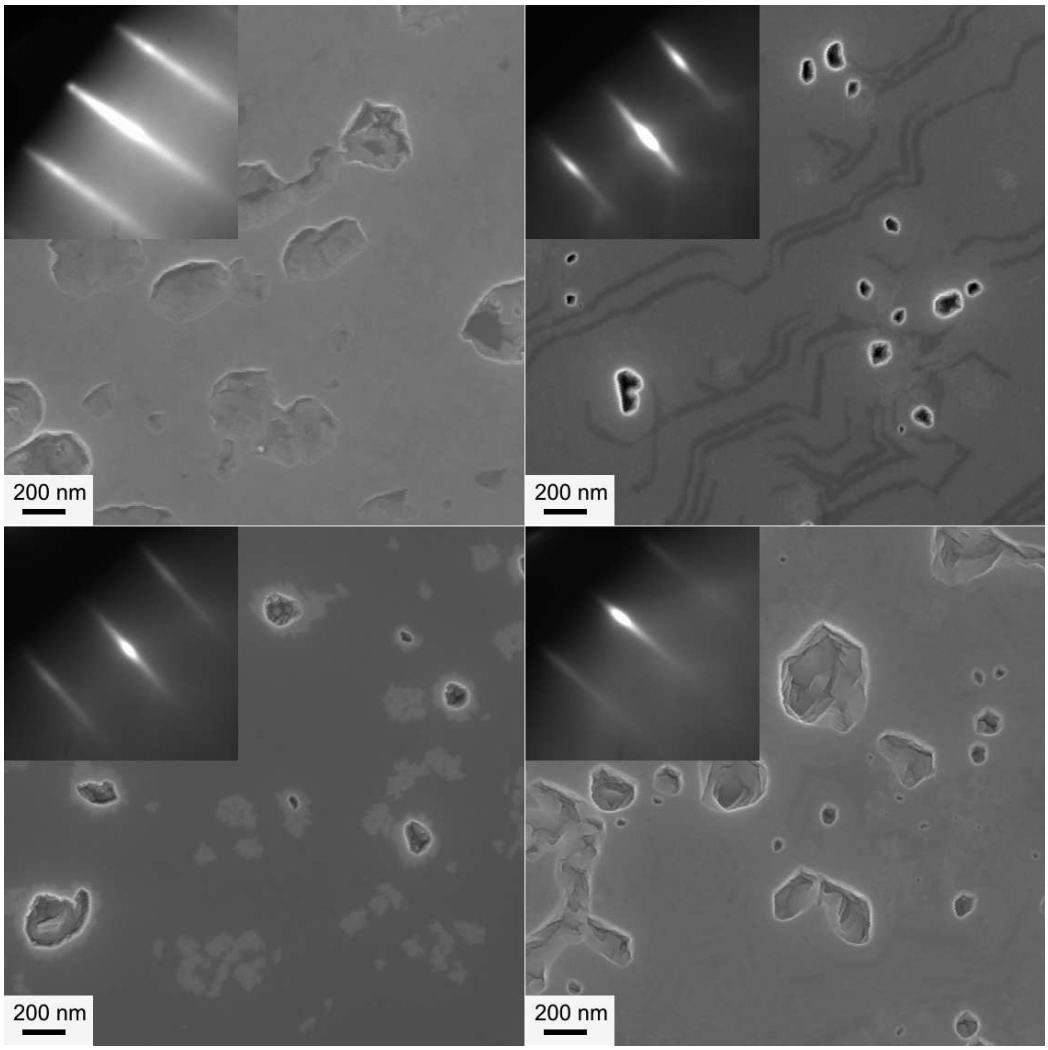

Figure 3.9 SEM and RHEED images (inset) of the temperature dependent GaN growths. Top left: 667–GaN–GaN (730°C); Top right: 633-GaN–GaN (750°C); bottom left: 635–GaN–GaN (770°C); and bottom right: 636–GaN–GaN (790°C).

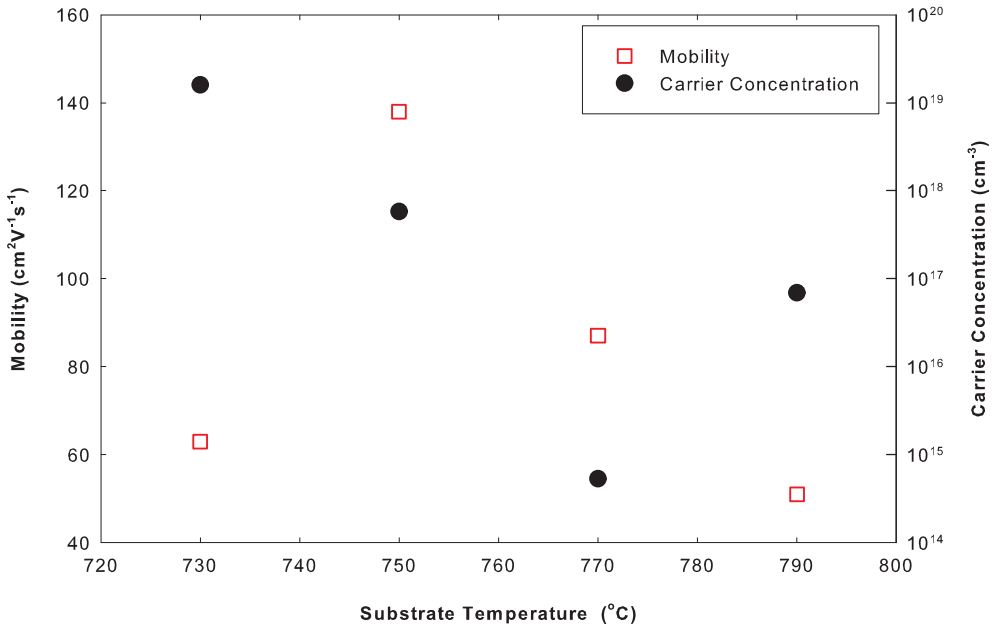

Figure 3.10 Electrical properties of the substrate temperature dependent GaN growths.

Table 3.4 Electrical properties of the substrate temperature dependent growths.

Film number	Substrate Temperature °C	Mobility $(cm^2V^{-1}s^{-1})$	Carrier Concentration (cm^{-3})
667-GaN-GaN	730	63	1.6×10^{19}
633-GaN-GaN	750	138	5.8×10^{17}
635-GaN-GaN	770	870	5.3×10^{14}
635-GaN-GaN	770	86	7.3×10^{16}
636-GaN-GaN	790	51	6.9×10^{16}

have been measured at the University of Canterbury for GaN on MOCVD GaN is 870 $cm^2V^{-1}s^{-1}$. The highest reported mobility for GaN on a MOCVD GaN template is 1191 $cm^2V^{-1}s^{-1}$ for a 1μm thick film [26], therefore our highest GaN is of reasonable quality but improvements still could be made. The carrier concentrations show a similar trend to the electron mobility, with concentrations as low as 5×10^{16} cm^{-3}.

The photoluminescence from the film 633–GaN–GaN (grown at 750°C) has been discussed in the previous section. The two films at 770°C (635–GaN–GaN) and 790°C (636-GaN-GaN) have significantly different spectra to that of the growth at 750°C, as shown in fig. 3.11. The two films grown at and above 770°C lack any fine structure in the band edge luminescence. Instead the emission is dominated by a D_h^0X (neutral

donor bound exciton) which is located at 3.473 eV in sample 635–GaN–GaN and at 3.481 eV in sample 636–GaN–GaN. The D_h^0X is normally located around 3.476 eV [122], the difference observed here possibly being due to strain effects [122]. The films 635–GaN–GaN and 636–GaN–GaN also show a prominent peak at 3.415 eV and 3.423 eV, respectively. This peak is 58 meV below the dominant UV emission in both samples. Chung et al. attributed the peak to oxygen or silicon donors [125]. Reshchikov et al. tentatively assigned a 3.42 eV emission to exciton bound to a surface defect [116]. Between 3.25 eV and 3.38 eV, at least 3 peaks are observed. These lines can be matched to $Y_4 = 3.35$ eV, $Y_6 = 3.32$ eV and free electron to bound hole type = 3.29 eV. These are tentatively assigned to excitons bound to structural defects. The free electron to bound hole (eA) transition is assigned to an unknown acceptor.

The last feature in the near band edge PL spectra of samples 635–GaN–GaN and 636–GaN–GaN, is a donor-acceptor pair (DAP) or eA-type transition at 3.22 eV. Shown in fig. 3.12 is the ultraviolet versus the defect band spectrum, which also shows reduced intensity ratio between the UV and defect band with increasing temperature, which correlates with the observations in the surface morphology and electrical properties. Therefore, the film 636–GaN–GaN produces the best surface and optical properties, however to increase the electrical properties a higher substrate temperature of 770°C is required. Although this does lead to nonuniformities of the growth regime observed by the substrate, the use of back coated substrates and the BandiT to measure the growth temperature might be able to improve the growth. Improved crucible and effusion cells design would also likely result in improved film growth.

3.2 INDIUM NITRIDE GROWTH

3.2.1 Indium Nitride Growth Regimes

Compared to GaN and AlN, InN is a more challenging material to grow. InN has the poorest thermal stability of all the nitrides [130, 131]. This is due to the weak In–N bond energy of 2.0 eV [132], compared to the bond of Ga–N which is 3.1 eV [133]; this leads to a high dissociation rate for InN. For GaN [105] and AlN [134], self surfactant

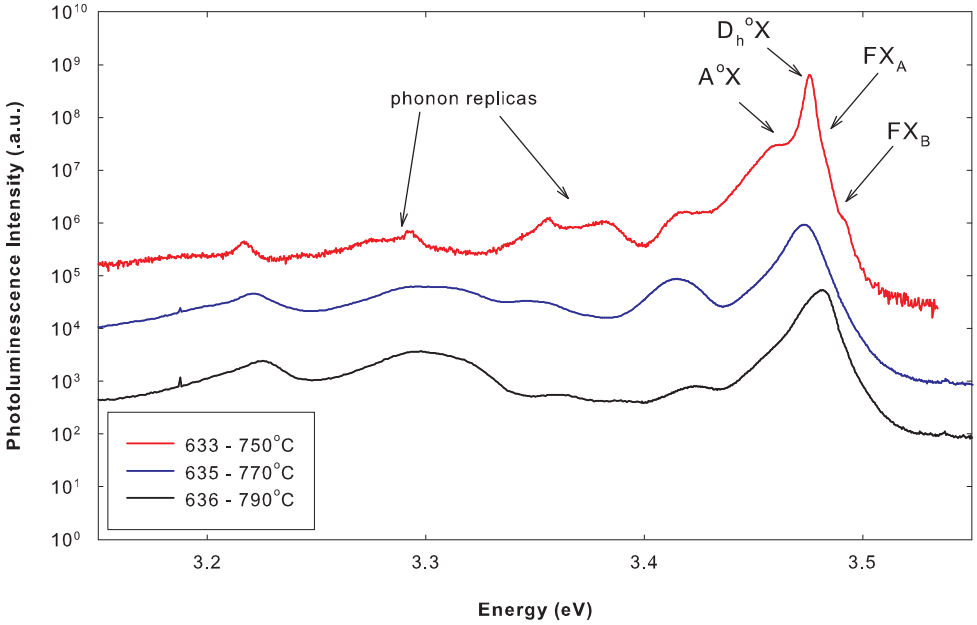

Figure 3.11 Near band edge 4 K photoluminescence (log scale) of the temperature dependent GaN growths.

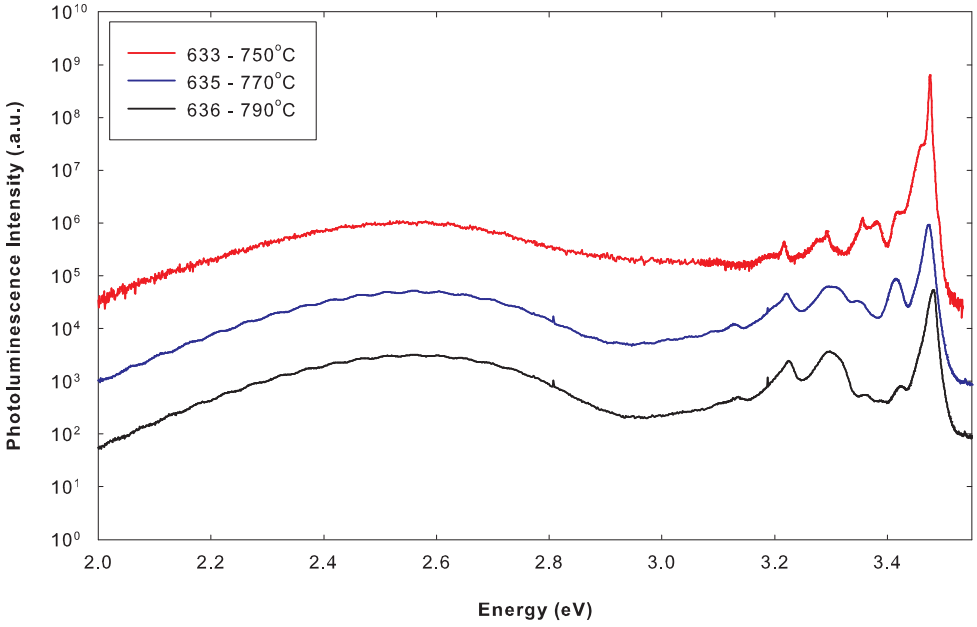

Figure 3.12 4 K photoluminescence (log scale) of the temperature dependent GaN growths across the visible and UV range.

growth at high growth temperatures and metal–rich conditions produce smooth, high quality epitaxial films. The ideal growth temperatures for InN are well below the temperature required to evaporate excess indium metal, however, so to achieve self-surfactant growth indium droplets will always be present.

Like GaN, growth diagrams are being established for InN (fig. 3.13), and are dependent on the surface polarity [135, 136]. In-polar InN is typically grown at 450°C, while the more thermally stable N-polar films can be grown as high as 600°C [137, 138]. The growth diagram for In-polar InN, as shown in fig. 3.13b, has three regions: In–droplet, N–rich and a dead zone. Like the GaN studies, the growth regimes here been mapped out using QSM and RHEED. The N–rich region is for growth where the nitrogen flux exceeds that of the indium flux. This region is known for its spotty RHEED pattern and rough pitted surface. The In–rich regime corresponds to where the indium flux is greater than the nitrogen flux. It is also known as the In–droplet region, as under these conditions indium droplets are supported. For growth temperatures less than 470°C the transition from N–rich to In–rich occurs at a constant In:N flux ratio. However, above 470°C dissociation of InN occurs,

$$2InN(s) = N_2(g) + 2In(l) \tag{3.2}$$

Therefore, at higher temperatures, not only is an indium flux being produced from the effusion cell, but the InN film also supplies additional indium to the surface. This leads to the lowering of the In:N flux ratio required for In–droplets to form. During the In–rich growth, like GaN, a metal adlayer is present. For the In–polar surface under In–rich conditions, Gallinat et al. suggests the indium droplets are on a 2.5 ML adlayer of indium [135], essentially the same as Ga-polar GaN. However, Veal et al. determined the In-adlayer thickness to be 3.5 ML and 2 ML for In-polar and N-polar InN, respectively, based on X-ray photoelectron spectroscopy [139]. The In-adlayer is one monolayer thicker compared to GaN, as it is more energetically favourable. There is a strong tendency for metallic overlayers to form on InN as the N radius is small in

relation to the In radius, therefore the spacing of the In-In bond in InN is similar to bulk In-In bonds in metallic In and it is easier for In to form In-terminated surfaces [139].

The N–polar surface, which is usually grown on MBE GaN on sapphire, can sustain growth temperatures up to 600°C. Therefore N–polar InN films are able to be grown with an indium droplet free In–adlayer [136], as shown in fig. 3.13c as the In-adlayer region. The In–adlayer is sustainable, as at temperatures greater than 610°C the desorption rate of the indium droplets exceeds the decomposition rate of the InN film. For growth into the N–rich region the same transitions exist for the N–rich growth of In–polar InN, but the region of In–droplets is replaced with an In–adlayer coverage as the droplets are again suppressed.

3.2.2 Determination of the InN Growth Regimes

When we began growing InN, the contemporary thinking was that depicted by the growth diagram of fig. 3.13a, with InN grown with an In:N flux ratio of unity to suppress indium droplets as they are undesirable for devices. This led to InN films with electrical properties of 300 $cm^2V^{-1}s^{-1}$ and 9×10^{18} cm^{-3}, as measured at 0.51 T. The films were grown on sapphire, where a nitridation process and GaN buffer layer were employed, and also on (111)YSZ that has a lattice mismatch of only 2.5% and produces In-polar InN [141]. The poor electrical properties were believed to stem from the plasma source, as many of the best reports employed a Veeco system. However, Dimakis et al. were able to produce InN films with electron mobility of 850 $cm^2V^{-1}s^{-1}$ and a carrier concentration of 1.6×10^{19} cm^{-3} respectively, with the same HD25 plasma source [142]. Therefore either the In:N flux ratio was the problem, or the plasma source settings still needed to be optimised. As plasma sources seem to vary even if they are the same model, we were more inclined to study the In:N flux ratio as we are therefore only changing one parameter.

To improve our InN film quality it was not possible to utilise the LRI setup employed in the growth of GaN, as the narrow band gap of InN absorbs the laser light too quickly with increasing thickness. Instead, RHEED was used to determine the change

(a)

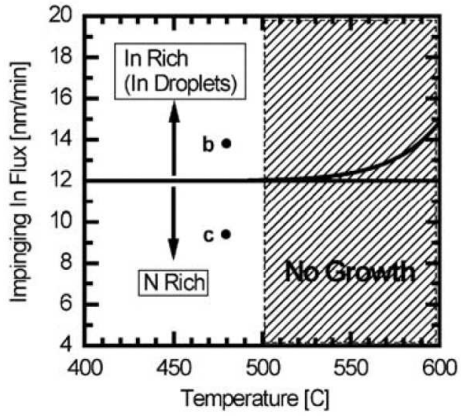

(b)

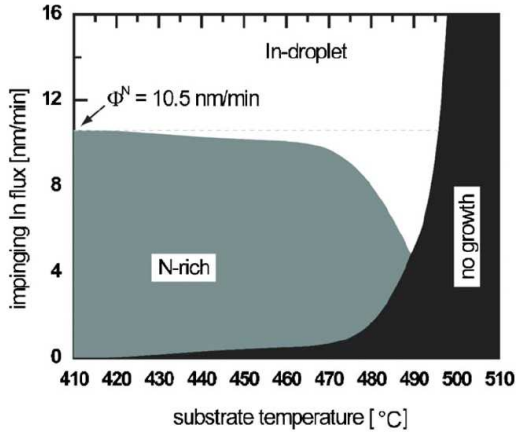

(c)

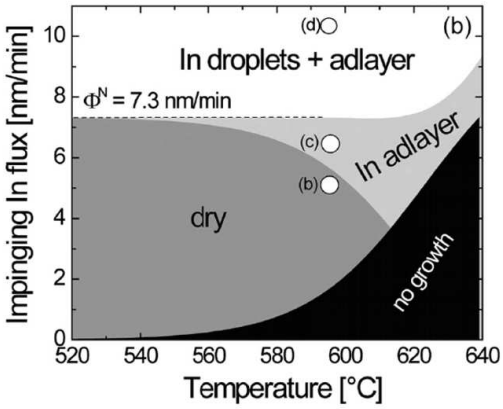

Figure 3.13 Initial InN growth rate diagram published in 2006 by Gallinat et al. [140], In-polar growth rate diagram published in 2007 by Gallinat et al. [135], N-polar growth rate diagram published in 2007 by Koblmüller et al. [136].

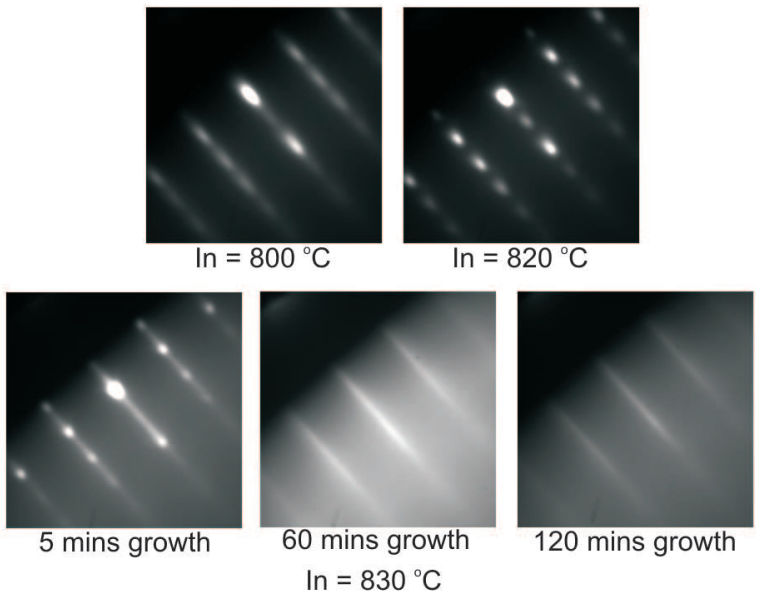

Figure 3.14 RHEED sequence for InN on (111)YSZ (film 634–InN–YSZ(111)) for different In fluxes.

in transition from the N–rich to In–rich growth regimes. By increasing the indium flux every ten minutes, the RHEED pattern can be monitored for change. With the change of growth regime from N–rich to In–rich, the RHEED pattern changes from a spotty RHEED pattern to a streaky RHEED pattern, as shown in 3.14. Also, the intensity of the RHEED is attenuated due to the formation of indium droplets on the InN film [143]. Originally an indium cell temperature of 780°C was used for the growth of the InN films, corresponding to a flux of 3.1×10^{14} atoms $\cdot$ cm^{-2}s^{-1}. For standard nitrogen plasma settings of 150 W and 1.25 sccm ($1 \times 10^{-5}\,Torr$), the transition between the N–rich and In–rich regimes occurs at an indium cell temperature of 830°C, corresponding to an In flux of 9.1×10^{14} atoms $\cdot$ cm^{-2}s^{-1}. The increase in flux by almost a factor of 3 is mirrored by the film thickness, which is 1250 nm for a three hour growth compared to 450 nm for the previous N–rich InN film growths.

Following the RHEED study an InN film was grown under In–rich conditions with a substrate temperature of 470°C, compared to 450°C that was used during the RHEED study; the increase in substrate temperature was to further improve the InN film quality [144]. With the In–rich growth the RHEED stayed streaky for the entire growth, although the intensity reduced over the growth period, consistent with indium metal

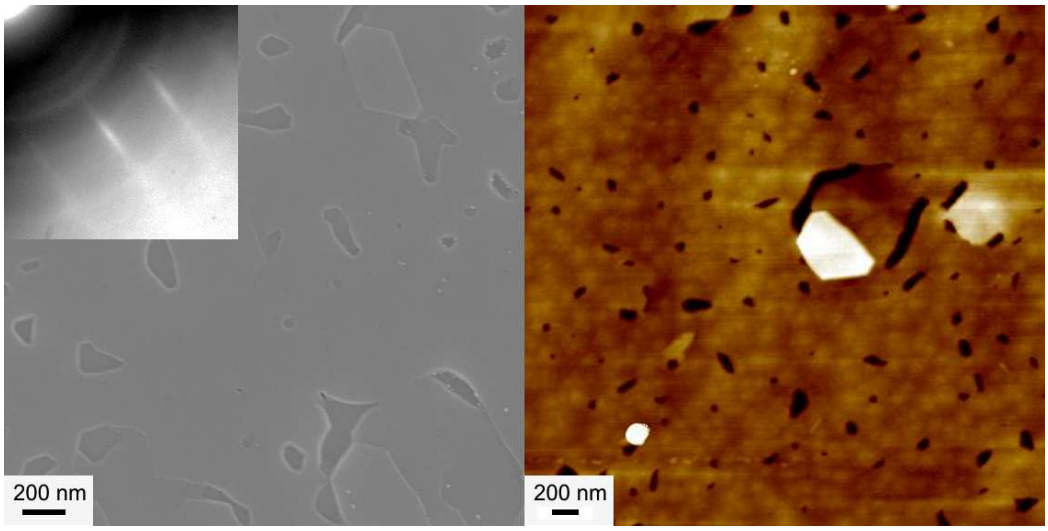

Figure 3.15 Surface morphology of the etched InN/(111)YSZ film grown under In-rich conditions. Left - SEM micrograph and end of growth RHEED (inset). Right - AFM micrograph with a height scale of 20 nm.

accumulating with increasing growth time. Compared to InN films grown under N-rich conditions which are typically black in appearance, the InN films grown under In–rich conditions are grey in colour due to the indium droplets that form on the surface. The excess indium is easily removed by etching in a solution of HCl, revealing the black InN film underneath. The surface morphology of the etched InN film is shown in Fig. 3.15. The vast majority of the surface has a flat appearance, with an RMS roughness of only 2 nm. However, there are regions where the film has not completely coalesced. The depth of these regions was determined to be as much as 100 nm; the hexagonal platelet in the AFM image of fig. 3.15 is 150 nm high. From the AFM there is no clear indication of terracing due to step-flow or layer-by-layer growth modes, however it has been reported by Gallinat et al. that growth under In–rich conditions leads to spiral hillock rich morphology [135]. Therefore it may be still possible to increase the quality of our InN films, and one way is to study the effect of substrate temperature.

From the single magnetic field Hall effect measurements a factor of five increase was observed for the electron mobility at room temperature by changing to In-rich growth. The electrical properties were 1120 $cm^2V^{-1}s^{-1}$ and 4.5×10^{18} cm^{-3}, for the electron mobility and carrier concentration respectively. So far, this represents the best reported electrical properties for an InN film grown on (111)YSZ. Due to the

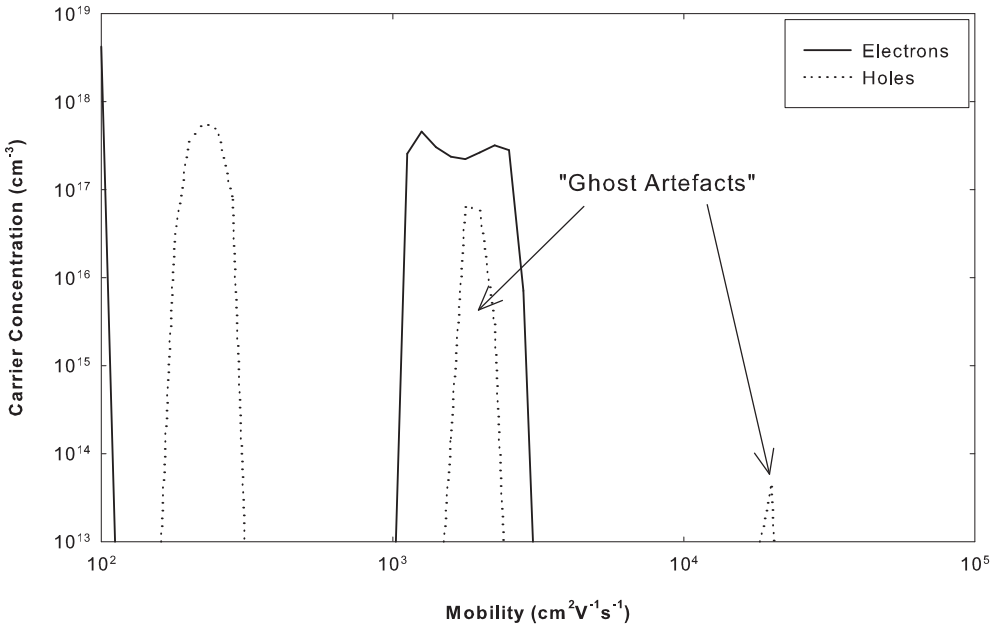

Figure 3.16 QMSA plot of an InN film on (111)YSZ, as measured by variable magnetic field Hall effect at 150 K.

surface accumulation layer that occurs in InN, this film was re-analysed using variable magnetic field Hall effect to obtain information about the bulk electrical properties. As shown in fig. 3.16, a bulk electron mobility was determined to be approximately 2000 $cm^2V^{-1}s^{-1}$, with a peak value as high as 2500 $cm^2V^{-1}s^{-1}$ for a temperature of 150 K. A hole related feature was also detected, which is present in all of our InN/(111)YSZ films. Its origin is unclear but is not thought to be an artefact, as the other hole-like features labelled as "ghosts" are in the figure and are fitting errors introduced by the software.

Most of the photoluminescence spectra produced from our InN films grown under N–rich conditions produce only a single Gaussian feature. This is expected as heavily doped degenerate semiconductors, such as n–type InN crystals with electron concentrations well above $10^{18}\,cm^{-3}$, are characterised by band–to–band PL. They are structureless because of screening of the Coulomb interaction followed by disappearance of excitons, shallow donor and acceptor states, and their complexes [145]. Optical properties of the In–rich InN film were taken from near the InN/(111)YSZ interface and near the front surface, as shown in fig. 3.17. The front surface PL spectrum was

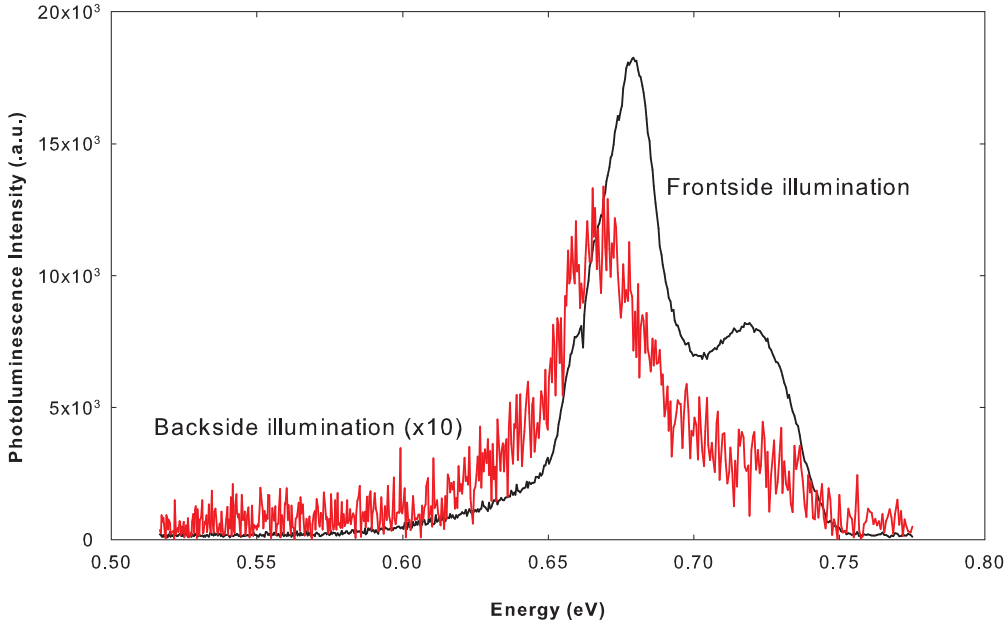

Figure 3.17 Photoluminescence from the InN film (637–InN–InN) grown under In–rich conditions.

made up of two dominant features, 0.677 eV and 0.720 eV. It has been reported that films grown under In–rich conditions can lead to indium inclusions which produce lower luminescence features [146]. Ho et al. has observed In inclusions in MBE grown InN films and report PL with a high energy feature at 0.85 eV, as well as a lower energy peak at 0.75eV [147]. However, we do not observe evidence of indium inclusions in our InN films. Instead the multiple peaks observed in fig. 3.17 may be from the recombination of degenerate electrons with holes trapped by deep acceptors [145].

3.2.3 Substrate Choice

(111)YSZ is not a commonly used substrate for InN growth, due to its cost and availability in $10\times10\ mm^2$ pieces only. GaN MOCVD templates are a more common substrate, so to determine how well the In–rich growth suited the larger mismatch on a GaN template several InN films were grown, as described in table 3.5. The substrate temperature of 470°C was retained to keep consistent with the InN/(111)YSZ growths, which also is the suggested upper substrate temperature limit of In–polar InN by Gallinat et al. [135].

Table 3.5 InN growth on GaN MOCVD templates.

Film number	Indium temperature (°C)	Indium flux (atoms · $cm^{-2}s^{-1}$)
660-InN-GaN	830	4.2×10^{14}
657-InN-GaN	820	3.7×10^{14}

The lattice mismatch of InN/(111)YSZ is 2.5% while InN/GaN is 10%. To determine the relaxation period for InN on YSZ(111) compared to an GaN, the spacing of the RHEED diffraction pattern can be monitored over time. The diffraction pattern can then be converted into a strain percentage using [148]

$$Strain = \frac{a_{InN} - a_{epi}}{a_{InN}} = \frac{d(t) - d(\infty)}{d(t)} \tag{3.3}$$

where a_{InN} is the lattice constant of strain free InN, a_{epi} is that of the epitaxial grown InN film, d(t) is the spacing between diffraction features at time t and d(∞) is for an extended growth period, when the spacing has reached a steady state. As both the RHEED captures were started at arbitrary times prior to opening the indium and nitrogen shutters, there is a period of negative thickness in fig. 3.18 that corresponds to when the substrate heater is raised and waiting for growth to begin. Also in the InN/GaN scan there was some instability in the RHEED intensity especially in the region of 20 - 40 nm of growth. The peak strain percentage for InN/GaN was 8% and for InN/(111)YSZ it was -2%; the difference in sign is due to the GaN having a larger lattice spacing in comparison to InN, whereas (111)YSZ has a smaller lattice. The InN/GaN growth seems to be relaxed when the thickness is only 3 nm, while the InN/(111)YSZ only reaches steady state at 15 nm.

Ng et al. have done a similar study, but looked at the differences in the InN growth regimes and their effect on the relaxation time [148]. For the N–rich growth, which results in the Stranski-Krastanov growth mode, the InN film fully relaxes relatively quickly and the 2D-3D transition occurs after 2-3 bilayers (1.52-1.73 nm). The In–rich InN/GaN had a rapid relaxation over 1 bilayer, but 2% of the strain remained in the film. For our In–rich InN/GaN the relaxation occurred over 5 nm, but the maximum

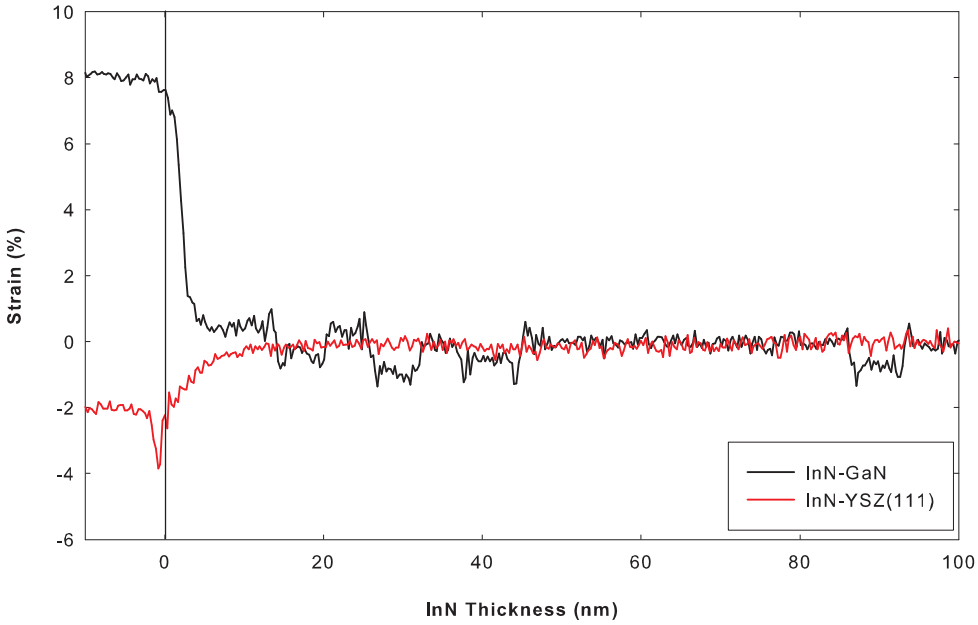

Figure 3.18 RHEED spacing for InN/(111)YSZ and InN(GaN); the InN/GaN plot shows the absolute values as the RHEED spacing of GaN is larger than InN.

strain we see is only 8% and we do not see a 2% retention of strain. However, this may due to our d(∞) value being incorrect, which would bring up the maximum strain to 10% and therefore we would also see the same 2% strain retention as Ng et al. Anderson et al. looked at the effect that the nitrogen species has on the strain incorporation, with low RF power (high $N_2^* : N$) leading to a 50 nm of InN before relaxation was complete, while with high RF power (low $N_2^* : N$) the relaxation period was completed over 1 nm [149]. With the inclusion of this work and Ng et al. it can be assumed that the change in the strain relaxation seen by Anderson et al. is due to a change in the In:N ratio and at the low RF power the In:N ratio has led to a N–rich environment due to the increased production of N_2^*, which for GaN is the desire nitrogen species although this has not been confirmed for InN.

In the case of the In–rich InN/GaN film (660-InN-GaN), the surface morphology (fig 3.19a) is similar to that obtained with growth on (111)YSZ substrate (637-InN/(111)YSZ). However, the measured electron mobility for the InN/GaN film is only 552 $cm^2V^{-1}s^{-1}$ and the carrier concentration is 6.7×10^{18} cm^{-3}. The change is possibly from the difference in the lattice mismatch introducing more defects from the

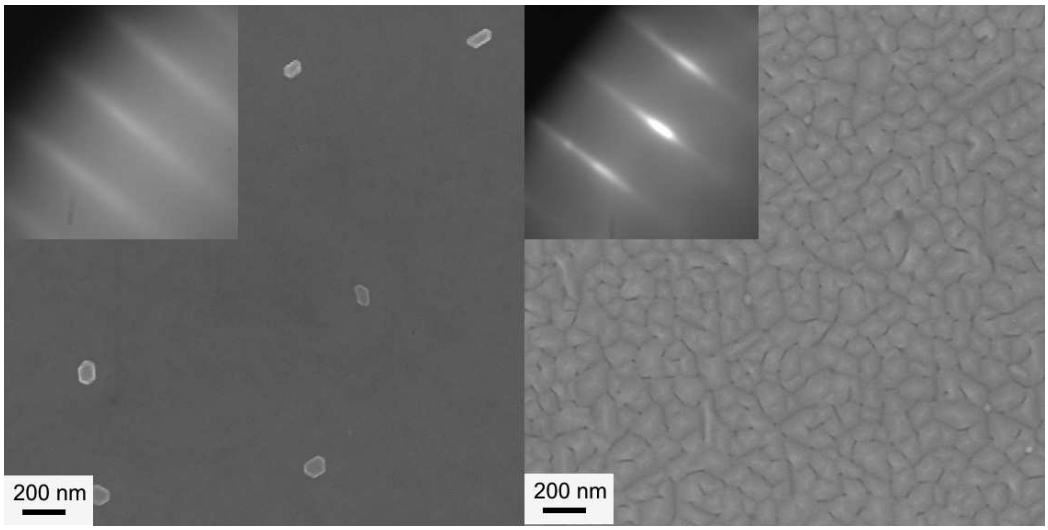

Figure 3.19 SEM images of the InN/GaN films a) grown under In-rich conditions (660–InN–GaN) and b) grown under near N-rich conditions (657–InN–GaN).

GaN/InN interface. However, when the indium flux was decreased to stop indium droplets forming on the growth surface, the electron mobility increased by a factor of two to 1150 $cm^2V^{-1}s^{-1}$, while the carrier concentration remained relatively unchanged at 6.9×10^{18} cm^{-3}. As the thickness of the two films is the same the single magnetic field Hall measurements will still be dominated by the surface accumulation layer, which is approximately 3×10^{13} cm^{-2} [95], therefore explaining the minimal variation in the carrier concentration.

The improvement in the electron mobility can be explained by the effect the indium droplets have on the surface morphology. For the film 660–InN–GaN grown under In–rich conditions, indium droplets formed on the InN surface. After the indium droplets were removed, instead of a continuation of the flat surface morphology where the droplets resided, large InN platelets were observed. These platelets may be produced though a vapour liquid solid process which enhances the InN growth rate. Therefore this change in growth rate introduces dislocations into the crystal structure that may hinder the electron path and therefore lead to a reduced electron mobility. How much of an effect the dislocations will have will depend on when the indium droplets form to a size that will support the enhanced growth.

3.2.4 Film Thickness Effect on the InN Film Quality

There have been several studies looking into the effect that the film thickness has on the electrical properties of InN [43, 150, 151, 152]. Typically the growth studies have looked at the poor electrical properties of thin films in relation to the density of dislocations versus film thickness. The results have shown that there is an exponential decay in the density of threading dislocations from the initial coalescence of the InN islands to the surface [150]. In comparison to GaN where the threading dislocations lead to acceptor states [153], those in InN actually form donor states, and add to the as-grown n-type concentration [154]. However, as the growth persists the reduction in threading dislocations is offset by the formation of point defects, therefore the as-grown n-type concentration can be modelled by [154]

$$n = \frac{1}{th} N_{S,0} + n_b + \frac{1}{th} \int_0^{th} n_{inhom} dz \tag{3.4}$$

where the three parts are: (i) a localised electron accumulation with specific sheet carrier concentration $N_{S,0}$, (ii) a homogeneous background volume concentration n_b and (iii) an inhomogeneous carrier distribution n_{inhom} over the InN film (th is the InN film thickness). Therefore, with increased thickness the electrical properties will improve, as both surface and interface states will have less relevance to the overall properties.

Single magnetic field Hall effect measurements take an average of the electrical properties, therefore for thin InN films the surface accumulation layer and interface layer will dominate. The accumulation layer has been investigated by Lu et al. using capacitance voltage (C–V) measurements, which show a surface sheet carrier density of 1.57×10^{13} cm^{-2} which penetrates 6 nm from the InN surface [95]. Analysis of a thick (7 μm) InN film by Swartz et al. using variable magnetic field Hall effect showed they are also able to observe the surface accumulation layer which has mobilities in the range of 100–200 $cm^2V^{-1}s^{-1}$, compared to bulk mobilities of 4000 $cm^2V^{-1}s^{-1}$ [92]. Swartz et al. also disclosed that the electrical properties are very inhomogeneous throughout

Table 3.6 Single magnetic field Hall effect electrical properties from the thickness dependent InN/YSZ(111) films (* - InN films that were grown on the annealed YSZ(111), which also required a high indium flux to sustain streaky RHEED).

Film number	Film thickness (nm)	Electron mobility ($cm^2V^{-1}s^{-1}$)	Carrier Concentration (cm^{-3})
683-InN-YSZ	5000	1281	6.8×10^{18}
678-InN-YSZ	5000	735	1.2×10^{19}
637-InN-YSZ	1250	1120	4.5×10^{18}
674-InN-YSZ*	500	442	1.5×10^{19}
672-InN-YSZ*	200	210	2.8×10^{19}
671-InN-YSZ*	100	230	3.7×10^{19}
670-InN-YSZ*	50	136	8.5×10^{19}
682-InN-YSZ	5	29	5.0×10^{20}

the bulk. After the properties of the surface accumulation were removed, they found that the first 1 μm of an InN film has an increased carrier concentration to the interface of the InN/buffer layer. Degenerate layers at the substrate interface are also seen in GaN/sapphire films grown by HVPE and dominate the electrical properties [84].

In previous thickness studies the growths were conducted on highly mismatched GaN or AlN buffers. Yamaguchi et al. observed that by growing on substrates/buffers with reduced lattice mismatch, an improvement in the electrical properties could be achieved [152]. Therefore with the growth on (111)YSZ it should be possible that we would see a further improvement in the electrical properties; also, optimised insulating buffer layers are not required. The films grown in the thickness dependent series on (111)YSZ are given in table 3.6. Some of the films were grown on (111)YSZ that was annealed at a temperature of 1200°C for 2 hours, resulting in a terraced surface as verified by AFM before growth. Two 5 μm films were grown, as the initial film had poorer electrical properties, similar to film 660–InN-GaN. The reduction in the electrical properties is possibly due to one of three things: excess indium accumulation that degrades the surface; heat absorption increase due to significant thickness therefore leading to overheating of the film as the InN becomes thicker and causes the film to decompose; and/or the indium cell flux may have decreased during the 12 and a half hour growth period, therefore causing a change in the growth regime [43].

Fig. 3.20 shows the electrical properties of the thickness dependent InN/(111)YSZ films using single magnetic field Hall effect. With the increase in the film thickness the mobilities and carrier concentration have improved, which is the same trend observed in other InN thickness dependent studies. These films do not reach the same mobilities as some of the highest reported electron mobilities of 2250 $cm^2V^{-1}s^{-1}$ and carrier concentrations of $3.5 \times 10^{17}\,cm^{-3}$ for a film thickness of 2 μm, using a Ga-droplet GaN buffer on a GaN template [140]. However, compared to Yamaguchi et al. we do produce better mobilities for just InN on (111)YSZ compared to their InN/GaN films [152]. If we instead compare the electron mobility to the carrier concentration, our InN/YSZ(111) films are consistent with the work by Lu et al. [43]. Therefore our limiting factor is the carrier concentration, which can be related to the defect density in the films.

The films grown thinner than a micron are most probably dominated by the surface accumulation layer and threading dislocations near the interface. Variable magnetic field Hall effect (VFH) measurements were conducted on all the samples to examine how the bulk carriers are affected by thickness. In all the samples, except 682-InN/(111)YSZ, three features were observed: the surface accumulation layer, in most cases with a mobility less than 100 $cm^2V^{-1}s^{-1}$, a bulk n–type feature, and a hole feature which seems to co-exist with the bulk feature. The hole feature could not be resolved from the 5 nm thick film (682-InN/(111)YSZ) data; this may be due to poor quality and incomplete coalescence of the film. The VFH data is given in table 3.7 and plotted as a comparison of the single magnetic field Hall effect (SFH) in fig 3.21. The overall improvement of the electrical properties with thickness is still seen in the VFH results. However, for the thickness range from 10 nm to 5000 nm the VFH results have higher mobilities and lower carrier concentration, as the surface accumulation layer and interface layer are having a significant effect on the SFH electrical properties. For the film grown to a thickness of 5 nm (682-InN/YSZ(111)), which is expected to be completely compensated by the threading dislocations and surface accumulation layer, the VFH data is not significantly different from the single field data. With the film thickness of 5000 nm, the bulk is large enough that single field measurements are be-

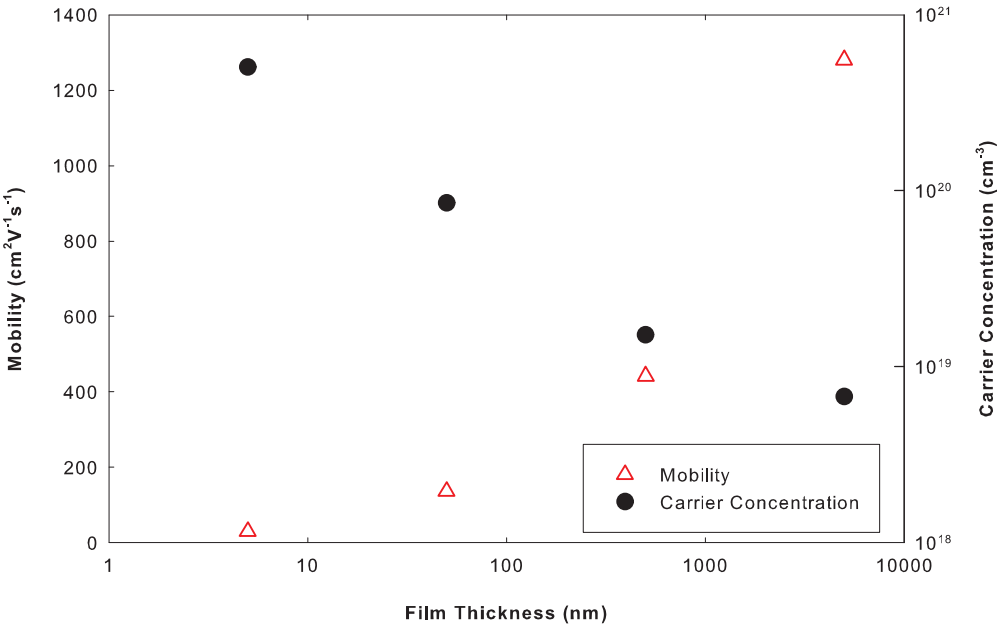

Figure 3.20 Electrical properties for the thickness dependent InN/YSZ(111) films using single magnetic field Hall effect to determine the electrical properties.

coming more reliable, although it is expected that SFH measurements will not be able to completely resolve the bulk properties even for thicker InN films. When it comes to the InN thickness dependent studies most groups only report single magnetic field Hall effect electrical properties.

In fig. 3.22 the photoluminescence taken from the complete range of InN films of differing thickness is shown. For all the films from 5 nm to 5 μm there is a PL feature in the region of 0.7-0.73 eV. The position of the main PL peak cannot be correlated to changes in the electrical properties, even though the carrier concentration ranges from 10^{19} to 10^{21} cm^{-3} which leads to conduction band filling and can affect the optical properties through the Moss-Burstein shift. In contrast to absorption, however, states near the bottom of the conduction band can participate in recombination. Therefore, the band filling has a smaller effect on the PL process than in absorption. The differences in the PL position likely arise from strain in the crystal lattice. The only trend that exists is that with increasing film thickness the intensity of the PL spectrum increases, and in the 5 μm thick film (683–InN–(111)YSZ) several additional features are observed and are possibly LO phonon replicas suggestive of a high quality InN film. It

Table 3.7 Variable magnetic field Hall effect electrical properties of the thickness dependent growths of InN/YSZ(111) films (* - InN films that were grown on the annealed YSZ(111), which also required a high indium flux to sustain streaky RHEED).

Film number	Film thickness (nm)	Electron mobility ($cm^2V^{-1}s^{-1}$)	Carrier Concentration (cm^{-3})	Feature
683-InN-YSZ	5000	1393	5.7×10^{18}	n–type bulk
	5000	1142	6.2×10^{17}	p–type
	5000	≤100	6.6×10^{18}	surface
674-InN-YSZ*	500	746	5.8×10^{18}	n–type bulk
	500	850	3.8×10^{17}	p–type bulk
	500	≤100	1.7×10^{19}	surface
672-InN-YSZ*	200	268	1.5×10^{19}	n–type bulk
	200	360	8.5×10^{17}	p–type bulk
	200	≤100	1.2×10^{19}	surface
671-InN-YSZ*	100	397	9.3×10^{18}	n–type bulk
	100	352	2.0×10^{18}	p–type bulk
	100	≤100	4.0×10^{19}	surface
670-InN-YSZ*	50	395	4.4×10^{18}	n–type bulk
	50	266	2.7×10^{18}	p–type bulk
	50	134	7.1×10^{19}	surface
682-InN-YSZ	5	11	9.4×10^{20}	n–type bulk

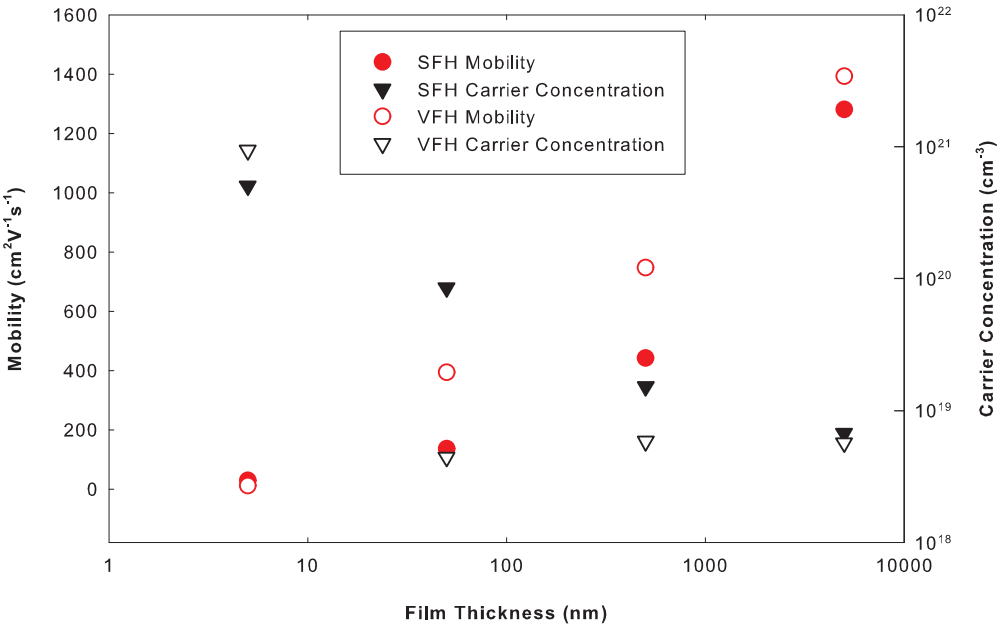

Figure 3.21 Comparison of the electrical properties determined using single magnetic field Hall effect and variable magnetic field Hall effect, for the thickness dependent InN/YSZ(111) films.

should also be noted that initially the PL from the 5 nm film was believed to be from the InN layer. However it is likely that it is instead from the YSZ(111) substrate, as photoluminescence from a bare (111)YSZ substrate exhibits a similar feature, with the addition of the 5 nm InN layer the spectrum does not have any additional features, although the intensity is slightly reduced.

3.2.5 Imaging of the Accumulation Layer

The surface accumulation layer is a feature that is present in all InN films. In the VFH data from the thickness dependent InN/(111)YSZ films a feature was resolved to have a low mobility of 100 $cm^2V^{-1}s^{-1}$ or less and was labelled the surface accumulation layer. To confirm that the low mobility feature is actually the surface accumulation layer the near surface profile of the film 683-InN-YSZ(111) was analysed using electrochemical capacitance voltage (ECV) profiling. Current voltage measurements of the electrolyte blocking contact is shown in fig. 2.15; the stability of the electrolyte allows for a scan range of -1.5 V to 0.5 V. Plotting the capacitance data as C^{-2} versus bias voltage (fig. 3.23) and using equations 2.28 and 2.29, the profile of the carrier concentration in relation to the depletion width can be calculated, as shown in fig. 3.24. From the ECV the near surface carrier concentration reduces from $5 \times 10^{19}\,cm^{-3}$ to a bulk carrier concentration of $5 \times 10^{18}\,cm^{-3}$. The bulk carrier concentration determined by ECV is consistent with the VFH value of $5.7 \times 10^{18}\ cm^{-3}$. The difference in the carrier concentration of the surface and bulk is around one order of magnitude, which is smaller in comparison to Li et al. who have reported a change in carrier concentration of around three orders of magnitude [155]. The sheet concentration from the ECV measurements was determined to be $9.2 \times 10^{12}\,cm^{-2}$, which is somewhat lower than the value of $3 \times 10^{13}\ cm^{-2}$ was reported by Lu et al. [95].

3.3 SUMMARY

During the course of this work we have been able to improve both our GaN and InN film quality through the use of metal rich growth. With the GaN there are still significant

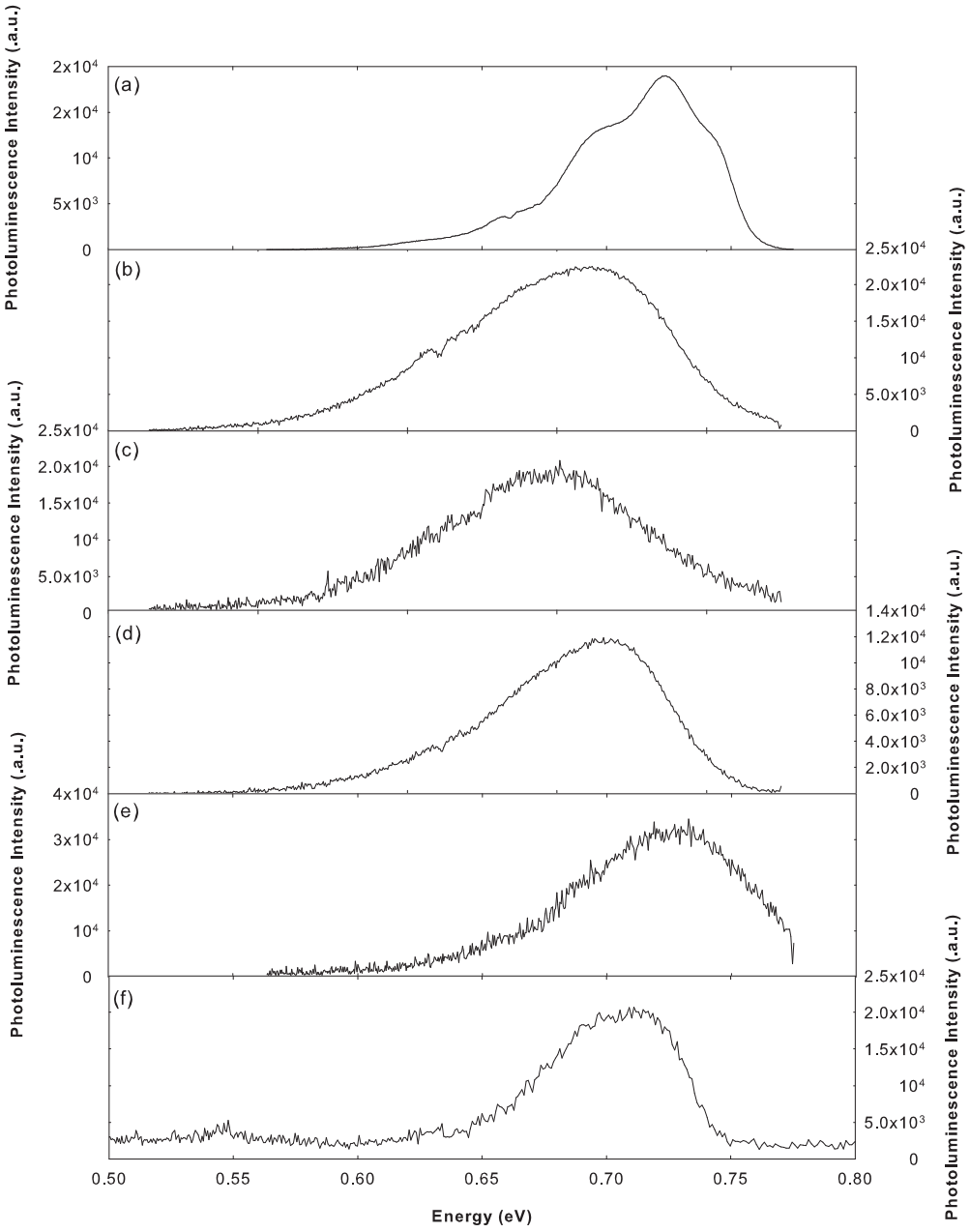

Figure 3.22 Photoluminescence spectra from the thickness dependent InN/YSZ(111) thin films, a) 5000 nm b) 500 nm, c) 200 nm, d) 100 nm, e) 50 nm and f) 5 nm.

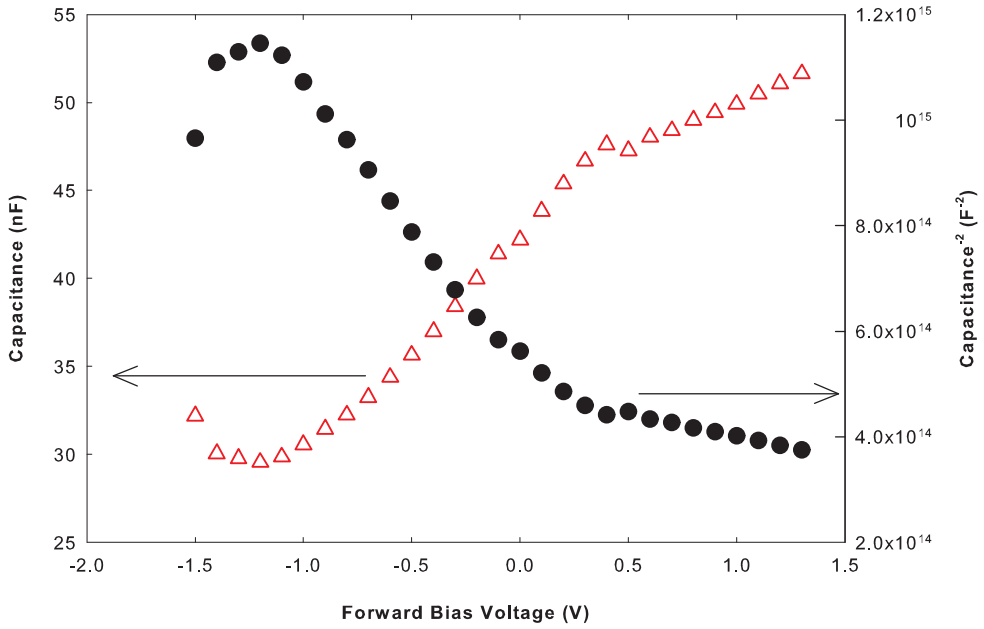

Figure 3.23 Capacitance versus forward bias voltage obtained using ECV with 0.2 molar NaOH and 0.2 molar EDTA electrolyte at a frequency of 3 kHz; also shown is C^{-2} versus voltage.

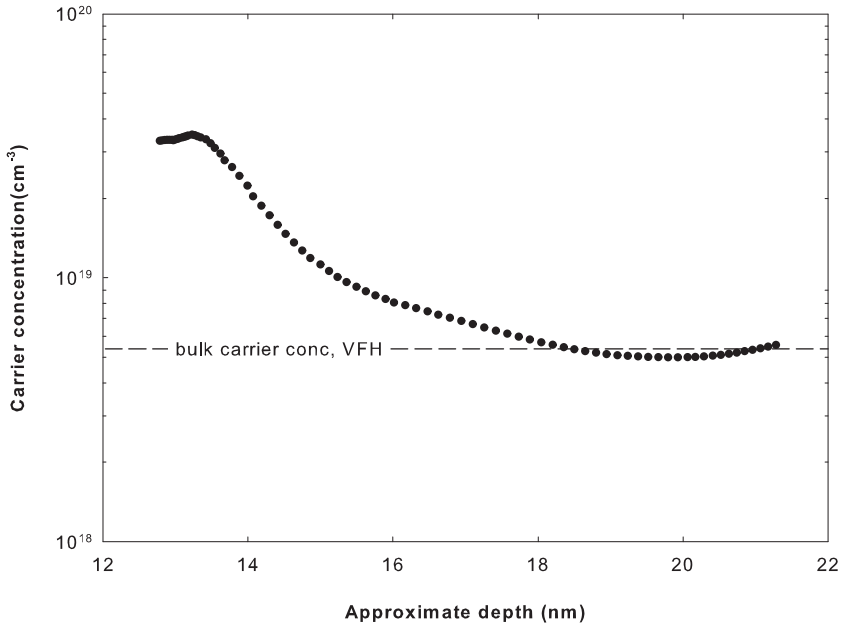

Figure 3.24 Carrier concentration versus depth determined using ECV, with a 0.2 molar NaOH and 0.2 molar EDTA electrolyte at a frequency of 3 kHz. The dashed line shows the bulk carrier concentration as determined by variable magnetic field Hall effect. The depth scale is uncalibrated.

steps that could be taken to further improve the electrical properties and uniformities of the film. For the InN we have been able to grow high quality InN, however some fine tuning of the growth parameters and exploring the high temperature limitations might allow for better material on (111)YSZ. One of the main issues is the actual substrate temperature. For the GaN and thick InN films, monitoring of the film surface temperature using BandiT would allow for better feedback to the substrate heater controller. Therefore this would ensure a consistent substrate temperature during the film growth.

Chapter 4

SELF SEEDED GALLIUM NITRIDE NANOWIRES

4.1 UNEXPECTED GROWTH

As described in section 1.3, there have been several reports on the growth of GaN nanowires by molecular beam epitaxy. The growth of GaN nanowires by MBE is typically conducted in the N–rich growth regime for both the vapour liquid solid and vapour solid techniques [56, 57, 58]. Geelhaar et al. demonstrated that GaN nanowires were able to be grown using a Ni catalyst and that the length of the nanowires saturates at 7.5 μm; also, when changing from the N–rich to Ga–rich regimes during growth, increased lateral growth resulted [56]. Debnath et al. used a silicon substrate to grow GaN nanowires with diameters from 15 to 300 nm without a catalyst using the N–rich growth regime [156]. Bertness et al. have used a Si/Al/AlN/GaN growth process to produce spontaneous GaN nanowires that are centred in hexagonal pits [57]. In this chapter, the unexpected growth of self-branched GaN nanostructures using the Ga–rich growth regime is described.

Determination of the flux required to achieve intermediate regime growth conditions is generally done by measuring the growth rate as the Ga flux is increased. This can be done using a sequence of film growths. Moreover, utilising LRI, it is possible to do the same by growing a series of 'films' on a single substrate. It was after such a series of experiments that the branched structures were discovered.

Fig. 4.1a shows the growth sequence for the gallium flux dependent growth. The reflected signal from the substrate was very weak and the growth rate oscillations were not pronounced enough to obtain reliable growth rate information. By the end of the

growth the intensity of the reflected beam did not exceed the ambient light intensity and the surface had a grey coating that could be associated with gallium metal. On the following day it was attempted to desorb the gallium layer by firstly heating to 800°C and then further increasing to 840°C. The substrate was also exposed to a nitrogen plasma to convert any remaining Ga to GaN. The GaN growth was then restarted and a temperature dependent study was conducted, as shown in fig. 4.1b. During the entire study the reflected beam was weak; this could be related to significant surface roughness as the RHEED exhibited a spotty pattern during the entire growth.

The as–grown GaN film had a non-uniform surface, as shown in fig. 4.2, and imaging of the different regions showed that the majority of the surface was rough with hexagonal cross section pillars consistent with the N–rich growth regime. In an area of 70 mm^2, nanowires were observed. The nanowires had base diameters of 150±50 nm and were typically 1–2 μm in length. A region inside of this area (approximately 20 mm^2) exhibited nanowires with base diameters of 300±50 nm, lengths up to 8 μm, and self-nucleated branches, as well as kinking. The non-uniformities are the result of imperfect coincidence of the Ga and nitrogen beams; several growth regimes could therefore be supported on the substrate simultaneously. Also, a single heating zone effusion cell was used for the gallium source, which can lead to gallium collection on the crucible lip, and gallium spitting and/or lack of gallium beam uniformity.

4.2 ANALYSING THE BRANCHING NANOWIRES

There are already several known methods for growing hierarchical branching structures and nanowires. A common approach employs an external catalyst: after initial growth of the primary nanowires (trunk), an additional application of the catalyst (as nanoparticles) can be used to seed the secondary nanowires (branches). The secondary deposition of the catalyst has been used to grow branching nanostructures of InAs [157] and GaP [158]. Su et al. have shown that in the case of AlGaN, that instead of growing AlGaN nanowires, the GaN forms a trunk and the AlN then forms branches [159]. In solution growth processes hierarchical nanowires have also been grown through a self-assembly process [160]. ZnO is known to produce a colourful range of nanostructures

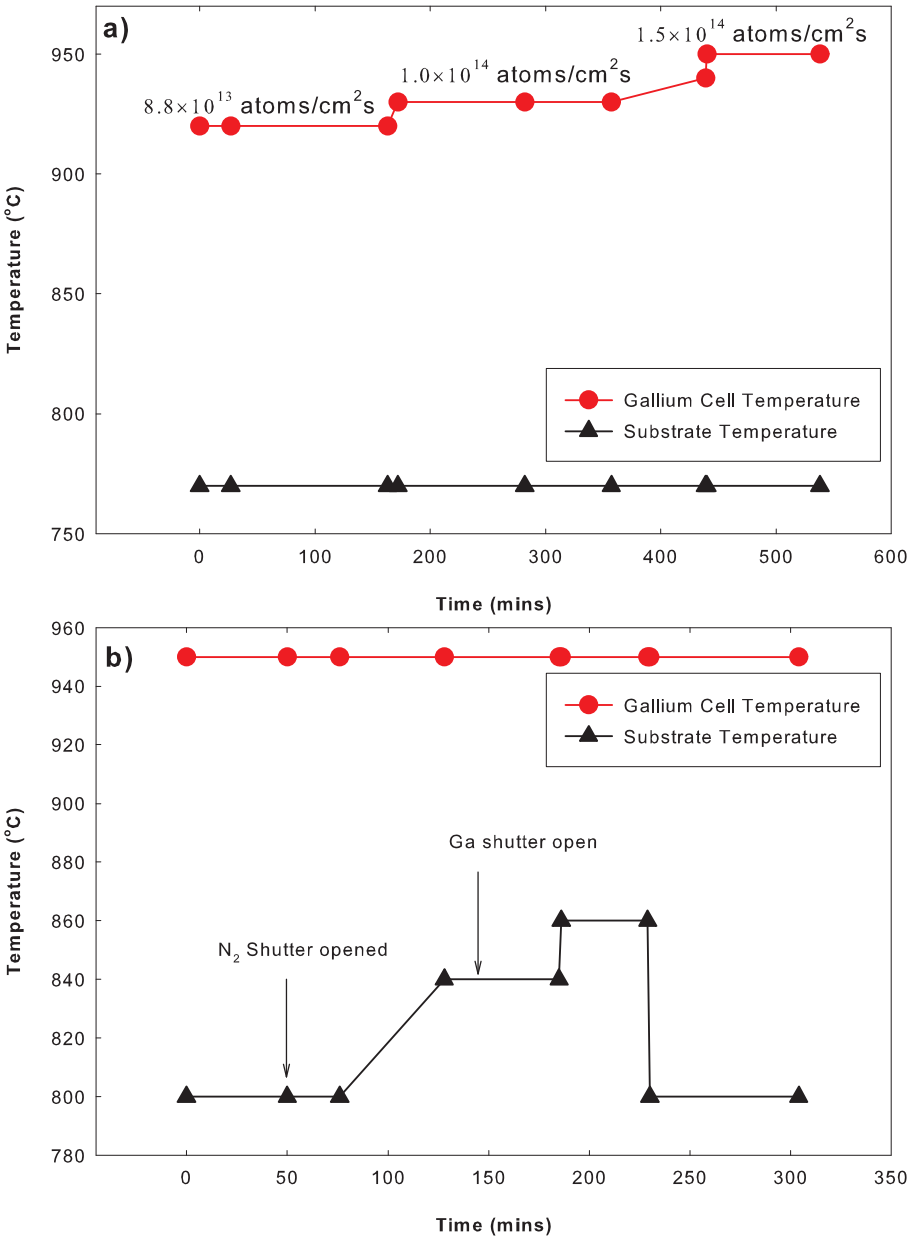

Figure 4.1 a) Gallium flux dependent growth sequence for GaN on sapphire. b) Subsequent temperature dependent growth of GaN on the same substrate used in the gallium flux dependent growth.

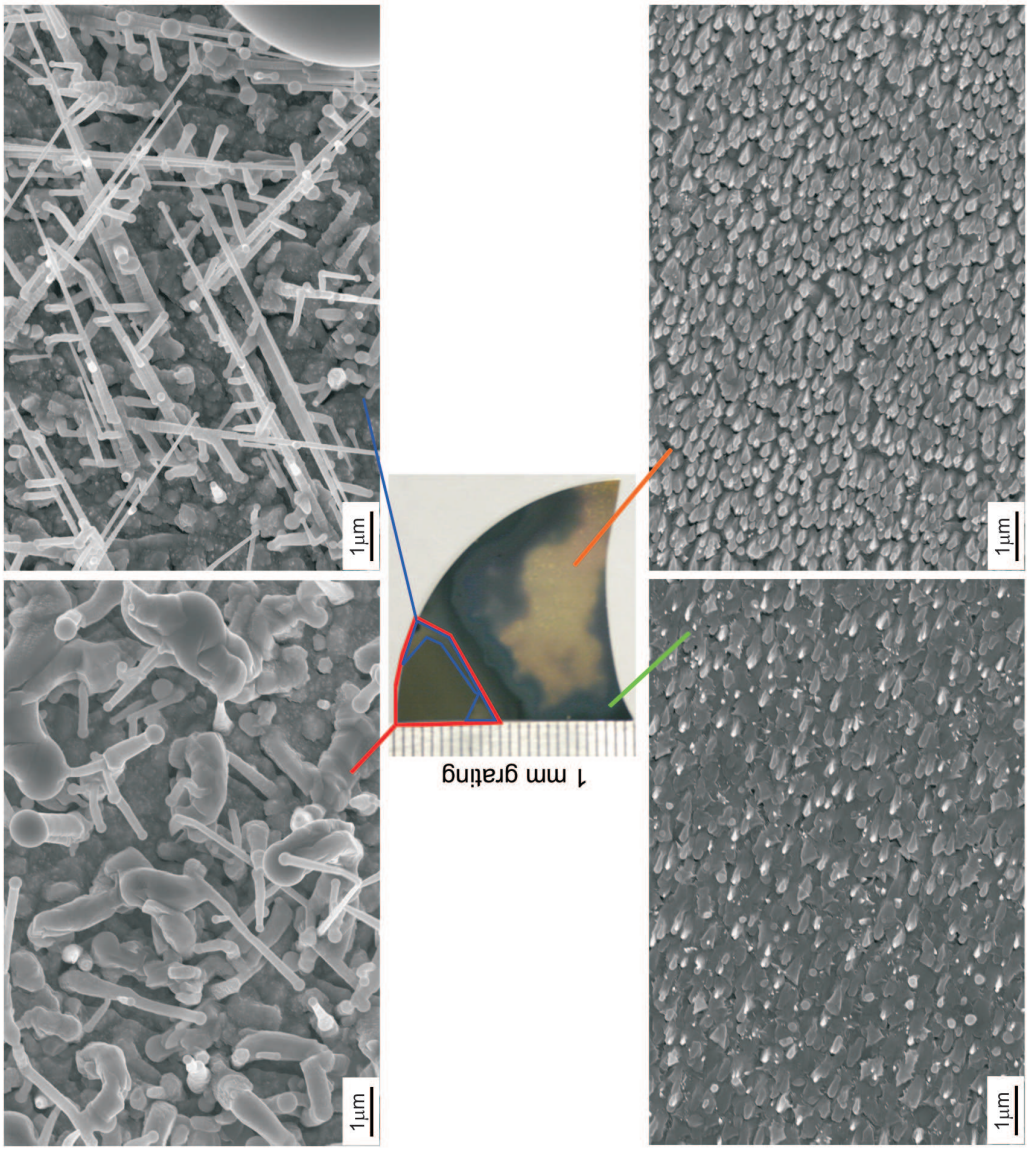

Figure 4.2 SEM micrographs taken for several regions of the substrate.

via a vapour solid (VS) process, and hierarchical nanostructures have been observed [161]. There are also reports of the growth of a self-seeding (self-catalytic) process, where in addition to growing the trunk, branches are nucleated at the same time during InN nanowire growth [162]. Typically the self-seeding process occurs when one of the constituent materials is tin, indium or gallium as they are liquid at most growth temperatures and have a low vapour pressure. Under the right conditions during growth the nucleation material can form additional droplets for the branch nucleation as a result of adatom segregation.

4.2.1 Branching Nanowire Composition

The droplets visible on the end of the trunks and branches in the upper-left SEM image of fig.4.2 are strongly suggestive that the growth is due to a vapour liquid solid (VLS) process. During the growth only the gallium and nitrogen sources were purposely exposed to the substrate. Although the substrates were mounted using an indium tin alloy, it is unlikely that this will directly affect the growth based on many experiments where GaN epilayers were grown. The nanowires were examined using energy dispersive spectroscopy (EDS) to determine their composition. Over a 100×100 μm^2 area, only features related to gallium and nitrogen were detected. However, due to the size and sparseness of nanowires the underlying GaN surface also contributed to the signal, so no unambiguous determination of the nanowire composition could be obtained by examining the as-grown film. EDS analysis of the 10 μm diameter droplet head on one of the larger wires that were also produced only detected gallium atoms, suggesting the growth was excited solely by gallium.

When the nanowires were transferred to a silicon substrate through sonication in solvents, the EDS spectrum exhibited carbon, oxygen, silicon, gallium, nitrogen and indium related peaks, as shown in fig. 4.3. The carbon is related to the coating applied to the structures to reduce charging, while the silicon is from the silicon substrate and the oxygen is possibly from Ga_2O_3 that readily forms on GaN. The indium peak is seen in all three point scans (fig. 4.3) with the same intensity. Therefore it is unlikely from the nanowires and is possibly from when the nanowires were removed from the substrate

using the ultrasonic bath, as indium was used to mount the original substrate. The point scan of the nanowire shows a gallium and nitrogen composition, while the droplet still only has gallium again suggesting a pure gallium droplet. Further clarification of the nanowire composition was observed when the nanowires were wet etched, leaving nanowires without any terminating droplets (see fig. 4.4). High resolution transmission diffraction of individual droplets showed an amorphous structure, possibly related to a liquid phase material. Given the low melting point of gallium (30°C) the droplets are expected to be liquid due to localised heating from the e-beam, however.

4.2.2 Branching Nanowire Structural Analysis

When growing nanowires using the VLS process the propagation angle of the nanowire is able to be controlled by the underlying surface, at least if epitaxial growth is achieved with the substrate. The propagation angle of the GaN nanowires in this study appears to have a random angle relative to the substrate. However, selected area electron diffraction (SAED) suggests that the trunk direction is along the c-axis, the expected growth direction of the GaN thin film. Also, the rough surface observed on the trunk, as shown in fig. 4.5a, has been reported for nanowires that grow in the c-axis direction [163]. The branches have a smooth surface morphology which would be consistent with a non-polar direction (see fig. 4.5b) [163]. Rough trunk surfaces have also be observed in silicon nanowires due to oscillations in the contact angle of the droplet [164].

HRTEM analysis of the junction between the branch and trunk revealed no defect structures. The growth direction of the crystal from the trunk to branch is along the [100] direction (m-plane or $[10\bar{1}0]$) as determined by SAED (fig. 4.6). Therefore the branches are expected to be at 90° to the trunk, yet SEM shows the branches are typically at angles of 105° to 115° with respect to the trunk. In the case of GaP nanotrees the region of the branch to trunk junction consists of twinning defects, specifically rotational twinning of the crystal lattice, perpendicular to the trunk growth direction and terminating at the edge of the branch. In that case, the crystal structure does not change direction to maintain the same crystal growth direction for the trunk and branch [165]. Moreover, the crystal structure direction at the branch droplet is perpendicular

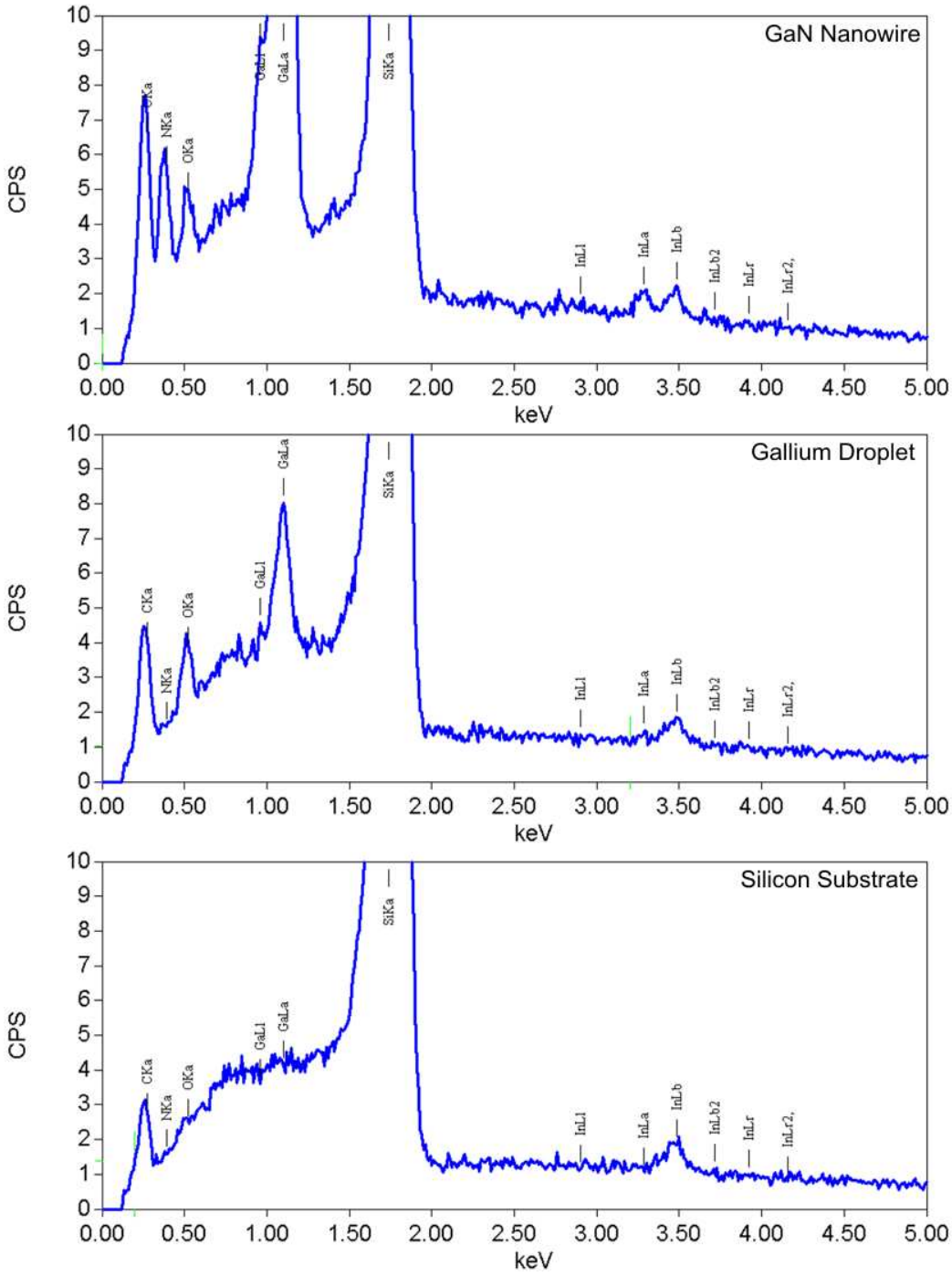

Figure 4.3 EDS analysis of the branching GaN nanowires that were dispersed onto a silicon substrate to reduce the imaging from the GaN substrate. The nanowire is composed of Ga and N, while the droplet only has a Ga composition. As the indium is seen even on the bare silicon it is likely from substrate handling as In is used in mounting.

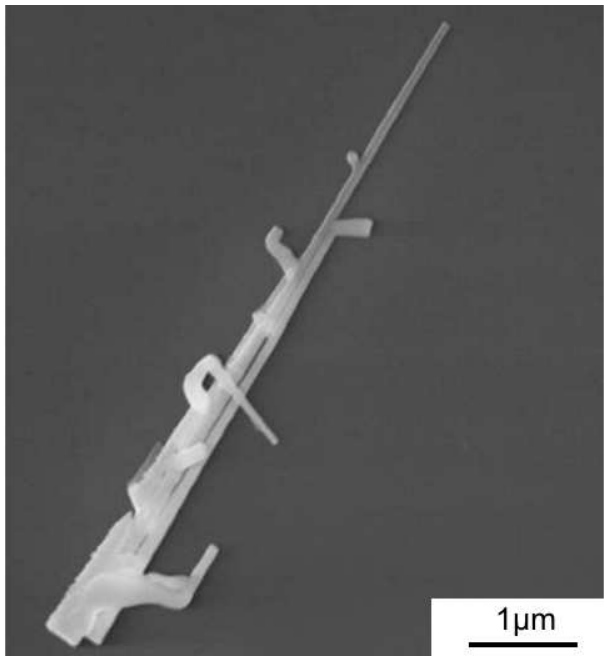

Figure 4.4 SEM imaging a branching GaN nanowire with the gallium droplets removed by wetting with HCl.

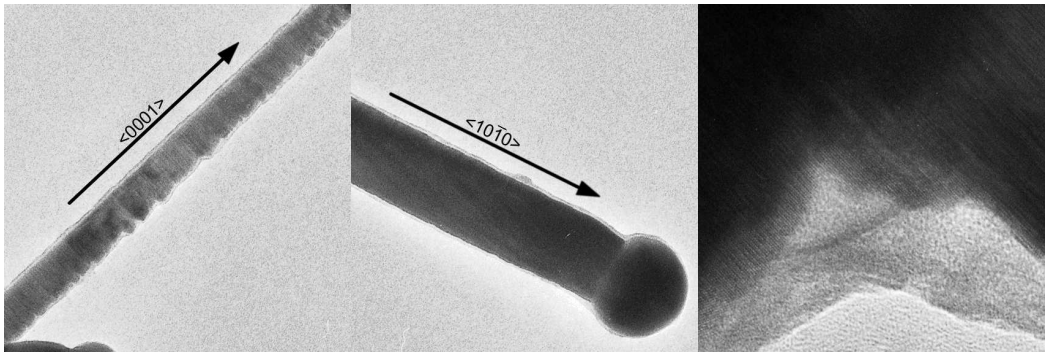

Figure 4.5 TEM images showing surface morphology of polar and non-polar nanowire growth: left – GaN trunk grown in the c-axis direction (polar surface); center – GaN branch growth in the m-axis direction (non-polar direction), and right – Junction region.

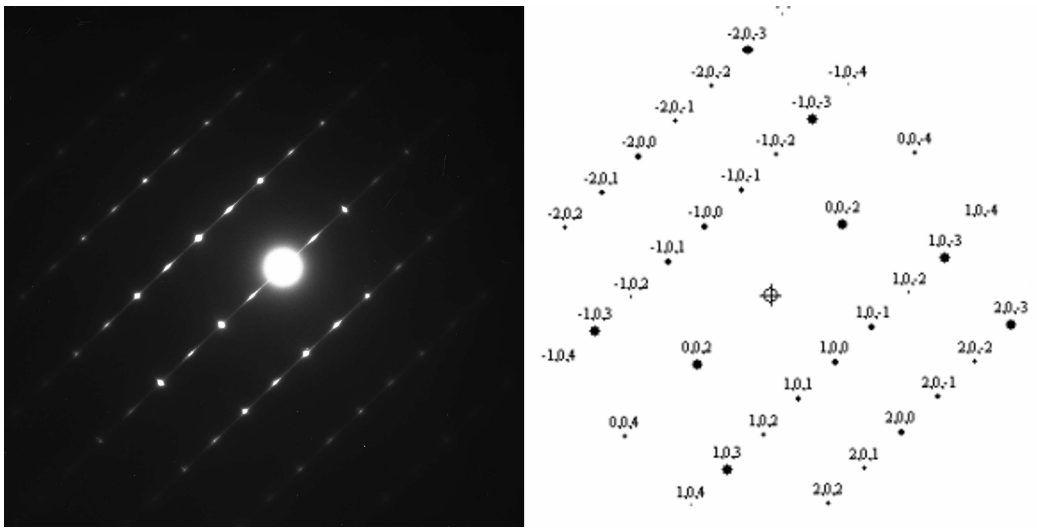

Figure 4.6 SAED analysis of the branch to trunk junction .

to the branch growth direction. A region of single crystal growth is seen acting as a buffer between the two crystals, as shown in fig. 4.7. For the case of InAs branching nanowires, where the branches grow 90° relative to the trunk, the twinning induced in the trunk propagates all the way along the branch and terminates at the droplet head, without a buffer crystal region [165]. Of all the GaN nanowires examined using LRTEM in this study, none have exhibited features that can be related to rotational twinning or other defects.

Dick et al., who grew their branching nanowires using the secondary catalyst process, observed the majority of branches nucleate at the same time [165]. Branches that are within a diffusion length of the adatoms from the substrate grow faster than the branches that are further up the trunk. This is because the collection area of adatoms on the substrate is greater than the collection area of the trunk. Branches that are further than a diffusion length away from the substrate all have the same growth rate as they evenly share the same collection of adatoms. Moreover, branches that are close to each other have to compete for the adatoms, so the branches will have reduced length compared to a single branch at the same site; the total length, however, is expected to be the same as a site with only one branch.

In the growth of the branching GaN nanowires in this study, it was observed that

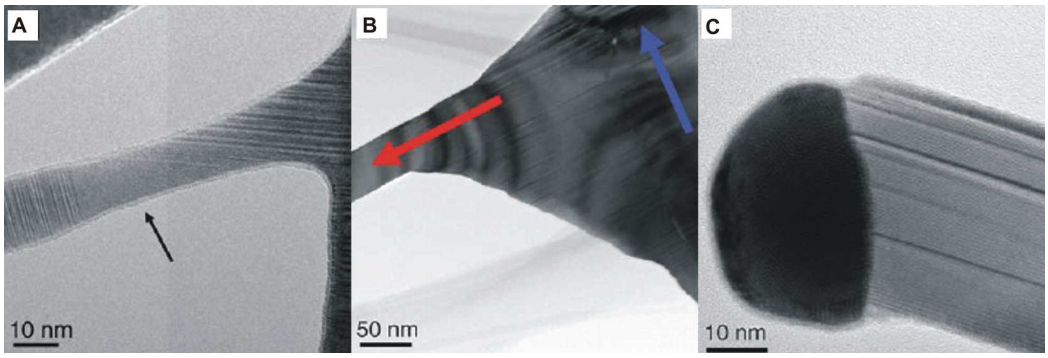

Figure 4.7 HRTEM images of the the crystal structure in the branching GaP nanowires and branching InAs nanowires of Dick et al. [165]. a) Branching GaP nanowire (the arrow indicates a region of single crystal growth between the trunk and branch regions that contain twin planes), b) branching InAs nanowire (the arrows indicate the growth direction of the trunk and branch) and c) the droplet region of the branching InAs nanowire that shows that the twin planes extend the entire length of the branch as the branch grows perpendicular to the trunk.

with increased trunk length the number of branches also increases (fig. 4.8a), which suggests that new branches are nucleating as the growth progresses. The distance between branches remains around 800 nm except for the branch closest to the tip of the trunk (fig. 4.8b), suggesting the main controlling factor is either adatom diffusion length or the arrival rate of adatoms. Moreover, the branches closest to the base of the nanowires are typically longer in length compared to the branches closest to the end of the trunk (fig. 4.8c). In the case of Dick et al., the number of branches did not change throughout the growth [165], however as we believe we are nucleating branches during the growth, the growth dynamics will be slightly different. Initially all the adatoms will only support one branch. Then, with the additional nucleation of branches, the amount of adatoms will be averaged over the total number of branches. With increasing length of the trunk and branches their growth rates become independent of the adatoms from the substrate, and instead their growth rate is dependent on the adatoms that are collected on the structure itself. It is therefore expected that the resulting structure will be a cone shape, which is what we observed from the analysis of several branching nanowires.

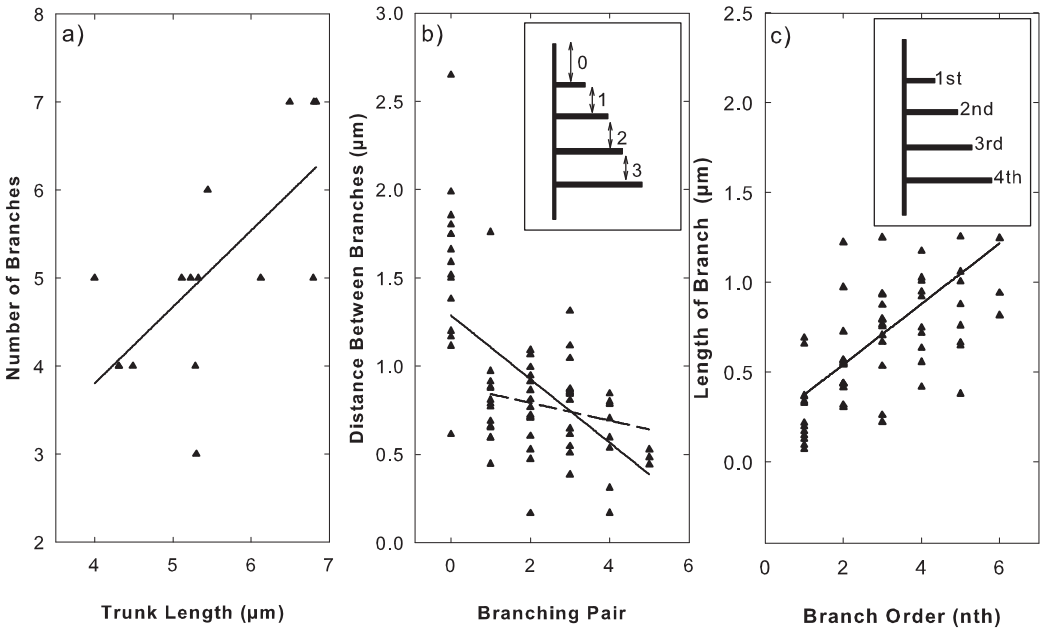

Figure 4.8 Analysis of 20 GaN branching nanowires, extracting a) number of branches versus trunk length (the solid line is a linear fit through the data points showing an increasing number of branches with trunk length), b) distance between pairs of branches, as describe by the inset (the solid line is a linear fit through all the data points, while the dash line is a linear fit ignoring the distance of the first branch to the tip of the trunk) and c) length of branches compared to position on trunk, as describe by the inset (the line is a linear fit through all the data points, showing that branches near the base have a longer length).

4.2.3 Optical Properties of the Branching Nanowires

A great deal is known about the optical properties of GaN and so such characterisation can be very useful. Given the size and sparsity of the nanostructures, photoluminescence can be problematic. A better alternative in this circumstance is cathodoluminescence (CL), which can provide information regarding spatial variation of emission across an individual structure. Room temperature CL of individual branching nanowires (fig. 4.9) show a clear indication that there are three distinct regions of luminescence. The terminating droplets did not emit any luminescence, which is further evidence that the droplets are essentially pure Ga metal. The trunk and branches exhibited luminescence at 3.44 eV, which correlates well with reported CL from an individual GaN nanorod with a 120 nm diameter at room temperature [166]. As the excitonic Bohr radius for GaN is 11 nm [167], there would be minimal difference in luminescence peak location between a nanowire/nanorod with diameter of 300 nm and one of 100 nm.

At the interface between the trunk of the nanowires and GaN epilayer, a lower energy peak at 3.1 eV was observed. To achieve a red shift of 300 meV, that portion of the nanowire would have to be under considerable tensile stress [168]. The change in lattice constant required to see a 300 meV shift in CL can be estimated by first determining the energy shift due to strain:

$$\Delta E_g = E_{g(GaN),strained} - E_{g(GaN),unstrained} \tag{4.1}$$

and then computing the in-plane strain, ϵ_1: [169]

$$\epsilon_1 = \frac{\Delta E_g}{2\left(a_{c\perp} - a_{c\parallel}\frac{C_{13}}{C_{33}}\right)}. \tag{4.2}$$

where $a_{c\perp}$ is the in-plane deformation potential and $a_{c\parallel}$ is the deformation potential in the growth direction. From ϵ_1 the change in lattice constants are obtained: [169]

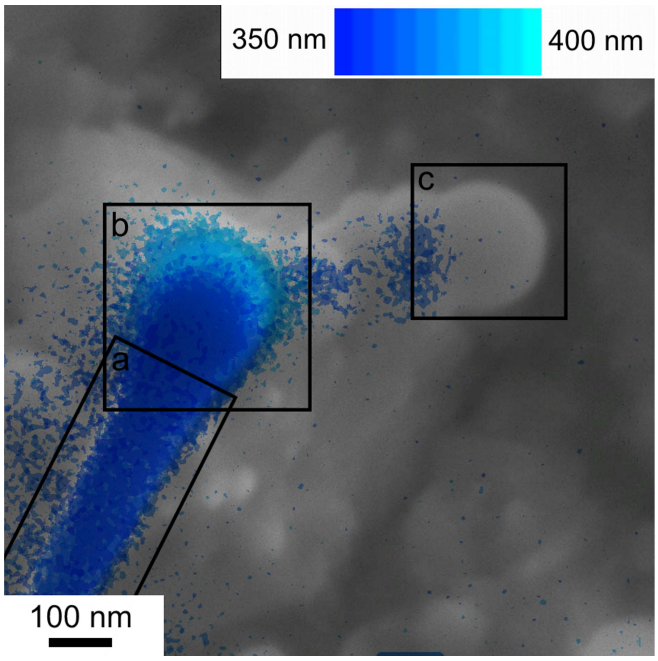

Figure 4.9 Cathodoluminescence, conducted at 80 K, examining a single GaN nanowire and the interface of the nanowire with the GaN underlying epilayer. The nanowire exhibits luminescence at 3.44 eV (360 nm), while the interface of the nanowire with the GaN epilayer luminescence at 3.1 eV (400 nm). Regions of interest: a) nanowire trunk, b) kink site or interface between the nanowire and that of the underlying GaN epilayer and c) Ga droplet head.

$$\epsilon_1 = \frac{a_{nanowire} - a_{bulk}}{a_{bulk}} \text{ and } \epsilon_3 = \frac{c_{nanowire} - c_{bulk}}{c_{bulk}} = -2\frac{C_{13}}{C_{33}}\epsilon_1. \tag{4.3}$$

The calculated deformation of the lattice is a 0.104 $\mathring{A}$ decrease in the a-axis (tensile) lattice constant while the c-axis lattice constant has an increase of 0.086 $\mathring{A}$ (compressive); values of $E_{g(GaN)} = 3.4$ eV, $a_{c\perp} = 7.24$, $a_{c\|} = 10.53$, $C_{11} = 396$, $C_{12} = 144$, $C_{13} = 103$, and $C_{33} = 405$ were used in the calculations, after references [170, 171]. These values for the changes in the lattice constants are an order of magnitude larger than for reported strain effects on the luminescence in smaller diameter nanowires that had a PL peak at 3.2 eV, where values of -0.0089 Å and 0.0080 Å were determined by x-ray diffraction for the a–axis and c–axis, respectively [168]. ZnO nanowires that have been investigated by CL also have a low energy feature at the wetting layer, which has been attributed to low quality crystal growth at the interface by HRTEM [81].

4.3 EXPLAINING THE GROWTH

The growth of nanowires by the VLS process can be broken down into three parts.

1. The first part is to apply a catalyst to the surface that will excite the growth.
2. Once the growth surface is prepared the catalyst needs to be supersaturated to start the growth.
3. The final stage of the growth is retaining a positive growth environment for nanowire growth to be maintained.

4.3.1 Role of the Catalyst

For the growth of nanowires by the VLS process a catalyst is introduced to excite the structured growth. The early requirements of the catalyst were that:

1. It forms a liquid with the desired growth material;
2. The solubility of the catalyst in the solid compared to the liquid is greater than unity;
3. The equilibrium vapour pressure of the catalyst is small;
4. The catalyst is inert;
5. The catalyst forms the desired contact angle to the surface, which is controlled by the interfacial energies – vapour-solid, vapour–liquid and liquid–solid;
6. The catalyst can be one of the growth materials;
7. Temperature control is required to ensure a solid intermediate phase is not formed; and
8. For unidirectional growth the solid-liquid interface needs to be well defined crystallographically [172].

An added requirement is the catalyst does not modify the growth apart from increasing the growth rate underneath the catalyst. Basically, the catalyst is seen as an entity that induces a faster growth in a localised area, preferably at the expense of growth in other areas.

On an epitaxial surface the energetic active adatoms diffuse around the surface until they find a site to join and release their remaining kinetic energy. The adatoms also have the option of desorbing from the surface and therefore not taking part in the growth. In the case of an ideal surface the adatoms will join a lattice site to promote layer-by-layer growth and the energy will be released into the lattice without causing defects. Also, the idealised epi-surface is flat and allows for near infinite diffusion until a step is found. In contrast, an epilayer with a liquid catalyst on it would act as a sink, as the catalyst is seen as an ideally rough surface. Therefore it is more likely that adatoms will be incorporated into the droplet and accelerate the growth under the droplet region.

In the situation where growth is self-seeded (loosely termed self-catalytic) there is no external material introduced to excite the nanowire growth. In the case of GaAs, InP and InN, either a substrate of the semiconductor can be used, or an epilayer deposited. It is then annealed to produce liquid droplets, possible due to a low thermal decomposition temperature [173, 174]. In the case of GaN the decomposition temperature does not lead to a reaction that supports gallium droplet formation on the GaN surface, but rather both constituents evaporate:

$$2GaN(s) = 2Ga(g) + N_2(g) \tag{4.4}$$

However, it has been reported that GaN can go into a liquid state in high vacuum and that this can lead to enhanced decomposition of the GaN [175]

$$4GaN(s) = 4Ga(l) + 2N(g) + N_2(g) \tag{4.5}$$

Koleske et al. also suggested that sublimation of GaN is possible [176],

$$GaN(s) = GaN(g) \text{ or } [GaN]_x(g) \tag{4.6}$$

For MBE growth of GaN equation 4.4 is the accepted reaction, as at the typical growth temperatures gallium droplets are not observed on the GaN surface [176]. Therefore, to produce the self-seeding GaN nanowires gallium needs to be either deposited on the surface to form gallium nucleation sites, else formed by growing under a Ga–rich growth environment. Initial efforts to recreate the self-seeding GaN growth involved depositing a layer of gallium directly onto the sapphire substrate at room temperature and, separately, at the substrate temperature of 800°C. In both of these cases the resulting growth did not lead to GaN nanowires, instead it represented GaN growth under N-rich conditions (fig. 4.10a), which suggests that the gallium layer has evaporated off the sapphire surface, or the contact angle of the gallium droplets is too shallow to support the nanowire growth (fig. 4.11). The contact angle of the gallium droplets follows Young's equation [177], which can be written as,

$$\gamma_s - \gamma_{sl} = \gamma_l \cos\theta \tag{4.7}$$

where γ_s is the surface tension of the solid (interfacial tension between the solid and gas), γ_{sl} is the interfacial tension between the solid and the liquid, γ_l is the liquid tension of the solid (interfacial tension between the liquid and gas) and θ is the droplet contact angle. A study of the droplet contact angle versus substrate temperature for gallium on GaAs showed that at high temperatures the contact angle is reduced and therefore wets the surface instead of balling up [178]. Also upon annealing a droplet undergoes Ostwald ripening, whereby small droplets migrate to larger droplets.

In a separate experiment a N-rich GaN layer was grown and 2 hours into the growth a gallium layer deposited before continuing the GaN growth for 5 mins. Very short (10 nm) GaN nanowires were observed as a result of the GaN growth (fig. 4.10b). The

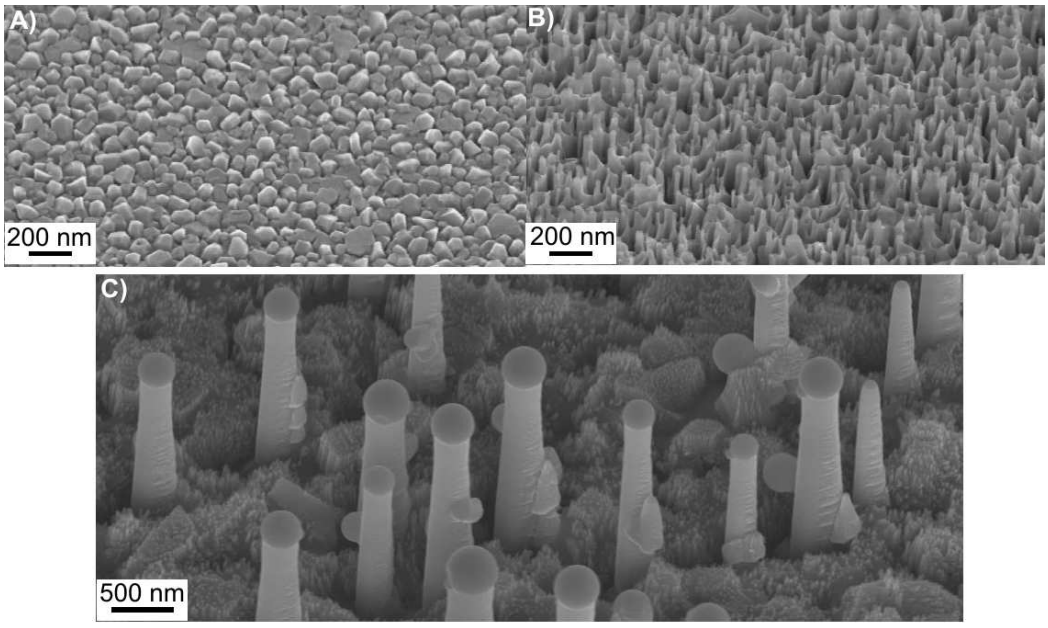

Figure 4.10 SEM images of GaN of a) Ga deposited on sapphire, b) Ga deposited on GaN and c) growth using the Ga–rich droplet formation.

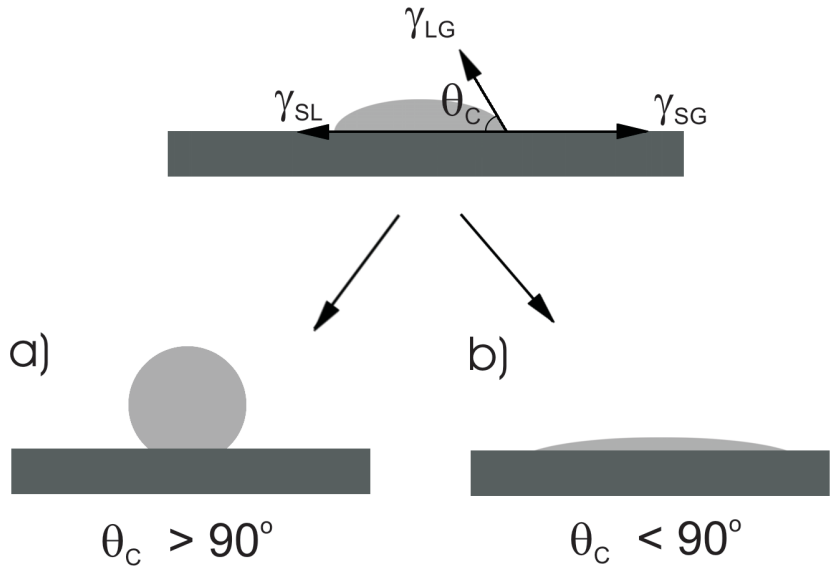

Figure 4.11 Droplet contact angle dependence on the interfacial energies, a) non-wetting and b) wetting.

mechanism for growth of nanowires this way is likely due to a change in the droplet contact angle, as droplets formed on a rough surface have larger contact angles (required for nanowire growth). Rough surfaces promote hydrophobic droplet formation:

$$r \times (\gamma_s - \gamma_{sl}) = \gamma_l \cos\theta \tag{4.8}$$

where r is the surface roughness factor [179, 180].

$$r = \frac{\text{actual surface}}{\text{geometric surface}} \tag{4.9}$$

Also, the strongly columnar growth that occurs in the N–rich GaN growth regime could lead to the gallium droplets becoming trapped on top of the GaN columns. Therefore the droplet is confined by a smaller surface area, resulting in enhanced growth in the axial direction [181].

When the deposition time of the gallium was increased in an effort to produce gallium droplets with the same diameter as that of the branching GaN nanowires, nanowire growth was not observed. Instead, the gallium droplets became multifaceted, possibly due to N–rich growth leading to formation of GaN on the exterior and prevention of VLS. Another way of producing gallium droplets is through the Ga–rich growth regime, which may also be the required growth regime to minimise the vapour solid growth. Using the Ga–rich growth regime and the heating process of the initial branching growth, as shown in fig. 4.1b, GaN nanowires that grow perpendicular to the substrate with intermediate branching growth have been achieved (fig. 4.10c). Therefore, the Ga–rich growth regime seems to be the most likely method for providing the catalyst to excite the nanostructures, as the structures produced are similar to those of the original branching GaN nanowire growth. However, this only explains the initial stage of the nanowire growth.

4.3.2 Supersaturation and Nanowire Growth

A key component in the traditional VLS process is supersaturation of the liquid layer with the growth material. In the case of Au–Si for example, supersaturation occurs when the amount of silicon in the gold droplets exceeds the solid–liquid equilibrium transition point at a constant growth temperature [172]. After the gold droplet is supersaturated, silicon is precipitated out of the droplet, leading to the growth of the nanowire. The composition of the liquid Au-Si alloy then returns to the solid-liquid equilibrium point unless more Si is supplied. Typically the gold catalyst will reside on the top of the nanowire. Also, during the supersaturation process the gold droplet contact angle increases, as the γ_{SG} tensor now extends down the nanowire.

In the case of self-seeding growth, there remain fundamental questions regarding the action of the catalyst in the formation of a nanowire, and it is unclear if the supersaturation process even applies. From various reports on the growth of self-catalytic SnO_2 [182] and GeO_2 [183] nanowires it is assumed that the liquid droplets of Sn and Ge readily absorb oxygen and the nanowire growth occurs at an unknown point of saturation. Vaddiraju et al. have grown self-catalytic InN nanostructures using reactive vapour transport and they explain the growth by two cases [162]. The first case is where InN initially forms and then indium droplets preferentially form on the incomplete InN crystals, leading to 1D nanowire growth on top of the InN crystal by liquid phase epitaxy (LPE). The second case is where indium droplets have formed on the bare substrate and atomic nitrogen from the decomposing NH_3 absorbs into the indium droplet producing multiple InN nanostructures from the one droplet. Again, the nucleation of InN is thought to occur through an LPE process. The LPE process that was suggested by Vaddiraju et al. is the expected process for the growth of the GaN nanowires in this study [162], since during the growth a N-rich GaN underlay is first grown then with the increased gallium flux gallium droplets form on the rough GaN surface to excite the nanowire growth.

The gallium droplet acts as the gallium source and confines the axial growth, while the nitrogen penetrates the droplet or the liquid solid interface between the droplet and the underlying GaN layer to form the GaN nanowire. When growing GaN in the GaN

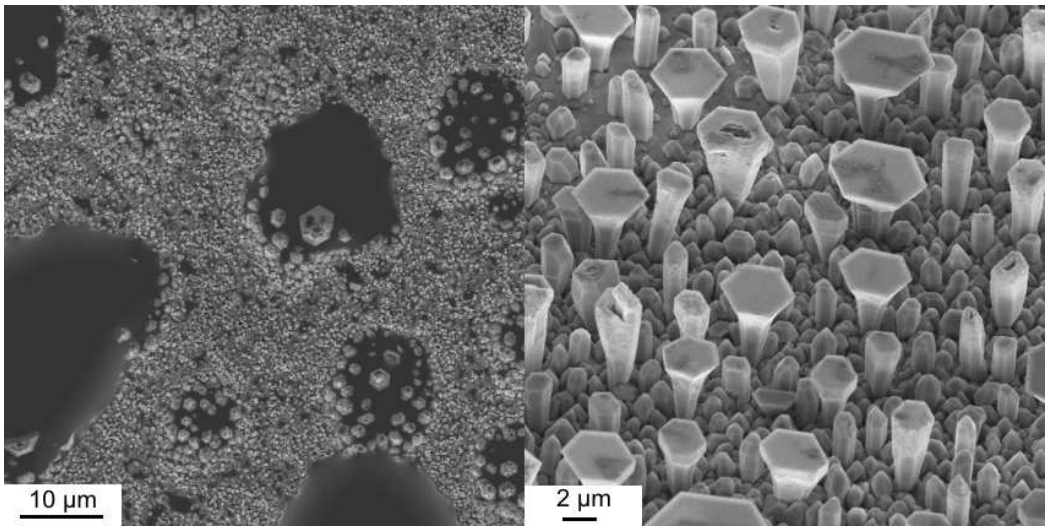

Figure 4.12 HCl etching of the micron size gallium droplets that form during the nanowire growth. Left - as-grown sample and Right - after etching in HCl exposing the structured growth within the droplets.

intermediate growth regime, the nitrogen is able to penetrate the 2.5 ML Ga adlayer on the GaN surface. For the growth of GaN nanowires in the presence of large gallium droplets, wet etching with HCl reveals GaN structures inside of the liquid droplets (fig. 4.12). This type of polynuclear growth mode has been modelled by Dubrovskii et al. who predicted that for small liquid droplets (an exact droplet size was not be proposed) mononuclear growth will be achieved [184], which is the desired growth mode for nanowires.

In all experiments which resulted in the growth of nanowires, the same heating process was used, where the substrate is taken to 860°C before reducing to 800°C as shown in fig. 4.1b. This heating process is expected to change the GaN growth regime at the GaN surface, in that it suppresses the growth of gallium droplets. The result is a suppression of polynuclear growth, as under either the N–rich or intermediate growth regimes, excess gallium should not accumulate on the film surface. Therefore the Ga droplets reduce in size, and will be confined to the top of the nanowire or column that has already started to grow due to polynucleation. Once the nanowires have started to grow, as long as the growth parameters are kept constant, it is expected that the nanowire growth will be sustained

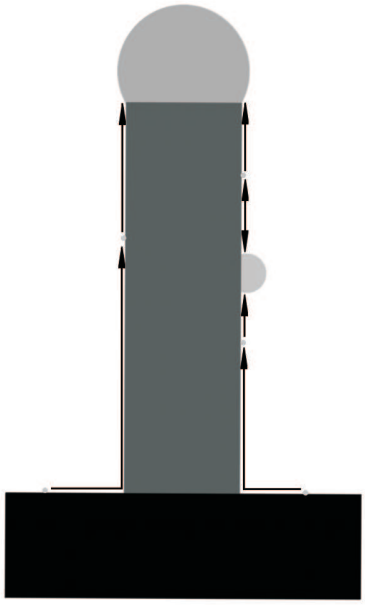

Figure 4.13 Branch nucleation through the accumulation of excess gallium on the trunk.

4.3.3 Branching Nucleation and Growth

The nucleation of branches can be understood in the context of the previous discussion. From the analysis in fig. 4.8 the branching growth appears to occur essentially simultaneously with the growth of the trunk. This would exclude a secondary catalyst deposition from another source in the chamber. Other reports [182] of self-seeding branching nanowire growth achieved through a VLS process generally assert that the growth material builds up on the trunk and a nucleation site for a branch is produced, as shown schematically in fig. 4.13. Such a process is possible in the present study, as the growth regime is expected to be Ga–rich, or near Ga-rich. In such a simple model however, the droplet formation would occur with a random spacing and there seems to be a high frequency of branches spaced apart by roughly 800 nm, as shown in fig. 4.8. This suggests that there is a controlling factor for the branch nucleation sites and that it may not be purely random.

In SEM micrographs of vertically grown GaN nanowires that show the nucleation of branches, some have a secondary droplet attached to the trunk droplet, or in close proximity to it, on the side of the trunk (fig. 4.14). The secondary droplet is possibly

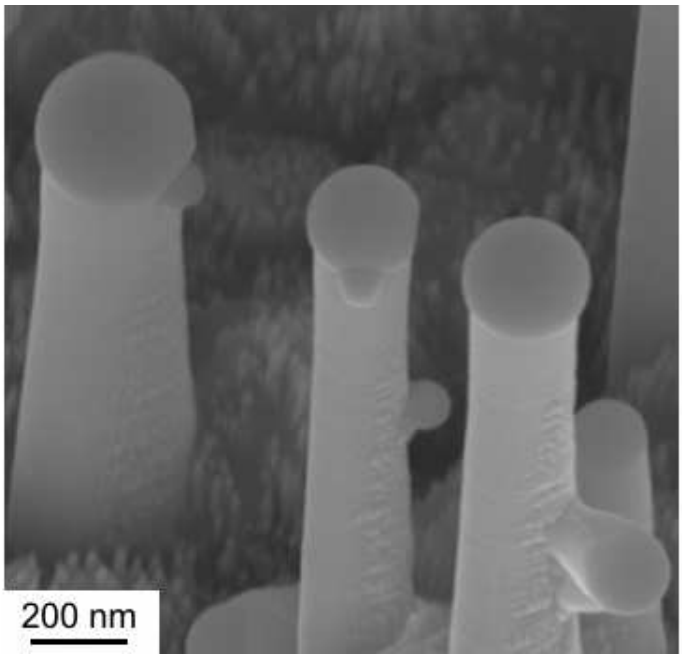

Figure 4.14 Self–seeding GaN nanowires that have a secondary droplet near the droplet of the trunk.

due to the trunk droplet wetting the side of the nanowire, and with increased growth of the trunk the droplet has elongated and separated. Whether this was in some way supported by the volume of the droplet increasing past some vertical value, or the contact angle decreasing as a result of thermal fluctuations, is unclear. It is interesting to note that in the case of silicon nanowires grown by MBE using a gold catalyst, the gold covers the entire structure, as well as the substrate, and even forms small droplets on both surfaces. Real time TEM of VLS nanowires has also shown that it is possible for the gold droplets at one nanowire to migrate to a neighbouring nanowire [185]. Therefore the flow of gallium on the sides of the trunk from the large droplets on the substrate or other droplets on the nanowire is possible, and due to the rough surface of the trunk may lead to the build up of a gallium nucleation site. However, this process would be heavily dependent on the diffusion length of the gallium adatoms.

There has also been some interesting research done in the past on the effect of thermal gradients in the growth of silicon whiskers [172]. When a gold particle is placed on a silicon surface and heated to the liquid stage, the droplet has a uniform hemisphere shape. When a thermal gradient is introduced across the silicon substrate, the gold

particle elongates in the direction of the highest temperature zone. Elongation can lead to the break up of the gold droplet if the surface energies are exceeded. Therefore, an array of silicon whiskers is grown. This could be achieved in the case of branching GaN nanowires if the tip of the trunk is sufficiently colder than the base, leading to a strong thermal gradient. To sustain the growth, the gallium in the droplet would need to be replenished, which is achievable in a self-seeding growth process under constant gallium flux.

There are a number of possible explanations for the branching growth. Several of the growth processes would require instabilities in the temperature to induce branching growth. As growth is under Ga–rich conditions the main reason for branching growth is going to be due to gallium droplet nucleation on the trunk structure.

4.3.4 Growth Sequence

From the analysis of the branching GaN nanowire growth a three process growth sequence has been developed, as shown in fig. 4.15. The first stage of the growth is the formation of gallium droplets which is achieved by growing in the Ga–rich regime. The next stage is still not completely resolved, but the combination of exposure of gallium and nitrogen and annealing of the GaN film leads to the conditioning of the gallium droplets to nucleate the nanowires. The final stage is the growth of the nanowires. The initial growth of the nanowires was done with a plasma source fitted with a 276 hole aperture plate and settings of 150 W and 1×10^{-5} Torr; the settings for the effusion cells and growth temperature are included in figs. 4.1a and 4.1b. With the change in the plasma source to an aperture plate with 488 holes, the plasma settings were retained, but this meant that the temperature settings for the gallium cell were required to be changed. Parameters that have been able to produce nanowires with the new plasma source configuration are shown in fig. 4.16. This film was grown on a 50 mm diameter sapphire substrate and only the outer edges exhibited growth between the large gallium droplets. When the growth parameters were modified to suppress the large droplets, nanowires $\sim$1 μm long were grown, as shown in fig. 4.10c; again, the growth only occurred on a small section of the substrate.

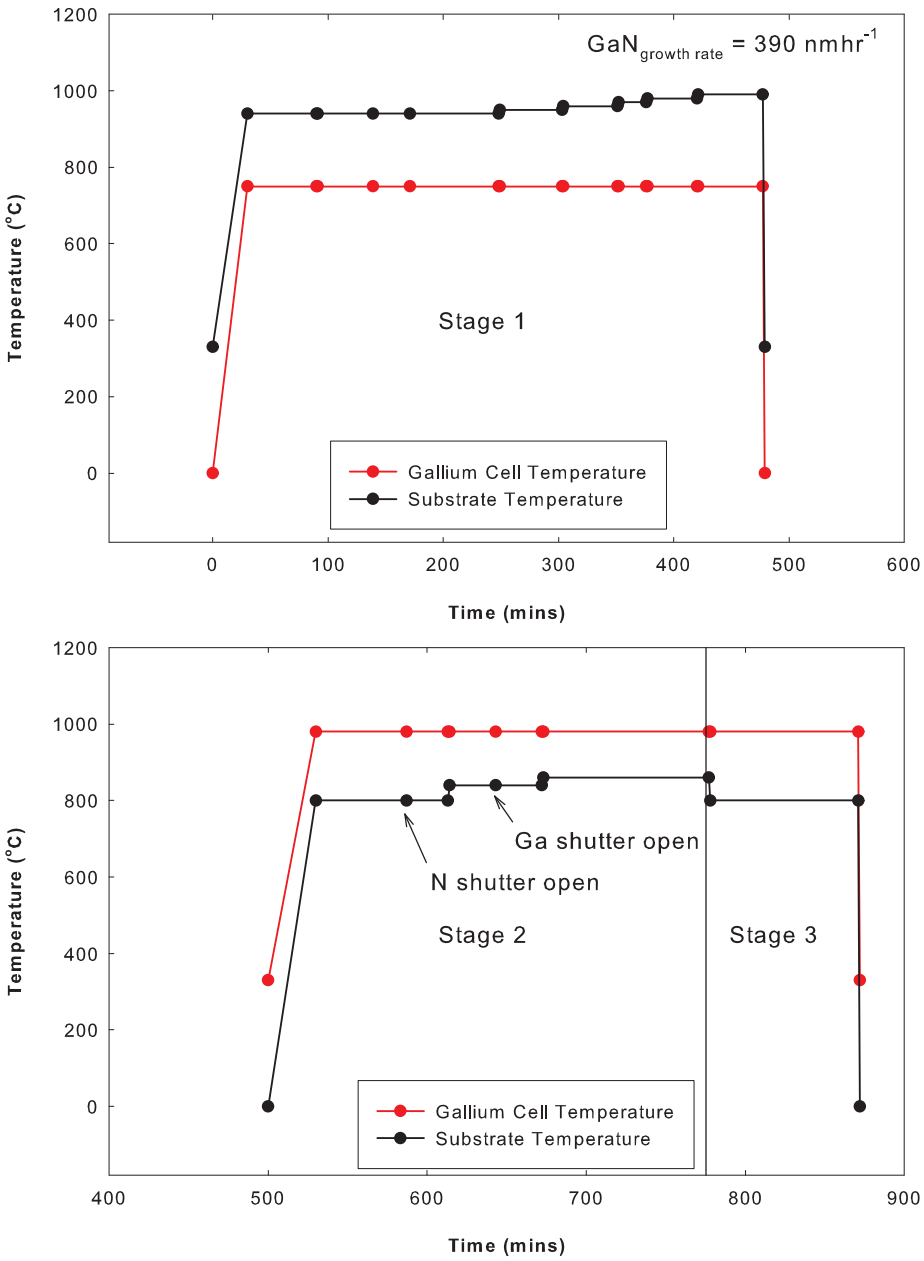

Figure 4.15 Self-seeding GaN nanowire process diagram. Stage 1 is where a Ga–rich growth regime is used to produce gallium droplets for the nanowire growth; typical growth rate that is required is 390 $\mathrm{nm}hr^{-1}$. Stage 2: increased substrate temperature, and Stage 3: the expected region for the growth of the nanowires.

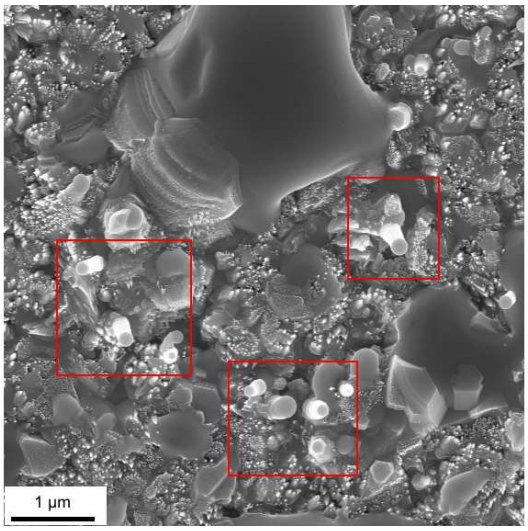

Figure 4.16 Additional self-seeded growths of GaN nanowires/rods using the growth diagram in fig. 4.15.

4.4 ISSUES PERTAINING TO CONTROL OF GROWTH

4.4.1 GaN Nanowire Growth Rate

A comparison of the growth rates achieved in this study can be made against the growth rates measured for self-catalytic growth of MBE GaN nanowires by Bertness et al. and Calarco et al. [186, 187], to MBE grown GaN nanowires using the VLS process with Ni acting as the catalyst by Geelhaar et al. [56]. Both Bertness et al. [186] and Debnath et al. [156] grew GaN nanowires using the N-rich regime without a catalyst. Debnath et al. reported growth rates of 0.32 $\mathring{A}$/s and 0.67 $\mathring{A}$/s for nanowires with diameters of 100 nm and 50 nm, respectively [156]. Specific growth rate values were not reported by Bertness et al. although they suggest that the growth rates in the spontaneous growth of GaN nanowires is typically 100× to 1000× slower than the VLS process. For the branching GaN nanowires in this study, the growth rates of the trunk are estimated to be 19 $\mathring{A}$/s, based on the growth of the nanowires occurring when the substrate temperature was decreased to 800°C. For the vertical self-seeded GaN nanowires the growth rate was 1.4 $\mathring{A}$/s, resulting in a diameter of 120 nm. Thus the Ga–rich growth seems to have significantly enhanced growth rates over the N–rich growth.

Geelhaar et al. has grown GaN nanowires by MBE, using the N–rich regime with a thin nickel layer on sapphire [56]. Axial growth rates of 2.2 $\mathring{A}$/s were achieved for 50 nm diameter nanowires, with the length of the nanowires saturating at 7.5 μm [56]. As 50 nm GaN nanowires have not been grown in this study the growth rates achieved by Geelhaar et al. cannot be directly compared. However, in the case of MBE nanowires the axial growth rate is inversely dependent on the nanowire diameter [188, 156]. Therefore it is expected that our growth rates would be higher for the self-seeding process than for the nickel catalyst. Overall the use of the Ga–rich growth regime seems to enhance the growth rates to compared typical MBE growth of GaN nanowires using the N–rich growth regime.

4.4.2 Effect of Nitrogen Species

For the growth of the vertical and branching GaN nanowires there is a significant difference in the growth rates. Several variables come into play here: substrate temperature, III/V ratio, and also the composition of the nitrogen plasma. For both types of growth the substrate temperature was maintained the same, while the effects of the III/V ratio and the nitrogen composition are dependent on each other. The main difference between the two sets of growths is that the plasma aperture was changed from having 276 holes to 488 holes. Bertness et al. have also looked at the effects of the plasma source on GaN nanowire growth [189]. From their study it was apparent that atomic nitrogen was associated with the nucleation of the GaN nanowires, while molecular nitrogen was the controlling species of the nanowire growth rate. In the case of the growth of self-seeding GaN nanowires a similar trend is seen. Going from the 276 hole (branching GaN nanowires) to the 488 hole (vertical nanowires) aperture plate results in an increase of the atomic to molecular nitrogen species ratio from 2.5 to 3.8, as determined using optical emission spectroscopy through the back of the plasma source (see fig. 4.17). In the case of the individual species, the molecular nitrogen population undergoes a decrease and the amount of atomic nitrogen increases, when changing aperture plate geometry from 276 holes to 488 holes. This is partly consistent with the results of Ptak et al., who reported that molecular nitrogen is the most efficient nitro-

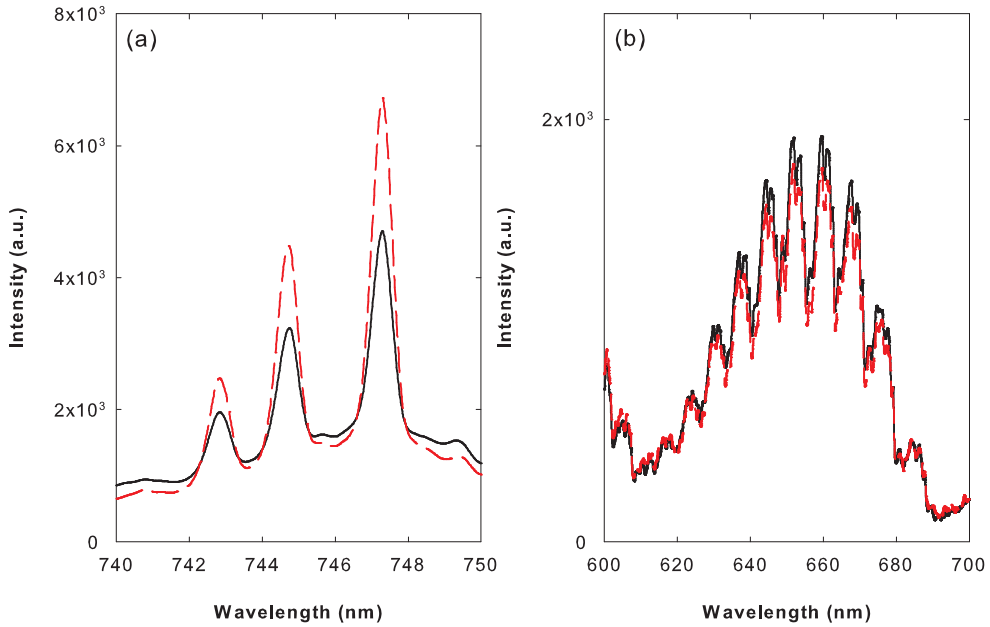

Figure 4.17 Optical emission spectroscopy for a) atomic nitrogen and b) molecular nitrogen. The black line is for the 276 hole aperture plate and the red line is for the 488 hole aperture plate.

gen species in terms of GaN epilayer growth and that the aperture plate configuration can significantly affect the composition of species exiting the plasma source [77].

4.4.3 Nanowire Growth Mode

There are two basic nanowire growth modes, equilibrium thermodynamics/diffusion (e.g. minimising surface energy) and kinetic (e.g. reactant supersaturation in a catalyst drop) [110]. Analysis of the vertical GaN nanowires in this study show that the length of the nanowires are typically 1200 nm long with a diameter of 120±40 nm, although the larger diameter nanowires that have been measured seem to be shorter in length which is seen when the nanowires are grow by diffusion, as shown in fig. 4.18. For GaN and silicon nanowires grown by MBE the growth rates are inversely dependent on the diameter of the nanowire [188, 156]. Instead of having to activate the growth material, in the case of CVD growth, MBE growth directly provides the adatoms to the surface of the nanowire and substrate, therefore the growth is based on adatom diffusion. For GaN nanowires the adatoms diffuse up the m-plane side to the c–axis tip of the nanowire that has a higher sticking coefficient leading to enhanced axial

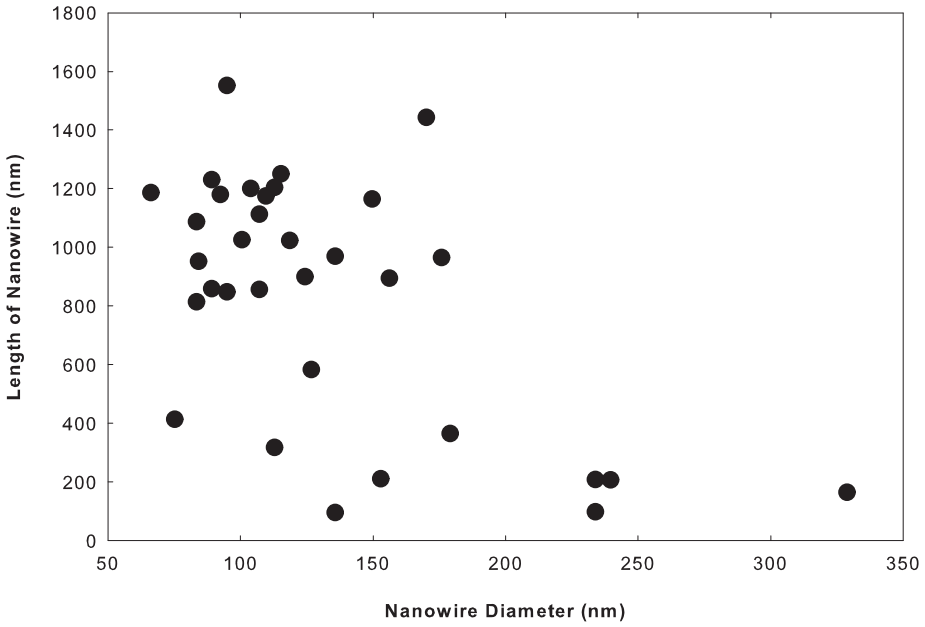

Figure 4.18 Growth rate dependence on the nanowire diameter, obtained from the vertical GaN nanostructures.

growth [110]. As the smaller nanowires also have a small surface area, completion of a monolayer is faster compared to a larger diameter nanowire.

In this study GaN no nanowires with diameters less than 80 nm have been grown using the self-seeding growth process. Also, in the branching GaN nanowire growth several wires with 100 μu diameters were observed with a length of several hundred microns. This lower diameter limit and growth rate that is dependent on the structure diameter has been observed by Givargizov et al. for the growth of VLS silicon whiskers [190]. They concluded that the growth mode was kinetic based on different supersaturation achieved by different diameter structures, with a decreasing diameter leading to a decrease in the supersaturation [190]. The decrease of the supersaturation is given by the Gibbs-Thomson expression as,

$$\Delta\mu = \Delta\mu_o - \frac{4\Omega\alpha}{d} \tag{4.10}$$

where $\Delta\mu$ is the effective difference between the chemical potentials of silicon in the

vapour phase and in the whisker (which is also the driving force for the whisker growth), $\Delta\mu_o$ is the same difference at a plane boundary ($d \to \infty$), α is the specific free energy of the whisker surface, and Ω is the atomic volume of silicon. The growth rate, V, of the whisker in relation to equation 4.10 is,

$$V \approx \left(\frac{\Delta\mu}{kT}\right)^{n} \tag{4.11}$$

which is determined from growth data. With reducing wire diameter the growth rate decreases because the supersaturation decreases. This is due to the increasing vapour pressure and solubility of silicon as the diameter of the whisker becomes smaller [190].

The GaN nanowires grown in this study show support for both the diffusion and kinetic growth modes. However, at the nanowire scale the growth rates are more suggestive of diffusion based growth which is expected for MBE growth of nanowires.

4.4.4 Nanowire Diameter Control

In traditional VLS growth, the diameter of the catalyst controls the diameter of the nanowire. The size of the droplet can be decreased through higher growth temperatures where the catalyst evaporates, although high growth temperatures may adversely affect the nanowire growth through the introduction of defects. For the self-seeding process, the size of the droplet can be modified by controlling the material that forms the droplet, in this case the gallium flux. With a higher gallium flux, excess gallium can lead to branching nanowires. However, if the gallium flux is reduced too much the droplet will be completely consumed. Under the right conditions reducing the gallium flux should lead to a reduction in the nanowire diameter, and the gallium droplet can be sustained at the smaller diameter as long as the gallium flux is equal to the combined desorption rate and consumption rate of gallium from the droplet for nanowire growth.

In film 560–GaN–GaSa the gallium cell temperature was reduced from 980°C to 960°C when the GaN nanowire growth was at stage 3 for 2 hours. This resulted in nanowires with morphologies as shown in fig. 4.19. The GaN nanowires had an initial

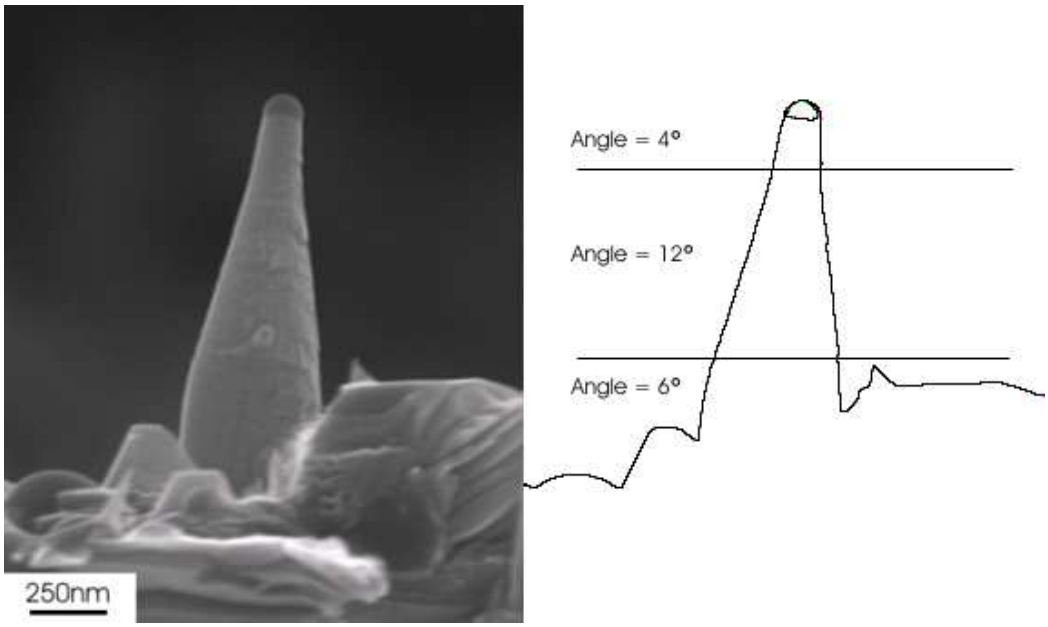

Figure 4.19 Modification of the diameter of the GaN nanowires by adjusting the gallium flux during growth.

taper angle of 6°, which is possibly from gallium evaporation, which then increased to 12° due to the imbalance in the conservation of gallium with the reduction of the Ga cell temperature. Therefore, the Ga droplet diameter has to reduce as not enough gallium is being supplied to support the gallium evaporation rate and consumption of gallium by the nanowire. In this case the taper angle then reduces to 4° representing a new equilibrium state. However, this would also mean that the nanowire growth rate has reduced as the Ga evaporation rate would still be the same. This process has demonstrated that the growth of small nanowires can be achieved by careful control of the gallium flux.

4.5 SUMMARY

Both vertical and hierarchical (branched) GaN nanostructures have been grown by MBE through a combination of annealing and use of the Ga–rich growth regime. The self-seeding process allows for a variety of nanostructures to be grown. With a high Ga–rich environment secondary gallium droplets and branches are observed on the trunks of nanowires. For conditions where the gallium flux is reduced the diameter of

the nanowire can be reduced due to the modification of the gallium droplet. Reduction of the gallium flux leads to the terminating droplet being completely consumed and the nanowire growth is then terminated. The branching nanowires exhibit a high degree of crystallinity, producing typical optical properties for GaN, except in regions of kinked and substrate interface growth. The growth of self-seeding nanowires is a way of reducing impurities that need to be added to start the nanowire growth using the standard VLS process. Further, the growth rates reported here are superior to what has been achieved for the N–rich growth of GaN nanowires by MBE.

Chapter 5

GALLIUM NITRIDE NANOWIRE DEVICE FABRICATION AND CHARACTERISATION

With the need to reduce the size of devices as well as their power consumption, nanowires have been seen by many as the way forward, as the growth of such structures is a comparatively simple process. However, even though most of the device processing involves scaling down fabrication techniques already in existence, working with such small structures presents new challenges. Usually the nanowires are dispersed onto an insulating surface after growth, and contacts are then fabricated to make planar devices (fig. 5.1a). This allows for the optical and electrical characteristics of single nanowires to be determined. Devices that have been fabricated in such a fashion do not greatly reduce the overall size of devices, but rather only the active area. To achieve smaller devices, structures based on as-grown vertical nanowires (fig. 5.1b) are being considered. Therefore, the device size can be expected to approach the cross sectional area of an individual nanowire. This chapter covers the fabrication of both planar and vertical nanowire devices using the branching GaN nanowires and vertical nanowires, respectively.

5.1 PLANAR DEVICES

5.1.1 Fabrication

There are three techniques that can be employed in the fabrication of contacts to nanowires: (1) standard photolithography, (2) electron beam lithography (EBL), and (3) focused ion beam (FIB) processing. Standard photolithography is a highly de-

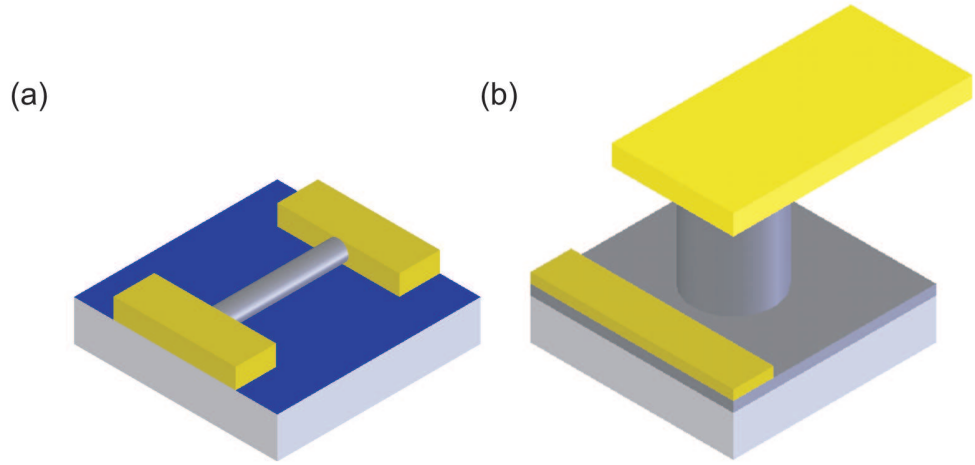

Figure 5.1 Typical structures of a) planar and b) vertical nanowire devices without a gating contact.

sirable method for fabricating contacts, as it does not require specialised equipment beyond that already used already by industry. However, the achievable feature sizes in photolithography are limited by physical characteristics of the mask, as well as the exposure optical wavelength and practical pattern alignment considerations. In the case of CVD-grown nanowires, where long structures ($>5\,\mu$m) are able to be grown over a short time, photolithography can be a viable contacting process. However, for MBE-grown nanowires and more so the branching GaN nanowires in this study, the size of the nanostructures does not allow for the chrome masks to be easily aligned under an optical microscope. Also, due to the unique shape of each branching nanowire a new mask would be required for each nanowire. Compared to photolithography, EBL has higher alignment resolution through the use of the electron microscope. Moreover, pattern fabrication can be customised for each individual nanowire, although the ability to view the nanowires through the e–beam resist can be an issue. FIB is a technique that uses a focused beam of gallium ions, instead of electrons, which allows for nano-machining of the sample. It can be used to deposit platinum layers for contacting between nanowires and pre–fabricated contact pads. FIB would be an ideal technique for the fabrication of contacts to nanowires, as the number of processing steps can be reduced and better contact transitions can be fabricated. Moreover, the visibility of the nanowires are not hindered by a resist layer. However, such instruments are expensive

and as not as common as EBL systems, and were not available for this work.

In this study a RAITH 150 EBL system was used to fabricate contacts to the branching GaN nanowires. The basic process is as follows: An e-beam resist (polymethyl methacrylate (PMMA)) is first spun onto a substrate which holds the nanowires. The EBL system is then used to write a pattern onto the resist layer. Subsequently a metal layer is evaporated onto the surface and lifted off to leave metal coverage where desired. This process is what is typically reported for contacting to nanowires and seems to work well for nanowires with small diameters (10–50 nm). However, the branching GaN nanowires have a diameter in the range of 50–200 nm, which can affect the quality of the contacts. For a thin metal layer the nanowire can act as a shadow mask, so that the metal does not completely encapsulate the nanowire, as shown in fig. 5.2. If the metal layer thickness is increased without changing the resist thickness, the metal is unable to be lifted off without the use of an ultrasonic bath, which unfortunately causes the nanowires to lose adhesion to the substrate surface. A metal layer thickness less than one quarter of the electron beam resist thickness can be lifted off successfully without the aid of an ultrasonic bath. However, a thicker resist layer makes it harder to see through to locate nanowires. Visibility can be increased by going to a higher accelerating voltage, but this leads to faster exposure rates of the electron beam resist which then reduces the visibility of the nanowire through the electron beam resist.

To overcome these obstacles, a new process was developed, shown schematically in fig. 5.3 and described in detail in Appendix A. The process involves creating metal alignment markers to improve the alignment of the following contact masks, which reduces the need to observe the actual nanowire. Before the contact pattern can be fabricated onto the nanowire an additional imaging step is essential so that the contact mask can be designed before the nanowire is buried under the electron beam resist. A thicker electron beam resist can then be applied to fabricate thicker contacts. The nanowires are nearly invisible under the thicker resist layer; although the metal markers are still able to be seen they are not as sharp as desired to achieve perfect alignment. So far an electron beam resist up to a thickness of 800 nm has been used, allowing for contacts as thick as 120 nm to be fabricated.

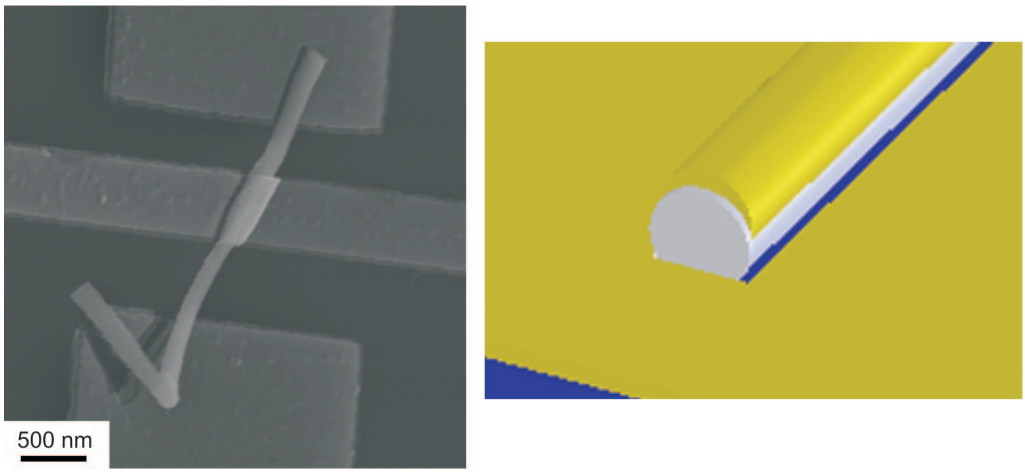

Figure 5.2 SEM micrograph taken of a GaN nanowire that was attempted to be contacted, which exhibits both incomplete metal wrapping and also the nanowire is not flat on the Si_3N_4 surface. Shown on the right is a schematic of the metal coating on the nanowires.

As alluded to previously, devices based on branching nanostructures pose a number of challenges. A key issue is that they rarely if ever lie entirely parallel to the substrate, making one or more contacts geometrically difficult. Nanowires that do not sit flat on the substrate can be detected when the resist layer is applied, as there is a change in contrast where an object is displaced from the substrate surface. Contacting such features requires additional steps to those described previously. By overexposing ($\times$20 energy dose) the PMMA layer, polymer chains strengthen such that when washed with acetone the PMMA remains. This allows the nanostructures to be partially embedded within an insulating PMMA layer, as shown in fig 5.4, allowing for contacts to be fabricated to branches not in touch with the substrate. Such a process has been used for the fabrication of GaN nanowire LEDs where n–type GaN nanowires are dispersed onto a p-type substrate and then a contact is applied to the substrate, while the PMMA/SiO_2 acts as an insulating layer for a top contact to be applied to the nanowire [191]. A similar nanowire LED structure was fabricated in this study, however larger metal particles generated from the ultrasonic process, possibly indium, led to shorting of the top contact with the p-Si substrate.

Aside from nanowires on the substrate surface, also present are organic and inorganic particulates. These contaminants can cause issues with the metal lift off, especially if they are larger than the thickness of the e-beam resist, as the tops of the

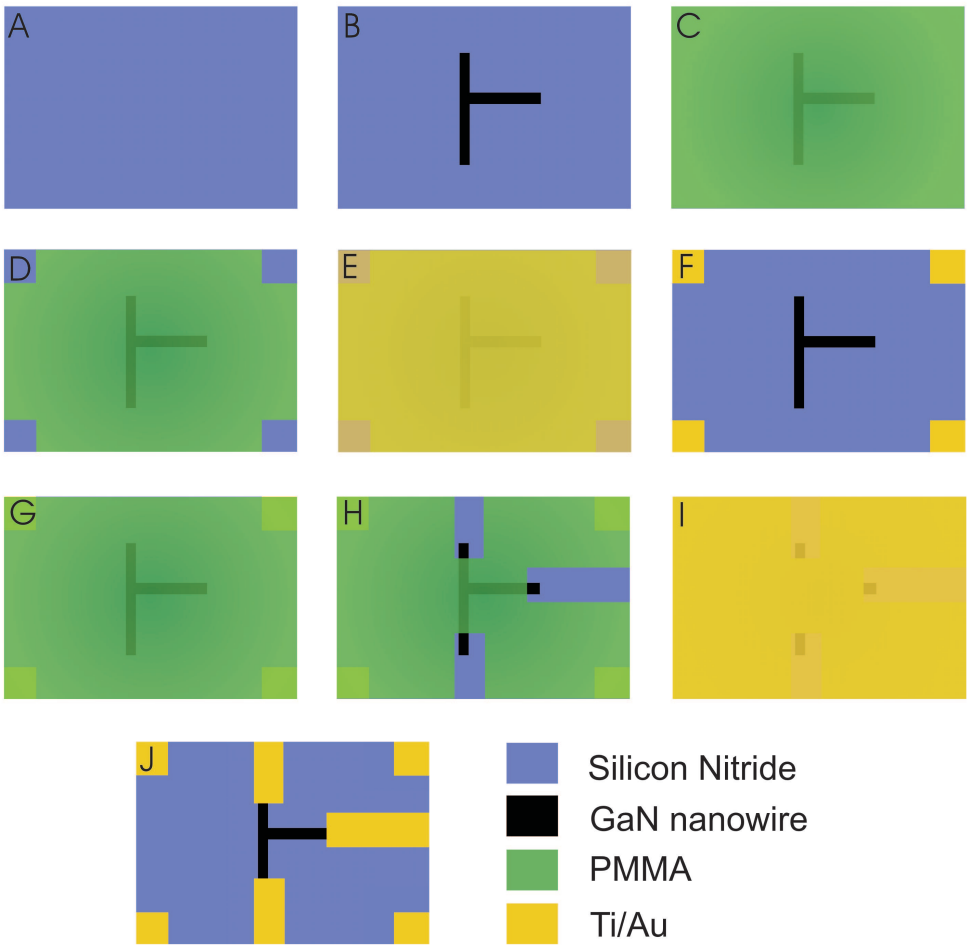

Figure 5.3 Process sequence used to fabricate contacts to the branching GaN nanowires. a) Starting with a Si_3N_4/Si substrate, b) nanowires are applied, c) 400 nm PMMA bilayer is spun on, d) markers are exposed using the EBL system, e) Ti/Au (10 nm/40 nm) contacts evaporated, f) markers are lifted off, g) 800 nm PMMA bilayer is spun on, h) contacts to the nanowire are exposed, i) Ti/Au (10 nm/90 nm) contacts evaporated and j) contacts are lifted off in boiling acetone.

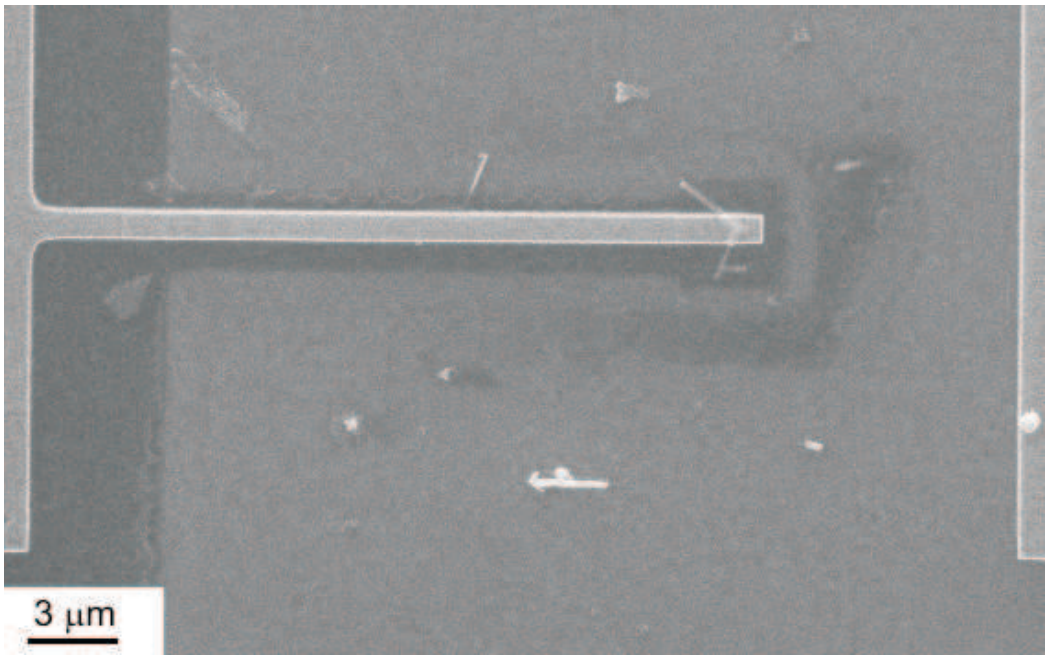

Figure 5.4 SEM image of a GaN nanowire that has been embedded into a PMMA layer, which was exposed with a dose twenty times stronger than typically required to expose contact areas into electron beam resist, then a Ti/Au contact has been applied on top of the PMMA.

particles lead to a metal coating and non-uniform lift-off. One means of reducing the contaminants is by etching the entire as-grown sample in HCl, removing metal from the back surface of the substrate (used for mounting to the growth block) and preventing it from releasing particles in the ultrasonic bath. Organics can be removed with a dip in aqua regia, or oxygen plasma ashing for several minutes. In this study dipping of the nanowires in HCl after placement on the Si_3N_4/SiO_2 substrate was done, as at the time contaminants from the substrate were not expected to be an issue. An oxygen plasma asher was also used, especially on samples that had signs of solvent residue on them, however it was not clear if this process had any adverse effects on the nanowires as contacting issues to both non-ashed and ashed samples prevented a large enough set of I-V data to be collected to determine a trend.

5.1.2 I-V Characteristics

For the I-V measurements of the nanowires an HP 4155A semiconductor parameter analyser was used. Only 10% of the contacted nanowires produced measurable I-V (i.e.

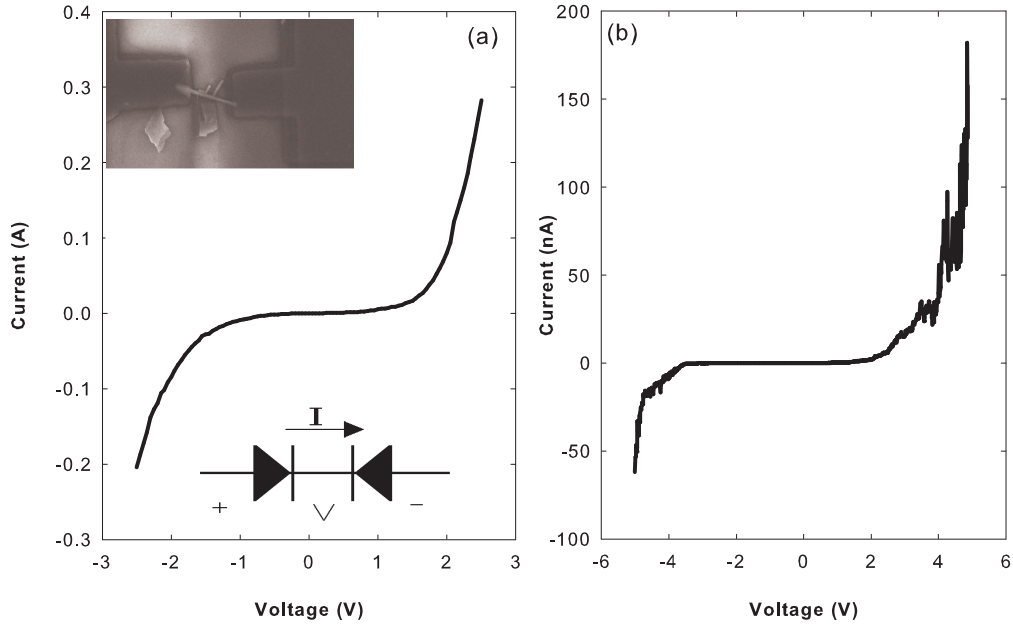

Figure 5.5 a) Non-linear I-V from the GaN nanowires, which can be represented as back to back leaky diodes (shown in the inset). b) I-V from some GaN nanowires is representative of a single electron charge.

were not an open circuit). I-V characteristics of the initial set of nanowire devices were in all cases non-linear as shown in fig. 5.5a, which can be modelled as two back-to-back leaky Schottky diodes. The most likely explanation is a thin Ti layer, allowing the Au layer to make a poor quality Schottky contact, although since the Ti and Au are not being evaporated from the same angle it is also possible for the gold to form on areas that are not coated with Ti. Improvement of the contacts can be achieved with increasing the Ti thickness to approximately 10 nm, resulting in reasonably linear I-V. This is comparable to what others have observed for GaN nanowires [192], although too thick of a Ti layer increases the contact resistance. Some of the I-V scans represent a spectrum related to a single electron charge [193], with the current being suppressed for low voltages and at high voltages the current shows a step like increase fig. 5.5b.

The resistance values obtained from linear I-V of GaN nanowires, 20 $k\Omega$ – 900 $k\Omega$ (fig. 5.6), are comparable for those of CVD GaN nanowires that have diameters ranging from 50 to 150 nm [194]. The equation of the resistivity of a homogeneous conductor is given as

$$R = \rho \frac{l}{A} \tag{5.1}$$

where ρ is the material resistivity, l is the length of the conductor along the direction of current flow and A is the cross sectional area of the current pathway. Shown in fig. 5.7 is the measured resistivity as a function of GaN nanowire diameter, which shows that nanowires with smaller diameters have a higher resistivity. An increase in the resistivity for GaN nanowires can be caused by surface Fermi-level pinning above the conduction band leading to band bending and a depletion region on the surface of the nanowires [195]. The depth of the depletion region is dependent on the material quality; for CVD grown nanowires the pinch off of the conduction channel occurs at a diameter of 20 nm while for MBE grown nanowires the pinch off is at 85 nm, with the depletion region typically 50 - 100 nm deep [195]. The difference in the two samples is that the background carrier concentration for the CVD samples is higher, leading to a small resistivity and reduced depletion region depth into the nanowires [196]. In this study the pinch off is occurring for GaN nanowire diameters of 100 nm, which is consistent with other GaN nanowires grown by MBE [196].

So far most of the branching structures have yielded conduction through only one pair of contacts. However, a three terminal nanowire device has been fabricated with linear I-V through only one pair of terminals (B-C), as shown in fig. 5.8, while the third terminal (A) is acting like a weak Schottky contact. It is possible that terminal A could be used as the gate for a transistor. To investigate this possibility I-V sweeps were performed across terminals B to C as A was varied between -2 V to 2 V (fig. 5.9). For a typical nanowire FET structure the I-V is centred at the origin and then with changes in the gate voltage the slope of the current (I_{DS}) is modified [68]. From the three terminal GaN nanowire device we observe a different I-V curve. With a zero gate voltage the I-V is linear. When a non–zero gate voltage is applied, the I_{DS} at a zero bias across the drain and source terminals is increased with a negative gate voltage and decreased with a positive voltage. The change in I_{DS} is possibly from leakage current from the gate contact. The modification of I_{DS} is not a constant along the entire

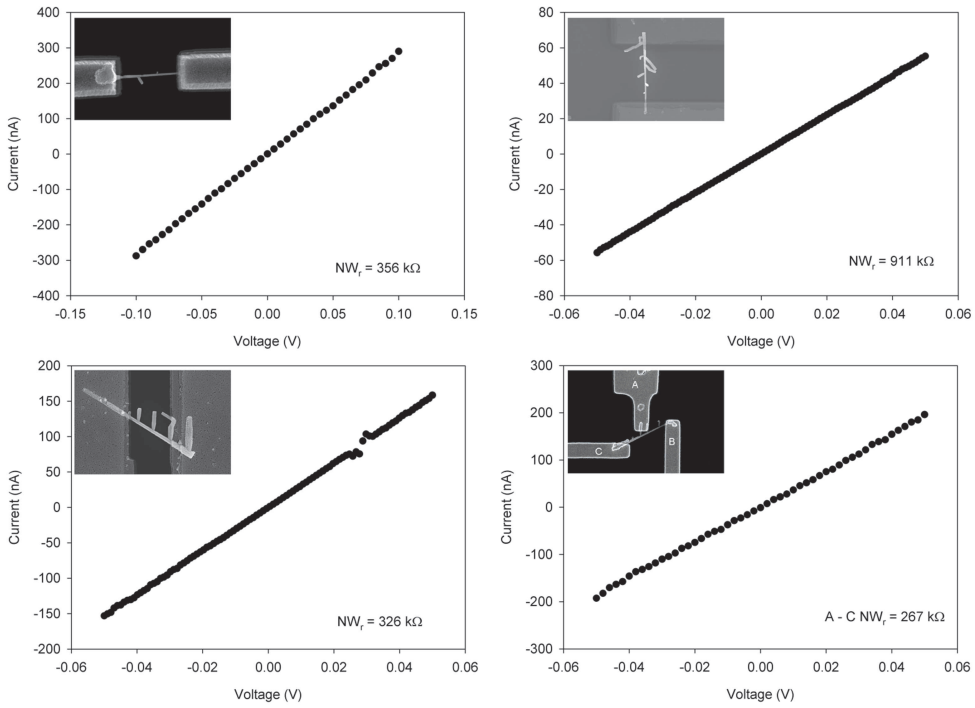

Figure 5.6 I-V scans taken from branching GaN nanowires that exhibited linear I-V.

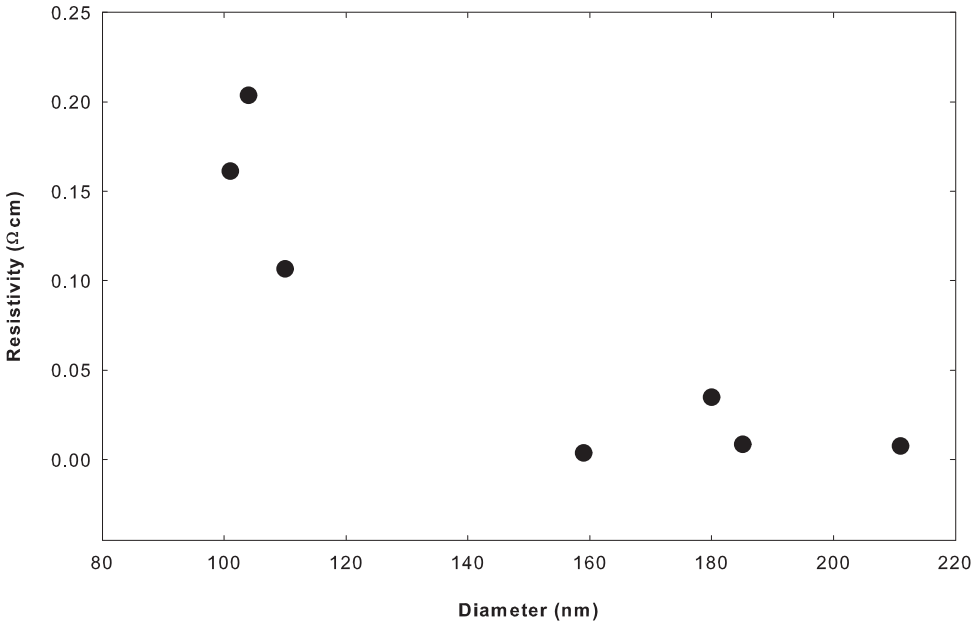

Figure 5.7 The resistivity of the GaN nanowires as a function of the nanowire diameter.

V_{DS} sweep from -0.5 to 0.5 V, which would be seen for a completely resistive junction. Instead, for an increase in the negative gate voltage, the slope of I_{DS} for V_{DS} in the range of 0 to 0.5 V increases more significantly than the decrease in slope of I_{DS}, over 0 to -0.5 V V_{DS}. The opposite is observed for a positive gate voltage. This non-linear change in I_{DS} is possibly due to some gating from the third terminal, or self-gating that can occur at the metal to nanowire contact [197].

In the literature there are only a couple of reports on 3-terminal contacts to branched semiconductor nanowires. Cui et al. reported non-linear I-V with suppressed current flow at low voltages and step like current at high voltages from CdTe tetrapods [193]. They attributed this to single electron transport. The main part of the report investigated using the substrate as a gate which allowed for control over the length of the zero conductance gap; when the third terminal was instead used to gate the single electron transistor, the coupling efficiency was only 70% compared to a standard back gate. Suyatin et al. have reported successfully making contacts to three terminals on a single InAs branching nanowire grown using a secondary deposition process [197]. They used the three terminal nanowire junction to mix together a 9 MHz and 10 MHz signal by applying each signal to one of the terminals and measuring the mixed signal on the third terminal. They also were able to analyse the phase difference when two signals of the same amplitude and frequency were applied.

To ensure that the observed I-V was characteristic of the nanowires themselves, I-V measurements were conducted under both dark and illuminated conditions. A UV light source designed for erasing EPROMs (wavelength 365 nm) was used to provide excitation. The I-V showed a detectable current change between dark and UV-illuminated conditions (fig. 5.10). A constant voltage of 100 mV was applied across the GaN nanowire, and the current was monitored as the lighting conditions were changed. For both the turn off and on transition the change in current is essentially instantaneous for the coarse time scale used (fig. 5.11). However, the transition for (UV) on to (UV) off sees a current change of only 600 nA, while in the (UV) off to (UV) on transition the current change is 200 nA. Had the current under illumination reached the same current level in both cases with only a difference in the dark current, it could be as-

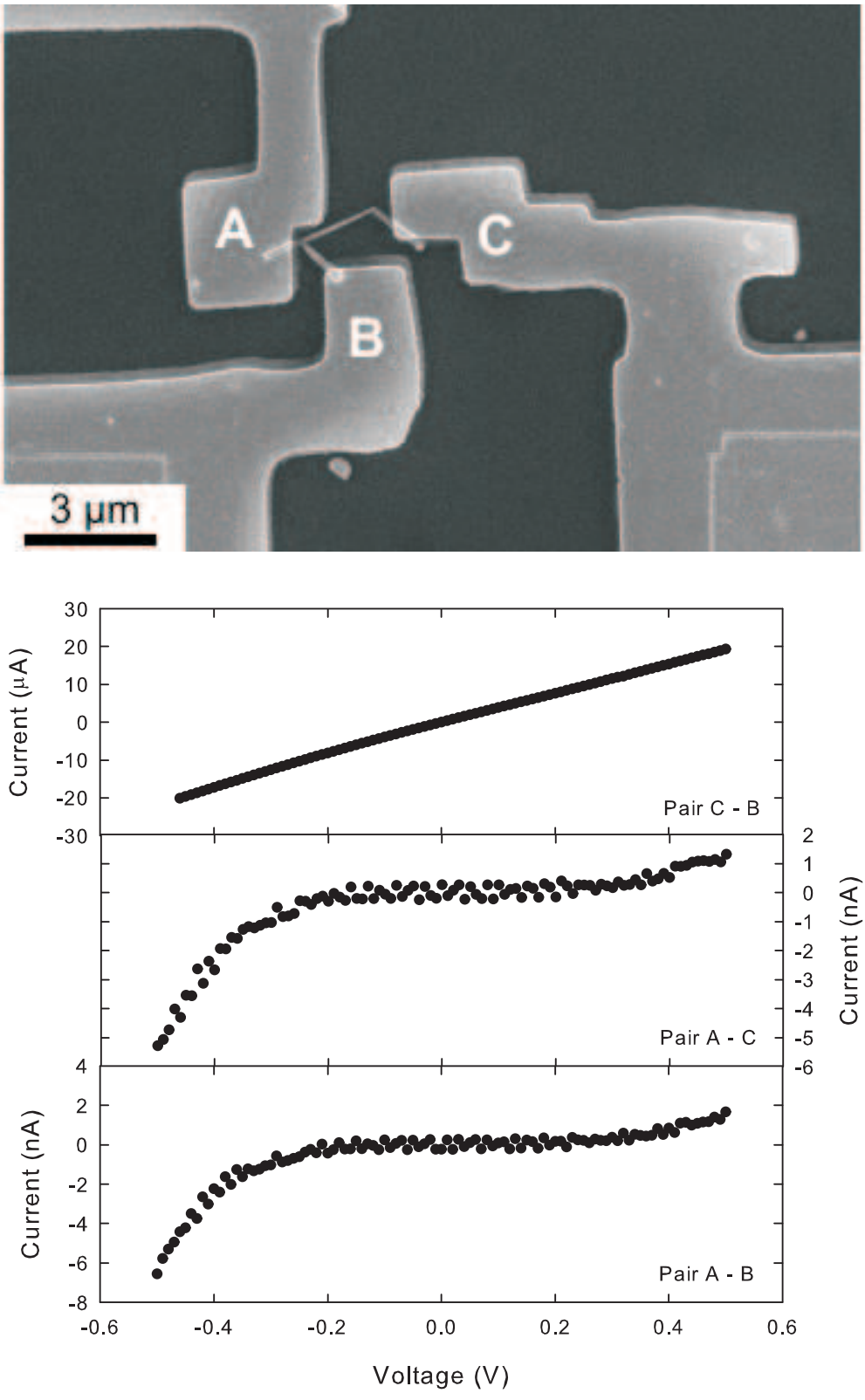

Figure 5.8 (a) Branching GaN nanowire device. (b) Current-voltage measurements for all combination of terminals.

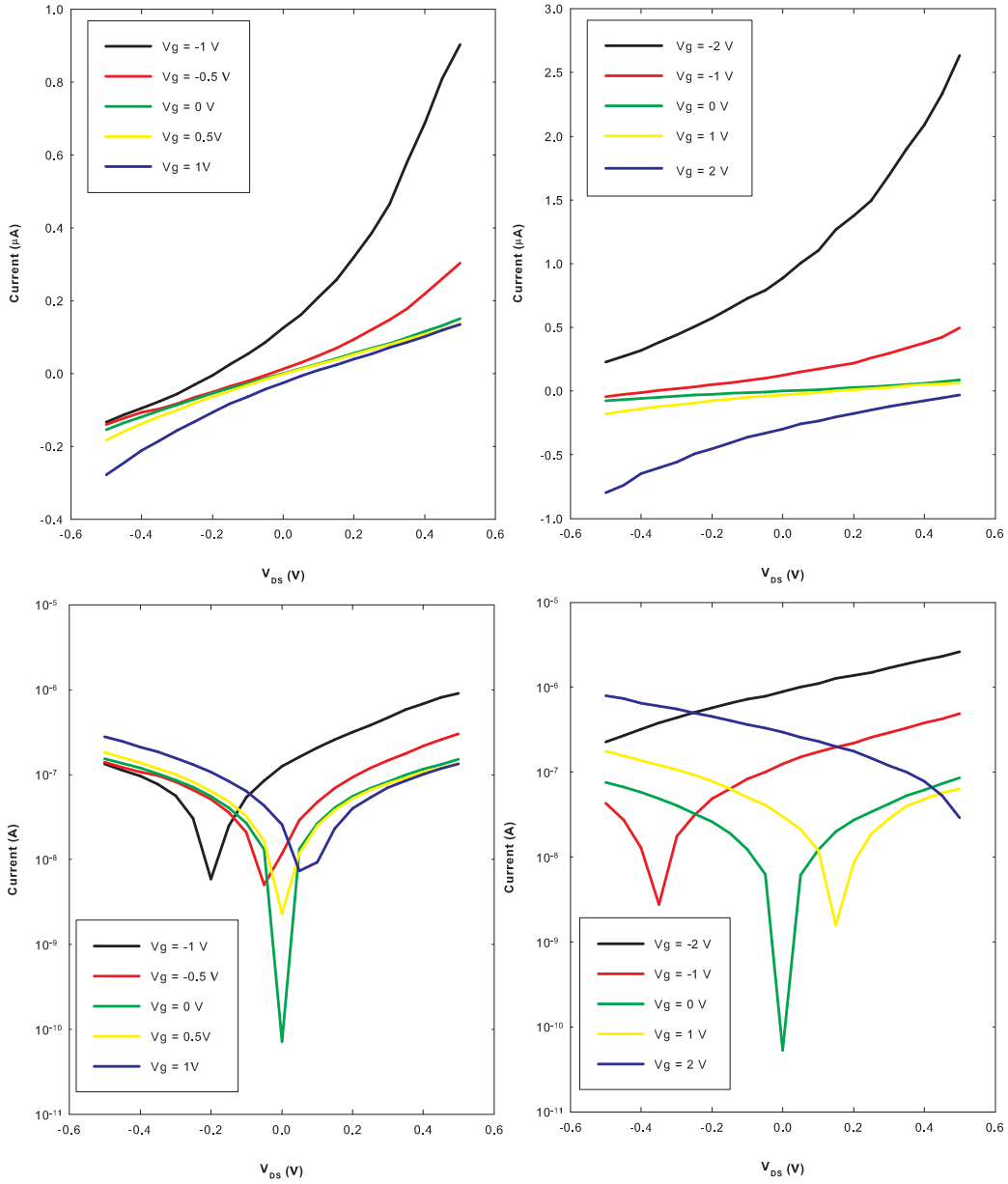

Figure 5.9 Gated current–voltage characteristics of the three terminal contacted branching GaN nanowire shown in 5.8a, with linear and log plots. Terminal A is the gate contact.

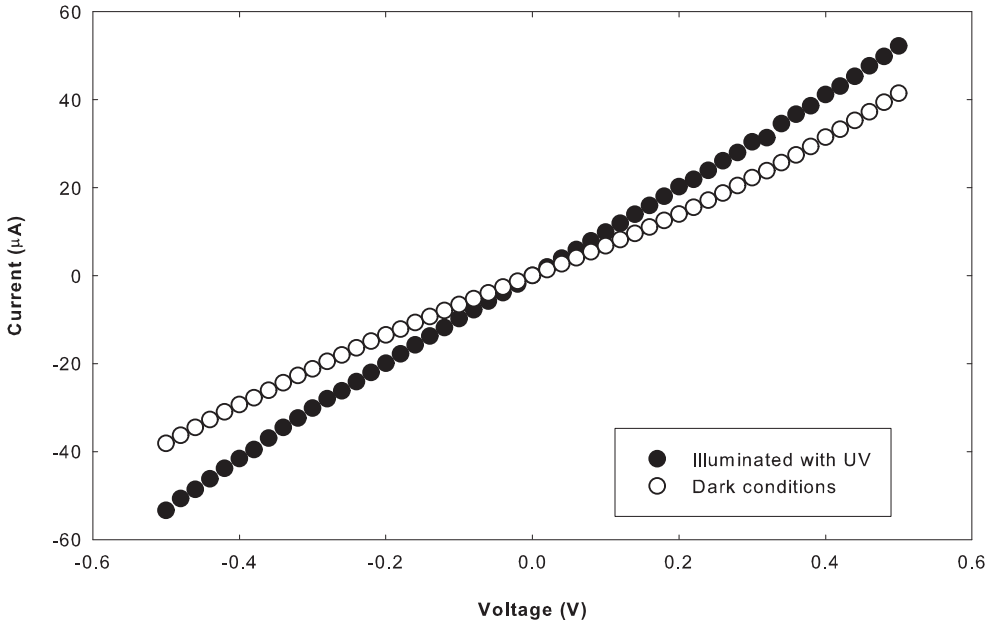

Figure 5.10 I-V from a GaN nanowire under dark conditions and then illuminated with a UV lamp.

sumed that there is a persistent photoconductivity effect occurring, which is known to occur in GaN nanowires [195]. However, the opposite is occurring so the difference is more likely due to settling of the UV lamp, as the transition from on to off was after the lamp was left on for a period of 5 mins before the measurement was conducted. After the scans the conduction path was completely lost due to mechanical failure of the nanowire.

FET structures are often used to measure the electrical properties (carrier concentration and mobility) of nanowires. The devices are often fabricated by using a standard two terminal contact scheme, with the substrate used as the gate and a SiN layer between the substrate and nanowire serving as an insulator, or else the nanowire can be coated with an oxide allowing for a top gate to be fabricated. Stern et al. have demonstrated that for GaN nanowires, there is little difference between using a top or bottom gate [194]. In the present work, a FET structure was fabricated using the silicon substrate as the gate contact. However, despite applying gate voltages as high as 20 V (the maximum value of the parameter analyser) essentially no modulation of the I-V was observed, as shown in fig. 5.12. Possible reasons for this are the SiN is too

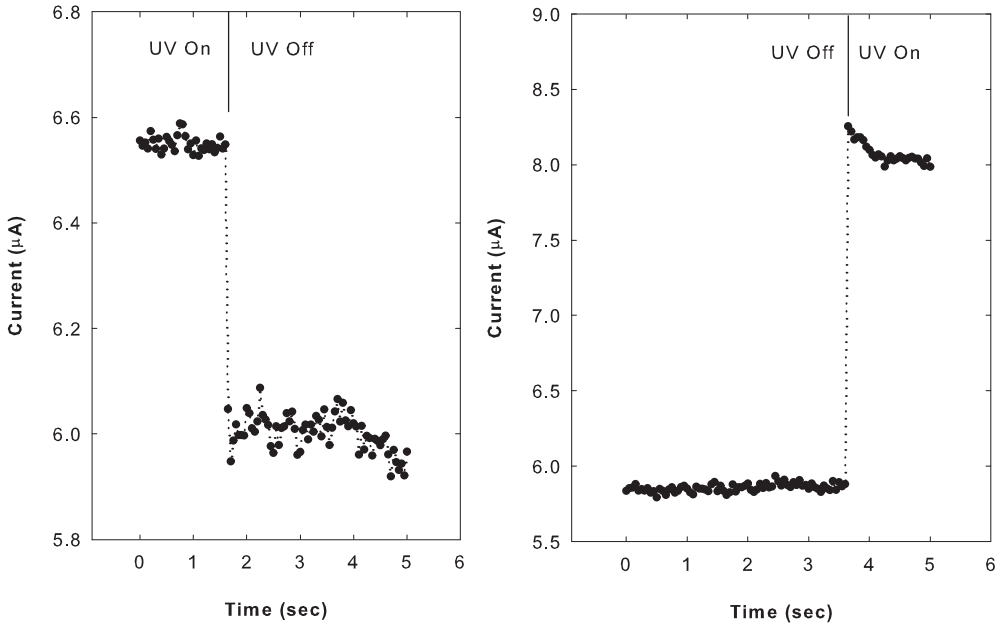

Figure 5.11 Transition from a) UV on to off and b) UV off to on, using a 100 mV bias applied across the GaN nanowire.

thick and therefore the field from the gate (substrate) had no effect on the current flow through the nanowire. It is also possible that the background carrier concentration level was too high to be affected by the gate.

5.2 VERTICAL DEVICES

Separately from the branching nanostructures, vertical devices were also fabricated. Planar nanowire devices are seen as a way of measuring electrical properties of individual nanowires. They are also useful for making gas sensors [198], photon detectors [60] and FETs [68]. However, as discussed earlier the way forward is through the fabrication of vertical structures, where the nanowires are retained on the substrate used for growth and the device is then fabricated from the standing nanowires. Vertical FET structures have been already fabricated by several groups interested in interfacing III-V semiconductors with silicon technology [199]. To date, there has been a lack of studies into the development of GaN devices in vertical geometries.

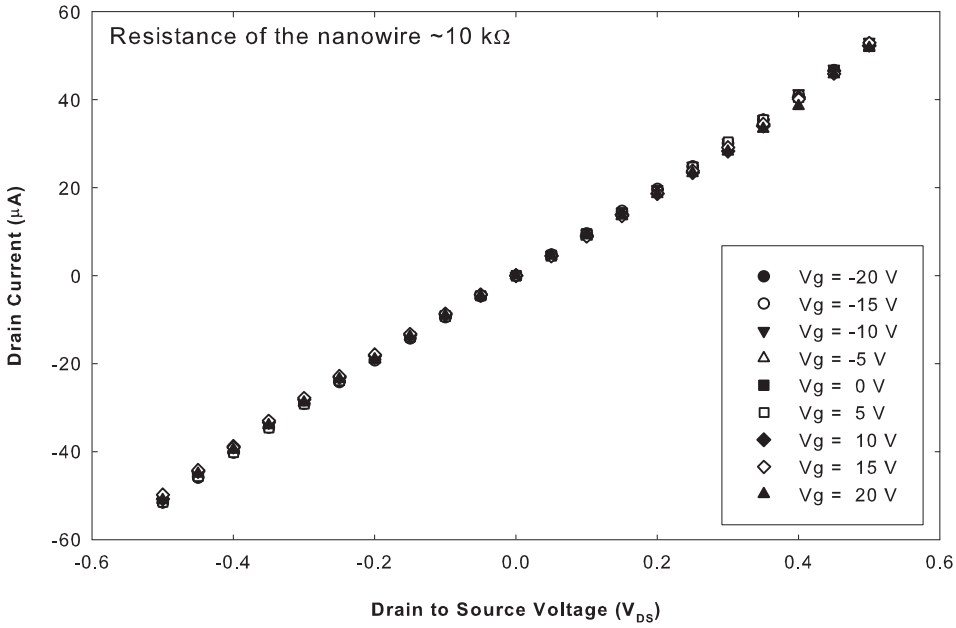

Figure 5.12 I-V from the attempted FET structure using the silicon substrate as the gate.

5.2.1 Fabrication

In contrast to planar devices, the main issue with vertical nanowire devices is getting the top metal contacts at the desired location, since contact to the base of the nanowires can make direct use of the substrate. To probe the top of individual nanowires a metal coated AFM cantilever can be used, although imaging of the nanowires can be hindered due to the roughness of a nanowire surface. To reduce the surface roughness, a layer of PMMA can be spun on, and annealing at 185°C has the effect of planarising the PMMA layer and exposing the tops of the nanowires (fig. 5.13). An additional oxygen plasma ashing can be used to remove residual PMMA on top of the nanowires, and etching with HCl removes the gallium droplet and exposes a flat surface for the AFM tip to probe. Using this same preparation technique, it is also possible to create large contact pads using a shadow mask, therefore allowing for multiple parallel nanowires to be analysed at one time, giving greater current flow. Assuming that each individual nanowire has similar properties, the data can be extrapolated to give that of an individual nanowire.

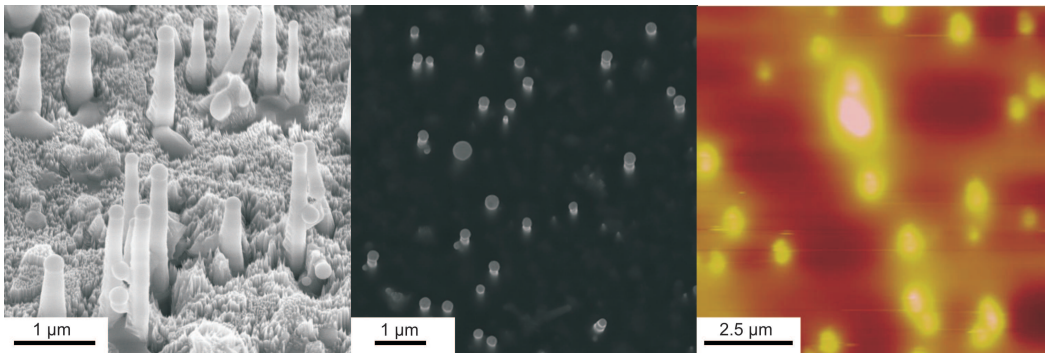

Figure 5.13 GaN nanowires from film 535-GaN-GaSa. a) As-grown GaN nanowires; b) GaN nanowires with a PMMA layer used for planarising the surface; and c) AFM imaging of the planarised GaN nanowires.

5.2.2 I-V Characteristics

I-V measurements were performed using commercial Au/Cr coated AFM tips, with the gold being the external metal layer. For the voltage supply the AFM tip was biased between -12 and 12 V. Using the extender and data signal boxes for the Nanoscope IIIa the current was collected using a Keithley 6457 picoammeter. Ten to twenty separate measurements were taken at each bias voltage to remove issues with stability of the current flow, as well as residual capacitance. Typical nanowire I-V resembled that of a Schottky diode (fig. 5.15), which is expected as gold has a higher work function in comparison to GaN. The diode characteristics, barrier height and ideality factor, can be determined using the expression for thermionic emission for a Schottky barrier

$$I = I_s \left(\exp \left[\frac{qV}{nkT} \right] - 1 \right) \tag{5.2}$$

where I_s is the saturation current and is determined from the ln(I) versus V plot at the V = 0 intercept. It can be calculated using

$$I_s = AA^*T^2 \exp \left(\frac{-q\phi_B}{kT} \right) \tag{5.3}$$

where A is the diode area, A* is the Richardson constant (for GaN it is 26 $AK^{-2}cm^{-2}$),

Table 5.1 Tabulated results for the Schottky contacts to GaN nanowires.

Contact Type	Effective Barrier Height (eV)	Ideality Factor	Rectification Ratio	Reference
Au on GaN thin film	1.07	1.37	-	[200]
Ag on GaN thin film	0.82	1.01	-	[104]
Contact AFM (Au/Cr) PMMA layer	0.39	80	-	
Contact AFM (Au/Cr) No PMMA layer	1.07	3.73	2.56	
Silver Pad	0.84	4.27	1.33	
Gold Pad	1.03	4.12	3.49	

ϕ_B is the effective barrier height, and n is the ideality factor. The ideality factor is determined from the slope of the ln(I) versus V plot using equation 5.2 and the barrier height is determined from the I_s value using equation 5.3. Analysis of the I-V is provided in table 5.1. The barrier height determined for the diode without the PMMA layer is similar for GaN thin film Schottky diodes in the literature (barrier height of 1.07 eV with ideality factor of 1.37), although the ideality factor is significantly higher [200]. Deb et al. have also conducted a similar study for GaN nanowires embedded in silicon dioxide, using Ti/Pt coated AFM tips; for n-type GaN they determined their ideality factor to be 6.5 with a barrier height of 0.62 eV assuming a contact area of 20 nm, compared to an ideality factor of 1.28 and a barrier height of 0.94 eV for a GaN thin film. [63]. The difference in the ideality factor can be associated with reducing the size of the diode, leading to a reduction of the barrier thickness and hence an increase in tunnelling current (non–ideal) [201]. There also seems to be a major difference in the ideality factor when the sample was coated with PMMA (80) compared to without (3.7). PMMA has been used to protect nanowire devices from ageing so this increase is not expected to be from surface effects [202]. The difference is possibly due in part to a fitting error as the AFM process does not allow for a large enough voltage spread to be measured due to contacting issues.

With the AFM a significant amount of time has to be devoted to imaging and

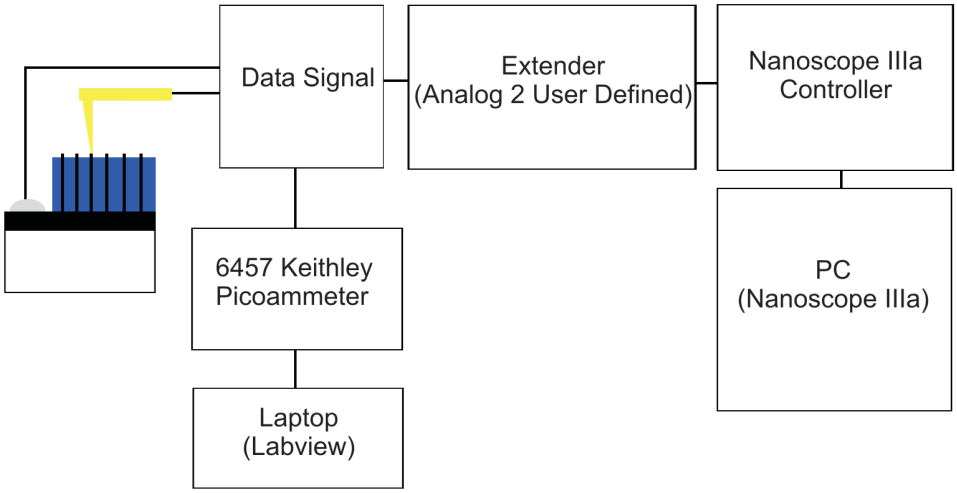

Figure 5.14 AFM setup for measuring the I-V from the vertical GaN nanowires without the PMMA layer.

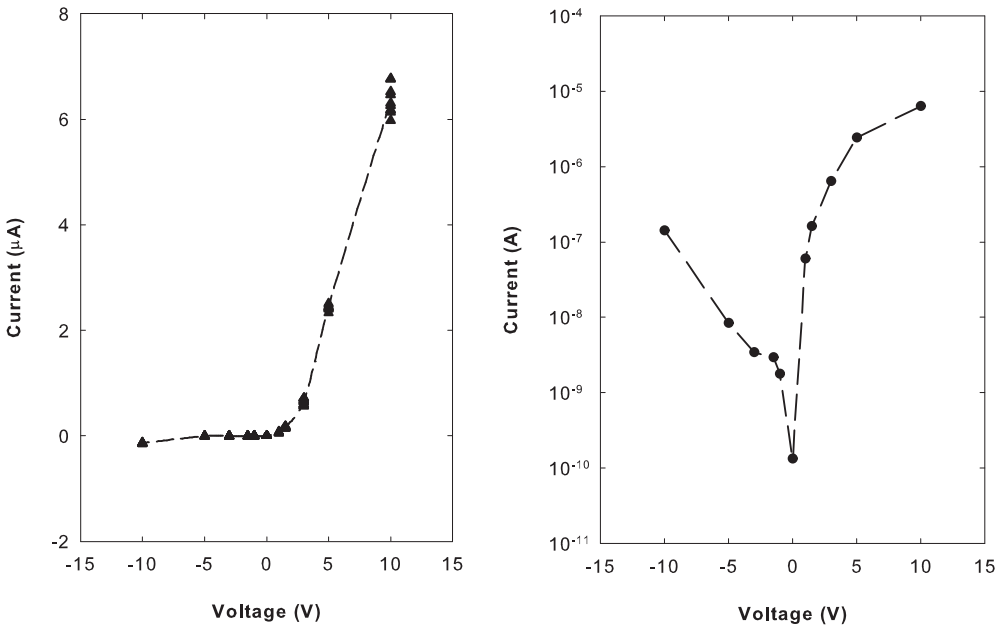

Figure 5.15 I-V measurement taken from the GaN nanowires using the gold coated AFM tip. a) linear scale and b) log scale.

moving the AFM tip to ensure that the tip is on top of a nanowire. Also, it is required that the force is great enough to maintain contact with the nanowire throughout the entire process without breaking the AFM tip or the nanowire. Also, as the metal coating has to be thin to ensure the imaging capabilities are maintained, the metal layer can be easily rubbed off. To remove some of the issues with the AFM, large contacts (circle with a diameter of 0.5 mm) of gold, silver and Ti/Al were deposited using a shadow mask onto a sample of GaN nanowires that were etched in HCl to remove the gallium droplet and expose the flat surface of the nanowire. The resulting I-V from the large contact pads all gave non-linear I-V, even the Ti/Al contacts which may have oxidised due to a lack of a non–oxidising capping layer (e.g. gold) (fig. 5.16). There was no current measured when the probes were directly touched to the PMMA coated GaN. The results are provided in table 5.1, which are similar to thin film diodes reported in the literature [104, 200]. Deb et al. did try to make Schottky diodes using this approach, however the diodes all had linear I-V curves [63]. They assumed the linear I-V was due to the metal forming on the non-polar sides of the nanowires, as the top of their nanowires had a cone shape, which has enhanced conduction [63]. As our GaN nanowires are left with a flat termination surface after HCl etching, we were therefore able to achieve Schottky diodes as the surface we fabricated contacts to was only the c-plane surface of the GaN. The ideality factor for both the gold and silver pads is still significantly high so the tunnelling current remains an issue for nanowire diameters of 100–200 nm [201].

5.3 SUMMARY

Branching GaN nanowires have been analysed using planar contacts, while vertical nanowires were retained on the substrate and analysed using a vertical contact structure. Contacts to the vertical nanowires were all Schottky in nature, with values for the barrier height consistent with those reported for gold and silver Schottky diodes. The GaN branching nanowires produced resistance values similar to CVD GaN nanowires. The three point contact results are limited, however from the results achieved suggest possible further applications for nanowires and maybe looking at the effect that the

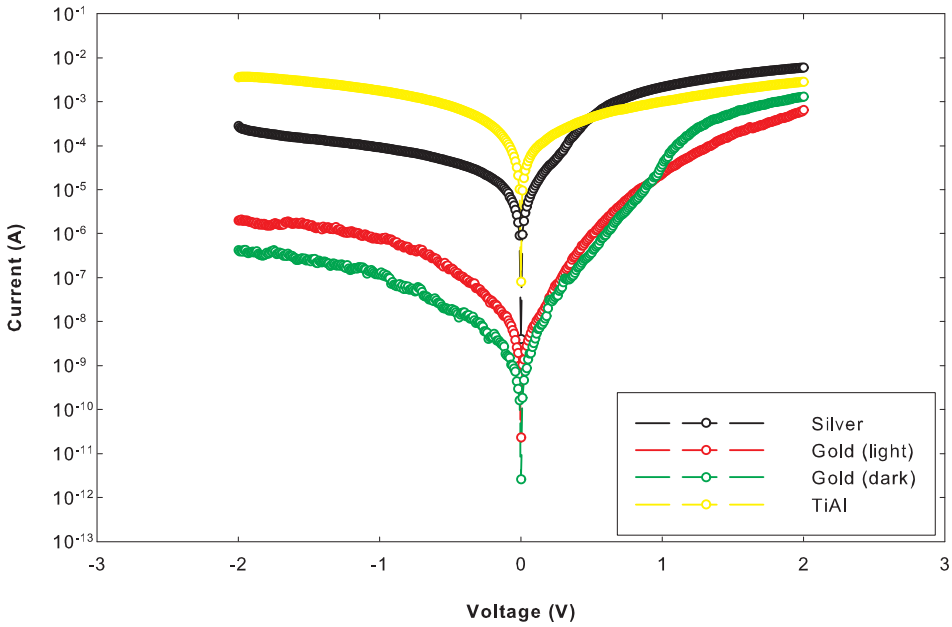

Figure 5.16 Semilog plot of the current - voltage characteristics of GaN nanowires contacted with gold, silver and Ti/Al contact pads respectively, fabricated by evaporating through a shadow mask placed in contact to a sample of GaN nanowires coated in PMMA and etched in HCl.

gating has on a frequency place across the nanowire.

Chapter 6

ACCEPTOR DOPING OF INDIUM NITRIDE

Research into the fundamental properties of InN has increased dramatically since Davydov et al. contended in 2001 that the actual band gap of InN was less than 1 eV, roughly half the conventionally accepted value at the time [9]. With subsequent improvements in growth techniques leading to even higher quality material, the currently accepted value is in the range of 0.6 - 0.7 eV. In the last two years, efforts have shifted from determining fundamental properties of InN, and refocused on the next big issue: how to realise p–type InN. With the growth of p–type InN, fabrication of photovoltaic cells, light emitting diodes and high mobility transistors could realistically be considered. Several obstacles remain at present, however.

For the fabrication of most semiconductor devices it is required that the material can be doped amphoterically – that is both n–type and p–type. To promote the different doping types impurities are typically introduced into the crystal structure. In the case of n–type doping an impurity that acts as an electron donor – in other words allows for excess electrons to be given up – needs to be introduced. For p–type doping an dopant that readily accepts electrons and introduces holes is required: this type of impurity is known as an acceptor. Effective donor impurities appear on the energy band diagram just below the conduction band, while useful acceptor impurities lie just above the valance band, as shown in fig. 6.1. The difference between the edge of the conduction band and that of the donor impurity band is the amount of energy that is required to ionise the donors; for the cases where the difference is less than 26 meV, which is the amount of thermal energy available at 300 K, essentially all donor atoms will be ionised. The same is true for the ionisation of the acceptor impurities. There are

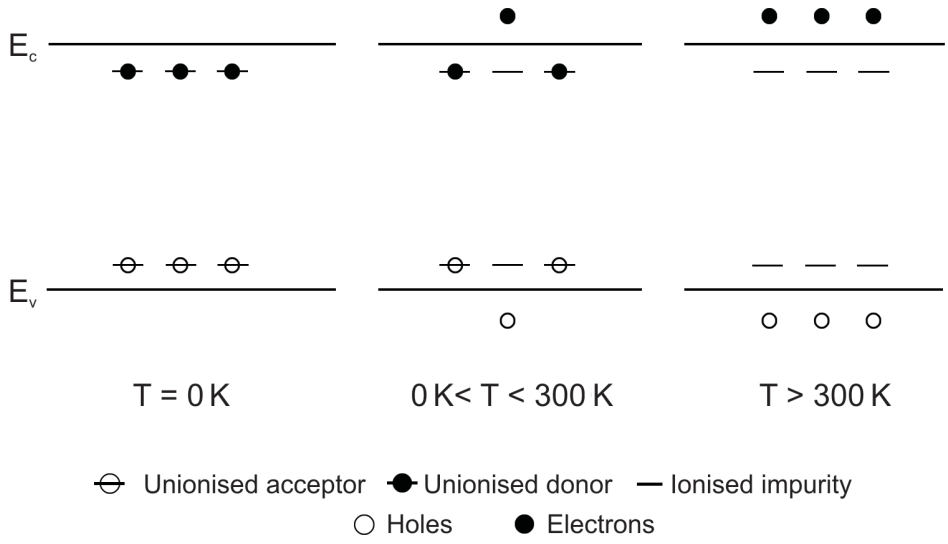

Figure 6.1 Band diagrams illustrating the ionisation of donors and acceptors with increasing temperature.

therefore two types of dopants: those that form shallow levels and those that form deep levels. Shallow impurities are used to enhance the conduction, and are characterised by a small energy difference between the appropriate band edge and the impurity level. Deep impurities are usually used to make semi-insulating material, and lie several k_BT from the respective band edge.

In the case of InN, GaN, and their alloys the cations are in the group III column of the periodic table, while nitrogen is a group V element (fig. 6.2). Among the possible donor atoms are those in group IV, as they have one additional electron compared to the group III atoms. Possible acceptors for III-nitrides include group II elements, which have one less electron than the group III atoms. For Mg (acceptor), a commonly used p-type dopant, calculations of the formation energies have shown that the Ga site is the preferred site for the dopant compared to the N antisite which has a higher formation energy [203]. Silicon (donor) atoms can also act as an acceptor if the nitrogen atoms are replaced, however Si_{Ga} is a very energetically stable configuration while the nitrogen substitutional site and the interstitial configurations are energetically unfavourable [204]. This can be understood by noting that silicon has an atomic radius very similar

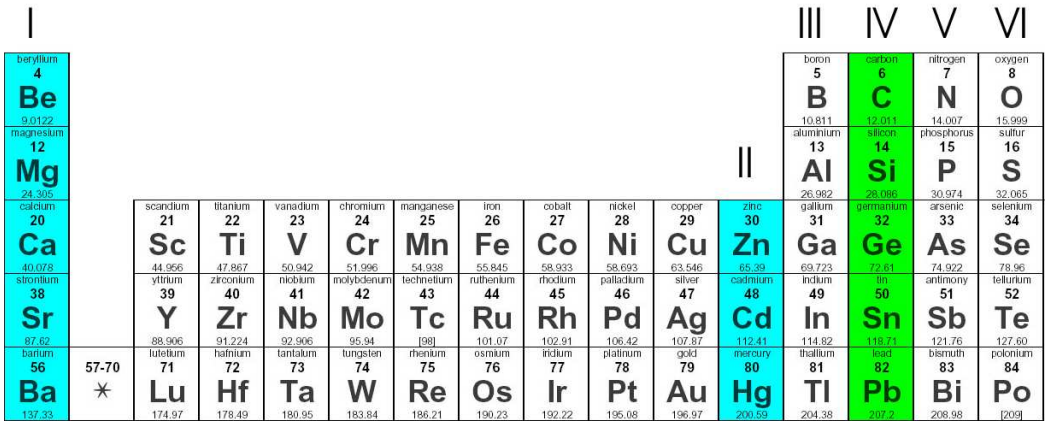

Figure 6.2 Abbreviated periodic table highlighting possible acceptor (blue) and donor (red) dopants for III-nitride semiconductors.

to gallium. Thus, it will easily fit on a Ga site, and cause a large strain if it replaces a small N atom or goes onto an interstitial site.

Impurities are incorporated into the lattice in three possible ways: (1) Substitution, where the impurity atoms replaces one of the host lattice atoms (fig. 6.3a); (2) Interstitially, where the dopant sits in between crystal lattice sites (fig. 6.3b); and (3) Complex doping, when both an acceptor and donor are introduced. In the case of GaN:Mg grown by MOCVD, decomposition of NH_3 to produce the active nitrogen also yields hydrogen. This leads to a MgH_2 complex that inhibits p–type conductivity; it is not until the GaN:Mg is annealed to remove the hydrogen that p–type GaN is achieved [28]. Although complex doping can in some instances be done intentionally, it is worth noting that the low decomposition temperature of InN prevents annealing. This also means alternative doping techniques such as diffusion and ion implantation are not feasible for this material.

When a semiconductor is completely compensated with native defects the Fermi level lies at the Fermi stabilisation level (F_{sl}), which for InN is 4.9 eV below the vacuum level [205]. The F_{sl} is independent of the doping level and therefore considered an intrinsic property of the material [205]. For a material that is not completely compensated by native defects the Fermi level can reside above or below F_{sl}. When the Fermi level is above F_{sl} the defects that form are acceptor-like; when the Fermi

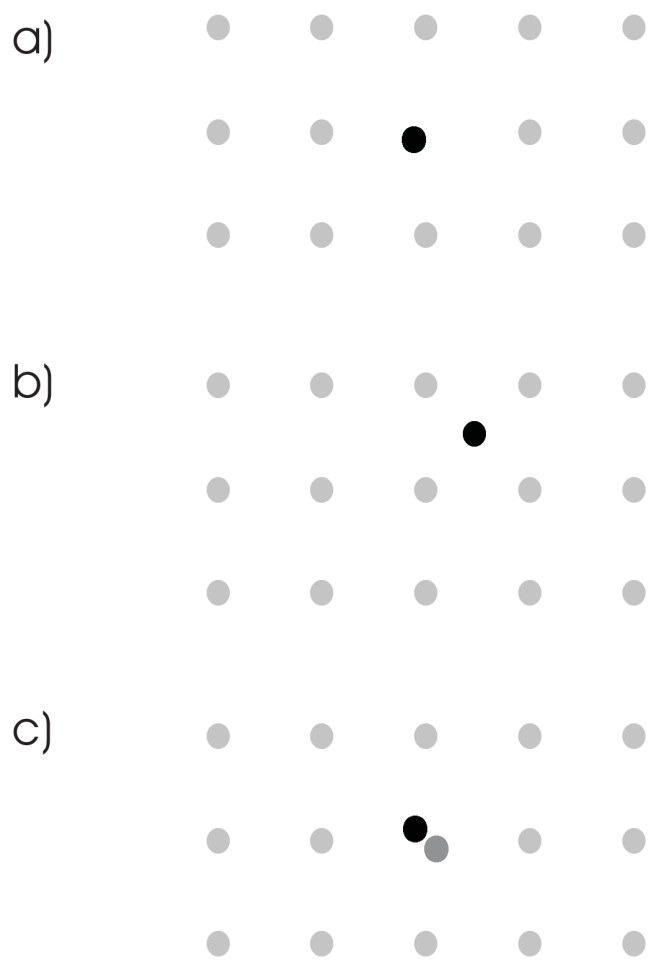

Figure 6.3 Dopant incorporation into the crystal lattice: a) substitution; b) interstitial; and c) complex.

level is below F_{sl} the defects that form are donor-like. The result is that the Fermi level moves towards F_{sl} [205]. At the F_{sl} energy level, donor and acceptor defects are equally generated resulting in no change to the Fermi level. For GaN the F_{sl} sits within the band gap, although slightly closer to the conduction band so it is expected that it is easier to dope n-type than p-type. However, for InN the surface Fermi level is typically 1.6 eV above the valence band and 0.9 eV above the conduction band, therefore at least p-type doping of the surface layer will be hindered [206].

The surface accumulation layer was initially suggested to be from oxygen, or hydrogen, which are often seen in SIMS analysis of InN films [140]. However, SIMS results have shown that the O and H concentrations are often too low to explain the electron concentration [207]. The surface accumulation has also been linked to F_{sl}, where the Fermi energy of the surface is pinned at F_{sl} due to the formation of point defects at the surface [155]. Mahboob et al. determined the surface accumulation layer is due to the presence of positively charged donor–type surface states using high-resolution electron-energy-loss spectroscopy (HREELS) [96]. As of yet there has been no reported way of significantly reducing the effect of the surface accumulation layer.

6.1 MAGNESIUM DOPING THEORY

Successful p-type doping of GaN with Mg suggests that is worth considering for InN as well. For PAMBE growth of GaN:Mg, annealing is not required as the nitrogen plasma source does not produce substantial hydrogen. This is ideal for InN as it suffers from low thermal stability and so annealing is not feasible.

A number of groups have already reported the growth of InN:Mg, several of which precede the band gap controversy. Blant et al. considered how magnesium incorporated into the lattice using x-ray absorption fine structure spectroscopy (EXAFS), a process for determining the bonding of solids by analysing oscillations in the x-ray absorption caused by interference [208]. They showed that the magnesium was mainly being incorporated on the indium sub-lattice sites, and interstitially within the InN crystal lattice. Unsurprisingly, given that the existence of the surface accumulation layer

was not yet known, their electrical measurements showed n-type conductivity with mobilities an order of magnitude lower than that of an undoped InN film [208]. The reason for the electrical properties were incorrectly attributed to reduced crystal quality . The only other InN:Mg paper from this era was by Mamutin et al., who studied heavily doped InN:Mg films. They reported an improvement in the crystal quality for magnesium concentrations between $10^{19} - 3 \times 10^{20}\, cm^{-3}$, which they related to a surfactant effect. However, above this range the quality of the films deteriorated [209]. As in the case of Blant et al., n–type conductivity was observed; no other methods aside from single magnetic field Hall effect were used to measure the electrical properties. There was no mention of the optical properties by either group.

In 2006, two reports of p-type doping in InN:Mg were published. Jones et al. used electrochemical capacitance-voltage to show that under the n–type accumulation layer a p–type bulk layer could be detected [210]. They did not observe photoluminescence from the as-grown films, although bombardment with 2 MeV He^+ particles to induce ion damage resulted in (barely) detectable photoluminescence, for a dosage above $4.5 \times 10^{14}\, cm^{-2}$. Anderson et al. (University of Canterbury) were the first group to report photoluminescence from an as-grown Mg-doped film, with a change in photoluminescence peak position from 0.68 eV to 0.55 eV with magnesium doping [45]. They also reported the same trend in ECV for an InN:Mg film with a buried p-type layer, and went on to observe what was suggested to be a light hole using variable magnetic field Hall effect measurements, as shown in fig. 6.4.

Wang et al. have published several papers on InN:Mg growth and characterisation [48, 211, 212]. They have observed polarity flipping from In–polar to N–polar when the Mg content was increased above $10^{19}\, cm^{-3}$; unlike GaN they did not observe a change in the sticking co-efficient for the different polarities [211]. Single magnetic field Hall effect measurements from their sample exhibited a decreasing trend in mobility with a Mg cell temperature exceeding 175°C, while the carrier concentration decreased with Mg cell temperature up to 175°C and then was observed to increase [48]. XRD results did not exhibit a significant change in the FWHM with Mg cell temperature, which suggests a surfactant process is not involved, although no other surface analysis results

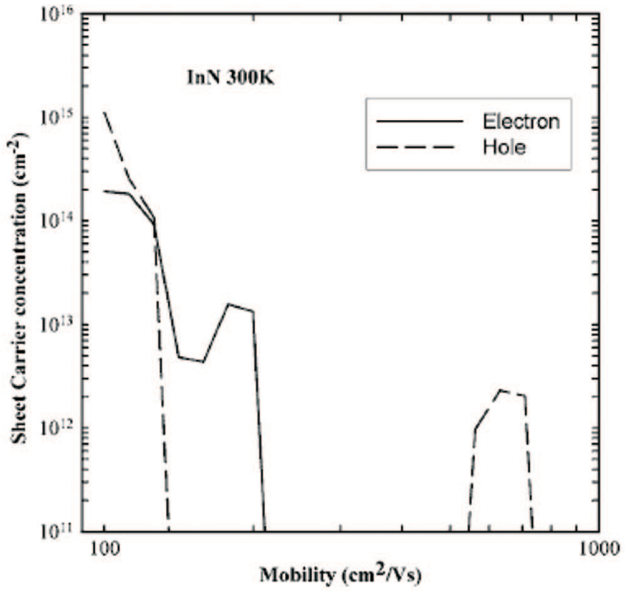

Figure 6.4 Quantitative mobility spectrum analysis (QMSA) of a Mg-doped InN film showing a clear hole feature at approximately $650 cm^2 V^{-1} s^{-1}$. Taken from Anderson et al.[45].

where shown. Examination of the PL showed the intensity decreasing once the Mg cell temperature exceeded 175°C and quenching of the spectrum was observed when the temperature of the Mg cell ranged from 225°C − 250°C and again when it exceeded 325°C. Also, when the Mg cell temperature was at 175°C two distinctive features were exhibited, one at 0.67 eV which was assigned to a band to band transition and the other at 0.611 eV which Wang et al. associated with a free-to-acceptor feature [48]. ECV showed the typical reduction in bias voltage required to achieve the peak in the C^{-2} versus bias voltage with magnesium content, which correlates with the previous reports, however with over doping the p-type behaviour is reduced and the bias voltage increases to represent an undoped film [212]. Using the C_{min} from the ECV measurements they calculated the net acceptor values, however they believe that interface states lead to a larger C_{min} than the true value therefore giving higher values for the net acceptors than theoretically expected. When they took into consideration the interface states, hole mobilities of $17 - 36\, cm^2 V^{-1} s^{-1}$ for hole concentrations of $1.4 - 3.0 \times 10^{18}\, cm^{-3}$ were calculated [213].

Khan et al. has examined photoluminescence from InN:Mg films grown by MOCVD

[214]. All of the films analysed produced PL emission. They observed a 0.82 eV band-to-band feature in undoped material and in heavily doped InN films they observed a peak shift to 0.76 eV which they related to a Mg-related feature. They did observe an improvement in the PL FWHM with Mg flow rate, however with the appearance of the 0.76 eV feature the FWHM increased and continued to do so with increases in Mg flow.

The electron potential in InN as a function of depth dictates the band bending and is related to the charge distribution by the one-dimensional Poisson equation [100]. Using this Yim et al. and Ager et al. have tried to model the ECV data using the Poisson equation [44, 100]. At present their model does not precisely fit the experimental data so reliable values have not yet been produced. Their work, however, indicates that n-type material can be misidentified as p-type, signified by a larger bias required to change the slope of C^{-2} versus V.

So far there is a lack of understanding for why the photoluminescence is quenching and there is still some uncertainty about the incorporation of the Mg into InN, also how the incorporation of Mg is affected by the N–rich growth regime. A series of InN:Mg films with varied Mg content is also required to understand the ECV results so a more complete understanding of the doping concentrations can be obtained.

6.2 MAGNESIUM DOPING

Former doctoral student Dr Phillip Anderson obtained direct evidence of p-type doping using Mg. However, at that stage little was known on the effect of Mg doping and also why the photoluminescence was quenching. To obtain a clearer picture of what happens when InN is doped with Mg a series of InN:Mg films was planned. The films were grown on (111)YSZ substrates for two reasons. First, independent measurements by Prof. Tom Myers (West Virginia University) indicated that even 0.5 μm thick InN films had low carrier concentrations on the order of $2 \times 10^{17}\, cm^{-3}$ in the bulk when grown on these substrates [215]. This was consistent with low threading dislocation densities (10^9 to $10^{10}\ cm^{-2}$) measured by Prof. Phil Ahrenkiel by TEM [215]. Second,

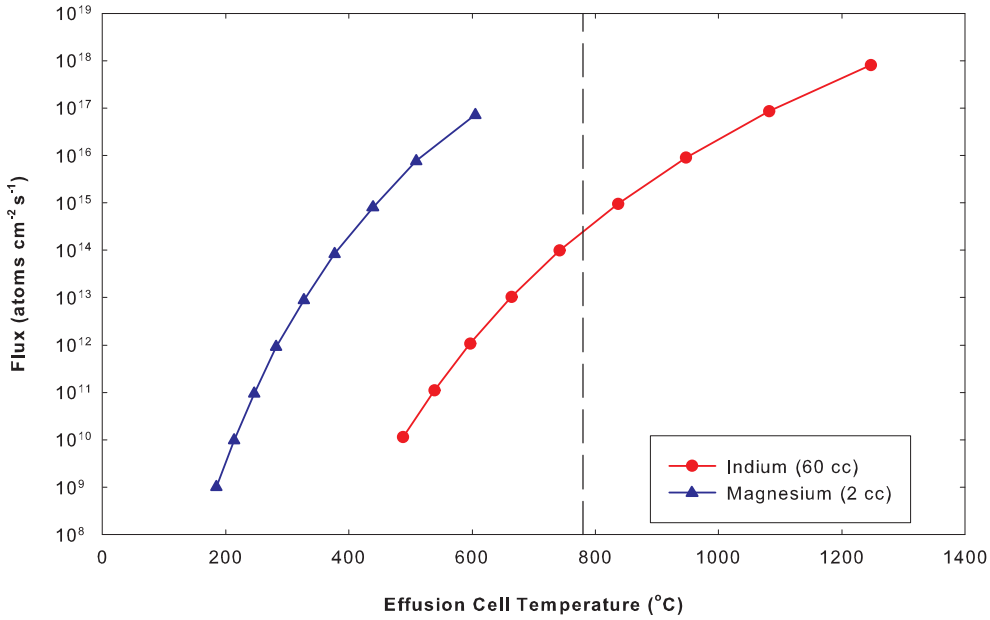

Figure 6.5 Theoretical flux curves for magnesium and indium.

initial etching experiments performed by Dr Anderson suggested that the polarity of InN 'flipped' from N–polar to In–polar at high Mg concentrations. Since previous work demonstrated InN grows as In–polar on (111)YSZ this was thought to prevent polarity issues with Mg doping [216, 215]. This was later found to be incorrect. The Mg flux produced from the effusion cell is too low to be measured using the crystal microbalance. Therefore, the required magnesium cell temperatures were determined from the theoretical flux curve for magnesium, as shown in fig. 6.5, using equation 2.2 with an orifice diameter of 1 cm (2 cc crucible). Based on an experimentally determined indium flux of $3.1 \times 10^{14} atoms\, cm^{-2} s^{-1}$ for the indium cell temperature of 780°C, a range of InN:Mg films were grown with target Mg content between 10^{17} and 10^{21} cm^{-3}.

To be consistent with previously grown InN:Mg/GaN films already studied [45] a set of InN:Mg/(111)YSZ films described in this section (table 6.1) were grown under the same conditions later determined to be N–rich conditions. This included using an indium cell temperature of 780°C, and the same substrate temperature of 450°C was also employed. The plasma source was operated at 150 W and 1×10^{-5} Torr. The films

Table 6.1 Magnesium doped InN films on (111)YSZ. Flux values were calculated, Mg content was measured using SIMS, with that of film 554 estimated by curve fitting the SIMS to the theoretical flux curve.

Film Number	Mg Temp. (°C)	Mg Flux $atoms\,cm^2s^{-1}$	Mg Content (SIMS) (cm^{-3})
579-InN:Mg	170	3.0×10^8	5.2×10^{17}
577-InN:Mg	200	4.1×10^9	1.3×10^{17}
601-InN:Mg	208	7.1×10^9	2.7×10^{17}
585-InN:Mg	216	1.2×10^{10}	6.2×10^{17}
590-InN:Mg	220	1.6×10^{10}	3.7×10^{17}
555-InN:Mg	225	2.2×10^{10}	8.7×10^{17}
594-InN:Mg	230	3.0×10^{10}	1.5×10^{18}
580-InN:Mg	240	5.6×10^{10}	3.3×10^{18}
584-InN:Mg	260	2.4×10^{11}	1.2×10^{19}
583-InN:Mg	276	5.8×10^{11}	3.6×10^{19}
557-InN:Mg	300	2.8×10^{12}	1.0×10^{20}
554-InN:Mg	370	5.8×10^{12}	(9.5×10^{21})

were all grown on as-received (111)YSZ substrates, after cleaning with trichloroethylene/acetone/methanol using an ultrasonic bath. The growth rate of the films was approximately 150 nmhr^{-1}, based on undoped InN films grown under the same conditions for three hours (all films 450 nm thick). Even though the films are presented in order of the Mg cell temperature, the film growths were actually designed depending on their photoluminescence properties to develop a range of films that precisely cover the change in PL peak position as a function of Mg cell temperature.

6.3 STRUCTURAL ANALYSIS

RHEED analysis of the InN:Mg films showed that for the first 3 nm of growth the RHEED pattern stays streaky. However, the streaky RHEED quickly breaks up to a spotty pattern and remains that way until termination. Across the range of InN:Mg samples grown there is for the most part no significant difference in the RHEED patterns between the films. However, films 579, 584 and 554 all have RHEED patterns that exhibit arc features related to polycrystalline growth. Film 594 was the only film to exhibit near streaky RHEED. Imaging of the surface morphology using SEM showed that the majority of the films have a rough surface morphology, consistent with RHEED. However, the morphology of the surfaces are not all similar (fig. 6.6), and

also there is no consistency with the Mg cell temperature. For film 554, grown with the highest Mg cell temperature of 370°C, the film actually broke up into individual nanopillars, likely due to the reduction in the surface migration of the indium adatoms resulting from the high magnesium flux.

6.4 MAGNESIUM CONTENT

The magnesium content of the films was determined using secondary ion mass spectrometry (SIMS), performed by Dr. Richard Morris and Mr. Philip King at the University of Warwick. SIMS is a technique used to analyse the composition of solid surfaces and thin films by sputtering the surface of the specimen with a focused primary ion beam and collecting and analysing ejected secondary ions to determine the composition. In order to permit quantitative determination of the Mg content, a standard was fabricated at the University of Warwick using implantation on an undoped specimen. The Mg results are shown in fig. 6.7 and listed in table 6.1. The incorporation of Mg seems to follow the theoretical Mg flux curve (shown as a dashed line in the fig. 6.7) as would be expected for low temperature growth; also, due to the N–rich growth, excess nitrogen should lead to nearly complete incorporation of the indium and magnesium adatoms. For InN:Mg growth under In-rich conditions a semi-logarithmic plot of Mg content versus $1000/T_{Mg}$ has a linear characteristic, suggesting complete sticking of the magnesium under even In-rich conditions [48], essentially identical to what is observed in the present experiments (fig. 6.7 inset). It also should be noted that the Mg content was constant with depth through all of the InN:Mg films.

6.5 POLARITY

In GaN, when the magnesium flux is high enough to produce a complete layer of magnesium, the GaN polarity is switched from Ga-polar to N-polar. Polarity flipping is more pronounced with N-rich growth of GaN:Mg, compared to Ga–rich growth where a complete gallium wetting layer is formed, which can suppress the polarity from flipping [217]. The different polarities of GaN can lead to a change in the incorporation of

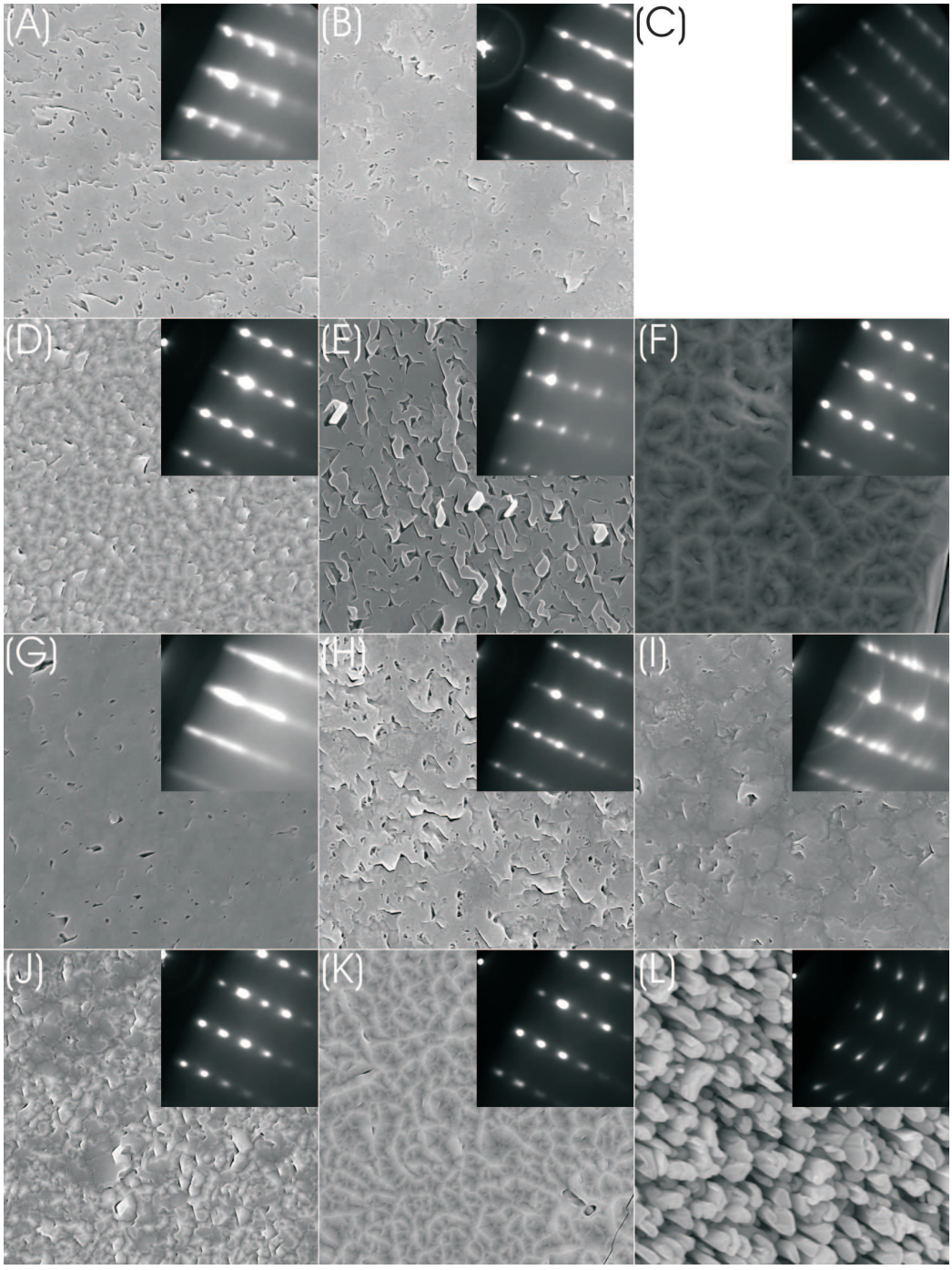

Figure 6.6 SEM images from the InN:Mg films; inset are the corresponding RHEED images at end of growth. Film numbers a) 579; b) 577; c) 601; d) 585; e) 590; f) 555; g) 594; h) 580; i) 584; j) 583; k) 557; and l) 554.

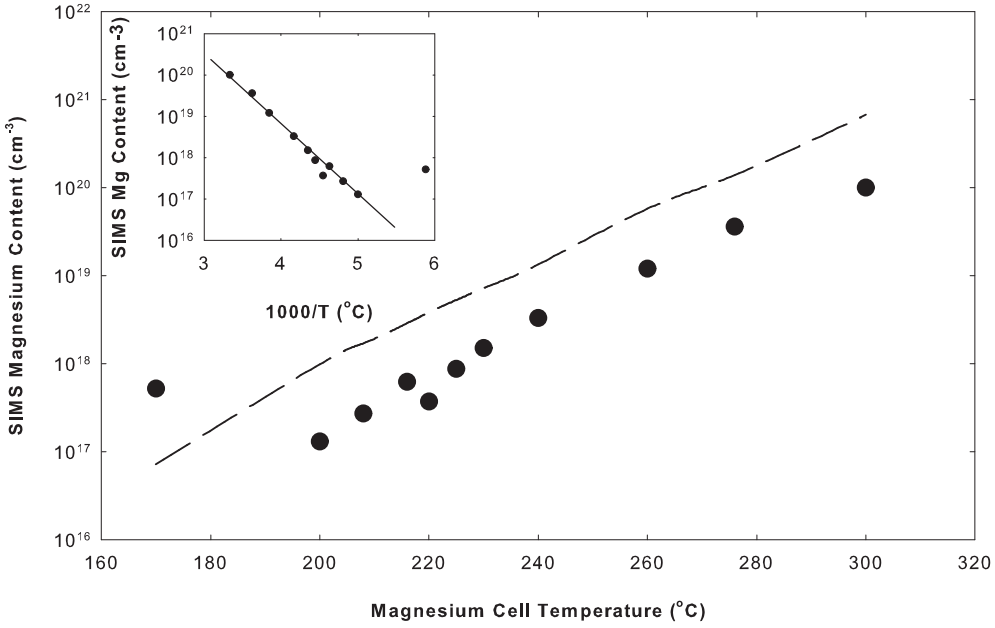

Figure 6.7 Magnesium incorporation into InN, grown under N–rich conditions, based on SIMS analysis. The dashed line is the expected Mg content from the theoretical flux curve for magnesium. Inset: plotted as a function of T^{-1} with a linear regression shown.

magnesium, as magnesium is more readily incorporated into Ga-polar GaN than N-polar GaN [103]. Therefore a switch in polarity would mean that more magnesium would be required to get the same amount of magnesium incorporated into an N-polar film than Ga-polar (In–polar) film, which could explain the step at a Mg cell temperature of 220°C in the SIMS data.

Wet etching of InN using a 10 Ml KOH solution is one method of determining film polarity. In-polar samples typically result in a uniformly etched surface with hexagonal etch pits while N-polar samples etch roughly and reveal hexagonal pyramids [218]. The determination of the polarity by wet etching is based on the judgement of the person doing the analysis and can often be hard to decide. From the wet etching of the InN:Mg films we observed a random switching of polarity with Mg cell temperature as presented in table 6.2. To try and clarify the polarity, valence band x-ray photoemission spectroscopy (XPS) was used as well. Shown in fig. 6.8 are the valance band spectra; the two features of interest are the peaks at 3 eV and 6.5 eV, which are offset in fig. 6.8 by 1 eV [139]. The relative dominance of the peaks is used to determine the polarity;

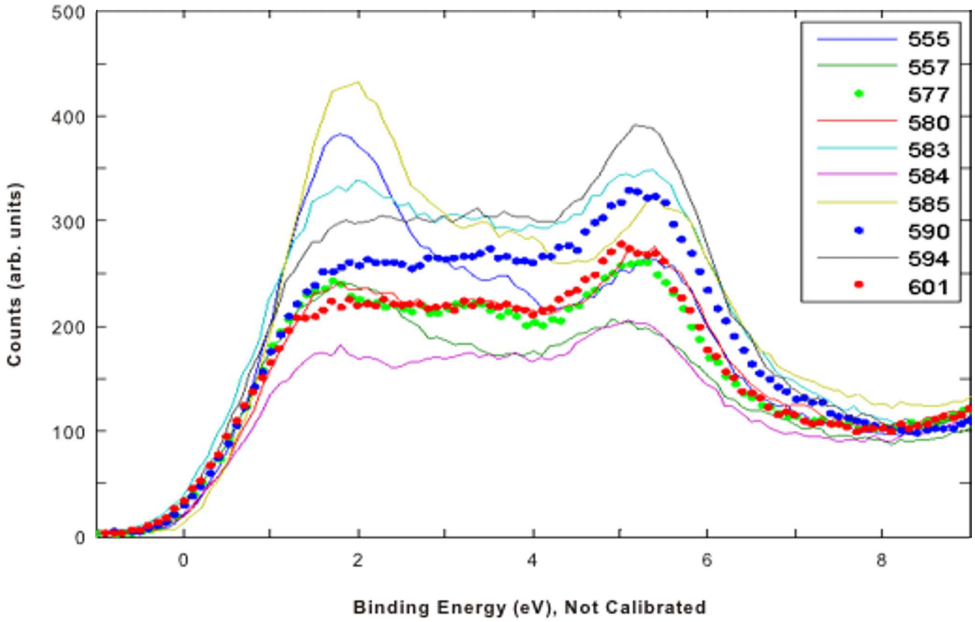

Figure 6.8 Valence band XPS spectra from the InN:Mg films.

a dominant 3 eV feature suggests an In–polar film while the 6.5 eV feature is related to an N-polar film. The existence of mixed polarity results in features with similar intensity. Using this reasoning the polarity of the InN:Mg films was determined and given in table 6.2. It should be noted that only the films that had mixed polarity were indeterminant by KOH etching, which is a human error based on judgement of the surface morphology. In this study we did not observe a clear transition from In-polar to N-polar with increased Mg content. InN polarity flipping has been observed for In-rich growth of InN:Mg by Wang et al. [211]. For GaN the Ga–adlayer can affect the polarity flipping and even suppress the polarity from flipping [217]. As we had grown under N–rich conditions we might be seeing more severe polarity flipping, or it occurs over a large range of Mg cell temperatures due to the lack of/or thinner In–adlayer under N–rich growth conditions.

6.6 ELECTRICAL TRENDS

As described earlier, traditional Hall effect measurements are unable to quantify or in any way separate the individual contribution of an inhomogeneous sample. By single

Table 6.2 Magnesium doped InN films on (111)YSZ and analysed using valence band XPS and KOH etching to determine the film polarity. Samples marked with "—" were samples that were not studied due to the lack of a suitable piece of the film.

Film Number	Mg Temp. (°C)	Mg Content SIMS (cm^{-3})	Polarity (XPS)	Polarity (KOH)
579-InN:Mg	170	5.2×10^{17}	—	—
577-InN:Mg	200	1.3×10^{17}	mixed	N-polar
601-InN:Mg	208	2.7×10^{17}	N-polar	—
585-InN:Mg	216	6.2×10^{17}	In-polar	In-polar
590-InN:Mg	220	3.7×10^{17}	N-polar	N-polar
555-InN:Mg	225	8.7×10^{17}	In-polar	In-polar
594-InN:Mg	230	1.5×10^{18}	N-polar	N-polar
580-InN:Mg	240	3.3×10^{18}	—	N-polar
584-InN:Mg	260	1.2×10^{19}	mixed	—
583-InN:Mg	276	3.6×10^{19}	mixed	N-polar
557-InN:Mg	300	1.0×10^{20}	mixed	In-polar
554-InN:Mg	370	(9.5×10^{21})	—	—

magnetic field Hall effect, the "apparent" carrier concentration of the films is scattered in the range of $n = 2 \times 10^{19}\,cm^{-3}$ to $5 \times 10^{18}\,cm^{-3}$ (fig. 6.9a). As the films were all grown to a thickness of 450 nm, this indicates the "apparent" carrier concentration is dominated by layers other than the bulk. It is worth noting that the "effective" volume concentration of the surface accumulation layer is approximately $5 \times 10^{13}\,cm^{-2}/5\,nm = 2 \times 10^{20}\,cm^{-3}$. The increase in the carrier concentration is a possible trade off from the incorporation of the Mg that can compensate the n-type conductivity while also introducing additional defects, through strain and lattice imperfections, that result in increased n-type conductivity. From the In–rich growths by Wang et al. they observed quite a clear trend, with an improvement in the carrier concentration up to a Mg cell temperature of 175°C peaking at $10^{18}\,cm^{-3}$ then a increase by an order of magnitude. They inferred the increase in the carrier concentration is due to the introduction of additional donors with high Mg cell temperatures [48].

In contrast electron mobilities determined from the single magnetic field Hall measurements do seem to follow a trend – decreasing for Mg cell temperatures above 220°C, as shown in fig. 6.9b. There are some outlying points around a magnesium cell temperature of $(216 - 225°C)$, which also relates to the area of uncertainty in the SIMS results. For the Mg cell temperature up to 216°C the Mg concentration is possibly

too low to affect the crystal structure and if the rapid increase in mobility is real this may be the required concentration of magnesium to act as a surfactant. The decrease in the mobility with magnesium cell temperature from 225°C could also be related to increased roughening of the surface. The films with mobilities below $60\,cm^2V^{-1}s^{-1}$ are either heavily pitted with cracks, or have columnar growth; for films with mobilities above $60\,cm^2V^{-1}s^{-1}$ their surface morphology are all similar with relatively smooth surfaces and the usual pitting occurring. The scatter in the mobility may also be due at least in part to the instability in polarity. Compared to the In-rich growths done by Wang et al. our electron mobilities are significantly lower (at least a factor of 5) due to the poor crystal quality, though the overall trend observed in our study is duplicated by theirs [48].

6.7 ECV ANALYSIS

Given the lack of useful information available from any Hall effect measurements, the best alternative is ECV [45, 210, 212]. Unlike measurements on metal-semiconductor Schottky diodes ECV offers limited information about the doping concentration, as the effect of the bias voltage, frequency and electrolyte solution concentration can affect the results [97]. However, a change in the slope of C^{-2} versus V is commonly regarded as a change in the type of majority carrier. Still, recent papers on modelling ECV results using the Poisson equation, suggest that this is by itself possibly misleading [44, 100]. The ECV process is limited by the stability of the electrolyte, in that a high bias voltage leads to the breakdown of the barrier. Increasing the reverse bias voltage leads to a flattening of the surface energy levels and depletion of the surface accumulation layer. By further increasing the reverse bias the bands can bend upwards at the surface and an "inversion" layer of holes is conceivable [100]. A signature of this occurrence would theoretically be a change in sign of dC^{-2}/dV at larger biases, seen in some undoped InN films [100].

For the InN:Mg/YSZ(111) films the ECV results are shown in fig. 6.10. Unknown at the time, the LabView program was using an ac voltage of 1 V which means the size of the depletion region was quite significant as the bias scans were only done

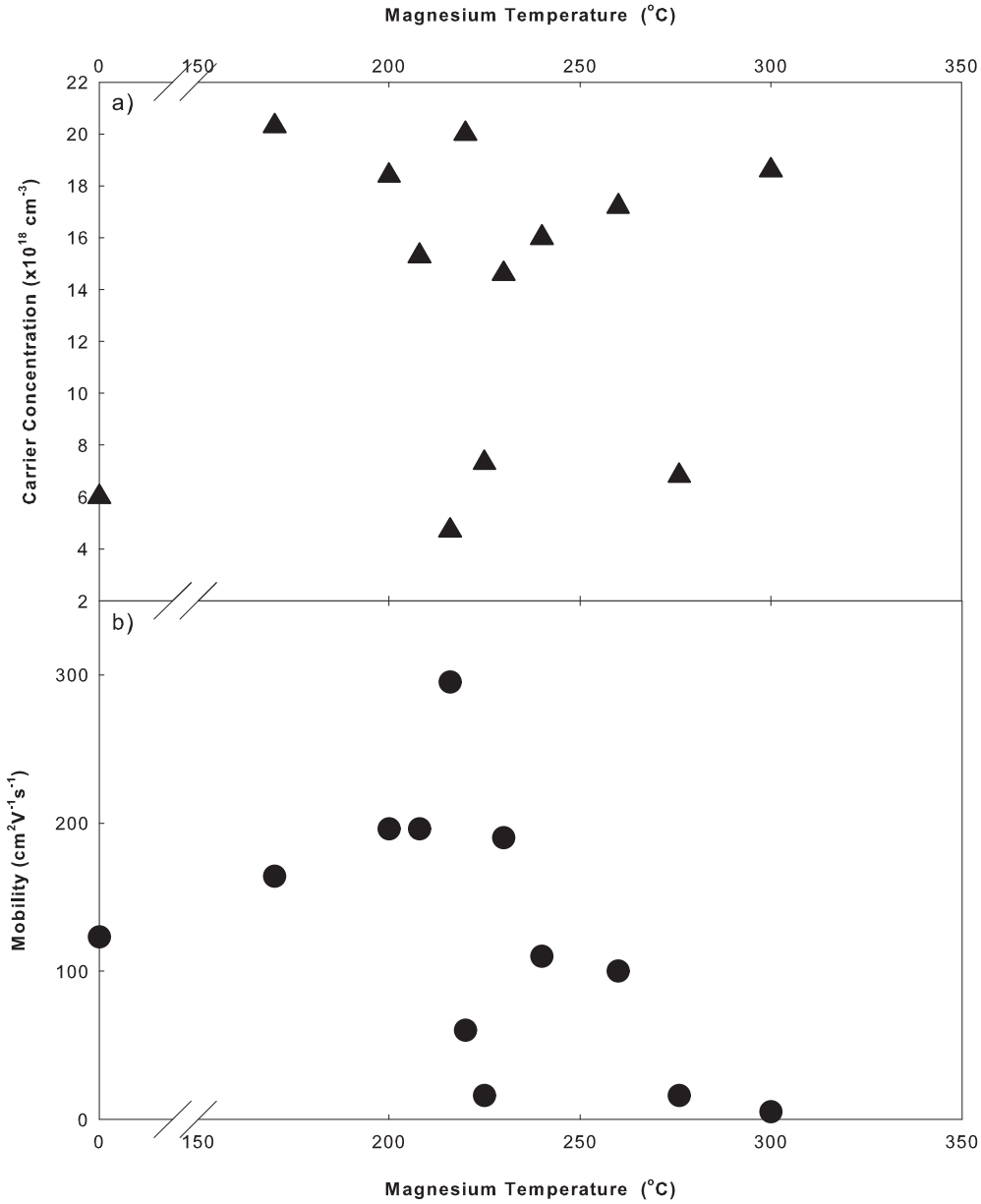

Figure 6.9 Room temperature electrical properties from the InN:Mg films from single magnetic field Hall effect, as a function of Mg flux. a) electron concentration; b) electron mobility. The control film is 267-InN-YSZ(111) which was grown with an In cell temperature of 780°C, plasma settings of 150 W and $1 \times 10^{-5}\,Torr$, and substrate temperature of 400°C which is 50°C lower than the InN:Mg films grown in this series.

from 0.7 to 1.5 V. The undoped InN sample has an increasing slope with a negative bias, representing n–type conduction. With increasing magnesium content the gradient becomes saturated and this is related to the compensation of the n–type conductivity with p–type conduction. It is not until the magnesium cell temperature is increased to 300°C that the ECV graph exhibits a shape that has been typically associated with an InN:Mg with a buried p–type conduction. High Mg cell temperatures produce films with columnar growth and ECV measurements were unable to be obtained. The p–type conduction occurs for a Mg concentration of $1 \times 10^{20} cm^{-3}$, which is lower than our past work on InN:Mg/GaN films where the bending of the ECV was observed at a Mg concentration of $1 \times 10^{21} cm^{-3}$ [45]. This is likely due to the lower bulk carrier concentrations observed using (111)YSZ substrates [215]. These values are still significantly higher than the values reported by Wang et al. [212], although this may be due to still higher residual n–type conduction in our films due to the poor quality of the InN:Mg films grown under N–rich conditions.

6.8 OPTICAL MEASUREMENTS

In the earliest studies of the optical properties of undoped InN, photoluminescence was unable to be observed, due at least in part to the very high electron concentration ($10^{20} - 10^{21}\, cm^{-3}$) [29]. With the improvement of crystal growth leading to electron concentrations of $10^{19}\, cm^{-3}$ the first infrared luminescence was observed, and then for less heavily doped (but still degenerate) semiconductors with electron concentrations above $10^{18}\, cm^{-3}$ band–to-band photoluminescence was observed [9]. Typically the spectra are structureless due to screening of the Coulomb interaction followed by the disappearance of excitons, and shallow donor and acceptor states. More recently thick n-InN films with carrier concentrations on the order of $10^{17}\, cm^{-3}$ have been grown and additional features in the PL spectrum are observed [219]. Often observed in the PL is the Urbach tail, which relates to the exponential tail of the respective conduction and valence band densities of states due to the formation of localised electrons and holes. From very high quality InN at least three features are observed in the photoluminescence spectrum, in the range of 0.50 eV to 0.67 eV [219]. The feature at 0.60 eV is

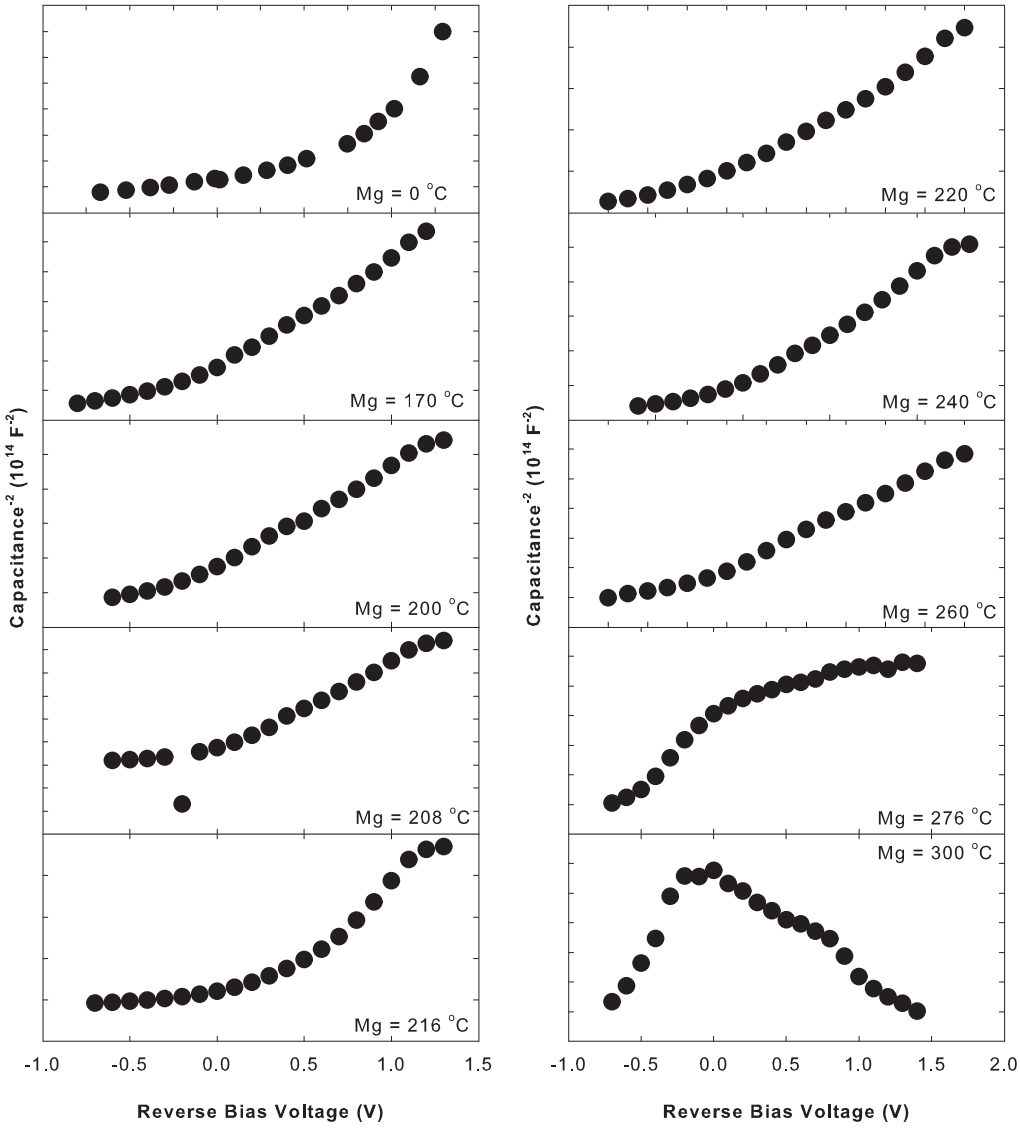

Figure 6.10 ECV results from the InN:Mg/YSZ(111) films, using a KOH solution as the electrolyte.

proposed to be from the recombination of degenerate electrons with holes trapped by deep acceptors with a binding energy of 50 – 55 meV, while the LO–phonon replica of this feature is at 0.55 eV. The higher energy feature at 0.66 eV is a complex made up of two mechanisms. The first is related to a transition of an electron to a shallow acceptor state with a binding energy of 5 - 10 meV and/or to the states of the Urbach tail populated by photoholes. The second mechanism is the band–to–band recombination of free holes and electrons.

Reports on the optical properties of InN:Mg films are limited due to the fact that with increasing Mg content the luminescence from the films becomes quenched. Preceding the process that causes the quenching, the photoluminescence spectra typically exhibit a change in PL peak position, with Khan et al. reporting a peak at 0.82 eV (band to band transition) for undoped and low Mg content, while a peak at 0.76 eV (acceptor-related transition) appears with increasing Mg content [214]. The difference between the two peaks is 60 meV, and temperature dependent PL in the range of 100-300 K (where only the 0.78 eV feature is present) suggested an activation energy of 58 meV, leading then to conclude that the Mg acceptor in InN lies 60 meV above the valence band maximum. This value for the acceptor binding energy has also been supported by Wang et al. who measured 62 meV [48]. Our group has previously reported that the acceptor level for Mg could be on the order of 110 meV above the valance band, based on photoluminescence of low Mg content InN:Mg/GaN films [45], with some uncertainty in the precise value due to a defect in the spectrometer grating used.

In the present study, based on InN:Mg grown on (111)YSZ, the photoluminescence feature for the low Mg content InN films had PL peaks around 0.68 eV, and with increasing Mg content the PL peak position shifted to 0.6–0.61 eV before the signal dropped below the sensitivity limit of the InSb detector (fig. 6.11). Based on the work by Anderson et al. [45], Wang et al. [48] and Khan et al. [214] it could be assumed that the secondary feature is related to Mg, especially since it becomes the dominant feature with increased Mg concentration, and the difference between the two peaks is 70 meV, similar to the suggested binding energy of 60 meV. The PL is summarised in fig. 6.12 based on Mg parameters. The intensity of the PL spectrum, determined by

curve fitting to the peak, in relation to the magnesium content and cell temperature exhibits a decreasing trend with increasing amounts of magnesium, as shown in fig. 6.13.

Compared to the work by Wang et al. a spectrum containing multiple peaks is not observed [48]; instead, the main peak in all the films seems to have a small shoulder feature, which is similar to the PL published by Khan et al. [214]. The carrier concentration for our films are $6to20 \times 10^{18}\, cm^{-3}$ which agrees with Khan et al., while Wang et al. reports an order of magnitude lower carrier concentration ($10^{18}\, cm^{-3}$) for his film that exhibits multiple features. Therefore the lack of definition of the shoulder feature maybe due to our growths being under N–rich conditions leading to the lower crystal quality and high background carrier concentration that is known to limit PL analysis [219]. For the low magnesium content films the shoulder is always at a lower energy than the main PL feature, while the reverse is true for the high magnesium content films. Further analysis of the film 577-InN:Mg/YSZ(111) (Mg content of $1.3 \times 10^{17}\, cm^{-3}$) shows that the dominant peak is at 0.68 eV, while the shoulder feature is at 0.63 eV, determined by multiple peak fitting to the experimental data. The dependence of the two peaks excitation shows that both feature intensities increase with laser power. There is a clear blue shift in peak position of the 0.68 eV peak, which is suggestive of filling of the conduction band. Both PL peaks undergo a red shift with increasing temperature, which can be attributed to thermal expansion of the crystal resulting in band gap shrinkage.

Results of multiple peak curve fitting of the PL versus temperature, across the range of 4 K to 80 K, is shown in fig. 6.14. Initially using the fitting equation [214],

$$I_{emi}\,(T) = \frac{I_o}{\left[1 + C\exp\left(-\frac{E_1}{KT}\right)\right]} \tag{6.1}$$

where E_1 is the activation energy and C represents the magnitude of the quenching process, results in a poor fit (fig. 6.14). If, instead, the fit is modified to include two distinct recombination pathways [220],

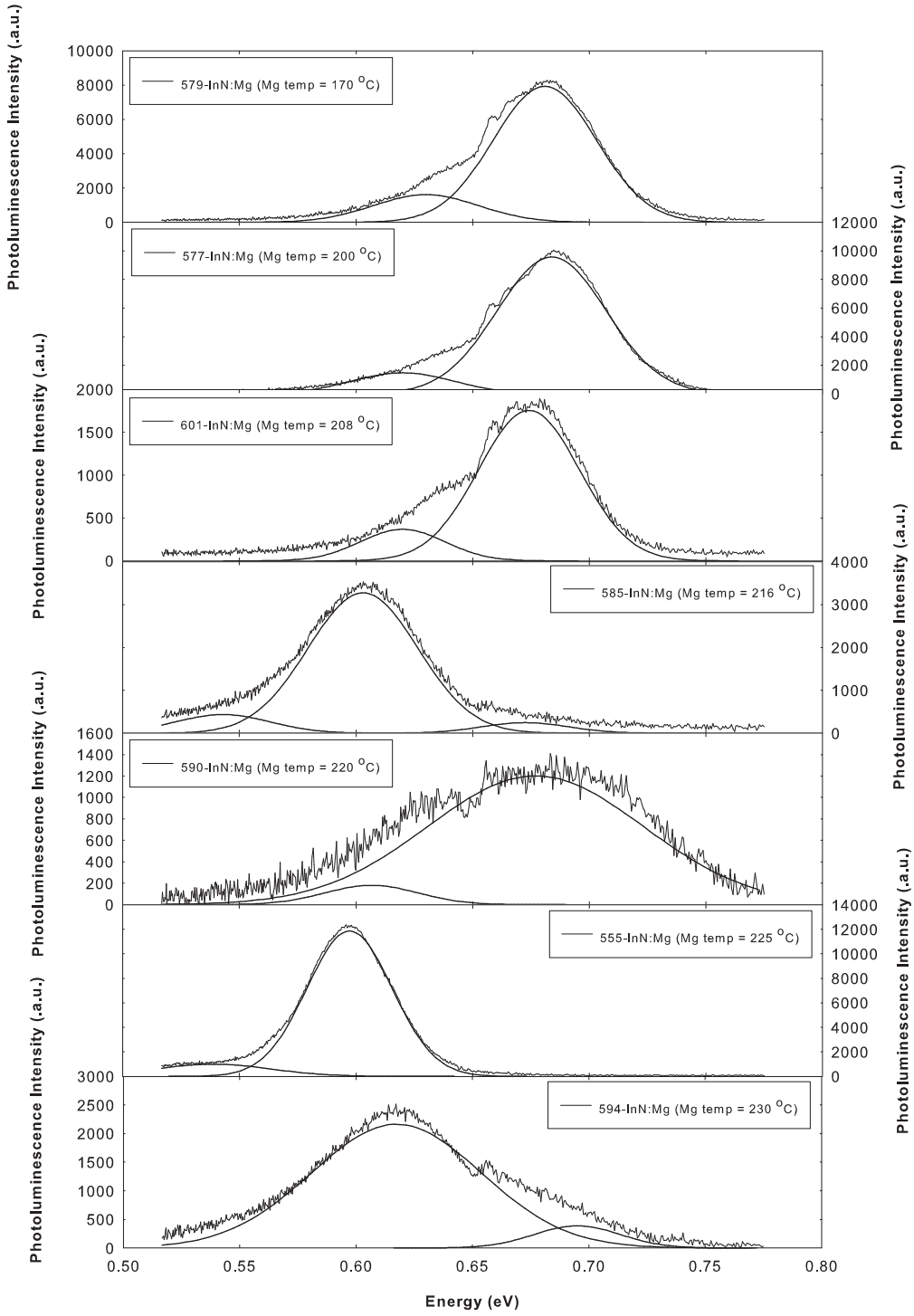

Figure 6.11 4 K Photoluminescence spectra of InN:Mg on (111)YSZ obtained using a 532 nm diode laser and an InSb detector. Also shown are Gaussian fits.

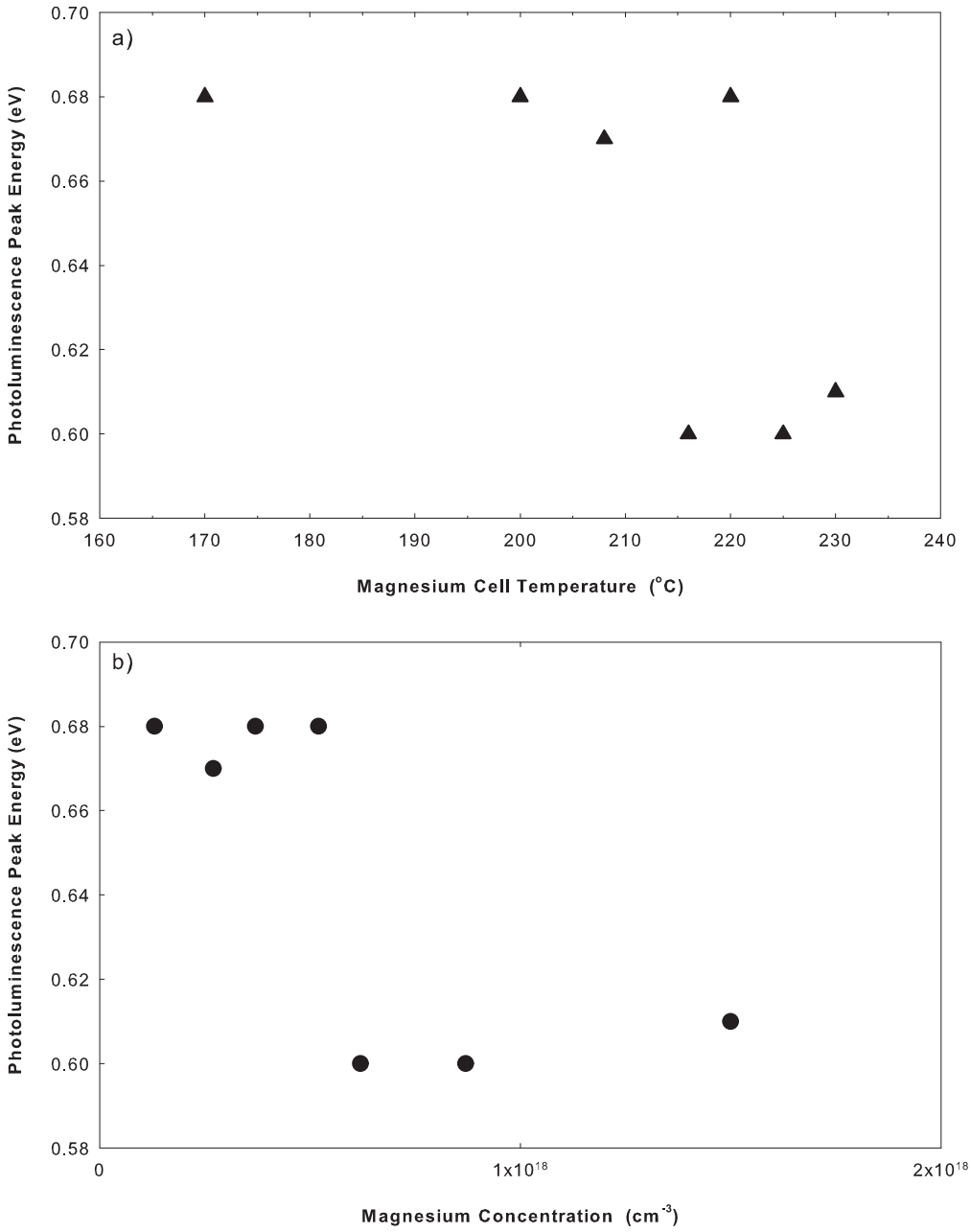

Figure 6.12 Photoluminescence peak position a) as a function of the magnesium cell temperature and b) of the magnesium content determined by SIMS.

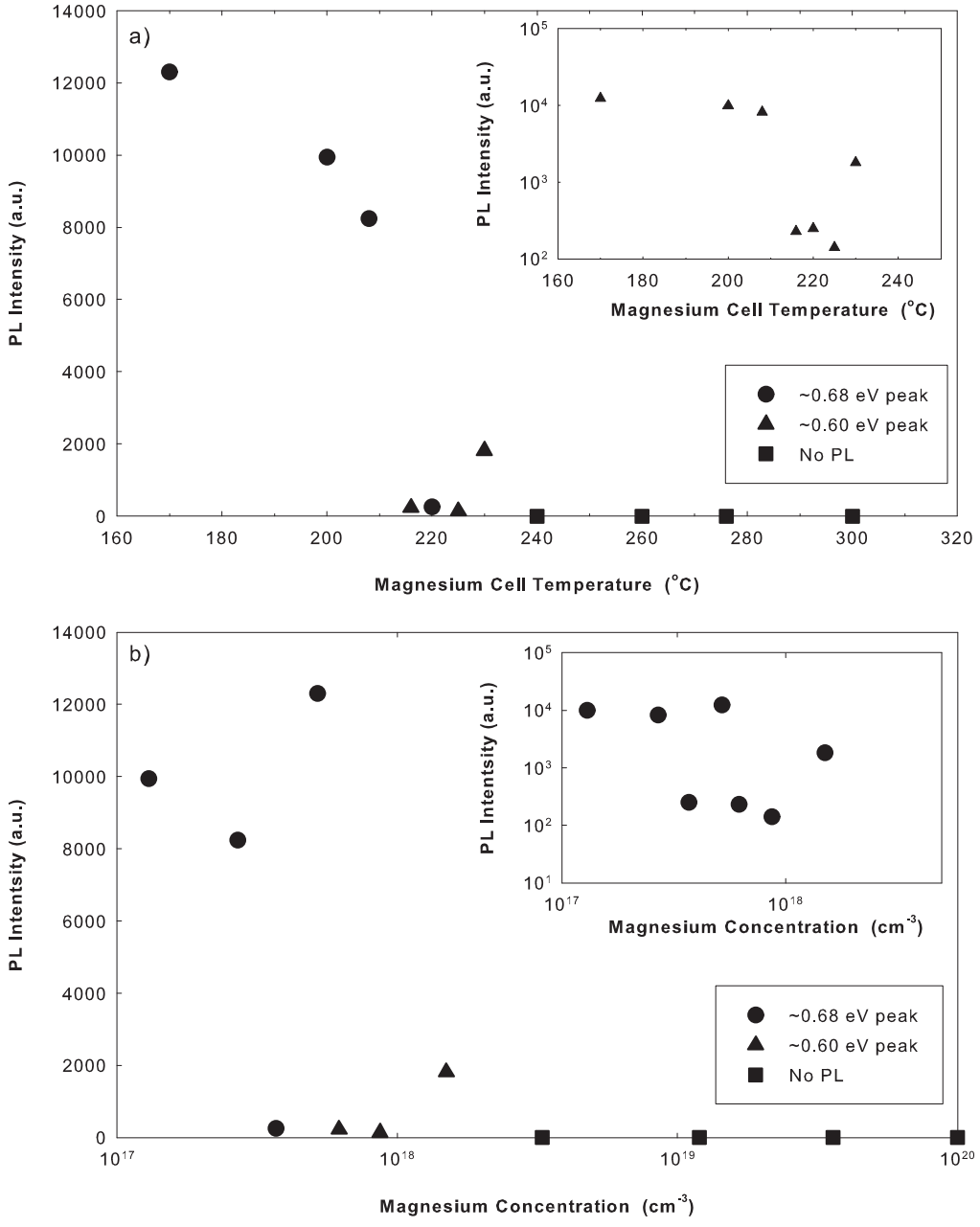

Figure 6.13 Photoluminescence intensity a) as a function of the magnesium cell temperature and b) of the magnesium content determined by SIMS. Insets are the log scale plots.

Table 6.3 Analysis of the temperature dependent photoluminescence of Film 577-InN:Mg/YSZ, using single and double path models.

	I_o	C_1	E_1 (meV)	C_2	E_2 (meV)
Single path, peak A (0.63 eV)	1785	12.7	7.66		
Double path, peak A (0.63 eV)	1895	95.5	20.7	2.85	3.53
Single path, peak B (0.68 eV)	13177	36.3	10.6		
Double path, peak B (0.68 eV)	14433	124	17.7	2.04	2.86

$$I_{emi}(T) = \frac{I_o}{\left[1 + C_1 \exp\left(-\frac{E_1}{KT}\right) + C_2 \exp\left(-\frac{E_2}{KT}\right)\right]} \tag{6.2}$$

where E_1 and E_2 are the activation energies for the two mechanisms and C_1 and C_2 are the quenching mechanisms, a more reasonable fit is achieved (see fig. 6.14). The corresponding fitting parameters are shown in table 6.3. For the single path fit activation energies of 7.66 meV and 10.6 meV were obtained. Even though the values of the peak positions are lower than what Kahn et al. reported the calculated activation energies are very similar: 7.5 meV for their Mg-related feature of 0.76 eV and 10 meV for the peak located at 0.82 eV (band-to-band transition) [214]. Khan et al. suggests that the activation energies can be accounted for by non-radiative recombination channels. Two features have been observed in undoped InN at 0.67 eV and 0.61 eV, which have been attributed to transitions of electrons near the bottom of the conduction band to two acceptor levels, one shallow and the other a deep acceptor [221]. The activation energies of 21 meV and 18 meV from the Arrhenius plots are in agreement with the calculated binding energy for a hydrogen like shallow acceptor [221]. The physical origin of the remaining activation energy ($E_2 = 3.53$ meV and 2.86 meV) is at present unclear.

For film 555-InN:Mg/YSZ(111) (Mg content of $8.7 \times 10^{17}\, cm^{-3}$) the dominant PL peak is at 0.59 eV; a small feature at 0.55 eV appears for only measurements where the laser power is above 80% of the maximum intensity, 24 mW. As with the case for the low Mg film (577-InN:Mg/YSZ(111)) the peak at 0.59 eV undergoes an increase in energy with power (blue shift), possibly due to the band-filling effect. However, a high energy peak at 0.68 eV is also observed when the temperature is raised to 100 K.

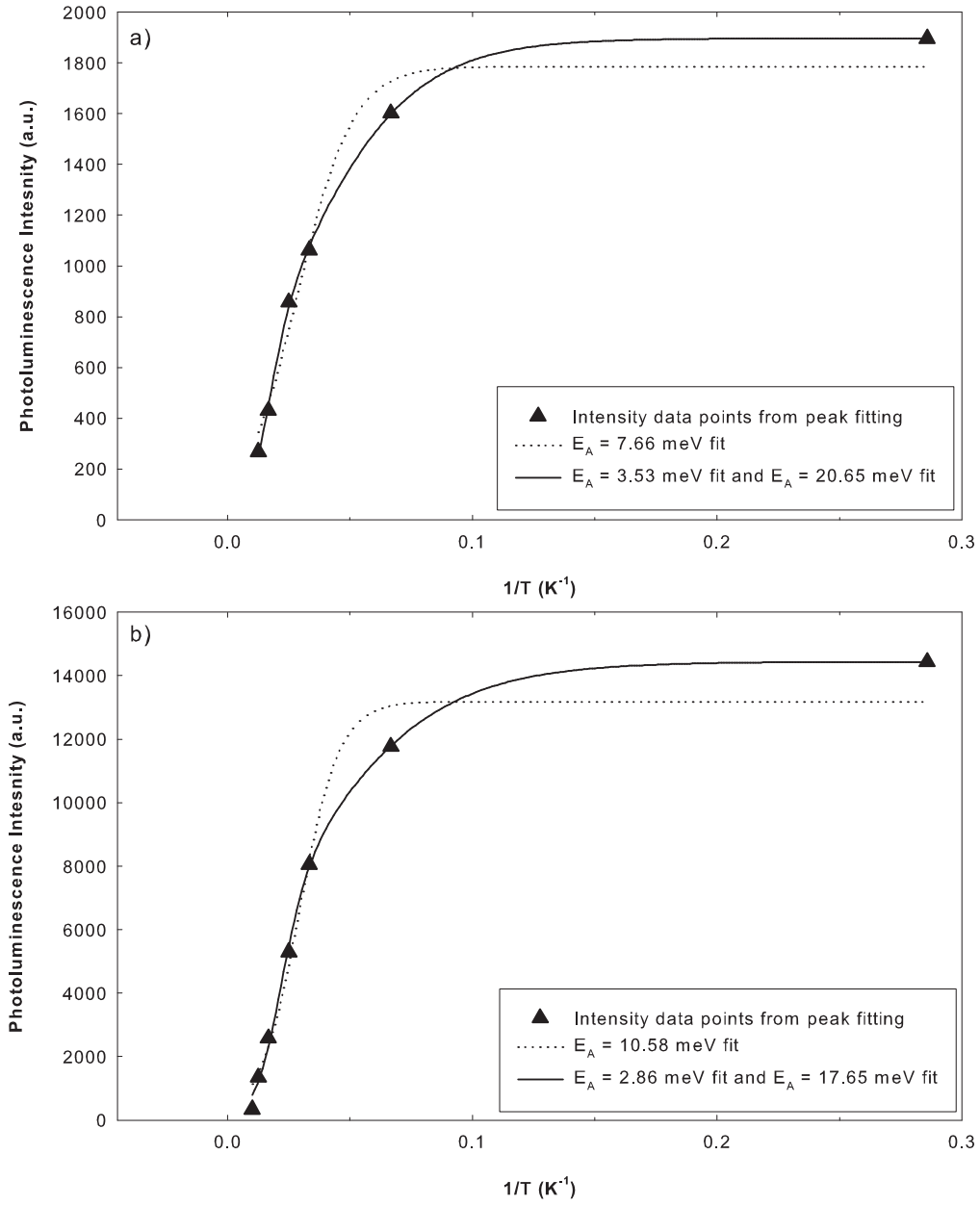

Figure 6.14 Arrhenius plots of the photoluminescence intensity versus temperature for peaks at a) 0.63 eV and b) 0.68 eV from film 577-InN:Mg.

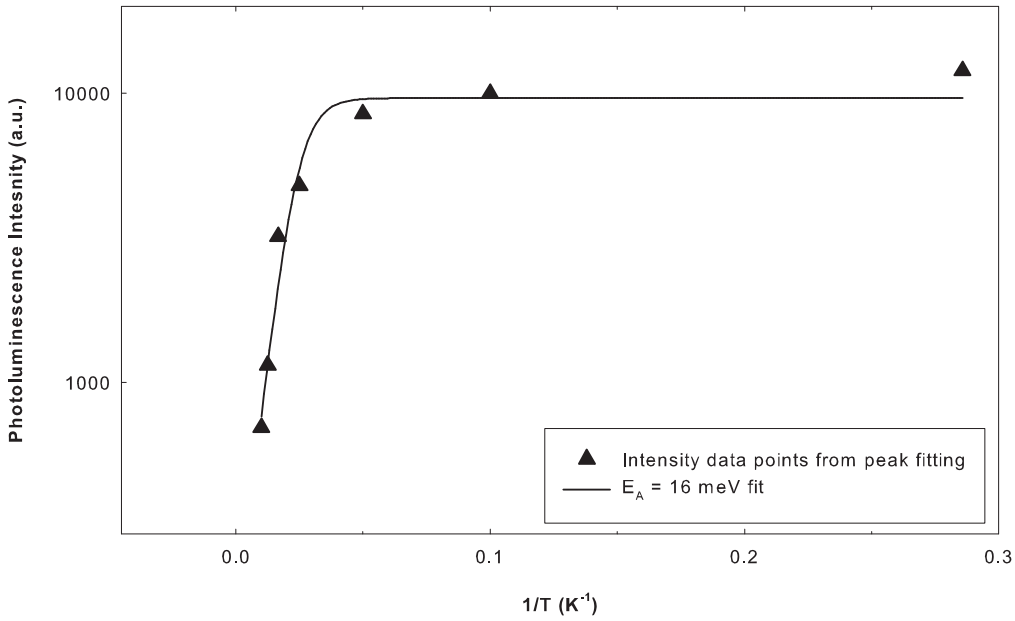

Figure 6.15 Arrhenius plot of the photoluminescence intensity (log scale) for the PL at 0.60 eV versus temperature for film 555-InN:Mg.

Arrhenius plot analysis of the dominant peak versus temperature is shown in fig. 6.15. Using the single pathway model (equation 6.1) results in a good fit, with values for I_o, E_1 and C_1 determined to be 9633, 16 meV and 72, respectively. The activation energy is again consistent with a PL peak associated with the calculated binding energy for a hydrogen like shallow acceptor [221].

The origin of the observed photoluminescence quenching has been the subject of considerable debate [48, 206, 210]. Recent measurements by Mr Bin Qu and Dr. Maurice Cheng in the group of Prof. Alex Cartwright at the University of Buffalo, State University of New York, have indicated the likely explanation is Auger recombination. This is consistent with recent reports of a large Auger recombination coefficient in undoped InN and In-rich InGaN [222, 223]. Fig. 6.16 shows the time dependence of transmission as measured by a pump-probe technique [224]. The non-exponential decay observed for films with high Mg content reveals a strong carrier concentration dependence of the lifetime, a signature of Auger recombination. Undoped and nominally Mg doped samples require a much higher pumping intensity to obtain a similar non-exponential decay behaviour. Fitting of the results, requiring modification of the

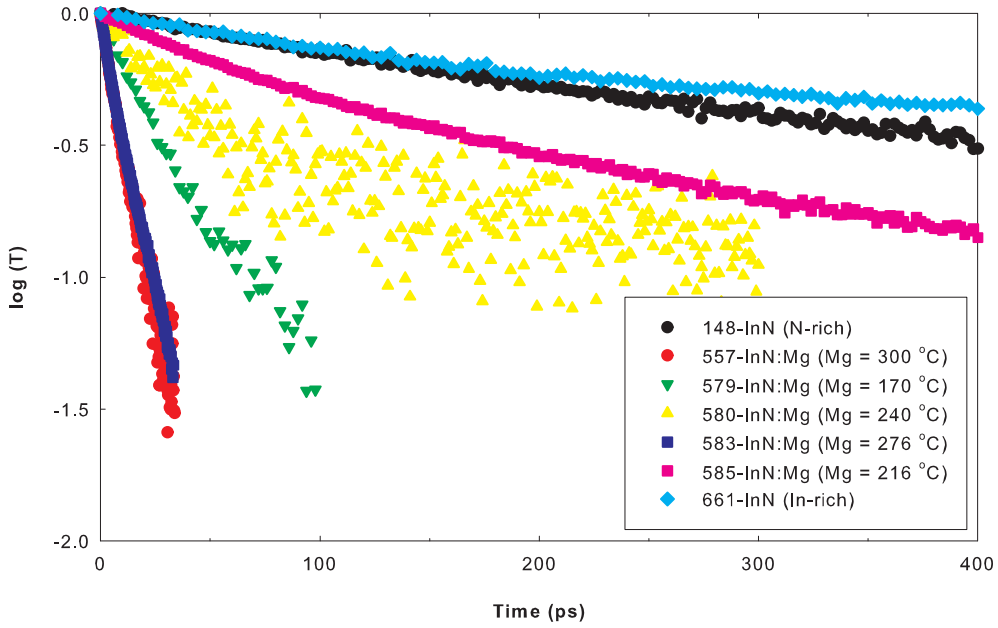

Figure 6.16 Time dependent transmission from the InN:Mg films and also film 148-InN (undoped InN) grown under N-rich conditions, and 661-InN undoped InN grown under In-rich conditions.

standard rate equation to account for the combined effects of degenerate doping and compensation, is ongoing.

6.9 SUMMARY

A series of InN:Mg films was grown on (111)YSZ to elucidate the transition in the PL peak and also where the luminescence is "quenched". The films had a rough surface which is in agreement with the RHEED images and the N–rich growth conditions. We did not see any evidence of a change in surface morphology due to a surfactant effect. The incorporation of Mg seems to be close to unity although at the Mg cell temperature of 216°C there was some scatter, which we associate to polarity instability through KOH etching and valence band XPS. There was no clear transition from In–polar to N–polar; instead, the polarity seems unstable possibly due to the N–rich growth. The electron concentration seems to stay within the range of $10^{19}\,cm^{-3}$ which was expected from the single magnetic field Hall effect measurements. Whereas the electron mobility reduced for a Mg cell temperature above 216°C, that cannot be related to the surface morphology and the ECV does not show the formation of a buried p-type layer until

the Mg cell temperature was above 300°C. It is therefore unlikely that the mobility change is due to the formation of a depletion layer leading to the measuring of only the surface accumulation layer.

From the optical measurements we observed two features in the photoluminescence before the PL intensity is quenched. It should be noted that at present we now believe that the quenching process is related to Auger recombination. The two features were at 0.63 eV and 0.68 eV and temperature dependent photoluminescence of the two PL features suggests that they are due to free electrons in the conduction band and acceptor levels, with one being a shallow acceptor and the other a deep level acceptor.

Chapter 7

ZINC-DOPING OF III-NITRIDES

Often overlooked in the study of InN is the In-containing narrow band gap semiconductor InAs which also suffers from an electron accumulation layer at the surface [225]. Zinc has been successfully used for p-type doping of InAs ($E_A = 16\,meV$) [226], with incorporation typically achieved by diffusion. If for no other reason, zinc is therefore another obvious dopant to try and dope InN p–type.

Zinc has also be used in Ga-V semiconductors, allowing for acceptors in gallium arsenide ($E_A = 25 - 40\,meV$) [227] and gallium phosphide ($E_A = 69\,meV$) [228]. Before p–type GaN was achieved using Mg, research was focused on Zn-doping. However, heavy Zn concentrations rendered GaN films semi-insulating; the films never exhibited p-type conductivity. Despite this, Pankove et al. was able to demonstrate the first GaN:Zn based light emitting diode (LED) in 1971 [229]. This device consisted of an undoped n-type region, a semi–insulating Zn-doped layer and an indium surface contact. Devices emitted blue, green, yellow or red light depending on the Zn concentration in the light emitting region [229]. Doping of GaN with a sufficiently high Zn concentration results in semi–insulating GaN, as Zn compensates the residual donors in GaN [230]. GaN:Zn layers are therefore useful in devices that require high-resistivity buffer layers, and this may also be the case for InN:Zn. Zn doping of GaN introduces four acceptor-like centres, corresponding to broad red (RL), yellow (YL), green (GL), and blue (BL) luminescence bands peaking at 1.8, 2.2, 2.6, and 2.9 eV respectively [231]. The UV PL peaks seen in undoped films are reduced in Zn–doped GaN, and a large 2.75 eV band is present, believed to be associated with either a donor to acceptor transition, or a conduction band to acceptor transition involving Zn [232].

There have only been a couple of reports of Zn-doping of InN, both by Chen et al. [233, 234], who studied the annealing of InN and InN:Zn to obtain p-type In_2O_3 [233]. They used sputtering to achieve the films and from the as-grown samples they observed optical absorption edges of 1.8-1.9 eV for both the Zn-doped and undoped material; with the conversion to In_2O_3 the absorption edge moved to 3.5 eV. The as-grown Zn-doped InN films exhibited n–type conductivity, with carrier concentrations of $5.6 \times 10^{20}\ cm^{-3}$ and a Hall mobility of 14.6 $cm^2V^{-1}s^{-1}$ [234]. The high carrier concentration explains why the absorption edge is at such a high energy, due to band filling leading to the Burstein-Moss effect. Oxygen contamination is a likely cause, as are native defects, due to the growth technique.

7.1 OVERVIEW

To study the effects of the Zn-doping of InN a series of InN:Zn films were grown under N–rich conditions on (111)YSZ and GaN; an additional series of films was grown under In-rich conditions on GaN. The N-rich InN films were grown under the same conditions as the Mg-doped films, while In-rich growth was done with an indium cell temperature of 830°C, corresponding to an indium flux of $9.1 \times 10^{14}\ atoms \cdot cm^{-2}s^{-1}$. The effusion cell initially used for Zn doping was a 10 cc high temperature cell, designed for temperatures in excess of 1200°C. This meant that at the low temperatures required for Zn doping (<300°C) the zinc flux (fig. 7.1) was unstable. To resolve the issue with the effusion cell, zinc was installed into a 60 cc effusion cell, allowing for better control over the zinc flux at low temperatures. Due to the proximity of the zinc cell to the indium and gallium sources, secondary heating from the indium and gallium sources limited the lowest operating temperature of the zinc cell to about 70°C. As with the magnesium cell, the zinc flux was initially determined from theoretical curves, shown in fig. 7.1.

To determine the exact Zn incorporation particle induced x-ray emission (PIXE), performed by Dr. John Kennedy at GNS Science Ltd. was used to examine several InN:Zn films. The technique employs bombardment with ions of sufficient energy (usually MeV protons) produced by an ion accelerator, which cause inner shell ionisation of

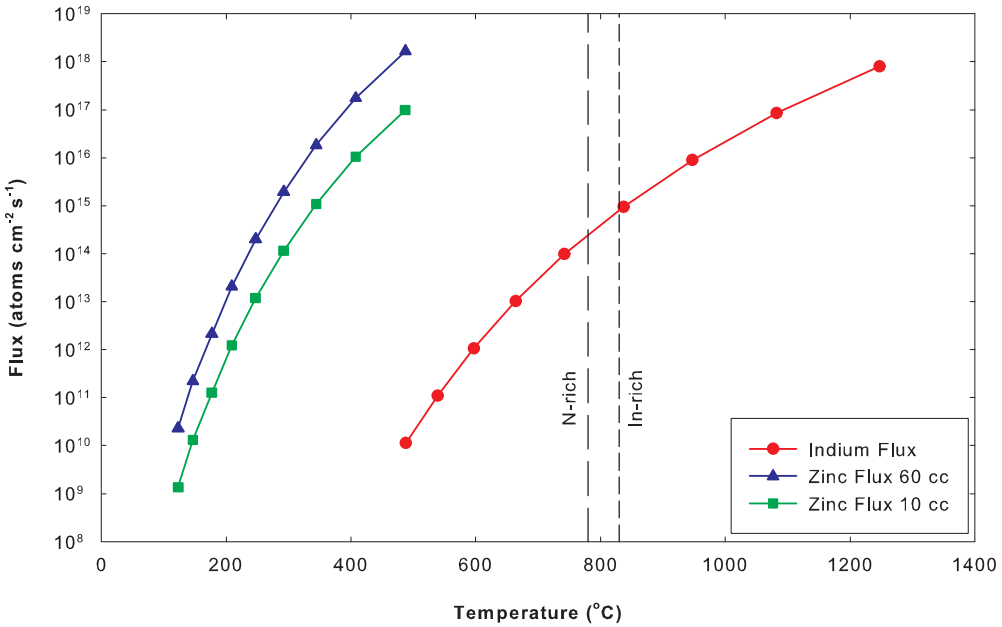

Figure 7.1 Theoretical flux curve for zinc produced from the 10 cc and 60 cc effusion cells.

atoms in a specimen. Outer shell electrons drop down to replace inner shell vacancies, however only certain transitions are allowed. X-rays of a characteristic energy of the element are then emitted. An energy dispersive detector is used to record and measure these x-rays and the intensities are then converted to elemental concentrations. Ignoring sample 604-InN:Zn which was grown with the high temperature cell, the zinc concentration of the InN:Zn films increased with zinc flux (table 7.1). For the In–rich films with the Zn cell temperature above 192°C, the amount of Zn incorporated increased with increased Zn cell temperature, as for the N–rich growth, although a lower concentration was seen for the In–rich films (table 7.2). While the film grown with the Zn cell temperature of 75°C has the highest Zn concentration, it is close to the Zn detection limit of $1 \times 10^{15}\, atoms \cdot cm^{-2}$, in part due to the background contributions from the neighbouring Ga x-ray peak of the GaN substrates. The Zn content determined by PIXE is within an order of magnitude of the theoretical Zn flux curve (fig. 7.2), however for the PIXE determined Zn content neither the N-rich or In-rich growth keep the same displacement from the theoretical curve with increasing Zn flux. This is either related to a discrepancy in the theoretical curve or reduced incorporation of Zn,

Table 7.1 Zinc doped InN films on YSZ(111).

Film Number	Zinc Temp. (°C)	Zinc conc. PIXE ($atoms \cdot cm^{-2}$)
617-InN:Zn	75	-
615-InN:Zn	100	-
604-InN:Zn	114	4.4×10^{16}
611-InN:Zn	127	-
610-InN:Zn	143	-
613-InN:Zn	192	1.8×10^{16}
612-InN:Zn	248	7.1×10^{16}

Table 7.2 Zinc doped InN films on GaN template.

Film Number	Zinc Temp. (°C)	Zinc conc. PIXE ($atoms \cdot cm^{-2}$)
N-rich growth		
627-InN:Zn	75	-
621-InN:Zn	192	-
619-InN:Zn	248	-
In-rich growth		
656-InN:Zn	75	8.9×10^{15}
653-InN:Zn	192	1.0×10^{15}
655-InN:Zn	248	3.1×10^{15}

although with such a small sample it is impossible to determine. It is unlikely that the variability in the incorporation rate is due to polarity change, as there are no reports of polarity reversal occurring in GaN:Zn, and KOH etching of the N–rich growth InN:Zn films suggest that the polarity of the films does not change from In-polar. There is a significant difference in Zn concentration between the N-rich and In-rich growths, possibly due to differences in growth temperature, as the N–rich films were grown at 450°C compared to 470°C for In–rich growth. The indium droplets that occur on the InN surface may also act as a blocking layer for the incorporation of Zn, or reduce the rate of absorption of Zn, as an In-Zn liquid phase occurs around 470°C.

7.2 ELECTRICAL AND OPTICAL PROPERTIES OF ZINC–DOPED INDIUM NITRIDE ON (111)YSZ

Single magnetic field Hall effect measurements reveal essentially no correlation between either electron concentration or mobility with Zn flux (fig. 7.3). For the InN:Zn films the

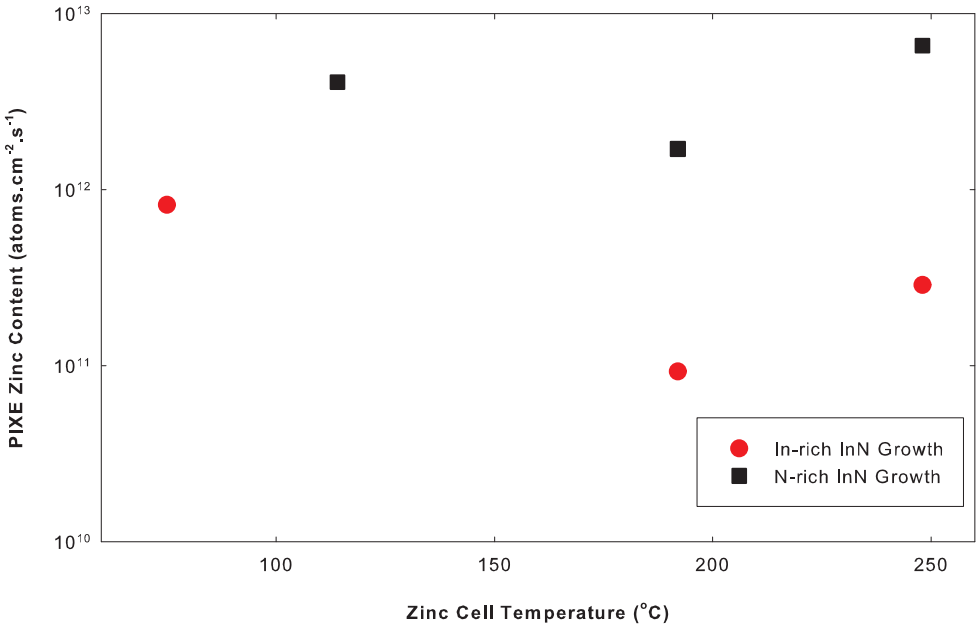

Figure 7.2 Zinc incorporation into InN, grown under N–rich and In–rich conditions, as determined using PIXE.

mobility values are clustered around $100\,cm^2V^{-1}s^{-1}$, ranging between $43\,cm^2V^{-1}s^{-1}$ and $150\,cm^2V^{-1}s^{-1}$, while in the stable region of the InN:Mg series (Mg <230°C) the mobility values are around $170\,cm^2V^{-1}s^{-1}$, possibly due to a surfactant effect that Mg can have on nitride growth. In terms of carrier concentration the InN:Zn and InN:Mg films exhibited a random spread of values centred around $1.8\times10^{19}\,cm^{-3}$; given the similar film thickness the surface accumulation layer will have a similar effect on both film sets. Examining the carrier concentration as a function of Zn concentration, an increasing trend (fig. 7.4) is apparent. The change in the electrical properties is correlated to the surface morphology, as with increasing zinc content the films also display a change in morphology with a relatively smooth surface occurring for the film 613-InN:Zn (Zn cell temperature of 192°C) compared to the other two films that have surfaces with the start of columnar growth, or inversion domains, as shown in fig. 7.5.

In order to better compare with the Mg doped films, ECV was also performed on the series of InN:Zn films grown on (111)YSZ substrates under N-rich conditions (fig. 7.6). In the case of InN:Mg, Wang et al. [212] reported that the peak bias voltage (in a C^{-2} versus voltage plot) increased with Mg concentration, except in the case of over

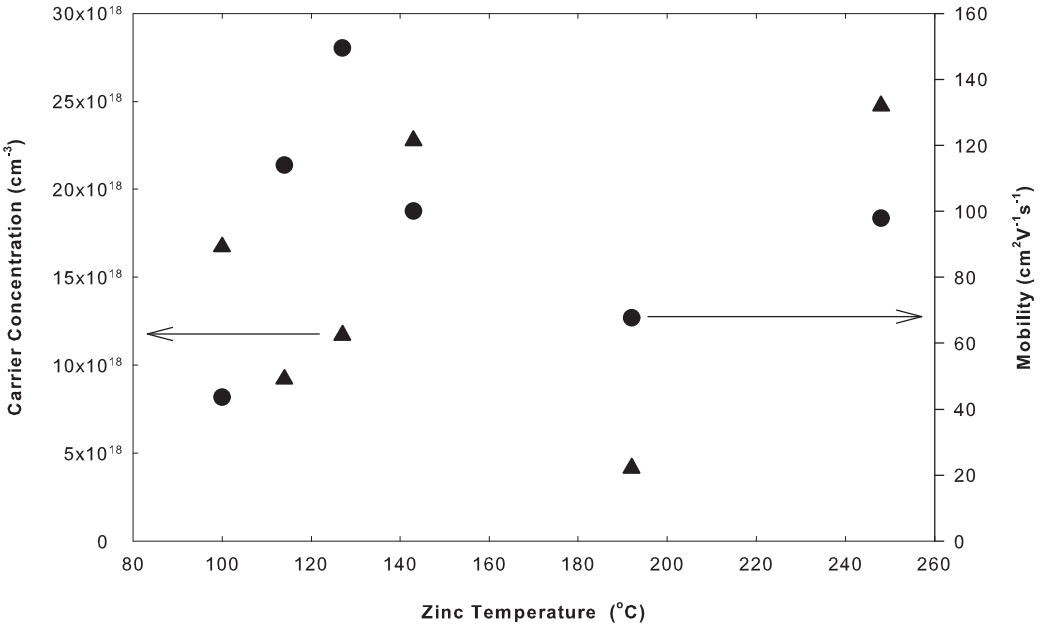

Figure 7.3 Room temperature electrical properties from the InN:Zn films as a function of Zn cell temperature.

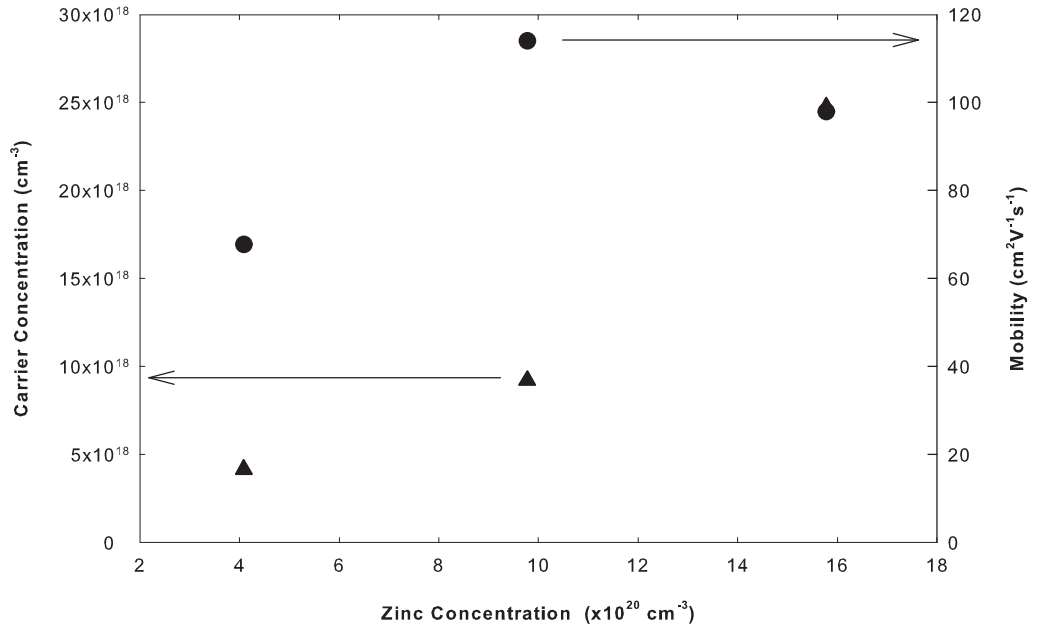

Figure 7.4 Room temperature electrical properties from the InN:Zn films as a function of zinc concentration determined by PIXE.

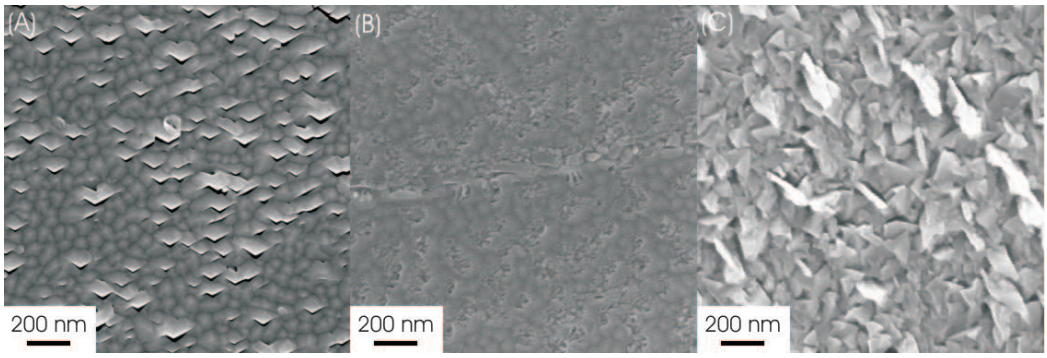

Figure 7.5 SEM micrographs for the InN:Zn/YSZ(111) films grown under N-rich growth conditions for Zn cell temperature of a) 75°C, b) 192°C and c) 248°C.

doping (Mg $>1.8 \times 10^{20}\, cm^{-3}$, slight different between polarities). With increasing Zn cell temperature the position of the peak position moves monotonically to lower reverse bias. This may be taken as an increasing amount of p–type conduction. However, as has been pointed out by Yim et al. [100], a change in slope in C^{-2} versus voltage plots can also be achieved for an n-type film if sufficient reverse bias can be applied to flatten and then invert the band bending of the surface. Given the Hall effect results, however, an alternative explanation is that the Zn doping leads to increased electron concentration (directly or indirectly), moving the bulk Fermi energy deeper into the conduction band and therefore requiring a smaller bias to achieve flat band conditions.

Of the films grown, the one with a zinc cell temperature of 75°C was the only film that exhibited PL. The signal was weak, as shown in fig. 7.7, although it was centred around 0.6 eV at 70 K. There is a water absorption line at 0.65 eV that obscures the exact position of the peak. However, this does show that photoluminescence is possible from InN:Zn films. The lack of photoluminescence is possibly due to a high electron concentration (or hole) decreasing the emission efficiency due to donor-like (acceptor-like) defects or impurities producing non-radiative recombination centers, which reduce the carrier lifetime and the internal quantum efficiency [235].

7.3 ZINC–DOPED INDIUM NITRIDE ON GALLIUM NITRIDE

For the growth of InN:Zn/(111)YSZ variable magnetic field Hall effect (VFH) measurements were not performed due to the unknown hole feature observed for InN

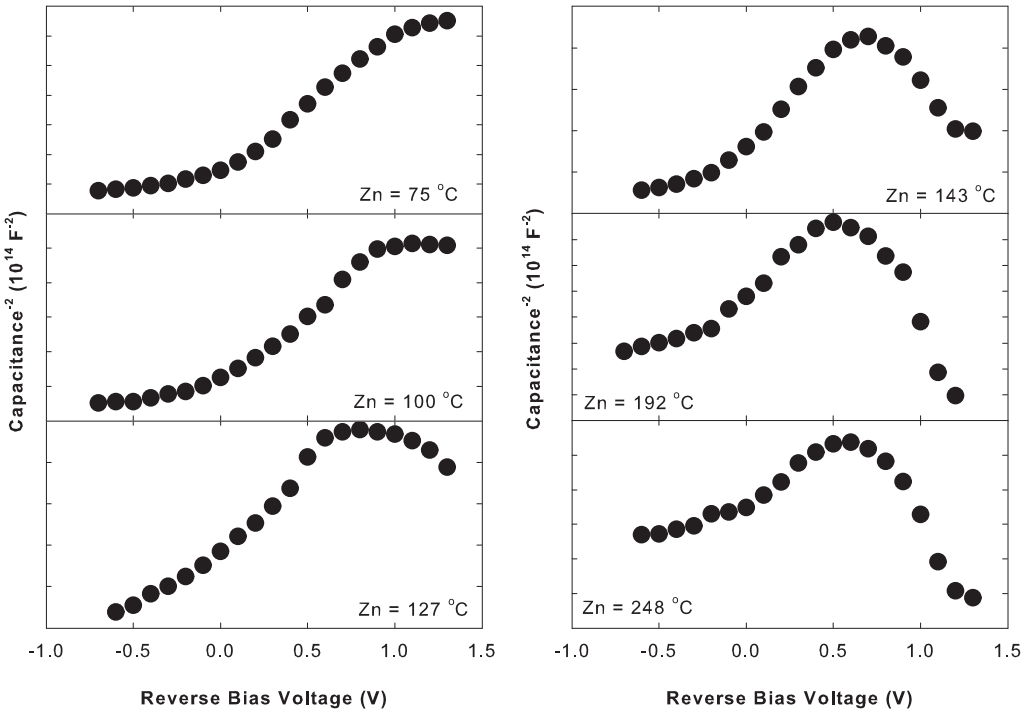

Figure 7.6 ECV C^{-2} versus voltage plots for the InN:Zn/YSZ(111) films grown under N-rich conditions.

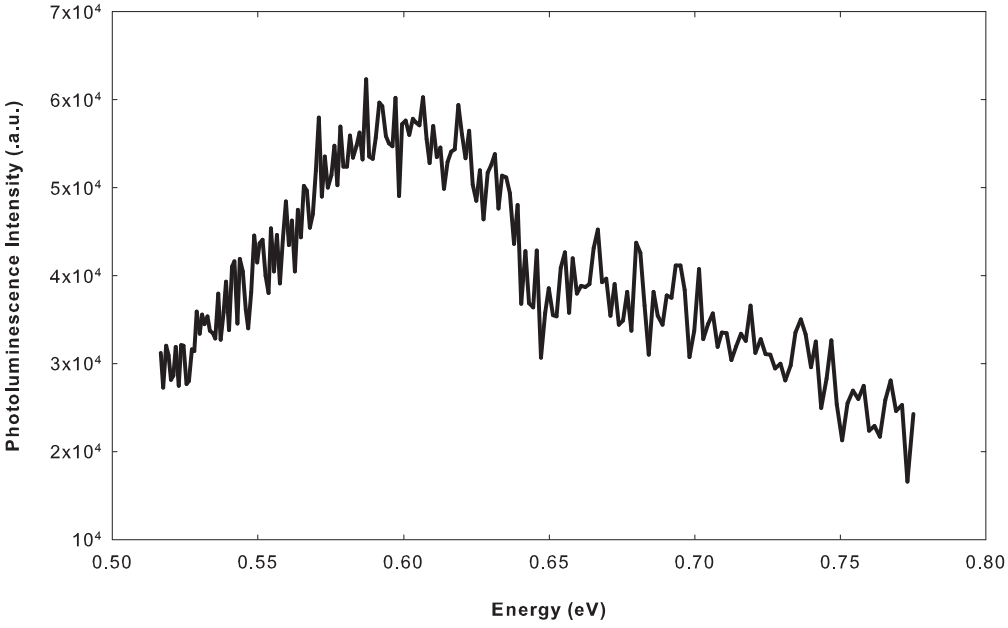

Figure 7.7 4 K photoluminescence from film 617–InN:Zn/YSZ(111) grown with a zinc cell temperature of 75°C.

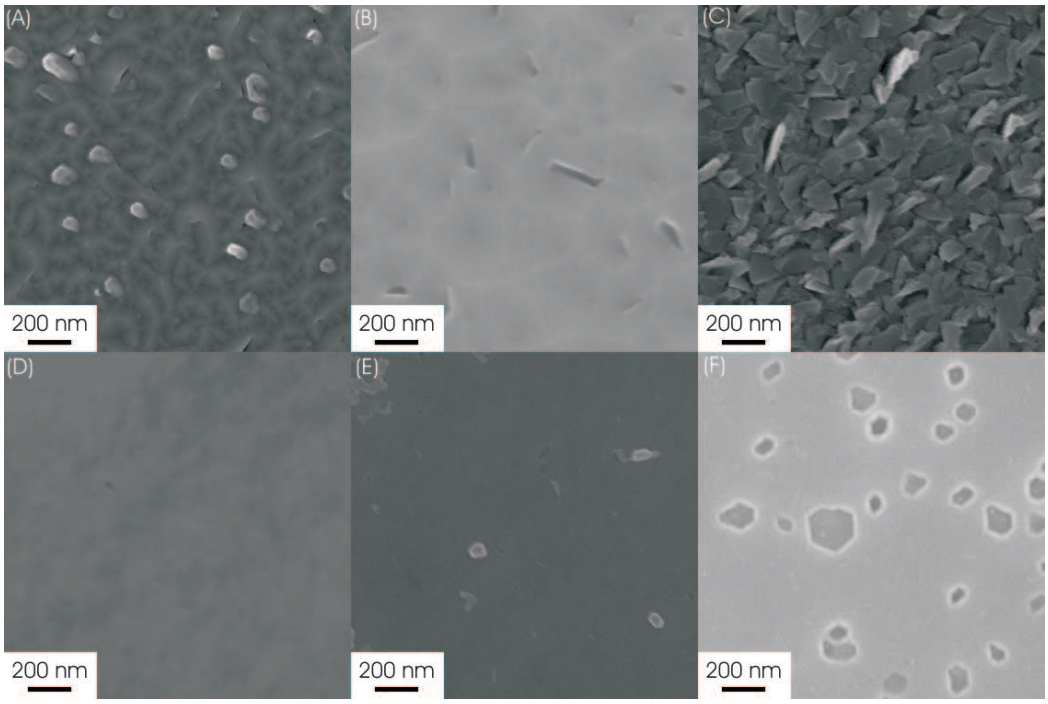

Figure 7.8 SEM micrographs for the InN:Zn/GaN films. a) Zn cell temperature of 75°C N-rich, b) Zn cell temperature of 192°C N-rich, c) Zn cell temperature of 248°C N-rich, d) Zn cell temperature of 75°C In-rich, e) Zn cell temperature of 192°C In-rich and f) Zn cell temperature of 248°C In-rich.

on (111)YSZ [215]. Therefore, InN:Zn films were also grown on semi-insulating Ga-polar MOCVD GaN templates to avoid this issue. With the re-evaluation of the InN growth regime to produce higher quality InN by this time, as specified in chapter 3, the InN:Zn/GaN films were grown under In-rich conditions, and at the slightly higher growth temperature of 470°C. The surface morphologies obtained on the In-rich growths showed an improvement compared to the films on (111)YSZ and GaN grown under N-rich conditions, with a reduction of the pitting; in the case of the film grown with the highest Zn flux, the columnar growth is largely suppressed (fig. 7.8) due to a reduction of the diffusion energy barrier in the presence of an In-adlayer on the surface.

With the improved film quality the electrical properties are also improved (table 7.3). This is not only due to the In–rich growth conditions, but also because the films are over a micron thick, so the significance of the accumulation layer and substrate interface will be reduced simply from a volume perspective. The Zn content is reduced, due to the higher In flux and possibly the higher growth temperature. Due to the

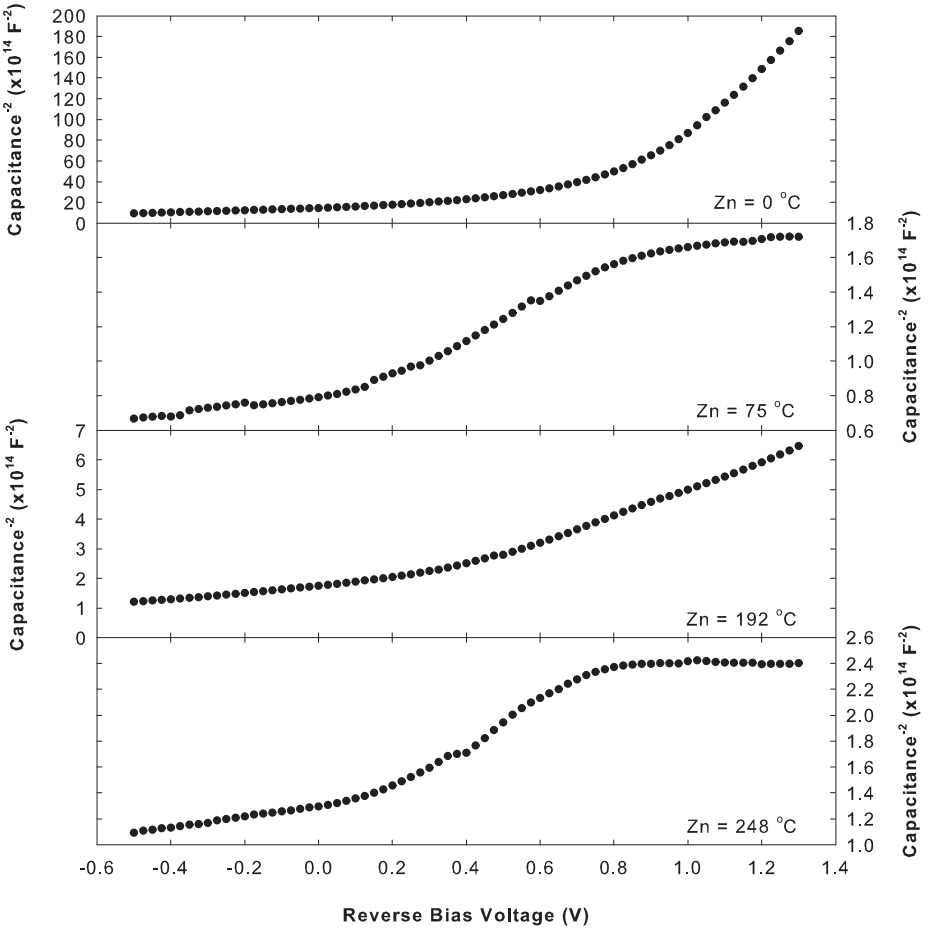

Figure 7.9 ECV measurements from the InN:Zn films grown under In-rich growth conditions, the electrolyte was 0.2 Mol NaOH and 0.2 Mol KOH using a 1V ac bias voltage.

reduction of the Zn content the films did not exhibit the same ECV response, and the shape of the C^{-2} versus V_{bias} curve is more representative of an un-doped or lightly doped InN:Mg film (fig. 7.9). This would explain the high mobility and bulk electron carrier concentrations. With such a small sample set, it is difficult to draw conclusions regarding any direct correlation between carrier concentration and Zn content. Examining the InN:Zn/GaN films that were grown under In-rich conditions with variable magnetic field Hall effect exhibited both high mobility electron and hole features (fig. 7.10 and table 7.3); the hole feature is likely a ghost peak as hole mobilities that high are unexpected.

Photoluminescence from the In–rich InN:Zn samples was obtained using the 488 nm line from an argon laser (150 mW) and collected using an InSb detector. With the

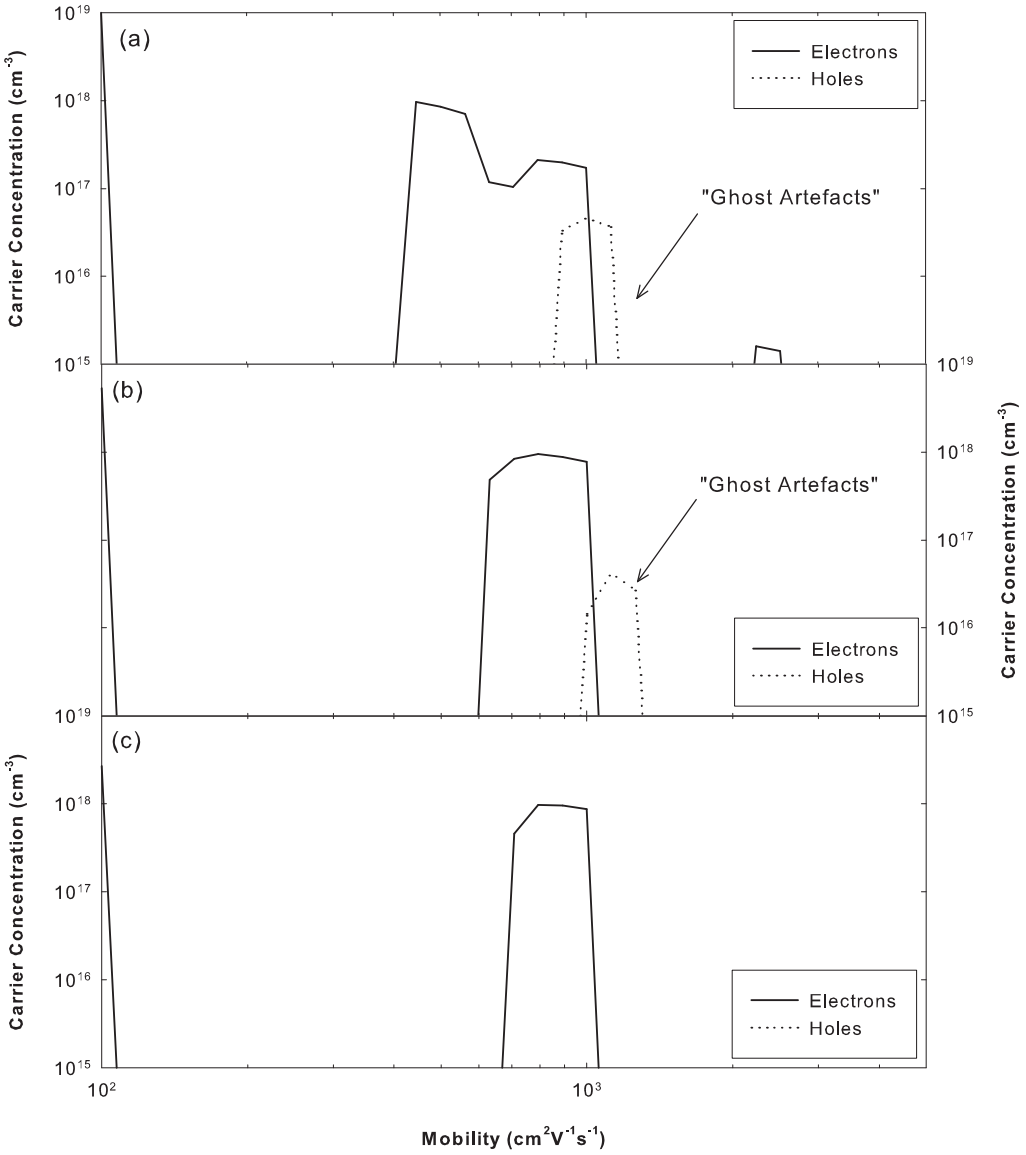

Figure 7.10 Variable magnetic field Hall effect measurements from the InN:Zn/GaN films grown under In-rich conditions. Zn cell temperatures were a) 75°C, b) 192°C and c) 248°C.

Table 7.3 Results of multiple carrier fitting to variable magnetic field Hall effect data for the InN:Zn/GaN films grown under In-rich conditions. In each case two distinct electron population could be resolved.

Film Number	Zn Cell Temperature °C	Mobility $cm^2V^{-1}s^{-1}$	Carrier Concentration cm^{-3}	Carrier type
653-InN:Zn	198	864	3.4×10^{18}	n–type
		90	9.5×10^{18}	n–type
655-InN:Zn	248	875	3.2×10^{18}	n–type
		143	2.1×10^{18}	n–type
656-InN:Zn	75	621	2.1×10^{18}	n–type
		100	1.7×10^{19}	n–type

In–rich growth all the films produced PL spectra with multiple features, as shown in fig. 7.11. With increasing Zn cell temperature the intensity of the PL decreases and also the features are shifted. The film (656-InN:Zn/GaN) grown with a zinc cell temperature of 75°C had a main feature at 0.677 eV, and two smaller peaks, one at 0.705 eV and the other at 0.651 eV. The two features at 0.677 eV and 0.705 eV are seen in both of the undoped InN films, so they are unlikely to be associated with the Zn-doping, but possibly due to localisation of carriers. Carrier localisation can be due to random impurity potentials or indium inclusions [220]. However, the activation energy is often dependent on the carrier concentration, with films having a high carrier concentration characterised by larger activation energies, which suggests a larger fluctuation of the impurity potentials [220]. The inhomogeneous impurity distribution may produce a density-of-states tail by electron-impurity interactions. Such a band tail localises the photogenerated carriers and can be treated as an acceptor-type center [236].

To gain information about the activation energies of the features, film 656-InN:Zn was measured as a function of temperature. The dominant PL feature exhibits a red shift with increasing temperature, and above 150 K the PL combines into a single feature peaked at 0.68 eV. The main feature at 0.677 eV shows an increasing width with increasing temperature which can be attributed to thermal excitation of carriers [237]. The variation of peak position with temperature has an S-shape characteristic which is an indication of inhomogeneity of the carrier concentration [238]. Arrhenius plots of the peaks at 0.677 eV and 0.705 eV with single and double energy activations are shown in fig. 7.12, and summarised in table 7.4. The small activation energies of

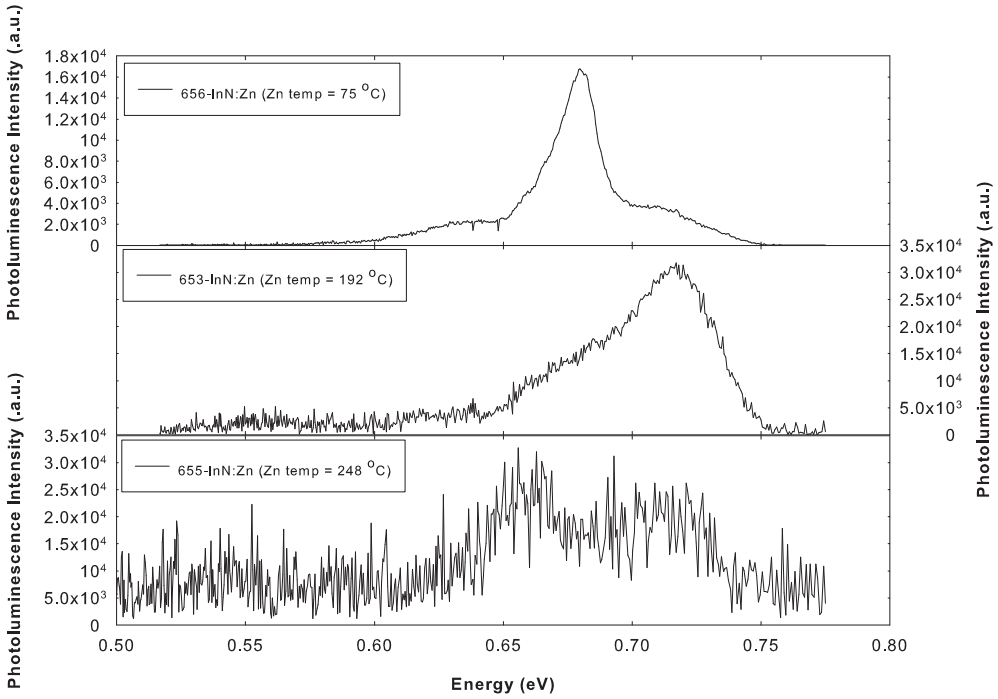

Figure 7.11 Photoluminescence spectra of the InN:Zn/GaN films that were grown under In-rich growth conditions.

Table 7.4 Values from fitting the equations 6.1 and 6.2 to the temperature dependent photoluminescence of Film 656-InN:Zn/GaN (fig. 7.12).

	I_o	C_1	E_1 (meV)	C_2	E_2 (meV)
Single path (0.677 eV)	13349	14.3	9.70		
Double path (0.677 eV)	13684	332	37.9	5.00	6.34
Single path (0.705 eV)	3252	17.1	8.64		
Double path (0.705 eV)	3550	76.7	16.2	1.26	2.39

6.3 meV and 2.4 meV agree with localised carriers [220]. The high activation energy of 16 meV can be related to conduction band to acceptor levels; shallow acceptors levels are around 5–18 meV while deep acceptor states are typically 50–60 meV [239]. The other high activation energy of 38 meV cannot be related to an acceptor level as the peak position is at a higher energy, and so it is possibly a near band edge transition.

The film grown with a zinc cell temperature of 192°C sees the reduction of the main feature (0.677 eV), while the feature at 0.72 eV becomes the main feature, accompanied by the appearance of a feature at 0.63 eV and also a weak feature at 0.545 eV. The film grown with a zinc cell temperature of 248°C (655-InN:Zn/GaN) sees all the features

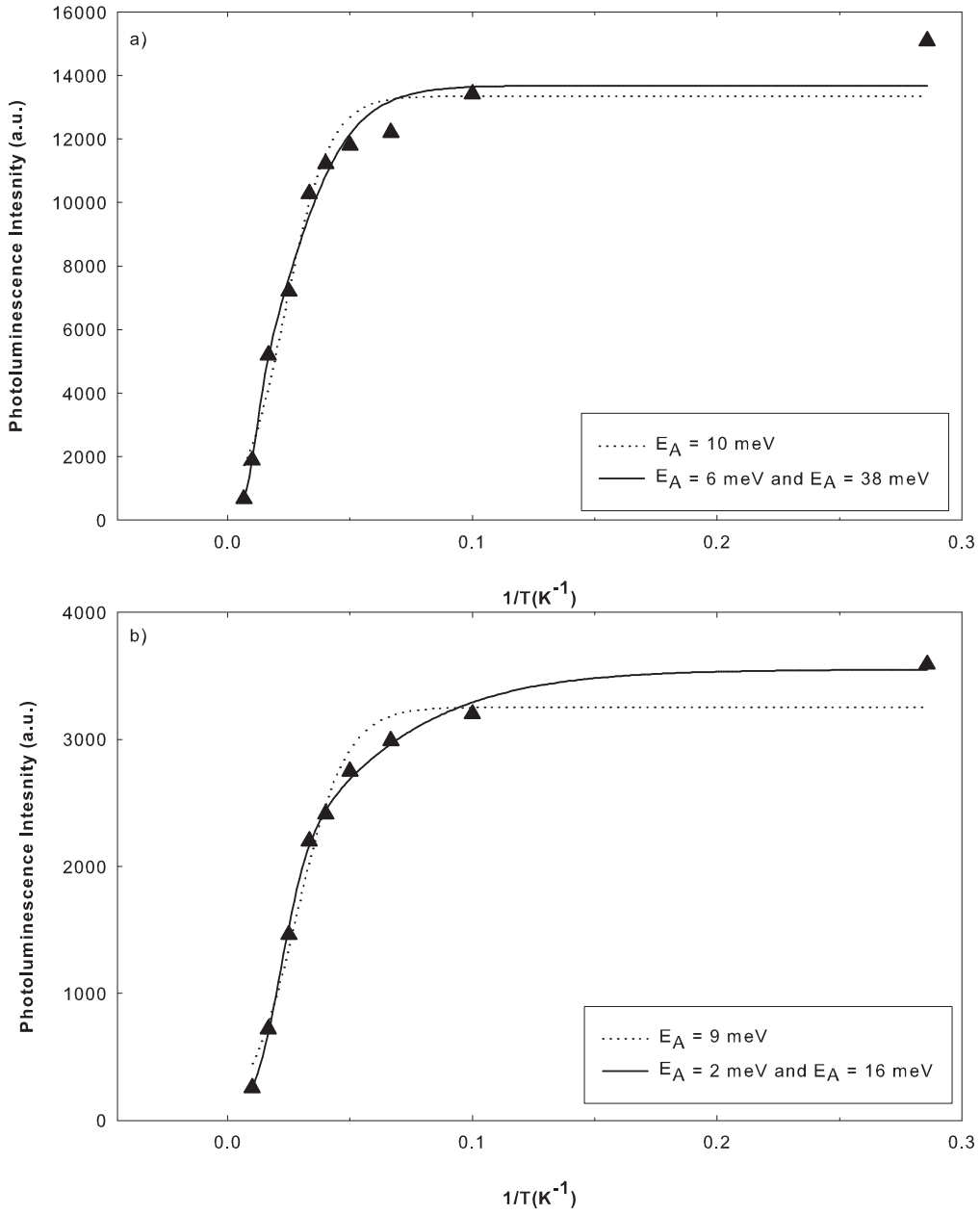

Figure 7.12 Arrhenius plots of the photoluminescence intensity versus temperature for peaks at a) 0.677 eV and b) 0.705 eV from film 656-InN:Zn/GaN.

Table 7.5 Values from fitting the equations 6.1 and 6.2 to the temperature dependent photoluminescence of Film 655-InN:Zn/GaN (fig. 7.13).

	I_o	C_1	E_1 (meV)	C_2	E_2 (meV)
Single path (0.719 eV)	261840	39.4	11.2		
Double path (0.719 eV)	299072	9.33	6.15	178	25.5
Single path (0.668 eV)	356436	30.7	10.6		
Double path (0.668 eV)	401758	5.96	5.39	67.7	18.6
Single path (0.602 eV)	117018	1.70	7.31		
Single path (0.547 eV)	251909	2908	46.5		
Double path (0.547 eV)	267389	1.92	8.41	44103	69.9

at similar intensities, with features at 0.710 eV, 0.661 eV, 0.607 eV and 0.547 eV. Film 655-InN:Zn/GaN was analysed as a function of the laser excitation power. The intensity of all the features increases with excitation power while the peak positions only shift by 3 – 7 meV, with all of the peaks blueshifting except the feature at 0.547 eV. The blueshift can be associated with the band filling effect due to the increase of the Fermi energy in the conduction band [235]. To further explain the four PL features the films were also investigated as a function of temperature. The peaks at 0.719 eV and 0.668 eV only redshift with increasing temperature and they have similar gradients, suggesting that the components that make up these two peaks are similar. Peaks at 0.602 eV and 0.547 eV have an overall redshift, however the peak position also oscillates which can be related to localised carriers. Plotting these features as (fig. 7.13) leads to the calculated activation energies shown in table 7.5. Each of the features has a low energy part which can be related to inhomogeneities in the carrier profile. The activation energies of 25 meV (peak 0.719 eV) and 18 meV (peak 0.668 eV) are similar to the activation energy for a transition from the conduction band to acceptor (5–18 meV). For the feature at 0.547 eV the activation energy is 70 meV which is possibly a transition to a deep level acceptor [219]. The feature at 0.547 eV is possibly from the Zn as it has not been seen in our undoped InN films, and Zn doping of GaN leads to the reduction of the high energy features with a dominant low energy feature.

The InN:Zn/GaN films that were grown under N-rich growth conditions were examined by time dependent transmission to see if the observed trend in the photoluminescence intensity could be related to Auger recombination. As with the InN:Mg films the carrier lifetime is strongly reduced as a function of the Zn cell temperature (fig.

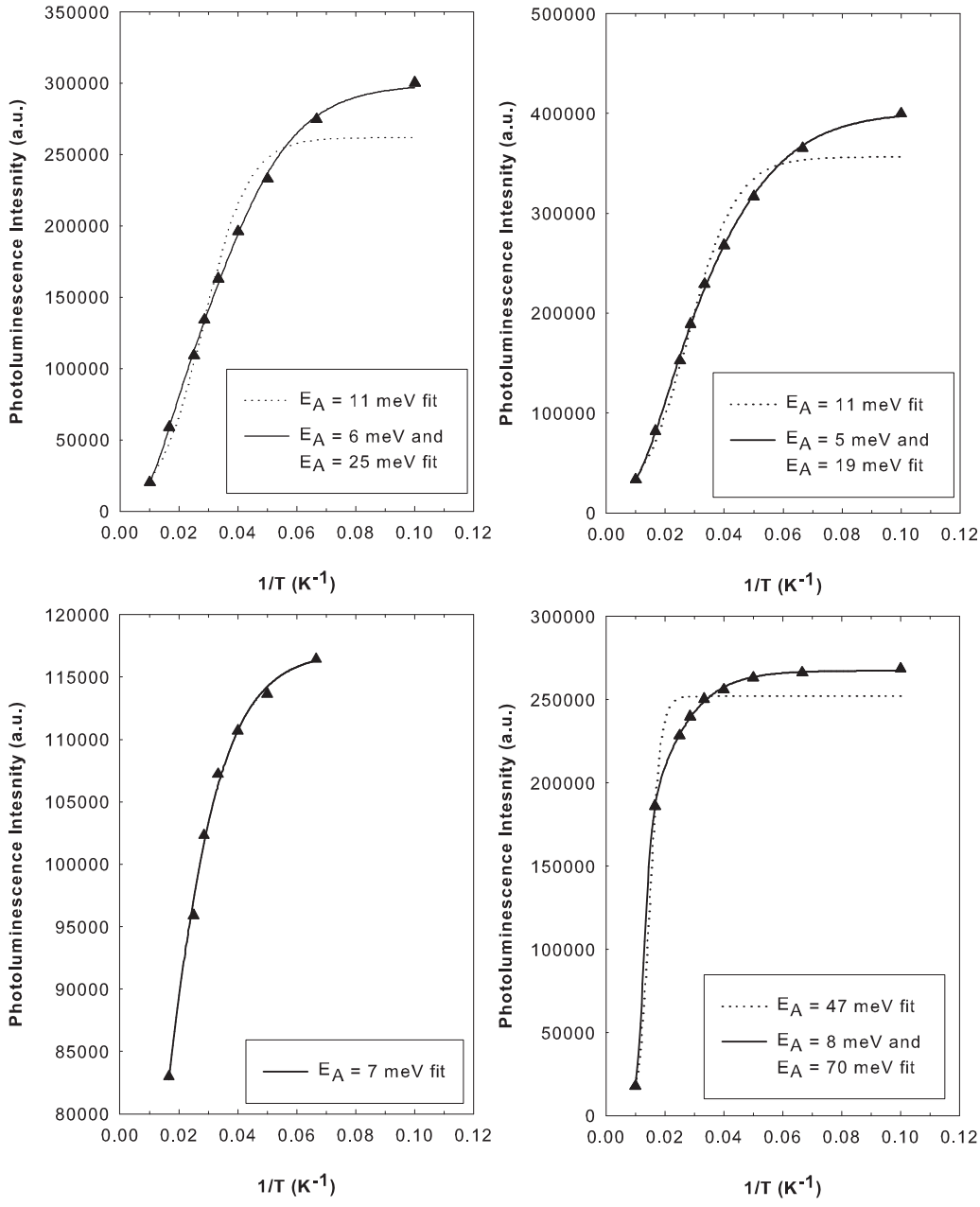

Figure 7.13 Arrhenius plots of the photoluminescence intensity versus temperature for peaks at a) 0.719 eV, b) 0.668 eV, c) 0.602 eV and d) 0.547 eV from film 655-InN:Zn/GaN.

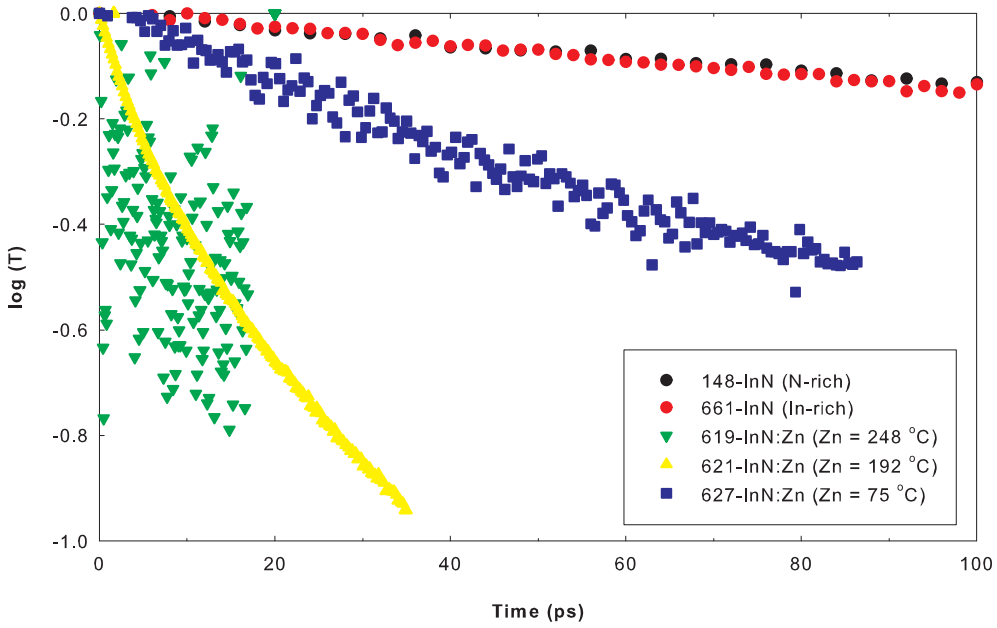

Figure 7.14 Time dependent transmission from the InN:Zn films and also an undoped InN film grown under N-rich conditions, and an undoped InN film grown under In-rich conditions.

7.14).

7.4 SUMMARY

For the study on InN:Zn a series of films were grown on (111)YSZ and also GaN. Films grown on (111)YSZ were all n-type, while the Hall mobility did not have the same reduction with Zn cell temperature as seen in the InN:Mg films. ECV measurements suggest that the Zn is affecting the bulk carrier concentration although in this case it may be due to the Fermi level moving further into the conduction band. It has been reported anecdotally that high electron concentrations also lead to PL quenching, and this would be consistent with the time dependent transmission measurement. When the growth conditions were increased into the In-rich region, electrical properties of the film were improved, which allowed the samples to be analysed by variable magnetic field Hall effect. A hole feature was observed, however this is most probably a "ghost" artefact as the mobility of the holes was on the order of that of the electrons. Furthermore the ECV measurements did not reveal a peak in the C^{-2} versus bias plot, which would represent a p-type layer as seen in InN:Mg films. Photoluminescence of these high

quality InN:Zn/GaN films exhibited multiple features at 0.710 eV, 0.661 eV, 0.607 eV, 0.547 eV. All of the features show localised carrier effects as determined by fitting to the temperature dependent photoluminescence. The features at 0.710 eV and 0.661 eV are possibly conduction band to shallow acceptor transitions while the feature at 0.547 eV could be related to a deep acceptor due to zinc.

Chapter 8

CONCLUSIONS AND FUTURE WORK

8.1 III-NITRIDE THIN FILMS

High quality single crystal InN and GaN were grown by plasma assisted molecular beam epitaxy. Optimisation of film properties was performed by determining the onset of metal-rich growth conditions. As already universally acknowledged for GaN, metal-rich growth allows for significant adatom diffusion and therefore smooth layers. A sufficiently high growth temperature should see the formation of gallium droplets suppressed, however in this study the films grown always seem to feature metal droplets on some portion of the surface. High substrate temperatures (790°C) lead to reduced electrical properties which is possibly due to the reduced surface quality due to decomposition. InN is a more complex semiconductor to grow due to its low thermal stability; for In-polar films the maximum substrate temperature is approximately 470°C. Metal-rich growth conditions improved the quality of the InN films, and also in the case of growth on (111)YSZ the formation of micron sized cracks is also suppressed. However, over time the indium droplets have an adverse effect on the InN electrical properties due to the formation of InN platelets in the indium droplets formed through a vapour liquid solid process. For the 5 μm thick InN films a reduction in the indium flux is required to reduce the indium droplet growth rate and thereby allow for further improvements in the bulk electrical properties to $\mu_n = 1393\ cm^2V^{-1}s^{-1}$ and n = $5.7 \times 10^{18}\, cm^{-3}$, as determined by variable field magnetic Hall effect.

From the InN thickness dependent growth the electrical properties show a distinctive improvement with film thickness. Due to the increased film thickness the effective

volume contribution of the substrate interface and surface accumulation layer are decreased and therefore both experience a reduced effect on the bulk electrical properties. Also with increased film thickness, it is expected that the defects from the substrate interface will decrease with thickness as the threading dislocations self annihilate. The bulk layer is still expected to contain point defects, which are also believed to cause the well known surface accumulation layer. Using electrochemical capacitive voltage the accumulation layer density was determined to be $9.2 \times 10^{12}\, cm^{-2}$, slightly smaller than other reported values of typically $3 \times 10^{13}\, cm^{-2}$. For an InN film with thickness of $5\,\mu$m the single magnetic field Hall effect results are consistent with the more sophisticated variable magnetic field Hall effect measurements demonstrating that it can be a reliable technique for characterising thick ($> 5\mu$m) InN films. All the InN films exhibit a PL feature at 0.6 - 0.7 eV, which can be related to a near band edge transition. Under In-rich growth conditions the PL spectra contain several peaks and further studies are required to understand their physical origin. For the $5\,\mu$m thick film what appears to be an LO photon replica was observed, suggesting overall a very high quality film in which thickness has played a role in reducing the effects of defects from the 2.5% lattice mismatch.

The GaN and InN films grown were of reasonable quality to characterise the electrical and optical properties as well as to enable doping studies. However, there are several improvements to the growth process that could still be performed. Issues with uniformity and temperature control can profoundly affect the growth of III-nitrides, and InN more so than GaN. Thermal uniformities maybe be improved through sputter coating the back of the substrates with molybdenum and an indium layer to ensure uniform wetting of the back surface with the InSn mounting layer between the substrate and the molybdenum growth blocks, allowing for more uniform heat transfer from the mounting block. This adds another degree of complexity, however, and also means steps must be taken to not only protect the growth surface but to remove any organics used for that purpose after cleaning. Determination of the film temperature has historically been problematic although is recognised as significant parameter. The newly installed BandiT absorption edge based system appears to be a viable solu-

tion, at least when growing on a thick GaN layer. Using this system as the feedback control to the substrate heater PID controller, in theory a constant film temperature could be maintained. This may prove challenging but the benefits are likely to make it worthwhile.

In this study it was seen that the InN/GaN and InN/(111)YSZ films relax in the first several seconds (15 nm) of the growth, but the InN/GaN films do not completely relax. A study into the strain would be interesting not only to see how films cope with different lattice mismatches, but also whether over a long period if the strain actually remains constant. For thick InN films, the number of threading dislocations are reduced with increasing thickness, and therefore the strain should also plateau. The newly acquired MOS laser interferometry system could be used to observe the strain relaxation in the InN/(111)YSZ films. TEM should also be done on both of the 5 μm thick films, as they have differing electrical properties most likely due to variations in indium flux, and this may allow for the issues with surface quality due to excessive In-rich growth to be resolved.

Still to be resolved is the hole feature observed in the variable magnetic field Hall effect data from the undoped InN/(111)YSZ films. From the variable magnetic field Hall effect data the hole feature was maintained with reducing film thickness, except when the film thickness was reduced to 5 nm, which is where the electrical properties would be dominated by the accumulation layer. At this point it appears that the hole feature may be an interface effect, but there is no good model at present. Therefore, a technique like coherent Bragg rod analysis (COBRA) should be brought to bear [240]; samples have been prepared but at present the measurements have not been completed.

8.2 BRANCHING GALLIUM NITRIDE NANOWIRES

There is intensive interest worldwide in nanowires for device applications. Branched nanostructures bring additional functionality depending on geometry. In this work, by exploiting the non-uniformities in the gallium and nitrogen sources, self-seeded (non-catalytic) GaN nanowires were grown including branching (hierarchical) GaN

nanowires. A growth diagram for the GaN nanowires has been developed, although it was determined that the main concern when growing such structures is being able to produce the gallium droplets with proper size and shape to support the nanowire growth. When the gallium flux is too high, the gallium droplets increase in size due to the contact angle of the droplets being less than 90°. GaN structures form inside the droplets, similar to a liquid phase epitaxy growth, as revealed by simple etching. To achieve mononucleation, which is required to nucleate a single wire, the gallium flux needs to be at a level that ensures that the droplet is under equilibrium and confines the growth under the entire droplet, therefore leading to a higher contact angle and nanowire growth. In the present study this was done by using a complex heating process that changes the growth regime at the surface to the intermediate or N-rich regime after the initial gallium droplets were produced under Ga-rich growth conditions. However, the exact gallium flux changes with each film growth, possibly due to substrate mounting issues and the reliance on the non-uniformities of the gallium and nitrogen beams. Once the nanowires are growing it has been shown that a Ga–rich Ga:N ratio can lead to branching growth, while a reduction in the gallium flux leads to tapered growth allowing for controlled growth of the nanowire diameter. However, if the decrease in gallium flux is too severe the droplet will be completely consumed and the nanowire growth is then terminated. With this control over the liquid droplet the self-seeded growth process could allow for growth of specific nanowire structures for unique devices compared to the standard vapour liquid solid process that uses an external catalyst and lacks controllability. The branching growth seems to occur as the growth of the trunk occurs. Several models were proposed for the growth but the branch nucleation is more than likely due to excess build up of gallium on the nanowires compared to other processes which stem from temperature instabilities.

The growth rate of nanowires, using the catalyst-free VLS process, can either be diffusion or kinetic based. The diffusion based process is typical of MBE growth as the active growth material arrives as adatoms and they can diffuse along the nanowire surface to get to the liquid droplet, so smaller nanowires grow faster than larger nanowires. In the kinetic model the supersaturation is affected by the diameter of the nanowire,

with the supersaturation reducing for smaller diameter nanowires and therefore the nanowire growth rate is reduced, while larger nanowires have higher growth rates. For the nanowires that were 80 to 300 nm in diameter the growth rate of the nanowires follows the diffusion based process. However, a lower diameter limit of 80 nm was also observed, which suggests that supersaturation cannot occur for nanowires with diameters less than 80 nm and this is one of the factors in the kinetic process. Moreover, on the branching nanowire film micron sized wires were also produced which were several hundred microns long, which is supportive of (or consistent with) the kinetic process as wires with larger diameters grow faster than smaller diameter wires.

The growth of the GaN nanowires by the self-seeding process is presently hindered by the shape and size of the gallium droplets. There are also reproducibility issues due to the reliance on the non-uniformities in the MBE system that change with each growth run and growth block. During this study it was shown that the nanowires could be nucleated from a layer of gallium deposited on a GaN surface, however thicker gallium layers did not support the nanowire growth. This may have resulted from the gallium droplets being too large to nucleate an individual nanowire, therefore a study into the droplet growth with gallium deposition time and also the shape of the gallium droplets might improve the reproducibility of the nanowires. Also, monitoring the growth of the gallium droplets under the Ga-rich growth regime might lead to further understanding of the growth. The use of a patterned dielectric (e.g. SiO_2) masking layer might be a way of controlling the gallium droplet size and remove the uncertainty in the gallium droplet production as a layer of gallium metal could be deposited instead of using the Ga-rich growth to produce the nucleation droplets. InN has a low thermal stability, therefore annealing of an InN layer to produce indium droplets might be a way of exciting this type of self–seeding growth of InN nanowires.

In this study it was suggested that the nitrogen species can affect the nucleation and growth rate of the GaN nanowires. Although this introduces many more parameters to an already complex growth, if at higher atomic nitrogen levels, achieved by going to high RF powers using the nitrogen plasma source, nanowire nucleation is improved this would help us understand the self–seeding nanowire growth. Further identification of

the nitrogen species can be explored by changing the aperture plate geometry as well as the voltage on the ion removal plate. It should be noted that most of the nanowire growth was done with a 488 hole aperture plate and with the recent change back to the 276 hole aperture plate geometry the gallium flux required for the nanowire growth still needs to be recalibrated.

8.3 NANOWIRE DEVICES

Both two point and three point planar GaN nanowire devices were fabricated, as well as vertical GaN nanowire devices using the AFM and large contact pads. The results from the two-point planar devices produced resistive values similar to published values for CVD and MBE grown nanowires. Also we observe the pinch off of the nanowire at a diameter of 100 nm due to pinning of the surface Fermi level. The FET structures made using a back gate showed no modulation of the I_{ds} current with gate voltage. The GaN nanowires were able to detect UVC, with fast turn on and off transitions, although sustained operation (10 secs) led to burnout of the nanowires. The three-point contact device is affected by leakage current through the Schottky contact, which sees the I_{ds} current shifted with changes in the gate voltage when no current is flowing through the drain-source terminals. Although the shift is not constant along the entire V_{ds} voltage sweep, amplification of the current occurs at the extremities of the voltage sweep possibly from gating action of the leaky Schottky contact or self gating of the metal contact.

The results from the vertical structures show clear evidence of Schottky contact formation. The barrier heights from the AFM, and large contact pads, are consistent with thin film Schottky diodes from the literature. The ideality factors are somewhat larger, which is possibly due to the reduced size of the diodes leading to the tunnelling current becoming a factor and therefore increased conduction occurs. Still these initial devices represent proof-of-concept in that the potential exists for the structures to be used in device fabrication.

Contacting the nanowires remains a major issue. The patterning process has been

resolved but the metal-to-nanowire interface is problematic. Even though the annealing experiments did not show any improvement, other groups have reported annealing (at lower temperatures) and an improvement in the I-V characteristics. However, prior to annealing they are able to measure a non-linear I-V, which we are not [241]. To improve the contact, it might be worth investigating whether removing the Ti layer may be beneficial, as it could be causing a high resistance interface to the nanowire. Lower temperature annealing may also be worthwhile. Interestingly, it has been recently shown that the growth temperature of the nanowires can greatly affect the nanowire I-V results [242], indicating a detailed temperature study may be warranted.

For the three point contacts to the branching GaN nanowires it might be interesting to try some ac inputs into the branching nanowire device. Also a better Schottky diode to one, or multiple, contacts might make a better transistor structure (this would be easier to fabricate as the Ti layer would not be required). For the vertical nanowires, the introduction of a gate contact to make a FET would allow for the electrical properties of the GaN nanowires to be fully characterised; this would require a SiO_2 or similar insulating layer to be deposited. The Schottky diodes could also be used for CV measurements to gain information about the doping levels.

8.4 INDIUM NITRIDE DOPING

Considerable effort is now being directed at controlling the electronic properties of InN. Several groups have reported success with Mg to achieve p-type materials, but many questions remain.

As part of this work, a series of Mg doped films were grown in order to better examine the effect on electrical and optical properties. The incorporation of Mg into the films seems to dip around a magnesium cell temperature of 220°C ($1.6 \times 10^{10}\, atoms \cdot cm^{-2}s^{-1}$), which may be associated with polarity flipping and/or where inversion domains form leading to a need for increased Mg flux to achieve the same concentration. KOH wet etching is imprecise here, as the surface morphology was typically associated with a mixed polar surface. Confirmation of this, and the instability of the surface

polarity in general, was obtained by valence band XPS measurements. Polarity flip has been observed by other groups, although they do not report changes in Mg incorporation. However, their growth was under In-rich conditions compared to the N–rich growth that we have explored, which may affect the behaviour of Mg incorporation as well as polarity stability. It has been reported that for GaN:Mg films grown under Ga–rich conditions polarity flipping can be suppressed [217], which does not seem to be the case for InN, at least based on the present study.

The behaviour of the InN:Mg films is consistent with what has already been reported for In-rich growth. The carrier concentration remains approximately constant as the accumulation layer and interface defects are expected to dominate Hall effect measurements, due to the InN:Mg film thickness being only 450 nm. For the InN:Mg films that exhibited strong PL, ECV was similar to that of undoped films, which suggests that the change in the PL peak position from 0.68 eV to 0.61 eV may be associated with a change in polarity. Temperature dependent photoluminescence reveals the 0.68 eV feature has an activation energy of 20 meV which is close to the expected 18 meV for a shallow acceptor level. No 0.55 eV feature was observed, as was observed in one film from the initial study of InN:Mg on GaN [45]. Initial time dependent measurements show clear evidence of a pumping-dependent lifetime, characteristic of Auger recombination. This effect is much more pronounced on Mg-doped samples, but separation of the hole contribution is problematic as all samples are compensated due to the ever-present degenerate electron background even in very thick samples. Achieving non-degenerate n-type material would be a strong step forward to a better understanding of p-type samples.

The results from the Zn–doping of the InN/YSZ(111) and InN/GaN had several commonalities with what has been seen in the Mg–doping InN studies and what has been reported in the literature for InN:Mg films. For the growth under N–rich conditions, which is what the InN:Mg films were also grown under prior to this study, the PL is quenched with increasing zinc content. Only once the ECV from the InN:Zn films was essentially the same as that of undoped films did the PL become easily detectable. However, electrical properties were not consistent with the InN:Mg films, as instead of

seeing the reduction in mobility observed with increasing Mg content, the mobility was independent of Zn cell temperature and Zn concentration determined using PIXE. The carrier concentration does not have a significant correlation to Zn cell temperature, although the PIXE results suggest increasing n–type conduction with Zn content. For GaN:Zn studies the carrier concentration shows a reduction with Zn cell temperature and also the mobility undergoes the same trend, but these trends are not seen in the InN:Zn films. This is most probably due to the surface accumulation layer and interface layer. The In-rich InN:Zn/GaN films had the same electrical properties as the N–rich growth, although due to reduction in the Zn content and improved crystal quality the PL is more easily detectable. It would be worth growing a new series of InN:Zn films under In–rich conditions and with a higher Zn flux to see if the PL is still quenched in films with a higher crystal quality. In the PL a feature at 0.54 eV is observed in the most heavily doped InN:Zn film. From previous work on InN:Mg/GaN a feature at 0.57 eV appears, which was assumed to possibly be the conduction band to acceptor transition, determined to be 110 meV. The difference in the main PL peak (0.72 eV) to the feature at 0.54 eV is 180 meV, which is deeper than Mg which is expected if Zn is a deep acceptor in InN as it is in GaN. The activation energy for the 0.54 meV feature is about 60 meV, which would suggest a deep level acceptor; the ionisation energy for Zn in InAs is only 16 meV while for Ga based III-V semiconductors is around 60 meV. The other peaks observed in the InN:Zn films have been observed in the undoped InN films grown under In-rich conditions and they are either associated with a band to band transition or conduction band to acceptor transition.

The accumulation layer still remains an issue that no one has been able to solve. It has been shown that GaN and Ga-rich InGaN does not suffer from an accumulation layer. Either using GaN, or InGaN, it maybe possible to cap the InN and block the accumulation layer. However, GaN is typically grown at much higher temperatures than InN, so the layer might have to be a gradient structure from InN to a InGaN layer with an indium composition that is not affected by the accumulation layer. If a layer could be deposited with a hole accumulation this might be able to flatten the bands. Regardless, it is clear that despite progress in both material quality and obtaining p-

type doping, in order to realise practical devices based on InN and In-rich InGaN, some type of strategy to mitigate the effects of this accumulation layer is required.

REFERENCES

[1] S. Nakamura, M. Senoh, and T. Mukai, "P-GaN/N-InGaN/N-GaN double-heterostructure blue-light-emitting diodes," *Jap. J. Appl. Phys. Part 2: Lett.*, vol. 32, no. 1 A-B, pp. L8–L11, 1993.

[2] S. Nakamura, T. Mukai, and M. Senoh, "High-power GaN P-N junction blue-light-emitting diodes," *Jap. J. Appl. Phys. Part 2: Lett.*, vol. 30, no. 12 A, pp. L1998–L2001, 1991.

[3] S. Nakamura, "InGaN/AlGaN blue-light-emitting diodes," *J. Vac. Sci. Tech. A*, vol. 13, no. 3 pt 1, pp. 705–710, 1995.

[4] S. Nakamura, M. Senoh, S.-i. Nagahama, N. Iwasa, T. Yamada, T. Matsushita, H. Kiyoku, and Y. Sugimoto, "InGaN-based multi-quantum-well-structure laser diodes," *Jap. J. Appl. Phys. Part 2: Lett.*, vol. 35, no. 1 B, pp. L74–L76, 1996.

[5] S. Nakamura, "Blue-green light-emitting diodes and violet laser diodes," *MRS Bulletin*, vol. 22, no. 2, pp. 29–35, 1996.

[6] R. Sims, R. Schock, A. Adegbululgbe, J. Fenhann, I. Konstantinaviciute, W. Moomaw, H. Nimir, B. Schlamadinger, J. Torres-Martnez, C. Turner, Y. Uchiyama, S. Vuori, N. Wamukonya, and X. Zhang, *Energy supply - In Climate Change 2007: Mitigation. Contribution of Working Group III to the Fourth Assessment Report of the Intergovernmental Panel on Climate Change*. Cambridge, United Kingdom and New York,NY, USA: Cambridge University Press, 2007.

[7] W. Shockley and H. J. Queisser, "Detailed balance limit of efficiency of p-n junction solar cells," *J. Appl. Phys.*, vol. 32, no. 3, pp. 510–519, 1961.

[8] T. L. Tansley and C. P. Foley, "Optical Band-Gap of Indium Nitride," *J. Appl. Phys.*, vol. 59, no. 9, pp. 3241–3244, 1986.

[9] V. Y. Davydov, A. A. Klochikhin, R. P. Seisyan, V. V. Emtsev, S. V. Ivanov, F. Bechstedt, J. Furthmuller, H. Harima, V. Mudryi, J. Aderhold, O. Semchinova, and J. Graul, "Absorption and emission of hexagonal InN. Evidence of narrow fundamental band gap," *Phys. Stat. Sol. (b)*, vol. 229, no. 3, pp. R1–R3, 2002.

[10] D. B. Haddad, H. Dai, R. Naik, C. Morgan, V. M. Naik, J. S. Thakur, G. W. Auner, L. E. Wenger, H. Lu, and W. J. Schaff, "Optical and electrical properties of low to highly-degenerate InN films," *Mater. Res. Soc. Symp. Proc.*, vol. 798, 2004.

[11] M. Higashiwaki and T. Matsui, "Estimation of band-gap energy of intrinsic InN from photoluminescence properties of undoped and Si-doped InN films grown by plasma-assisted molecular-beam epitaxy," *J. Cryst. Growth*, vol. 269, no. 1, pp. 162–166, 2004.

[12] J. Wu, W. Walukiewicz, K. M. Yu, J. W. Ager III, E. E. Haller, H. Lu, W. J. Schaff, Y. Saito, and Y. Nanishi, "Unusual properties of the fundamental band gap of InN," *Appl. Phys. Lett.*, vol. 80, no. 21, p. 3967, 2002.

[13] Y. Nanishi, Y. Saito, and T. Yamaguchi, "RF-molecular beam epitaxy growth and properties of InN and related alloys," *Jap. J. Appl. Phys. Part 1: Regular Papers and Short Notes and Review Papers*, vol. 42, no. 5 A, pp. 2549–2559, 2003.

[14] A. Marti and G. L. Araujo, "Limiting efficiencies for photovoltaic energy conversion in multigap systems," *Solar Energy Materials and Solar Cells*, vol. 43, no. 2, pp. 203–222, 1996.

[15] J. F. Geisz, D. J. Friedman, J. S. Ward, A. Duda, W. J. Olavarria, T. E. Moriarty, J. T. Kiehl, M. J. Romero, A. G. Norman, and K. M. Jones, "40.8% efficient inverted triple-junction solar cell with two independently metamorphic junctions," *Appl. Phys. Lett.*, vol. 93, no. 12, p. 123505, 2008.

[16] M. T. Bjork, O. Hayden, H. Schmid, H. Riel, and W. Riess, "Vertical surround-gated silicon nanowire impact ionization field-effect transistors," *Appl. Phys. Lett.*, vol. 90, no. 14, 2007.

[17] T. Bryllert, L. . Wernersson, T. Lowgren, and L. Samuelson, "Vertical wrap-gated nanowire transistors," *Nanotechnology*, vol. 17, no. 11, pp. S227–S230, 2006.

[18] A. B. Greytak, L. J. Lauhon, M. S. Gudiksen, and C. M. Lieber, "Growth and transport properties of complementary germanium nanowire field-effect transistors," *Appl. Phys. Lett.*, vol. 84, no. 21, pp. 4176–4178, 2004.

[19] G. Zheng, W. Lu, S. Jin, and C. M. Lieber, "Synthesis and fabrication of high-performance n-type silicon nanowire transistors," *Adv. Mat.*, vol. 16, no. 21, pp. 1890–1893, 2004.

[20] Y. Cui, Z. Zhong, D. Wang, W. U. Wang, and C. M. Lieber, "High performance silicon nanowire field effect transistors," *Nano Lett.*, vol. 3, no. 2, pp. 149–152, 2003.

[21] B. Kayes, C. Richardson, N. Lewis, and H. Atwater, "Radial pn junction nanorod solar cells: device physics principles and routes to fabrication in silicon," *Photovoltaic Specialists Conference, 2005. Conference Record of the Thirty-first IEEE*, pp. 55–58, 2005.

[22] H. Yamashita, K. Fukui, S. Misawa, and S. Yoshida, "Optical properties of AlN epitaxial thin films in the vacuum ultraviolet region," *J. Appl. Phys.*, vol. 50, no. 2, pp. 896–898, 1979.

[23] W. Kim, A. E. Botchkarev, A. Salvador, G. Popovici, H. Tang, and H. Morkoc, "On the incorporation of Mg and the role of oxygen, silicon, and hydrogen in GaN prepared by reactive molecular beam epitaxy," *J. Appl. Phys.*, vol. 82, no. 1, pp. 219–226, 1997.

[24] J. Neugebauer and C. G. V. de Walle, "Gallium vacancies and the yellow luminescence in GaN," *Appl. Phys. Lett.*, vol. 69, no. 4, pp. 503–505, 1996.

[25] T. Mattila and R. M. Nieminen, "Point-defect complexes and broadband luminescence in GaN and AlN," *Phys. Rev. B*, vol. 55, no. 15, pp. 9571–9576, 1997.

[26] B. Heying, I. Smorchkova, C. Poblenz, C. Elsass, P. Fini, S. D. Baars, U. Mishra, and J. S. Speck, "Optimization of the surface morphologies and electron mobilities in GaN grown by plasma-assisted molecular beam epitaxy," *Appl. Phys. Lett.*, vol. 77, no. 18, pp. 2885–2887, 2000.

[27] I. P. Smorchkova, E. Haus, B. Heying, P. Kozodoy, P. Fini, J. P. Ibbetson, S. Keller, S. P. DenBaars, J. S. Speck, and U. K. Mishra, "Mg doping of GaN layers grown by plasma-assisted molecular-beam epitaxy," *Appl. Phys. Lett.*, vol. 76, no. 6, pp. 718–720, 2000.

[28] P. Ruterana, M. Albrecht, and J. Neugebauer, *Nitride Semiconductors Handbook on Materials and Devices*. Weiheim: WILEY-VCH, 2003.

[29] T. L. Tansley and C. P. Foley, "Electron mobility of Indium Nitride," *Elec. Lett.*, vol. 20, no. 25-26, pp. 1066–1068, 1984.

[30] J. Pankove, *Optical Processes in Semiconductors*. New York: Courier Dover Publications, 1975.

[31] W. Walukiewicz, S. X. Li, J. Wu, K. M. Yu, J. W. Ager III, E. E. Haller, H. Lu, and W. J. Schaff, "Optical properties and electronic structure of InN and In-rich group III-nitride alloys," *J. Cryst. Growth*, vol. 269, no. 1, pp. 119–127, 2004.

[32] K. S. A. Butcher, H. Hirshy, R. M. Perks, M. Wintrebert-Fouquet, and P. P. Chen, "Stoichiometry effects and the Moss-Burstein effect for InN," *Phys. Stat. Sol. (a)*, vol. 203, no. 1, pp. 66–74, 2006.

[33] T. Inushima, V. V. Mamutin, V. A. Vekshin, S. V. Ivanov, T. Sakon, M. Motokawa, and S. Ohoya, "Physical properties of InN with the band gap energy of 1.1 eV," *J. Cryst. Growth*, vol. 227-228, pp. 481–485, 2001.

[34] V. Y. Davydov, A. A. Klochikhin, V. V. Emtsev, D. A. Kurdyukov, S. V. Ivanov, V. A. Vekshin, F. Bechstedt, J. Furthmuller, J. Aderhold, J. Graul, A. V. Mudryi, H. Harma, A. Hashimoto, A. Yamamoto, and E. E. Haller, "Band gap of hexagonal InN and InGaN alloys," *Phys. Stat. Sol. (b)*, vol. 234, no. 3, pp. 787–795, 2002.

[35] B. Arnaudov, T. Paskova, P. P. Paskov, B. Magnusson, E. Valcheva, B. Monemar, H. Lu, W. J. Schaff, H. Amano, and I. Akasaki, "Energy position of near-band-edge emission spectra of InN epitaxial layers with different doping levels," *Phys. Rev. B*, vol. 69, no. 11, p. 115216, 2004.

[36] A. Kasic, M. Schubert, Y. Saito, Y. Nanishi, and G. Wagner, "Effective electron mass and phonon modes in n-type hexagonal InN," *Phys. Rev. B*, vol. 65, no. 11, p. 115206, 2002.

[37] C. H. Swartz, R. P. Tomkins, T. H. Myers, H. Lu, and W. J. Schaff, "Demonstration of nearly non-degenerate electron conduction in InN grown by molecular beam epitaxy," *Phys. Stat. Sol. (c)*, vol. 2, no. 7, pp. 2250–2253, 2005.

[38] V. W. L. Chin, T. L. Tansley, and T. Osotchan, "Electron mobilities in gallium, indium, and aluminum nitrides," *J. Appl. Phys.*, vol. 75, no. 11, pp. 7365–7372, 1994.

[39] B. R. Nag, "Electron mobility in indium nitride," *J. Cryst. Growth*, vol. 269, no. 1, pp. 34–40, 2004.

[40] V. M. Polyakov and F. Schwierz, "Low-field electron mobility in wurtzite InN," *Appl. Phys. Lett.*, vol. 88, p. 032101, 2006.

[41] L. O. Olsson, C. B. M. Andersson, M. C. Hakansson, J. Kanski, L. Ilver, and U. O. Karlsson, "Charge accumulation at InAs surfaces," *Phys. Rev. Lett.*, vol. 76, no. 19, pp. 3626–3629, 1996.

[42] T. D. Veal, I. Mahboob, L. F. J. Piper, C. F. McConville, H. Lu, and W. J. Schaff, "Indium nitride: Evidence of electron accumulation," *J. Vac. Sci. Tech. B*, vol. 22, no. 4, pp. 2175–2178, 2004.

[43] H. Lu, W. J. Schaff, L. F. Eastman, J. Wu, W. Walukiewicz, D. C. Look, and R. J. Molnar, "Growth of thick InN by molecular beam epitaxy," *Mat. Res. Soc. Symp. Proc.*, vol. 743, pp. 317–322, 2002.

[44] J. W. Ager III, R. E. Jones, D. M. Yamaguchi, K. M. Yu, W. Walukiewicz, S. X. Li, E. E. Haller, H. Lu, and W. J. Schaff, "p-Type InN and In-rich InGaN," *Phys. Stat. Sol. (b)*, vol. 244, no. 6, pp. 1820–1824, 2007.

[45] P. A. Anderson, C. H. Swartz, D. Carder, R. J. Reeves, S. M. Durbin, S. Chandril, and T. H. Myers, "Buried p -type layers in Mg-doped InN," *Appl. Phys. Lett.*, vol. 89, no. 18, p. 184104, 2006.

[46] K. D. Matthews, X. Chen, D. Hao, W. J. Schaff, and L. F. Eastman, "MBE growth and characterization of Mg-doped InGaN and InAlN," *phys. stat. sol. (c)*, vol. 5, no. 6, pp. 1863–1865, 2008.

[47] W. Schaff, X. Chen, D. Hao, K. Matthews, T. Richards, L. Eastman, H. Lu, C. Cho, and H. Cha, "Electrical properties of InGaN grown by molecular beam epitaxy," *phys. stat. sol. (b)*, vol. 245, no. 5, pp. 868–872, 2008.

[48] X. Wang, S.-B. Che, Y. Ishitani, and A. Yoshikawa, "Growth and properties of Mg-doped In-polar InN films," *Appl. Phys. Lett.*, vol. 90, no. 20, p. 201913, 2007.

[49] Z. L. Wang, "Piezoelectric nanostructures: From growth phenomena to electric nanogenerators," *MRS Bulletin*, vol. 32, no. 2, pp. 109–116, 2007.

[50] Z. L. Wang, "Nanowires promise battery-fee powering of small devices," *Compound Semiconductor*, vol. 13, no. 6, pp. 16–18, 2007.

[51] D. M. Eigler and E. K. Schweizer, "Positioning single atoms with a scanning tunnelling microscope," *Nature*, vol. 344, no. 6266, pp. 524–526, 1990.

[52] R. S. Wagner and W. C. Ellis, "Vapor-liquid-solid mechanism of single crystal growth," *Appl. Phys. Lett.*, vol. 4, no. 5, pp. 89–90, 1964.

[53] A. M. Morales and C. M. Lieber, "A laser ablation method for the synthesis of crystalline semiconductor nanowires," *Science*, vol. 279, no. 5348, pp. 208–211, 1998.

[54] "Magnus T. Borgström, Private Communication, 2007.,"

[55] A. I. Persson, M. W. Larsson, S. Stenstrom, B. J. Ohlsson, L. Samuelson, and L. R. Wallenberg, "Solid-phase diffusion mechanism for GaAs nanowire growth," *Nat. Mat.*, vol. 3, no. 10, pp. 677–681, 2004.

[56] L. Geelhaar, C. Cheze, W. M. Weber, R. Averbeck, H. Riechert, T. Kehagias, P. Komninou, G. P. Dimitrakopulos, and T. Karakostas, "Axial and radial growth of Ni-induced GaN nanowires," *Appl. Phys. Lett.*, vol. 91, no. 9, p. 093113, 2007.

[57] K. A. Bertness, A. Roshko, N. A. Sanford, J. M. Barker, and A. V. Davydov, "Spontaneously grown GaN and AlGaN nanowires," *J. Cryst. Growth*, vol. 287, no. 2, pp. 522–527, 2006.

[58] R. Meijers, T. Richter, R. Calarco, T. Stoica, H. . Bochem, M. Marso, and H. Luth, "GaN-nanowhiskers: MBE-growth conditions and optical properties," *J. Cryst. Growth*, vol. 289, no. 1, pp. 381–386, 2006.

[59] T. Stoica, R. Meijers, R. Calarco, T. Richter, and H. Luth, "MBE growth optimization of InN nanowires," *J. Cryst. Growth*, vol. 290, no. 1, pp. 241–247, 2006.

[60] J. Kim, H. Oh, H. M. So, J. Kim, and J. Kim, "Rectifying diode made of individual gallium nitride nanowire," *Physica E*, vol. 18, no. 1-3, pp. 225–226, 2003.

[61] C. Hwang, J. Hyung, S. Lee, C. Jang, T. Kim, P. Choi, and S. Lee, "The formation and characterization of electrical contacts (Schottky and Ohmic) on gallium nitride nanowires," *J. Phys. D*, vol. 41, no. 10, p. 105103, 2008.

[62] S. Lee and S. Lee, "Current transport mechanism in a metal–GaN nanowire Schottky diode," *Nanotechnology*, vol. 18, no. 49, p. 495701, 2007.

[63] P. Deb, H. Kim, Y. Qin, R. Lahiji, M. Oliver, R. Reifenberger, and T. Sands, "GaN nanorod Schottky and p-n junction diodes," *Nano Lett.*, vol. 6, no. 12, pp. 2893–2898, 2006.

[64] P. J. Pauzauskie and P. Yang, "Nanowire photonics," *Materials Today*, vol. 9, no. 10, pp. 36–45, 2006.

[65] A. B. Greytak, C. J. Barrelet, Y. Li, and C. M. Lieber, "Semiconductor nanowire laser and nanowire waveguide electro-optic modulators," *Appl. Phys. Lett.*, vol. 87, no. 15, pp. 1–3, 2005.

[66] H. Park, F. Qian, C. J. Barrelet, and Y. Li, "Microstadium single-nanowire laser," *Appl. Phys. Lett.*, vol. 91, no. 25, p. 251115, 2007.

[67] S. Lee, T. Kim, S. Lee, K. Choi, and P. Yang, "High-brightness gallium nitride nanowire UV-blue light emitting diodes," *Philosophical Magazine*, vol. 87, no. 14-15, pp. 2105–2115, 2007.

[68] Y. Huang, X. Duan, Y. Cui, and C. M. Lieber, "Gallium Nitride Nanowire Nanodevices," *Nano Lett.*, vol. 2, no. 2, pp. 101–104, 2002.

[69] H. Kim, T. W. Kang, and K. S. Chung, "Nanoscale ultraviolet-light-emitting diodes using wide-bandgap gallium nitride nanorods," *Adv. Mat.*, vol. 15, no. 7-8, pp. 567–568, 2003.

[70] H. Kim, Y. Cho, H. Lee, S. I. I. Kim, S. R. Ryu, D. Y. Kim, T. W. Kang, and K. S. Chung, "High-brightness light emitting diodes using dislocation-free indium gallium nitride/gallium nitride multiquantum-well nanorod arrays," *Nano Lett.*, vol. 4, no. 6, pp. 1059–1062, 2004.

[71] M. Bockowski, P. P. Strak, P. P. Kempisty, I. I. Grzegory, B. B. Lucznik, S. Krukowski, and S. S. Porowski, "Liquid phase epitaxy of GaN on MOCVD GaN/sapphire and HVPE free-standing substrates under high nitrogen pressure," *Phys. Stat. Sol. (c)*, vol. 5, no. 6, pp. 1539 – 1542, 2008.

[72] S. Li, J. Su, G. Fan, Y. Zhang, S. Zheng, H. Sun, and J. Cao, "Influence of growth rate in the early stage of high temperature GaN layer growth on quality of GaN films," *J. Cryst. Growth*, p. In publication, 2008.

[73] K. Klima, M. Kaniewska, K. Reginski, and J. Kaniewski, "Oval Defects in the MBE Grown AlGaAs/InGaAs/GaAs and InGaAs/GaAs Structures," *Cryst. Res. Tech.*, vol. 34, no. 5, pp. 683–687, 1999.

[74] M. A. Herman and H. Sitter, "Molecular beam epitaxy fundamentals and current status," *Springer Series in Materials Science*, vol. 7, 1996.

[75] T. Kikuchi, A. S. Somintac, O. Ariyada, M. Wada, and T. Ohachi, "Role of excited nitrogen species in the growth of GaN by RF-MBE," *J. Cryst. Growth*, vol. 292, no. 2, pp. 221–226, 2006.

[76] E. Iliopoulos, A. Adikimenakis, E. Dimakis, K. Tsagaraki, G. Konstantinidis, and A. Georgakilas, "Active nitrogen species dependence on radiofrequency plasma source operating parameters and their role in GaN growth," *J. Cryst. Growth*, vol. 278, no. 1-4, pp. 426–430, 2005.

[77] A. Ptak, *Thesis: Growth Kinetics and Doping of Gallium Nitride Grown by rf-Plasma Assisted Molecular Beam Epitaxy.* Morgantown: West Virginia, 2001.

[78] J. Osaka, M. S. Kumar, H. Toyoda, T. Ishijima, H. Sugai, and T. Mizutani, "Role of atomic nitrogen during GaN growth by plasma-assisted molecular beam epitaxy revealed by appearance mass spectrometry," *Appl. Phys. Lett.*, vol. 90, no. 17, p. 172114, 2007.

[79] W. Braun, "Applied RHEED - Reflection high-energy electron diffraction during crystal growth," *Springer Tracts in Modern Physics*, vol. 154, 1999.

[80] O. Auciello and A. R. Krauss, *In situ real-time characterization of thin films.* New York: Wiley, 2001.

[81] H. J. Fan, R. Scholz, M. Zacharias, U. Gösele, F. Bertram, D. Forster, and J. Christen, "Local luminescence of ZnO nanowire-covered surface: A cathodoluminescence microscopy study," *Appl. Phys. Lett.*, vol. 86, no. 2, p. 023113, 2005.

[82] L. van der Pauw, "A method of measuring the resistivity and Hall coefficient on lamellae of arbitrary shape," *Philips Technical Review*, vol. 20, pp. 220–224, 1958.

[83] L. van der Pauw, "A method of measuring specific resistivity and Hall effect of discs of arbitrary shape," *Philips Research Reports*, vol. 13, pp. 1–9, 1958.

[84] D. Look and R. Molnar, "Degenerate layer at GaN/sapphire interface: Influence on hall-effect measurements," *Appl. Phys. Lett.*, vol. 70, no. 25, pp. 3377–3379, 1997.

[85] D. Look and J. Sizelove, "Predicted maximum mobility in bulk GaN," *Appl. Phys. Lett.*, vol. 79, no. 8, pp. 1133–1135, 2001.

[86] D. Look, R. Jones, X. Sun, L. Brillson, J. Ager, S. Park, J. Han, R. Molnar, and J. Maslar, "Electrical and optical properties of GaN/Al_2O_3 interfaces," *J. Phys. Matt.*, vol. 14, no. 48, pp. 13337–13344, 2002.

[87] C. Swartz, R. Tompkins, T. Myers, D. Look, and J. Sizelove, "Characterization of multiple carriers in GaN using variable magnetic-field Hall measurements," *J. Elec. Mat.*, vol. 33, no. 5, pp. 412–417, 2004.

[88] J. G. Tian, C. P. Zhang, and G. Y. Zhang, "Anomalous Hall effect and the anomalous infrared absorption in n-type bulk Hg[sub 0.8]Cd[sub 0.2]Te," *Appl. Phys. Lett.*, vol. 59, no. 20, pp. 2591–2593, 1991.

[89] A. Zemel, A. Sher, and D. Eger, "Anomalous Hall effect in p-type Hg[sub 1 - x]Cd[sub x]Te liquid-phase-epitaxial layers," *J. Appl. Phys.*, vol. 62, no. 5, pp. 1861–1868, 1987.

[90] J. R. Meyer, C. A. Hoffman, F. J. Bartoli, D. A. Arnold, S. Sivananthan, and J. P. Fauri, "Methods for magnetotransport characterization of IR detector materials," *Semi. Sci. Tech.*, vol. 8, no. 6S, pp. 805–823, 1993.

[91] C. H. Swartz, R. P. Tompkins, N. C. Giles, T. H. Myers, D. D. Edwall, J. Ellsworth, E. Piquette, J. Arias, M. Berding, S. Krishnamurthy, I. Vurgaftman, and J. R. Meyer, "Fundamental materials studies of undoped, in-doped, and as-doped $Hg_{1-x}Cd_xTe$," *J. Elec. Mat.*, vol. 33, no. 6, pp. 728–736, 2004.

[92] C. H. Swartz, R. P. Tompkins, N. C. Giles, T. H. Myers, H. Lu, W. J. Schaff, and L. F. Eastman, "Investigation of multiple carrier effects in InN epilayers using

variable magnetic field Hall measurements," *J. Cryst. Growth*, vol. 269, no. 1, pp. 29–34, 2004.

[93] I. Vurgaftman, J. R. Meyer, C. A. Hoffman, D. Redfern, J. Antoszewski, L. Faraone, and J. R. Lindemuth, "Improved quantitative mobility spectrum analysis for Hall characterization," *J. Appl. Phys.*, vol. 84, no. 9, pp. 4966–4973, 1998.

[94] D. Schroder, *Semiconductor material and device characterization*. 1900.

[95] H. Lu, W. J. Schaff, L. F. Eastman, and C. E. Stutz, "Surface charge accumulation of InN films grown by molecular-beam epitaxy," *Appl. Phys. Lett.*, vol. 82, no. 11, pp. 1736–1738, 2003.

[96] I. Mahboob, T. D. Veal, C. F. McConville, H. Lu, and W. J. Schaff, "Intrinsic Electron Accumulation at Clean InN Surfaces," *Phys. Rev. Lett.*, vol. 92, no. 3, pp. 368041–368044, 2004.

[97] P. Blood, "Capacitance-voltage profiling and the characterisation of III-V semiconductors using electrolyte barriers," *Semi. Sci. Tech.*, vol. 1, no. 1, pp. 7–27, 1986.

[98] T. Ambridge, C. R. Elliott, and M. M. Faktor, "The electrochemical characterization of n-type gallium arsenide," *J. Appl. Electrochem.*, vol. 3, no. 1, pp. 1–15, 1973.

[99] B. Sell, C. Gatzke, and J. Fernández, "Electrochemical capacitance-voltage profiling of heterostructures using small contact areas," *Semiconductor Science and Technology*, vol. 13, no. 4, pp. 423–427, 1998.

[100] J. W. L. Yim, R. E. Jones, K. M. Yu, J. W. Ager III, W. Walukiewicz, W. J. Schaff, and J. Wu, "Effects of surface states on electrical characteristics of InN and $In_{1-x}Ga_N$," *Phys. Rev. B*, vol. 76, no. 4, p. 041303, 2007.

[101] A. J. Ptak, K. S. Ziemer, M. R. Millecchia, C. D. Stinespring, and T. H. Myers, "Influence of active nitrogen species on the nitridation rate of sapphire," *MRS Internet J. Nitride Semicond. Res.*, vol. 537, no. 4S1, p. G3.10, 1999.

[102] F. Widmann, G. Feuillet, B. Daudin, and J. L. Rouviere, "Low temperature sapphire nitridation: A clue to optimize GaN layers grown by molecular beam epitaxy," *J. Appl. Phys.*, vol. 85, no. 3, pp. 1550–1555, 1999.

[103] A. J. Ptak, T. H. Myers, L. T. Romano, C. G. V. de Walle, and J. E. Northrup, "Magnesium incorporation in GaN grown by molecular-beam epitaxy," *Appl. Phys. Lett.*, vol. 78, no. 3, pp. 285–287, 2001.

[104] T. U. Kampen and W. Monch, "Barrier heights of GaN Schottky contacts," *Appl. Surf. Sci.*, vol. 117-118, pp. 388–393, 1997.

[105] B. Heying, R. Averbeck, L. F. Chen, E. Haus, H. Riechert, and J. S. Speck, "Control of GaN surface morphologies using plasma-assisted molecular beam epitaxy," *J. Appl. Phys.*, vol. 88, no. 4, pp. 1855–1860, 2000.

[106] C. Adelmann, J. Brault, D. Jalabert, P. Gentile, H. Mariette, G. Mula, and B. Daudin, "Dynamically stable gallium surface coverages during plasma-assisted molecular-beam epitaxy of (0001) GaN," *J. Appl. Phys.*, vol. 91, no. 12, pp. 9638–9645, 2002.

[107] G. Koblmuller, S. Fernandez-Garrido, E. Calleja, and J. S. Speck, "In situ investigation of growth modes during plasma-assisted molecular beam epitaxy of (0001) GaN," *Appl. Phys. Lett.*, vol. 91, no. 16, p. 161904, 2007.

[108] E. J. Tarsa, B. Heying, X. H. Wu, P. Fini, S. P. DenBaars, and J. S. Speck, "Homoepitaxial growth of GaN under Ga-stable and N-stable conditions by plasma-assisted molecular beam epitaxy," *J. Appl. Phys.*, vol. 82, no. 11, pp. 5472–5479, 1997.

[109] T. Zywietz, J. Neugebauer, and M. Scheffler, "Adatom diffusion at GaN (0001) and (000$\bar{1}$bar) surfaces," *Applied Physics Letters*, vol. 73, no. 4, pp. 487–489, 1998.

[110] K. A. Bertness, A. Roshko, L. M. Mansfield, T. E. Harvey, and N. A. Sanford, "Mechanism for spontaneous growth of GaN nanowires with molecular beam epitaxy," *J. Cryst. Growth*, vol. 310, no. 13, pp. 3154–3158, 2008.

[111] G. Koblmuller, J. Brown, R. Averbeck, H. Riechert, P. Pongratz, and J. S. Speck, "Continuous evolution of Ga adlayer coverages during plasma-assisted molecular-beam epitaxy of (0001) GaN," *Appl. Phys. Lett.*, vol. 86, no. 4, p. 041908, 2005.

[112] G. Koblmüller, R. Averbeck, H. Riechert, and P. Pongratz, "Direct observation of different equilibrium Ga adlayer coverages and their desorption kinetics on GaN (0001) and (000$\bar{1}$) surfaces," *Phys. Rev. B*, vol. 69, no. 3, p. 035325, 2004.

[113] L. He, X. Gu, J. Xie, F. Yun, A. A. Baski, and H. Morkoc, "GaN layers re-grown on etched GaN templates by plasma assisted molecular beam epitaxy," *MRS proceedings*, vol. 798, pp. 365–368, 2003.

[114] W. Qian, G. S. Rohrer, M. Skowronski, K. Doverspike, L. B. Rowland, and D. K. Gaskill, "Open-core screw dislocations in GaN epilayers observed by scanning force microscopy and high-resolution transmission electron microscopy," *Appl.Phys. Lett.*, vol. 67, no. 16, pp. 2284–2286, 1995.

[115] Z. Liliental-Weber, Y. Chen, S. Ruvimov, and J. Washburn, "Formation mechanism of nanotubes in GaN," *Phys. Rev. Lett.*, vol. 79, no. 15, pp. 2835–2838, 1997.

[116] M. A. Reshchikov and H. Morkoc, "Luminescence properties of defects in GaN," *J. Appl. Phys.*, vol. 97, no. 6, p. 061301, 2005.

[117] G. D. Chen, M. Smith, J. Y. Lin, H. X. Jiang, S.-H. Wei, M. A. Khan, and C. J. Sun, "Fundamental optical transitions in GaN," *Appl. Phys. Lett.*, vol. 68, no. 20, pp. 2784–2786, 1996.

[118] D. C. Reynolds, D. C. Look, W. Kim, O. Aktas, A. Botchkarev, A. Salvador, H. Morkoc, and D. N. Talwar, "Ground and excited state exciton spectra from GaN grown by molecular-beam epitaxy," *J. Appl. Phys.*, vol. 80, no. 1, pp. 594–596, 1996.

[119] G. Pozina, J. P. Bergman, T. Paskova, and B. Monemar, "Bound exciton dynamics in GaN grown by hydride vapor-phase epitaxy," *Appl. Phys. Lett.*, vol. 75, no. 26, pp. 4124–4126, 1999.

[120] W. Liu, M. F. Li, S. J. Xu, K. Uchida, and K. Matsumoto, "Phonon-assisted photoluminescence in wurtzite GaN epilayer," *Semi. Sci. Tech.*, vol. 13, no. 7, pp. 769–772, 1998.

[121] B. Monemar, J. Bergman, H. Amano, I. Akasaki, T. Detchprohm, K. Hiramatsu, and N. Sawaki, "Optical properties of GaN and related materials," *Proc International Symposium on Blue Laser and Light Emitting Diodes*, pp. 135–140, 1996.

[122] M. A. Reshchikov, D. Huang, F. Yun, P. Visconti, L. He, H. Morkoc, J. Jasinski, Z. Liliental-Weber, R. J. Molnar, S. S. Park, and K. Y. Lee, "Unusual luminescence lines in GaN," *J. Appl. Phys.*, vol. 94, no. 9, pp. 5623–5632, 2003.

[123] M. A. Reshchikov, J. Jasinski, Z. Liliental-Weber, D. Huang, L. He, P. Visconti, and H. Morkoc, "Photoluminescence from structural defects in GaN," *Physica B*, vol. 340-342, pp. 440–443, 2003.

[124] E. Calleja, M. A. Sánchez-García, F. J. Sánchez, F. Calle, F. B. Naranjo, E. Muñoz, U. Jahn, and K. Ploog, "Luminescence properties and defects in GaN nanocolumns grown by molecular beam epitaxy," *Phys. Rev. B*, vol. 62, no. 24, pp. 16826–16834, 2000.

[125] B.-C. Chung and M. Gershenzon, "The influence of oxygen on the electrical and optical properties of GaN crystals grown by metalorganic vapor phase epitaxy," *J. Appl. Phys.*, vol. 72, no. 2, pp. 651–659, 1992.

[126] C. Wetzel, S. Fischer, J. Kruger, E. E. Haller, R. J. Molnar, T. D. Moustakas, E. N. Mokhov, and P. G. Baranov, "Strongly localized excitons in gallium nitride," *Appl. Phys.Lett.*, vol. 68, no. 18, pp. 2556–2558, 1996.

[127] X. Zhang, P. Kung, D. Walker, A. Saxler, and M. Razeghi, "Growth of GaN without yellow luminescence," *MRS proceedings*, vol. 395, pp. 625–629, 1996.

[128] N. Grandjean, J. Massies, F. Semond, S. Y. Karpov, and R. A. Talalaev, "GaN evaporation in molecular-beam epitaxy environment," *Appl. Phys. Lett.*, vol. 74, no. 13, pp. 1854–1856, 1999.

[129] B. L. VanMil, H. Guo, L. J. Holbert, K. Lee, T. H. Myers, T. Liu, and D. Korakakis, "High temperature limitations for GaN growth by rf-plasma assisted molecular beam epitaxy: Effects of active nitrogen species, surface polarity, hydrogen, and excess Ga-overpressure," *J. Vac. Sci. Tech. B*, vol. 22, no. 4, pp. 2149–2154, 2004.

[130] Q. Guo, O. Kato, and A. Yoshida, "Thermal stability of indium nitride single crystal films," *J. Appl. Phys.*, vol. 73, no. 11, pp. 7969–7971, 1993.

[131] R. D. Jones and K. Rose, "Thermal Stability of InN," *J. Phys. Chem. Sol.*, vol. 48, no. 6, pp. 587–590, 1987.

[132] Y. Huang, H. Wang, Q. Sun, J. Chen, J. F. Wang, Y. T. Wang, and H. Yang, "Study on the thermal stability of InN by in-situ laser reflectance system," *J. Cryst. Growth*, vol. 281, no. 2-4, pp. 310–317, 2005.

[133] D. D. Koleske, A. E. Wickenden, R. L. Henry, W. J. DeSisto, and R. J. Gorman, "Growth model for GaN with comparison to structural, optical, and electrical properties," *J. Appl. Phys.*, vol. 84, no. 4, pp. 1998–2010, 1998.

[134] G. Koblmuller, R. Averbeck, L. Geelhaar, H. Riechert, W. Hosler, and P. Pongratz, "Growth diagram and morphologies of AlN thin films grown by molecular beam epitaxy," *J. Appl. Phys.*, vol. 93, no. 12, pp. 9591–9596, 2003.

[135] C. S. Gallinat, G. Koblmuller, J. S. Brown, and J. S. Speck, "A growth diagram for plasma-assisted molecular beam epitaxy of In-face InN," *J. Appl. Phys.*, vol. 102, no. 6, p. 064907, 2007.

[136] G. Koblmuller, C. S. Gallinat, and J. S. Speck, "Surface kinetics and thermal instability of N-face InN grown by plasma-assisted molecular beam epitaxy," *J. Appl. Phys.*, vol. 101, no. 8, p. 083516, 2007.

[137] H. Naoi, F. Matsuda, T. Araki, A. Suzuki, and Y. Nanishi, "The effect of substrate polarity on the growth of InN by RF-MBE," *J. Cryst. Growth*, vol. 269, no. 1, pp. 155–161, 2004.

[138] K. Xu and A. Yoshikawa, "Effects of film polarities on InN growth by molecular-beam epitaxy," *Appl. Phys. Lett.*, vol. 83, no. 2, pp. 251–253, 2003.

[139] T. D. Veal, P. D. C. King, P. H. Jefferson, L. F. J. Piper, C. F. McConville, H. Lu, W. J. Schaff, P. A. Anderson, S. M. Durbin, D. Muto, H. Naoi, and Y. Nanishi, "In adlayers on c -plane InN surfaces: A polarity-dependent study by x-ray photoemission spectroscopy," *Phys. Rev. B*, vol. 76, no. 7, p. 075313, 2007.

[140] C. S. Gallinat, G. Koblmüller, J. S. Brown, S. Bernardis, J. S. Speck, G. D. Chern, E. D. Readinger, H. Shen, and M. Wraback, "In-polar InN grown by plasma-assisted molecular beam epitaxy," *Appl. Phys. Lett.*, vol. 89, no. 3, p. 032109, 2006.

[141] P. A. Anderson, C. E. Kendrick, R. J. Kinsey, A. Asadov, W. Gao, R. J. Reeves, and S. M. Durbin, "(111) and (100) YSZ as substrates for indium nitride growth," *Phys. Stat. Sol. (c)*, vol. 2, no. 7, pp. 2320–2323, 2005.

[142] E. Dimakis, E. Iliopoulos, K. Tsagaraki, T. Kehagias, P. Komninou, and A. Georgakilas, "Heteroepitaxial growth of In-face InN on GaN (0001) by plasma-assisted molecular-beam epitaxy," *J. Appl. Phys.*, vol. 97, no. 11, p. 113520, 2005.

[143] G. Mula, C. Adelmann, S. Moehl, J. Oullier, and B. Daudin, "Surfactant effect of gallium during molecular-beam epitaxy of GaN on AlN (0001)," *Phys. Rev. B*, vol. 64, no. 19, p. 195406, 2001.

[144] P. P. Chen, H. Makino, T. X. Li, J. B. Wang, W. Lu, and T. Yao, "Optical properties of InN films grown by molecular beam epitaxy at different conditions," *Thin Solid Films*, vol. 513, no. 1-2, pp. 166–169, 2006.

[145] A. Klochikhin, V. Davydov, V. Emtsev, A. Sakharov, V. Kapitonov, B. Andreev, H. Lu, and W. J. Schaff, "Photoluminescence of n-InN with low electron concentrations," *Phys. Stat. Sol. (a)*, vol. 203, no. 1, pp. 50–58, 2006.

[146] T. V. Shubina, S. V. Ivanov, V. N. Jmerik, D. D. Solnyshkov, V. A. Vekshin, P. S. Kopev, A. Vasson, J. Leymarie, A. Kavokin, H. Amano, K. Shimono, A. Kasic, and B. Monemar, "Mie Resonances, Infrared Emission, and the Band Gap of InN," *Phys. Rev. Lett.*, vol. 92, no. 11, p. 117407, 2004.

[147] J. C. Ho, P. Specht, Q. Yang, X. Xu, D. Hao, and E. R. Weber, "Effects of stoichiometry on electrical, optical, and structural properties of indium nitride," *J. Appl. Phys.*, vol. 98, no. 9, p. 093712, 2005.

[148] Y. F. Ng, Y. G. Cao, M. H. Xie, X. L. Wang, and S. Y. Tong, "Growth mode and strain evolution during InN growth on GaN(0001) by molecular-beam epitaxy," *Appl. Phys. Lett.*, vol. 81, no. 21, pp. 3960–3962, 2002.

[149] P. A. Anderson, R. J. Reeves, and S. M. Durbin, "RF plasma sources for III-nitrides growth: Influence of operating conditions and device geometry on active species production and InN film properties," *Phys. Stat. Sol. (a)*, vol. 203, no. 1, pp. 106–111, 2006.

[150] V. Lebedev, F. M. Morales, V. Cimalla, J. G. Lozano, D. Gonzalez, M. Himmerlich, S. Krischok, J. A. Schaefer, and O. Ambacher, "Correlation between structural and electrical properties of InN thin films prepared by molecular beam epitaxy," *Superlattices and Microstructures*, vol. 40, no. 4-6 SPEC. ISS., pp. 289–294, 2006.

[151] H. Lu, W. J. Schaff, J. Hwang, H. Wu, G. Koley, and L. F. Eastman, "Effect of an AlN buffer layer on the epitaxial growth of InN by molecular-beam epitaxy," *Appl. Phys. Lett.*, vol. 79, no. 10, pp. 1489–1491, 2001.

[152] S. Yamaguchi, M. Kariya, S. Nitta, T. Takeuchi, C. Wetzel, H. Amano, and I. Akasaki, "Structural properties of InN on GaN grown by metalorganic vapor-phase epitaxy," *J. Appl. Phys.*, vol. 85, no. 11, pp. 7682–7688, 1999.

[153] J. S. Speck and S. J. Rosner, "The role of threading dislocations in the physical properties of GaN and its alloys," *Physica B*, vol. 273-274, pp. 24–32, 1999.

[154] V. Cimalla, V. Lebedev, F. M. Morales, M. Niebelschutz, G. Ecke, R. Goldhahn, and O. Ambacher, "Origin of n-type conductivity in nominally undoped InN," *Materialwissenschaft und Werkstofftechnik*, vol. 37, no. 11, pp. 924–928, 2006.

[155] S. X. Li, K. M. Yu, J. Wu, R. E. Jones, W. Walukiewicz, J. W. Ager, W. Shan, E. E. Haller, H. Lu, and W. J. Schaff, "Fermi-level stabilization energy in group III nitrides," *Phys. Rev. B*, vol. 71, no. 16, pp. 1–4, 2005.

[156] R. K. Debnath, R. Meijers, T. Richter, T. Stoica, R. Calarco, and H. Luth, "Mechanism of molecular beam epitaxy growth of GaN nanowires on Si(111)," *Appl. Phys. Lett.*, vol. 90, no. 12, p. 123117, 2007.

[157] K. A. Dick, Z. Geretovszky, A. Mikkelsen, L. S. Karlsson, E. Lundgren, J. Malm, J. N. Andersen, L. Samuelson, W. Seifert, B. A. Wacaser, and K. Deppert, "Improving InAs nanotree growth with composition-controlled Au-In nanoparticles," *Nanotechnology*, vol. 17, no. 5, pp. 1344–1350, 2006.

[158] K. A. Dick, K. Deppert, T. Martensson, W. Seifert, and L. Samuelson, "Growth of GaP nanotree structures by sequential seeding of 1D nanowires," *J. Cryst. Growth*, vol. 272, no. 1-4 SPEC. ISS., pp. 131–137, 2004.

[159] J. Su, G. Cui, M. Gherasimova, H. Tsukamoto, J. Han, D. Ciuparu, S. Lim, L. Pfefferle, Y. He, A. V. Nurmikko, C. Broadbridge, and A. Lehman, "Catalytic growth of group III-nitride nanowires and nanostructures by metalorganic chemical vapor deposition," *Appl. Phys. Lett.*, vol. 86, no. 1, p. 013105, 2005.

[160] L. Manna, D. J. Milliron, A. Meisel, E. C. Scher, and A. P. Alivisatos, "Controlled growth of tetrapod-branched inorganic nanocrystals," *Nature Mat.*, vol. 2, no. 6, pp. 382–385, 2003.

[161] Y. Yang, D. S. Kim, R. Scholz, M. Knez, S. M. Lee, U. Gosele, and M. Zacharias, "Hierarchical three-dimensional ZnO and their shape-preserving transformation into hollow $ZnAl_2O_4$ nanostructures," *Chem. Mat.*, vol. 20, no. 10, pp. 3487–3494, 2008.

[162] S. Vaddiraju, A. Mohite, A. Chin, M. Meyyappan, G. Sumanasekera, B. W. Alphenaar, and M. K. Sunkara, "Mechanisms of 1D crystal growth in reactive vapor transport: Indium nitride nanowires," *Nano Lett.*, vol. 5, no. 8, pp. 1625–1631, 2005.

[163] C. Y. Nam, D. Tham, and J. E. Fischer, "Effect of the polar surface on GaN nanostructure morphology and growth orientation," *Appl. Phys. Lett.*, vol. 85, no. 23, pp. 5676–5678, 2004.

[164] F. M. Ross, J. Tersoff, and M. C. Reuter, "Sawtooth Faceting in Silicon Nanowires," *Phy. Rev. Lett.*, vol. 95, no. 14, p. 146104, 2005.

[165] K. A. Dick, K. Deppert, L. S. Karlsson, M. W. Larsson, W. Seifert, L. R. Wallenberg, and L. Samuelson, "Directed growth of branched nanowire structures," *MRS Bulletin*, vol. 32, no. 2, pp. 127–133, 2007.

[166] H. M. Kim, D. S. Kim, D. Y. Kim, T. W. Kang, Y. H. Cho, and K. S. Chung, "Growth and characterization of single-crystal GaN nanorods by hydride vapor phase epitaxy," *Appl. Phys. Lett.*, vol. 81, no. 12, pp. 2193–2195, 2002.

[167] R. Ghosh and D. Basak, "Quantum confinement of excitons in dendrite-like GaN nanowires," *J. Appl. Phys.*, vol. 98, no. 8, p. 086104, 2005.

[168] H. W. Seo, S. Y. Bae, J. Park, H. N. Yang, K. S. Park, and S. Kim, "Strained gallium nitride nanowires," *J. Chem. Phys.*, vol. 116, no. 21, pp. 9492–9499, 2002.

[169] P. Harrison, *Quantum Wells, Wires and Dots.* West Sussex: John Wiley and Sons Ltd, 2005.

[170] W. W. Chow and S. W. Koch, *GaN and Related II.* GaN and Related II, Amsterdam: Gordon and Breach Science, 2000.

[171] M. Suzuki and T. Uenoyama, "Strain effect on electronic and optical properties of GaN/AlGaN quantum-well lasers," *J. Appl. Phys.*, vol. 80, no. 12, pp. 6868–6874, 1996.

[172] A. Levitt, *Whisker Technology.* New York: Wiley-Interscience, 1970.

[173] K. Shorlin and M. Zinke-Allmang, "Shape cycle of Ga clusters on GaAs during coalescence growth," *Surface Science*, vol. 601, no. 12, pp. 2438–2444, 2007.

[174] H. Naoi, D. Muto, T. Hioka, Y. Hayakawa, A. Suzuki, T. Araki, and Y. Nanishi, "Thermal and chemical stabilities of In- And N-polar InN surfaces," *Phys. Stat. Sol. (B)*, vol. 244, no. 6, pp. 1834–1838, 2007.

[175] B. V. L'vov, "Kinetics and mechanism of thermal decomposition of GaN," *Thermochimica Acta*, vol. 360, no. 1, pp. 85–91, 2000.

[176] D. D. Koleske, A. E. Wickenden, R. L. Henry, J. C. Culbertson, and M. E. Twigg, "GaN decomposition in H_2 and N_2 at MOVPE temperatures and pressures," *Journal of Crystal Growth*, vol. 223, no. 4, pp. 466–483, 2001.

[177] J. C. Berg, *Wettability.* New York: M. Dekker, 1993.

[178] K. Matsushita, T. Monbara, K. Nakayama, H. Naganuma, S. Okuyama, and K. Okuyama, "In-situ observation of GaAs surface in high vacuum by contact angle measurement," *Elec. Com. Part II: Elec.*, vol. 84, no. 11, pp. 51–59, 2001.

[179] R. J. Good, "A thermodynamic derivation of Wenzel's modification of young's equation for contact angles; together with a theory of hysteresis," *J. Am. Chem. Soc.*, vol. 74, no. 20, pp. 5041–5042, 1952.

[180] R. N. Wenzel, "Surface roughness and contact angle," *J. Phys. Col. Chem.*, vol. 53, no. 9, pp. 1466–1467, 1949.

[181] J. J. Bikerman, "Surface roughness and contact angle," *J. Phys. Col. Chem.*, vol. 54, no. 5, pp. 653–658, 1950.

[182] Y. X. Chen, L. J. Campbell, and W. L. Zhou, "Self-catalytic branch growth of SnO_2 nanowire junctions," *Journal of Crystal Growth*, vol. 270, no. 3-4, pp. 505–510, 2004.

[183] Y. Su, X. Liang, S. Li, Y. Chen, Q. Zhou, S. Yin, X. Meng, and M. Kong, ""self-catalytic vls growth and optical properties of single-crystalline geo_2 nanowire arrays"," *Mat. Lett.*, vol. 62, no. 6-7, pp. 1010–1013, 2008.

[184] V. G. Dubrovskii, N. V. Sibirev, G. E. Cirlin, J. C. Harmand, and V. M. Ustinov, "Theoretical analysis of the vapor-liquid-solid mechanism of nanowire growth during molecular beam epitaxy," *Phys. Rev. E*, vol. 73, no. 2, p. 021603, 2006.

[185] J. B. Hannon, S. Kodambaka, F. M. Ross, and R. M. Tromp, "The influence of the surface migration of gold on the growth of silicon nanowires," *Nature*, vol. 440, no. 7080, pp. 69–71, 2006.

[186] K. A. Bertness, N. A. Sanford, J. M. Barker, J. B. Schlager, A. Roshko, A. V. Davydov, and I. Levin, "Catalyst-free growth of GaN nanowires," *J. Elect. Mat.*, vol. 35, no. 4, pp. 576–580, 2006.

[187] R. Calarco and M. Marso, "GaN and InN nanowires grown by MBE: A comparison," *Appl. Phys. A*, vol. 87, no. 3, pp. 499–503, 2007.

[188] L. Schubert, P. Werner, N. D. Zakharov, G. Gerth, F. M. Kolb, L. Long, U. Gosele, and T. Y. Tan, "Silicon nanowhiskers grown on ¡111¿Si substrates by molecular-beam epitaxy," *Appl. Phys. Lett.*, vol. 84, no. 24, pp. 4968–4970, 2004.

[189] K. A. Bertness, A. Roshko, L. M. Mansfield, T. E. Harvey, and N. A. Sanford, "Nucleation conditions for catalyst-free GaN nanowires," *J. Cryst. Growth*, vol. 300, no. 1, pp. 94–99, 2007.

[190] E. I. Givargizov, "Fundamental aspects of VLS growth," *J. Cryst. Growth*, vol. 31, pp. 20–30, 1975.

[191] J. Bao, M. Zimmler, F. Capasso, X. Wang, and Z. Ren, "Broadband ZnO Single-Nanowire Light-Emitting Diode," *Nano Lett.*, vol. 6, no. 8, pp. 1719–1722, 2006.

[192] J. S. Hwang, D. Ahn, S. H. Hong, H. K. Kim, S. W. Hwang, B. Jeon, and J. Choi, "Effect of Ti thickness on contact resistance between GaN nanowires and Ti/Au electrodes," *Appl. Phys. Lett.*, vol. 85, no. 9, pp. 1636–1638, 2004.

[193] Y. Cui, U. Banin, M. T. Bjork, and A. P. Alivisatos, "Electrical transport through a single nanoscale semiconductor branch point," *Nano Lett.*, vol. 5, no. 7, pp. 1519–1523, 2005.

[194] E. Stern, G. Cheng, E. Cimpoiasu, R. Klie, S. Guthrie, J. Klemic, I. Kretzschmar, E. Steinlauf, D. Turner-Evans, E. Broomfield, J. Hyland, R. Koudelka, T. Boone, M. Young, A. Sanders, R. Munden, T. Lee, D. Routenberg, and M. A. Reed, "Electrical characterization of single GaN nanowires," *Nanotechnology*, vol. 16, no. 12, pp. 2941–2953, 2005.

[195] R. Calarco, M. Marso, T. Richter, A. I. Aykanat, R. Meijers, A. V. D. Hart, T. Stoica, and H. Luth, "Size-dependent photoconductivity in MBE-grown GaN - Nanowires," *Nano Lett.*, vol. 5, no. 5, pp. 981–984, 2005.

[196] M. Niebelschutz, V. Cimalla, O. Ambacher, T. Machleidt, J. Ristic, and E. Calleja, "Electrical performance of gallium nitride nanocolumns," *Physica E*, vol. 37, no. 1-2, pp. 200–203, 2007.

[197] D. Suyatin, j. Sun, A. Fuhrer, D. Wallin, L. Frberg, L. Karlsson, I. Maximov, L. Wallenberg, L. Samuelson, and H. Xu, "Electrical Properties of Self-assembled Branched InAs Nanowire Junctions," *Nano Lett.*, vol. 8, no. 4, pp. 1100–1104, 2008.

[198] C. A. Berven, V. Dobrokhotov, D. N. McIlroy, S. Chava, R. Abdelrahaman, A. Heieren, J. Dick, and W. Barredo, "Gas sensing with mats of gold-nanoparticle decorated GaN nanowires," *IEEE Sensors Journal*, vol. 8, no. 6, pp. 930–935, 2008.

[199] T. Martensson, C. Svensson, B. Wacaser, M. Larsson, W. Seifert, K. Deppert, A. Gustafsson, L. Wallenberg, and L. Samuelson, "Epitaxial III-V Nanowires on Silicon," *Nano Lett.*, vol. 4, no. 10, pp. 1987–1990, 2004.

[200] L. Dobos, B. Pecz, L. Toth, Z. J. Horvath, Z. E. Horvath, B. Beaumont, and Z. Bougrioua, "Structural and electrical properties of Au and Ti/Au contacts to n-type GaN," *Vacuum*, vol. 82, no. 8, pp. 794–798, 2008.

[201] G. D. J. Smit, S. Rogge, and T. M. Klapwijk, "Scaling of nano-Schottky-diodes," *Appl. Phys. Lett.*, vol. 81, no. 20, pp. 3852–3854, 2002.

[202] A. Khandelwal, D. Jena, J. Grebinski, K. Hull, and M. Kuno, "Ultrathin CdSe nanowire field-effect transistors," *J. Elec. Mat.*, vol. 35, no. 1, pp. 170–172, 2006.

[203] J. Neugebauer and C. G. Van de Walle, "Theory of point defects and complexes in GaN," *Mater. Res. Soc. Symp.*, vol. 395, pp. 645–656, 1996.

[204] C. G. Van De Walle and J. Neugebauer, "First-principles calculations for defects and impurities: Applications to III-nitrides," *J. Appl. Phys.*, vol. 95, no. 8, pp. 3851–3879, 2004.

[205] W. Walukiewicz, "Intrinsic limitations to the doping of wide-gap semiconductors," *Phys. B*, vol. 302-303, pp. 123–134, 2001.

[206] W. Walukiewicz, J. W. A. III, K. M. Yu, Z. Liliental-Weber, J. Wu, S. X. Li, R. E. Jones, and J. D. Denlinger, "Structure and electronic properties of InN and In-rich group III-nitride alloys," *J. Phys. D*, vol. 39, no. 5, pp. R83–R99, 2006.

[207] J. Wu, W. Walukiewicz, S. X. Li, R. Armitage, J. C. Ho, E. R. Weber, E. E. Haller, H. Lu, W. J. Schaff, A. Barcz, and R. Jakiela, "Effects of electron concentration on the optical absorption edge of InN," *Appl. Phys. Lett.*, vol. 84, no. 15, pp. 2805–2807, 2004.

[208] A. V. Blant, T. S. Cheng, N. J. Jeffs, L. B. Flannery, I. Harrison, J. F. W. Mosselmans, A. D. Smith, and C. T. Foxon, "EXAFS studies of Mg doped InN grown on Al_2O_3," *Mat. Sci. Eng. (b)*, vol. 59, no. 1-3, pp. 218–221, 1999.

[209] V. V. Mamutin, V. A. Vekshin, V. Y. Davydov, V. V. Ratnikov, Y. A. Kudriavtsev, B. Y. Ber, V. V. Emtsev, and S. V. Ivanov, "Mg-doped hexagonal InN/Al_2O_3 films grown by MBE," *Phys. Stat. Sol. (a)*, vol. 176, no. 1, pp. 373–378, 1999.

[210] R. E. Jones, K. M. Yu, S. X. Li, W. Walukiewicz, J. W. Ager, E. E. Haller, H. Lu, and W. J. Schaff, "Evidence for p-type doping of InN," *Phys. Rev. Lett.*, vol. 96, no. 12, p. 125505, 2006.

[211] X. Wang, S.-B. Che, Y. Ishitani, A. Yoshikawa, H. Sasaki, T. Shinagawa, and S. Yoshida, "Polarity inversion in high Mg-doped In-polar InN epitaxial layers," *Appl. Phys. Lett.*, vol. 91, no. 8, p. 081912, 2007.

[212] X. Wang, S.-B. Che, Y. Ishitani, and A. Yoshikawa, "Systematic study on p-type doping control of InN with different Mg concentrations in both In and N polarities," *Appl. Phys. Lett.*, vol. 91, no. 24, p. 242111, 2007.

[213] X. Wang, S. Che, Y. Ishitani, and A. Yoshikawa, "Hole mobility in Mg-doped p-type InN films," *Appl. Phys. Lett.*, vol. 92, no. 13, p. 132108, 2008.

[214] N. Khan, N. Nepal, A. Sedhain, J. Y. Lin, and H. X. Jiang, "Mg acceptor level in InN epilayers probed by photoluminescence," *Appl. Phys. Lett.*, vol. 91, no. 1, p. 012101, 2007.

[215] C. H. Swartz, S. M. Durbin, P. A. Anderson, D. Carder, R. J. Reeves, S. Chandril, T. H. Myers, V. J. Kennedy, and S. P. Ahrenkiel, "Mg doping of InN and the use of yttrium-stabilised zirconia substrates," *phys. stat. sol. (c)*, vol. 5, no. 2, pp. 508–510, 2008.

[216] P. Anderson, "Thesis: Indium Nitride: An Investigation of Growth, Electronic Structure and Doping," 2001.

[217] E. Haus, I. P. Smorchkova, B. Heying, P. Fini, C. Poblenz, T. Mates, U. K. Mishra, and J. S. Speck, "The role of growth conditions on the p-doping of GaN by plasma-assisted molecular beam epitaxy," *J. Cryst. Growth*, vol. 246, no. 1-2, pp. 55–63, 2002.

[218] D. Muto, T. Araki, H. Naoi, F. Matsuda, and Y. Nanishi, "Polarity determination of InN by wet etching," *Phys. Stat. Sol. a*, vol. 202, no. 5, pp. 773–776, 2005.

[219] A. A. Klochikhin, V. Y. Davydov, V. V. Emtsev, A. V. Sakharov, V. A. Kapitonov, B. A. Andreev, H. Lu, and W. J. Schaff, "Acceptor states in the

photoluminescence spectra of n-InN," *Phys. Rev. B*, vol. 71, no. 19, p. 195207, 2005.

[220] G. W. Shu, P. F. Wu, M. H. Lo, J. L. Shen, T. Y. Lin, H. J. Chang, Y. F. Chen, C. F. Shih, C. A. Chang, and N. C. Chen, "Concentration dependence of carrier localization in InN epilayers," *Appl. Phys. Lett.*, vol. 89, no. 13, p. 131913, 2006.

[221] B. Arnaudov, T. Paskova, P. P. Paskov, B. Magnusson, E. Valcheva, B. Monemar, H. Lu, W. J. Schaff, H. Amano, and I. Akasaki, "Energy position of near-band-edge emission spectra of InN epitaxial layers with different doping levels," *Phys. Rev. B*, vol. 69, no. 11, pp. 1152161–1152165, 2004.

[222] D.-J. Jang, G.-T. Lin, C.-L. Hsiao, L. W. Tu, and M.-E. Lee, "Auger recombination in InN thin films," *Appl. Phys. Lett.*, vol. 92, no. 4, p. 042101, 2008.

[223] Y. C. Shen, G. O. Mueller, S. Watanabe, N. F. Gardner, A. Munkholm, and M. R. Krames, "Auger recombination in InGaN measured by photoluminescence," *Appl. Phys. Lett.*, vol. 91, no. 14, p. 141101, 2007.

[224] F. Chen, A. N. Cartwright, H. Lu, and W. J. Schaff, "Ultrafast carrier dynamics in InN epilayers," *J. Cryst. Growth*, vol. 269, no. 1, pp. 10 – 14, 2004.

[225] J. R. Dixon, "Anomalous Electrical Properties of p-Type Indium Arsenide," *J. Appl. Phys.*, vol. 30, no. 9, pp. 1412–1416, 1959.

[226] I. Melngailis and R. H. Rediker, "Properties of InAs Lasers," *J Appl. Phys.*, vol. 37, no. 2, pp. 899–911, 1966.

[227] F. Ermanis and K. Wolfstirn, "Hall Effect and Resistivity of Zn-Doped GaAs," *J Appl. Phys.*, vol. 37, no. 5, pp. 1963–1966, 1966.

[228] P. J. Dean, E. G. Schönherr, and R. B. Zetterstrom, "Pair Spectra Involving the Shallow Acceptor Mg in GaP," *J. Appl. Phys.*, vol. 41, no. 8, pp. 3475–3479, 1970.

[229] J. I. Pankove and P. E. Norris, "Luminescence from GaN MIS diodes," *R.C.A. Review*, vol. 33, no. 2, pp. 377–382, 1972.

[230] J. I. Pankove, J. E. Berkeyheiser, and E. A. Miller, "Properties of Zn-doped GaN. I. Photoluminescence," *J. Appl. Phys.*, vol. 45, no. 3, pp. 1280–1286, 1974.

[231] B. Monemar, O. Lagerstedt, and H. P. Gislason, "Properties of Zn-doped VPE-grown GaN. I. Luminescence data in relation to doping conditions," *J. Appl. Phys.*, vol. 51, no. 1, pp. 625–639, 1980.

[232] N. I. Kuznetsov, A. E. Nikolaev, A. S. Zubrilov, Y. V. Melnik, and V. A. Dmitriev, "Insulating GaN:Zn layers grown by hydride vapor phase epitaxy on SiC substrates," *Appl. Phys. Lett.*, vol. 75, no. 20, pp. 3138–3140, 1999.

[233] L.-C. Chen, W.-H. Lan, R.-M. Lin, H.-T. Shen, and H.-C. Chen, "Optical properties of In_2O_3 oxidized from InN deposited by reactive magnetron sputtering," *Appl. Surf. Sci.*, vol. 252, no. 24, pp. 8438–8441, 2006.

[234] L.-C. Chen and H.-C. Chen, "Annealing characteristics of Zn-doped InN Films on sapphire substrates by reactive magnetron sputtering," *Jap. J. Appl. Phys. Part 1*, vol. 44, no. 5 A, pp. 2995–2997, 2005.

[235] F. Chen, A. N. Cartwright, H. Lu, and W. J. Schaff, "Temperature-dependent optical properties of wurtzite InN," *Physica E*, vol. 20, no. 3-4, pp. 308–312, 2004.

[236] M. D. Yang, J. L. Shen, M. C. Chen, C. C. Chiang, S. M. Lan, T. N. Yang, M. H. Lo, H. C. Kuo, T. C. Lu, P. J. Huang, S. C. Hung, G. C. Chi, and W. C. Chou, "Optical studies of InN epilayers on Si substrates with different buffer layers," *J. Appl. Phys.*, vol. 102, no. 11, p. 113514, 2007.

[237] G. Shu, M. Lo, M. Yang, C. Hsu, J. Shen, and S. Lan, "Carrier localization in InN epilayers grown on Si substrates," *Sol. Stat. Com*, vol. 141, no. 3, pp. 109–112, 2007.

[238] Q. Li, S. J. Xu, M. H. Xie, and S. Y. Tong, "Origin of the ‘S-shaped’ temperature dependence of luminescent peaks from semiconductors," *J. of Phys.: Condensed Matter*, vol. 17, no. 30, pp. 4853–4858, 2005.

[239] M. Feneberg, J. Daubler, K. Thonke, R. Sauer, P. Schley, and R. Goldhahn, "Mahan excitons in degenerate wurtzite InN: Photoluminescence spectroscopy and reflectivity measurements," *Phys. Rev. B*, vol. 77, no. 24, p. 245207, 2008.

[240] Y. Yacoby, M. Sowwan, E. Stern, J. O. Cross, D. Brewe, R. Pindak, J. Pitney, E. M. Dufresne, and R. Clarke, "Direct determination of epitaxial interface structure in Gd_2O_3 passivation of GaAs," *Nature Materials*, vol. 1, no. 2, pp. 99–101, 2002.

[241] E. Stern, G. Cheng, J. F. Klemic, E. Broomfield, D. Turner-Evans, C. Li, C. Zhou, and M. A. Reed, "Methods for fabricating Ohmic contacts to nanowires and nanotubes," *J. Vac. Sci. Tech. (b)*, vol. 24, no. 1, pp. 231–236, 2006.

[242] A. A. Talin, G. T. Wang, E. Lai, and R. J. Anderson, "Correlation of growth temperature, photoluminescence, and resistivity in GaN nanowires," *Appl. Phys. Lett.*, vol. 92, no. 9, p. 093105, 2008.

APPENDIX A: EBL PROCESS FOR CONTACTING TO GAN NANOWIRES

Preparation of the Substrate

1. First a piece of substrate containing the nanowires is placed in high purity methanol in a ultrasonic bath of 10 s, as a low quality solvent leads to residue on the processing substrate and nanowires.

2. A drop of the solution (now containing freed nanowires) is placed on a SiN/SiO_2 substrate.

3. The nanowire containing substrate is then baked at 185°C to dry out the sample.

4. A bilayer of polymethyl methacrylate (PMMA) is applied: first a 4% low molecular weight (LMW) layer is spun on at 3000 rpm and baked for half an hour at 185°C, then following this a 2.5% high molecular weight (HMW) layer is spun on at 4000 rpm and baked for half an hour at 185°C. The bilayer has a total thickness of 400 nm and due to the different weight of the PMMA layers an undercut is introduced when developed; as at the same energy dose the low molecular weight is overexposed compared to the high molecular weight PMMA, therefore improving the lift-off of the metal. This resist layer is used to create contact markers.

Pattern and Contact Fabrication

1. The actual contact process begins by locating a target nanowire with single scans of the e-beam, which allows for the surface to be viewed without exposing the resist.

2. Markers are exposed around the nanowire and then a Ti/Au (20 nm/ 40 nm) bilayer is evaporated on, using a thermal metal evaporator.

3. Boiling acetone is then employed to ensure a clean lift-off of the metal.

4. Using the markers, the nanowires are imaged with the SEM and a contact mask is designed.

5. The substrate is then coated with a double layer of the PMMA bilayer to increase the total PMMA thickness to 800 nm.

6. The resist thickness allows for Ti/Au contacts as thick as 120 nm to be fabricated, which has enabled current–voltage measurements to be made.

Using the new process it is possible to contact four branching GaN nanowires with three contact pads each in a total of ten hours fabricating time.